

An open-source based microscope for quantitative biological imaging with single molecule sensitivity

Inaugural-Dissertation
to obtain the academic degree
Doctor rerum naturalium (Dr. rer. nat.)

Fachbereich Biologie, Chemie, Pharmazie
Freie Universität Berlin

By:
Ando Christian Zehrer
Berlin, 2023

1. Reviewer **Dr. Helge Ewers**
Fachbereich Biologie, Chemie, Pharmazie
Freie Universität Berlin

2. Reviewer **Dr. Stephan Block**
Fachbereich Biologie, Chemie, Pharmazie
Freie Universität Berlin

Date of defense: *24th of November 2023*

Acknowledgements

First, I would like to thank Helge for the supervision and the guidance. I really found purpose in the project i worked on, and even though the project was at times challenging, I really appreciated the enthusiasm and the can-do attitude helping me to bring this project to completion.

Secondly, I thank Benedikt for all the help, the ideas, the moral support and the high degree of patience for assisting me with all the issues that seemed to appear on a weekly basis. This also includes Haoran, my friend and chinese food expert from Jena.

I am thankful for the productive collaboration with Saskia, the discussions and the moral support during the long and tiresome imaging sessions.

Many thanks to Jia, Purba, Alex and Raluca for the nice discussions, cinema thursdays and activities in and outside the lab.

Thank you also to Gresy, Giorgia, Alex and Luis for the coffee breaks, the mood boosts, the food adventures and the afternoon beers.

Thank you Claire, Andrea for all the help in the lab and Manuela for the administrative assistance.

Thanks to all the members of the Happy Lab: Mengfei, Jia, Iwona, Saskia, Purba, Jakob, Ria, Ella, Micha, Kita, Nadja, Vladka, Caroline, Reinmar, Andrea, Bas, Amin, Claire, Markus, Olivia, Hylkje, Steven, Valentin, Caro and all other members over the years, for the relaxed atmosphere, the advice, the cakes etc...

Thank you to Caroline and Roman who supported me as students and contributed to the completion of projects I worked on.

Many thanks to Bas, Chetana and Purba for proof-reading my thesis and for the constructive feedback.

Thank you to all my friends in Berlin, for the moral support, the unforgettable nights-out, the fun activities and so much more, truly making the time I spent in Berlin special.

Finally, I am thankful to my family who supported me my whole life and encouraged me in so many ways to pursue my path.

Selbstständigkeitserklärung

Name: Zehrer

Vorname: Ando Christian

Hierdurch versichere ich, dass ich meine Dissertation selbstständig verfasst und keine anderen als die von mir angegeben Quellen und Hilfsmittel verwendet habe. Geistiges Eigentum anderer Autoren wurde als entsprechend gekennzeichnet. Ebenso versichere ich, dass ich an keiner anderen Stelle ein Prüfungsverfahren beantragt bzw. die Dissertation in dieser oder anderer Form an keiner anderen Fakultät als Dissertation vorgelegt habe.

Berlin, den 15.12.2023

Abstract

Modern commercial fluorescence microscopes allow to study cellular features on the nanoscopic level, using innovative optical principles and continuously improving sample preparation technologies. However, the complexity of an instrument and the associated price scale with the attainable resolution and the image quality. Open-source concepts such as the UC2 (You. See. Too.) microscopy toolbox have proven to be low-cost versatile alternative to adapt a microscope to the requirements of an experiment, allowing to interface various optical components which were initially exclusive to commercial systems. Unfortunately, the versatility and the use of low-cost components often results in a loss of image quality and resolution.

To overcome this challenge, I incorporated a high quality objective into an UC2-based microscope assembled from easily available optics, affordable electronics and 3D printed parts. The setup is considerably cheaper than its commercial counterparts while providing a maximum of capabilities, thereby providing a proof of concept that high-quality quantitative data can be generated with a low-budget system. The modalities applied include high quality imaging of fixed and live cells in both fluorescent and bright-field channels, as well as continuous measurements of live-cells inside an incubator, single particle tracking of membrane molecules and super-resolution imaging. In one application, single particle tracking of GPI anchored GFP in the cellular plasma membrane was performed and a diffusion coefficient matching the values found in literature was determined. In a second application, single molecule localization microscopy was used to surpass the resolution limit imposed by light diffraction. Hereby, the extrapolated diameter of microtubules was in accordance with values measured on a higher cost setup. Low budget optics i.e. objectives have reduced light collection capability, are prone to optical aberrations and cannot correct irregularities within the wavefront. In an effort to further increase the setup's accessibility, low-budget objective lenses were assessed to determine for which imaging assays they were employable.

In a second part of the project, various tools have been used in order to facilitate the analysis of microscopy data, with emphasis on single molecule localization microscopy. Machine learning based techniques were tested to ensure the automation of image analysis pipelines, thereby aiming to reduce the demand for manual processing of large data-sets. Clustering of the single molecules positions is a technique that helps to understand the underlying pathways when studying the emergence of signaling events at the plasma membrane. Bayesian Cluster Analysis and visualization application is a software that facilitates the access to clustering through an user-friendly GUI, a reduced complexity for

the user and an increased efficiency of the computational load. After benchmarking the algorithm on simulations of clustered cell membranes, the clustering behaviour of the CD95 receptor was characterized on actual samples. Further experiments will investigate the receptor organisation upon ligand activation to gain insights into the pathways initiated by the receptor.

Zusammenfassung

Moderne handelsübliche Fluoreszenzmikroskope ermöglichen die Untersuchung zellulärer Merkmale auf nanoskopischer Ebene, durch den Einsatz innovativer optischer Prinzipien und sich ständig verbessernden Probenvorbereitungstechnologien. Die Komplexität eines Instruments sowie der damit einhergehende Preis hängen jedoch von der erreichbaren Auflösung und der Bildqualität ab. Open-Source-Konzepte wie die UC2 (You.See.To.)-Mikroskopie-Toolbox haben sich als kostengünstige und vielseitige Alternativen zur Anpassung eines Mikroskops an den Anforderungen eines Experiments erwiesen. Zugleich ermöglicht das System die Anbindung verschiedener optischer Komponenten, die ursprünglich für bestimmte kommerzielle Systeme konzipiert wurden. Leider führen die Vielseitigkeit des Systems sowie die Verwendung kostengünstiger Komponenten oft zu Einbußen in Bildqualität und Auflösung.

Um diese Herausforderung zu meistern, habe ich ein hochwertiges Objektiv in ein Mikroskop auf UC2-Basis eingebaut. Letzteres wurde aus leicht erhältlichen Optiken, erschwinglicher Elektronik und 3D-gedruckten Teilen zusammengesetzt. Der Aufbau ist deutlich günstiger als kommerzielle Alternativen mit ähnlichen Funktionen, bietet aber gleichzeitig ein Maximum an Anwendungen. Somit wird der grundlegende Beweis geliefert, dass mit einem Low-Budget-System qualitativ hochwertige Daten generiert werden können und dadurch quantitative Experimente ermöglicht werden. Zu den angewandten Modalitäten gehörten die Bildgebung von fixierten und lebenden Zellen sowohl im Fluoreszenz- als auch im Hellfeldkanal sowie kontinuierliche Messungen von lebenden Zellen in einem Inkubator, die Einzelpartikelverfolgung von Membranmolekülen und die supraauflösende Bildgebung. So wurden beispielsweise einzelne GPI-verankerte GFP Partikel an der Plasmamembran verfolgt und ein Diffusionskoeffizient ermittelt, der mit den in der Literatur gefundenen Werten übereinstimmt. In einem anderen Experiment wurde Einzelmolekül-Lokalisierungsmikroskopie eingesetzt, um die durch die Lichtbeugung auferlegte Auflösungsgrenze zu durchbrechen. Der dabei extrapolierte Durchmesser von zellulären Mikrotubuli war mit den Werten vereinbar, die mit einem teureren und qualitativ hochwertigen Mikroskop gemessen wurden. Low-Budget-Optiken, d. h. Objektive, haben eine geringere Lichtsammelfähigkeit, sind anfällig für optische Aberrationen und können die Wellenfront nicht effektiv korrigieren. Um den Zugang zu Mikroskopie Hardware zu erleichtern, wurden Low-Budget-Objektive getestet, um festzustellen, für welche Bildgebungsverfahren diese geeignet sein könnten.

In einem zweiten Teil des Projekts wurden verschiedene software Lösungen eingesetzt, um die Analyse von Mikroskopiebilder zu erleichtern, insbesondere die Verarbeitung von

durch Einzelmoleküllokalisierungsmikroskopie erzeugte Daten. Auf maschinellem Lernen basierende Techniken zur Automatisierung von Analysepipelines wurden getestet, um den Bedarf an manueller Verarbeitung großer Datensätze zu verringern. Das Clustering der Positionen einzelner Moleküle ist eine Methode, die bei der Untersuchung der Entstehung von Signalereignissen an der Zellmembran helfen kann, die zugrunde liegenden Wege zu verstehen. Die Bayes'sche Clusteranalyse- und Visualisierungsanwendung ist eine Software, die den Zugang zum Clustering erleichtert. Dies erfolgt durch eine benutzerfreundliche GUI sowie dadurch, dass die Komplexität für den Benutzer reduziert wird und die Verteilung der Rechenlast die Effizienz steigert. Nach einem Benchmarking des Algorithmus anhand von Simulationen von geclusterten Zellmembranen wurde das Clustering-Verhalten des CD95-Rezeptors an realen Proben charakterisiert. In weiteren Experimenten soll die Organisation des Rezeptors bei Ligandenaktivierung untersucht werden, um Einblicke in die vom Rezeptor initiierten Signalwege zu gewinnen.

Contents

1	Introduction	7
1.1	Scales in bio-imaging	7
1.2	The cell cytoskeleton	8
1.3	The cell membrane	9
1.3.1	Membrane molecule diffusion	10
1.4	Conventional light microscopy	11
1.5	Fluorescence	12
1.5.1	Fluorescence principles	12
1.5.2	Fluorescent probes and sample preparation	14
1.5.3	Fluorescence microscopy	15
1.6	Image quality and resolution	15
1.6.1	Image formation and optical resolution	16
1.6.2	Imaging errors	18
1.7	Cameras	19
1.7.1	Camera technologies	20
1.7.2	Camera resolution	20
1.7.3	Camera noise	22
1.8	Advanced microscopy settings	23
1.8.1	Angle of illumination	23
1.8.2	Confocal microscopy	24
1.8.3	Deconvolution	26
1.9	Super-resolution microscopy	26
1.9.1	SIM and STED	27
1.9.2	Other methods	28
1.9.3	Single molecule localization microscopy	28
1.9.4	Alternative SMLM methods to <i>d</i> STORM	32
1.9.5	Single particle tracking	33
1.9.6	SMLM in 3D	35
1.9.7	SMLM algorithm and further analysis and FIJI	35
1.9.8	Cross-correlation	36
1.9.9	How to measure resolution	36
1.9.10	Clustering of SMLM data	38
1.9.11	Clustering algorithms	39

1.9.12 Bayesian approach	40
1.10 Open-source concept	41
1.11 Open-source microscopy	41
2 Motivation and thesis aim	43
2.1 Motivation	43
3 Open source microscopy: results and discussion	45
3.1 Open-source UC2 based setup	45
3.1.1 Open-UC2 framework and 3D printing	45
3.1.2 Electronics and Software	47
3.1.3 Wide-field microscopy setup hardware	48
3.1.4 Stages	50
3.1.5 Imaging modalities	51
3.2 Wide-field image quality	52
3.2.1 Single molecule imaging and focusing	53
3.2.2 Drift characterization and stability	55
3.2.3 Large field of view imaging	57
3.3 Live-cell imaging	58
3.3.1 Photo-damage and photo-toxicity	59
3.3.2 Room temperature	60
3.3.3 Challenges in live-cell imaging	61
3.3.4 Incubator Measurements	62
3.3.5 Autofocus	65
3.4 Single molecule applications	65
3.4.1 Single particle tracking	66
3.4.2 SMLM: optimal number of frames	69
3.4.3 dSTORM of cellular microtubules	70
3.5 Image quality and resolution estimation	73
3.5.1 Camera quality	74
3.5.2 Resolution	74
3.6 Low-budget objectives	76
3.7 Possible Setup improvements	80
4 Data-analysis and clustering: results and discussion	83
4.1 Cell segmentation	83
4.2 Machine learning for SMLM data analysis	85
4.3 Clustering of SMLM data	86
4.3.1 Bayesian Cluster Analysis and visualization application	86
4.3.2 Benchmarking through raw-data simulation	87
4.3.3 Clustering biological proteins	90
5 Materials and methods	93

5.1	Microscopy setups	93
5.1.1	Low budget digital USB microscope	93
5.1.2	Llama Setup: a home-built wide-field microscope	93
5.1.3	Spinning disc	96
5.1.4	Pixel sizes	96
5.2	3D design and printing	98
5.2.1	Printing quality	99
5.3	UC2 setup alignment	100
5.3.1	Illumination	101
5.3.2	Bright-field illumination	101
5.3.3	Bright-field images background correction	102
5.3.4	Laser and filters	103
5.3.5	Illumination schemes	108
5.4	Software and hardware	108
5.4.1	Software	108
5.4.2	Fiji plugins	109
5.4.3	Hardware and computers	110
5.4.4	UC2 wide-field microscope materials and parts	110
5.5	Data processing	112
5.5.1	SMLM data analysis settings and camera parameters	112
5.5.2	CellProfiler pipeline	114
5.5.3	CellPose pipeline	115
5.5.4	Stitching and tiling	115
5.5.5	Wide-field image resolution estimation	116
5.5.6	Single particle tracking	116
5.6	Simulation of SMLM raw-data	117
5.6.1	FluoSIM	117
5.6.2	Sample geometry	117
5.6.3	Creating and analysing SMLM datasets	118
5.6.4	Selfmade simulations	119
5.7	Protocols for sample preparation and materials	120
5.7.1	Chemicals and buffers	120
5.7.2	Cell culture	121
5.7.3	Cover glass cleaning	121
5.7.4	Tetra speck surface	121
5.7.5	Cell seeding	122
5.7.6	CV-1 MT staining	122
5.7.7	CLC-GFP staining for SMLM measurement	122
5.7.8	CD95-GFP staining	123
5.7.9	GPI-GFP staining	123
5.7.10	Live cell staining	124
5.7.11	QD functionalizing for SPT	124

6 Conclusion and outlook	125
A Appendix	131
A.1 Alternative illumination possibilities	131
A.1.1 Fiber based laser as possible replacement for wide-field illumination	131
A.1.2 Possible auto-focus improvement	132
A.1.3 Wide-field imaging with different objectives	134
A.2 Imaging experiments	134
A.2.1 live-cell imaging	134
A.2.2 Llama setup <i>d</i> STORM of microtubules in TIRF-illumination	135
A.2.3 <i>d</i> STORM imaging of CCP on Llama setup	136
A.3 Scripts and analysis codes	137
Bibliography	145

List of abbreviations

ABS - Acrylnitril-Butadien-Styrol
ADC - Analog-to-Digital Converter
ADU - Analog-to-Digital Unit
AF647 - Alexa Fluor 647
AI - Artificial Intelligence
AOTF - Acousto-Optical Tunable Filter
BaClava - BAYesian Cluster Analysis and Visualization
BF - Bright-field
BFP - Back Focal Plane
BSA - Bovine Serum Albumin
CAD - Computer Aided Design
CCP - Clathrin Coated Pits
CLC - Clathrin Light Chain
CLEM - Correlative Light and Electron Microscopy
DL - Diffraction Limited
DoG - Difference-of-Gaussian
(s)CMOS - (scientific) Complementary Metal-Oxide-Semiconductor
DBSCAN - Density-Based Spatial Clustering of Applications with Noise
DMEM - Dulbecco's Modified Eagle Medium
DNA-PAINT - DNA Points Accumulation for Imaging in Nanoscale Topography
EMCCD - Electron Multiplying charge coupled device
FCS - Fluorescence Correlation Spectroscopy
FFT - Fast Fourier Transform(ation)
FRAP - Fluorescence Recovery After Photo-bleaching
FWHM - Full Width at Half Maximum
GFP - Green Fluorescent Protein
GPI - Glycosylphosphatidylinositol
GUI - Graphical User Interface
HDF5 - Hierarchical Data Format, (Version) 5
HILO - Highly Inclined and Laminated Optical (sheet)
HS - Horse Serum
ISC - Inter-System Crossing
LASER - Light Amplification by Stimulated Emission of Radiation
LED - Light Emitting Diode

MSD - Mean Squared Displacement
MSS - Moment Scaling Spectrum
NA - Numerical Aperture
PALM - Photoactivated Localization Microscopy
PBS - Phosphate-buffered saline
PLA - Polylactic Acid
PSF - Point Spread Function
QD - Quantum Dot
RAM - Random Access Memory
ROI - Region Of Interest
ROS - Reactive Oxygen Species
SBR - Signal to Background Ratio
SD - Spinning Disc
SIM - Structured Illumination Microscopy
SiR - Silicon Rhodamine
SMAP - Super-resolution Microscopy Analysis Platform
SMLM - Single Molecule Localization Microscopy
SNR - Signal to Noise Ratio
SPT - Single Particle Tracking
STED - STimulated Emission Depletion
dSTORM - direct Stochastic Optical Reconstruction Microscopy
TIFF - Tag Image File Format
TIRF - Total Internal Reflection Fluorescence
ToMato - Topological Mode Analysis Tool
TS - Tetra Speck (beads)

List of Figures

1.1	Scales in biological imaging	8
1.2	The cell membrane	9
1.3	Simplified Jablonsky diagram of electronic transitions	13
1.4	Simplified design of a wide-field fluorescence microscope	16
1.5	Light diffraction and interference	17
1.6	Convolution of an object with a PSF	18
1.7	Nyquist sampling theorem in the case of camera pixels	21
1.8	Angle of illumination in optical microscopy	23
1.9	Confocal microscope schematic	25
1.10	Detection and localization of single molecules	29
1.11	Rayleigh criterion for single molecule distinction	30
1.12	SMLM working principle	31
1.13	Principle of single particle tracking	33
1.14	Cross-correlation simplified one dimensional concept	37
1.15	Fourier ring correlation for resolution estimation	38
1.16	Simplified K-means and DBSCAN clustering methods.	39
3.1	UC2 setup and the open-source concept	46
3.2	Electronics and adapted ImSwitch GUI.	47
3.3	CAD design of the UC2 based wide-field microscope	49
3.4	Different samples imaged with the UC2, the Llama and the confocal setup.	52
3.5	Z-stack of single molecules and stage calibration	53
3.6	Z-stack of MT-stained cells	54
3.7	Drift characterization of the UC2 setup	56
3.8	Imaging large fields of view.	57
3.9	Live-cell imaging of CV-1 cells over five hours at room temperature.	61
3.10	Live-cell imaging of T98G cells over two days inside the incubator.	63
3.11	Single particle tracking of GPI-GFP labelled with quantum dots	67
3.12	Diffusion coefficient and MSS as determined from SPT	68
3.13	The optimal number of frames to acquire for SMLM imaging	70
3.14	<i>d</i> STORM of cellular microtubules with the UC2 setup.	72
3.15	<i>d</i> STORM of cellular microtubules with Llama setup in epi-illumination	73
3.16	Resolution estimation of the acquired <i>d</i> STORM images	75
3.17	Comparison of high- and low-budget objectives.	77

3.18	Single molecule applications on UC2 setup with low-budget objective. . . .	78
4.1	CellPose for automated training-free segmentation	84
4.2	Quantifying clathrin coated pits sizes	85
4.3	Benchmarking BaClAva with simulated SMLM data-sets.	88
4.4	Clustering with BaClAva on biological samples	91
5.1	Updated homebuilt wide-field microscope	94
5.2	Focus lock of the Llama microscope.	95
5.3	Pixel-size measurement method on the UC2 setup	97
5.4	3D printing process	99
5.5	Quality comparison between surfaces of 3D printed materials	100
5.6	Top-light illumination	102
5.7	Background correction for bright-field images	103
5.8	Laser profile characterisation	104
5.9	Excitation pathway sample illumination modalities	105
5.10	UC2-setup filter cube and laser spectral characteristics	107
5.11	MCT and ImScript acquisition patterns.	108
5.12	Segmenting the cell for resolution estimation.	116
5.13	FluoSIM simulations geometry	118
A.1	Intensity profile of SM laser and spatially filtered laser	132
A.2	LED matrix for auto-focus improvement	133
A.3	Wide-field fluorescence imaging of immuno-stained microtubules.	134
A.4	Live-cell imaging of HEK cells over five hours at room temperature.	135
A.5	<i>d</i> STORM of cellular microtubules with Llama setup in TIRF-illumination . . .	135
A.6	Clathrin coated pits <i>d</i> STORM reconstruction on Llama setup.	136

List of Tables

5.1	List of the AOTF frequencies set in micromanager	94
5.2	List of the pixel-sizes of different objectives and setups	96
5.3	Software list used in this thesis	109
5.4	Fiji plugins used in this project	109
5.5	List of used computers and specifications	110
5.6	Repositories and corresponding links of microscope materials.	111
5.7	Bill of materials of the setup	112
5.8	FluoSIM cluster densities for different binding times	118
5.9	List of chemicals and their manufacturers	120

Introduction

In this chapter, I summarize the theoretical background on which the experimental methods, simulations as well as analysis methods that are described in this thesis are based on. First, the cellular structures that are studied or simulated in different experiments are introduced. Afterwards, the conventional microscopy methods and their implications in the advances in life science are stated. Then, the different improvements over the past decades will be used to introduce fluorescence microscopy, a technique that has become indispensable in every life science laboratory. This also includes the principles of fluorescence itself as well as the strategies to label samples which largely contributed to the success light microscopy has had in the past decades. In the next section, the limitations of fluorescence microscopy (in terms of resolution) are discussed and completed by the most commonly used super-resolution methods to circumvent these limitations. Finally, the data processing and analysis methods such as clustering, which are methods to extract more information from the image acquisition of biological samples, will be presented.

1.1 Scales in bio-imaging

Biological processes happen at different spatial and temporal scales. Monitoring and studying these different processes requires optical instrumentation with application specific properties. I here briefly introduce an overview of the scales at which the use of an optical microscope is suited, maximizing the number of imaging applications that are feasible with the tool that will be developed. The different structures presented in figure 1.1 are examples of samples that can function as benchmarks to evaluate the imaging resolution attained by the setup presented in this thesis.

Different nanoscopy methods, which will be further developed in this chapter, allow to estimate the position of single molecules with several nanometers of precision. Using the same methodology, the position of a given molecule within a cell can be determined. The use of biological reagents at nanoscale level such as nanobodies and antibodies ([Im+19a; BG17; Rie+12]) enable sample preparation methods to image cellular structures. Antibodies are targeting specific antigens. By attaching fluorescent molecules to them, cellular structures can be reproduced by looking at the distribution of antibodies on it. The imaging of antibodies themselves is almost impossible with light microscopy, even though new studies are pushing against this limit [Sha+22]. The detection of single molecules is the spatial limit of a microscope with wide-field illumination, and is a feature that would be useful to implement in the planned low-budget microscope. Once single molecules can be visualized, the same techniques can be applied to image cellular substructures, and

can also find application in visualizing bacteria or complete cells. Size of samples are ranging from a single to several tens of microns. While lowering the magnification and subsequently increasing the size of the field of view (FOV), one can open up the possibility to image bigger structures e.g. tissues or small organisms, up to the millimeter range. Everything exceeding a millimeter can be imaged with other more simple instruments. As the criterion of high-quality data generation has to be maintained, the used hardware in the optical instrument has to be chosen accordingly, limiting the possible applications.

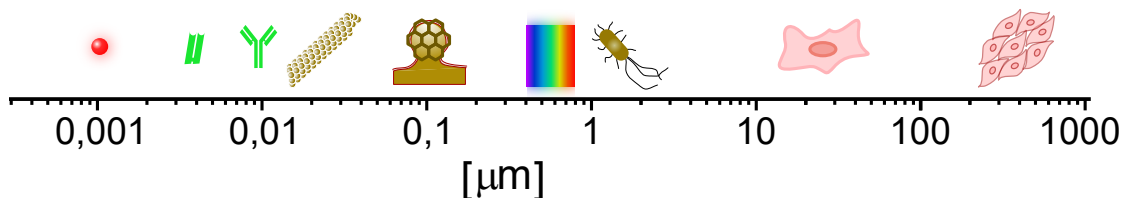


Fig. 1.1.: Scales in biological imaging. From left to right: Organic fluorophores: around 1 nm; Nanobodies and antibodies: 4 nm and 10 nm respectively; Microtubules diameter: 25 nm; Clathrin coated pits diameter 100-200 nm; Wavelength of visible light spectrum: 400-700 nm; Bacteria: around 1 μm ; Whole cells: 10-100 μm ; Cell tissue: up to millimeter range.

In addition to the size-scale of biological processes, the time-scales of biological processes are important to monitor dynamic pathways and processes within living cells. The necessary temporal sensitivity of the used devices need to match the speed of the observed process when planning an experiment. Obviously, the imaging of fixed cells is not time sensitive, but fluorescence based imaging will still rely on short detection times, especially for advanced microscopy methods that aim to detect changes in the fluorescence emission pattern of single molecules. All assays involving living cells are relying the ability to study time dependant cellular processes and characterize the underlying pathways, variable temporal resolution is thus paramount for such experiments. These range from fast particle diffusion within the cell membrane, over movement of cells or organelles and cell division. The sensitive part of a microscope in regard to the temporal acquisition capability necessarily comes down to the used detector. Possible other parameters are necessary, depending on the applied technique, but the choice of the detector of the here presented setup is influenced by the planned assays. This aspect will be further elaborated in 1.7.

1.2 The cell cytoskeleton

In this section a few of the structures of interest presented in this project are introduced. Various components of the cell cytoskeleton are chosen as they are well studied structures with already established staining methods for fluorescence microscopy.

The cytoskeleton of eucaryotic cells is a system of filaments and fibers within the cytoplasm. It provides structural stability, giving the cell its shape and is involved in the movement of the cell itself as well as in the positioning of organelles [Pol+17]. Globular

actin polymerises to form filaments (F-actin) that may branch, and build larger networks that provide morphological stability to cells. Various functions are relying on the formation of filamentous actin e.g. cell mobility, adhesion, contraction and migration (through myosin). Another important component of the cytoskeleton are microtubules, cylindrical polymers of 25 nm diameter composed of α - and β -tubulin dimers. Besides playing an important role in the cellular division processes, microtubules support various cellular structures and offer tracks for cellular transport functionalized by motor proteins such as dyneins and kinesins. Intermediate filaments and septins are further constituents of the cytoskeleton, but will not be further discussed in this project.

1.3 The cell membrane

The cell membrane is a complex organelle that encloses the cytosol and all organelles of the cell, separating them from the exterior, but simultaneously allowing selective passage of certain molecules. The plasma membrane is composed of a lipid-bilayer made of phospholipids, acting as a hydrophobic barrier to ions and molecules bearing a charge or a polarity. Specific pathways involving transport proteins can however enable their passage. The plasma membrane forms an interfaces by which the cell interacts with its surroundings, which in turn influences the cells morphology and enables it to move as well as to divide.

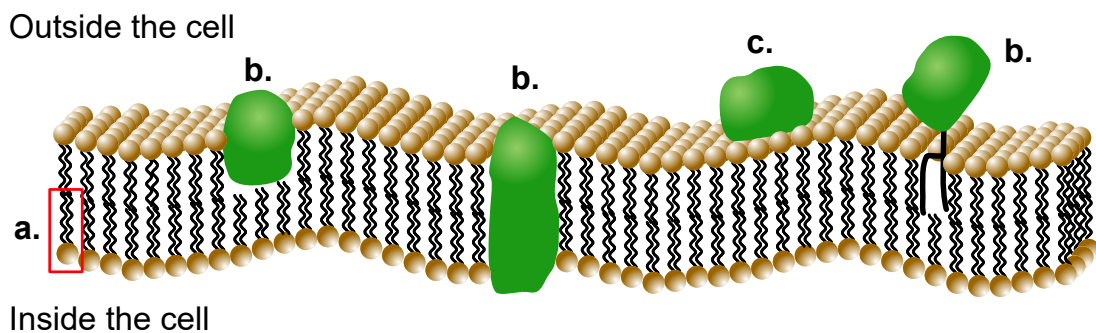


Fig. 1.2.: Schematic of the cell membrane according to the fluid mosaic model. Cell membrane is a two dimensional lipid bilayer composed of phospholipids in which proteins and molecules are embedded. **a.** Red rectangle displays a phospholipid composed of a head group and a fatty acid chain. **b.** Different types of integral proteins. **c.** Non-covalently bound peripheral proteins attached to the membrane.

A distinctive model still shaping present understanding of the cell membrane was the fluid mosaic model which as soon as 1972 described the nano-scale structure of the membrane as a fluid bilayer traversed by proteins. This model has been revised [Nic13] but still holds true for general considerations. Based on this membrane model, the motion of membrane proteins can be studied, as presented in following subsection.

1.3.1 Membrane molecule diffusion

The continuous irregular motion of small particles in water is a physical phenomenon first described by the Scottish botanist Robert Brown in 1828 and is nowadays commonly known as Brownian motion [Big09]. This random motion is suitable to describe anisotropic environments such as the movement properties of molecules within biological structures such as cellular membrane, when adapted to the sample geometry. In a first instance, Saffman and Delbrück [SD75] developed the hydrodynamic model of the molecule movement in a membrane. Thereby, the membrane is considered as a 2D sheet of increased viscosity surrounded by a medium (water) with a reduced viscosity above and below. The molecules are considered as cylinders (amongst other possible shapes) within this sheet and are experiencing translational and rotational displacement within the membrane [Gam+06]. The Brownian motion behaviour can be described with the diffusion coefficient of membrane molecules, which can be expressed as a function of the thermal energy ($E = k_B \cdot T$ k_B is the Boltzmann constant, T the temperature) according to the Einstein relation. For simplicity, only the translational mobility b_T is considered.

$$D = k_B \cdot T \cdot b_T \quad (1.1)$$

In the case of membrane diffusion, the particles can be approximated as cylinders of radius r trapped within a sheet of viscosity η_m and thickness h surrounded by an aqueous environment with lower viscosity η_{aq} , thus giving following approximation:

$$b_T = \frac{1}{4\pi\eta_m r} \left(\log \left(\frac{\eta_m h}{\eta_{aq} r} \right) - e \right) \quad (1.2)$$

Hereby e is the Euler number, k_B is the Boltzmann constant, T the temperature, η the fluids viscosity and r the hydrodynamic radius of the particle. With these parameters, a simplified model of membrane diffusion can be established. As measuring the diffusion properties of membrane molecules depends on the experimental approach, further details on its measurement will be provided in the single particle tracking subsection 1.9.5. Finally, membrane diffusion is not necessarily Brownian, a broader framework to qualify the type of motion is thus needed.

Different methods exist to study dynamic cellular processes, such as FRAP and FCS. Fluorescence recovery after photo-bleaching (FRAP) bleaches the fluorophore within a region of interest (ROI) of a stained living cell. The recovery of fluorescence in the bleached spot is provided by non-bleached molecules diffusing into the bleached region [Mey+99]. In the case on fluorescence correlation spectroscopy (FCS), a confined illuminated volume of a sparsely labelled cell surface is imaged to measure fluctuations in fluorescence intensity. These fluctuations correspond to labelled molecules diffusing through the confined volume. Auto-correlation of the acquired signal gives insights into the molecular dynamics and the concentration of the studied protein [Yu+21]. Both these methods need a point like

illumination or even a second laser, resulting in additional mechanical complexity of the setup. To enable the study of molecular dynamics on the cell surface, they are thus not suited in the planned setup and another method will be favoured, that can be implemented on a wide-field illuminated setup. The single particle tracking (SPT) will be introduced as the method of choice for monitoring molecular dynamics (section 1.9.5).

1.4 Conventional light microscopy

As early as in ancient Greece, the use of water droplets to magnify structures was documented. Over the centuries, the ability to make use of glass to produce reliable instruments to study the micro-cosmos was provided, with the first documented combination of two lenses as soon as the end of the 16th century [Rob15]. The development of optical instruments such as the microscope and the telescope was a driving force for scientific discoveries and technological advance in different fields of study. Nowadays, microscopy combined with spectroscopy has enabled to solve many challenges in life-sciences, and perpetual improvement of imaging techniques allow to understand complex processes on a nanoscopic scale and connect them to previously acquired knowledge [DB20]. The modern microscope is still based on first designs created by Van Leeuwenhoek in the 17th century.

A basic microscope is composed of an objective and an ocular lens. The ocular lens produces a seemingly infinitely distant image of the intermediary image generated by the objective lens. The magnification and image quality are strongly dependant on the manufacturing quality of the optics. The achievable resolution of a light microscope is also limited, an introduction in the established microscopy limitations will be provided in the upcoming sections. The light paths e.g. within a microscope, can be described in a simplified way. Geometric optics use rays which correspond to the propagation vector of a given light wave to visualize light propagation and effects of optics [Dem08]. This method is practical to display ray paths of an optical instrument. Another classical approach that is helpful when building a microscope is to use Fourier optics. Here, the optical waves are considered as a superposition of plane wave-fronts [Goo17]. The orientation and positioning of optics produce a Fourier transformed image in the back focal plane (BFP) of a lens, and can transform the signal in the BFP back into a real image. This description of optics can be used to spatially filter specific light emission components (e.g. [Bou+15]) or to calculate the positioning of optical elements within a setup.

$$B(x', y') \propto \iint_{-\infty}^{\infty} b(x, y) \exp \left\{ -i 2 \pi \left[\frac{\theta_x x'}{\lambda} + \frac{\theta_y y'}{\lambda} \right] \right\} dx dy \quad (1.3)$$

In equation 1.3, an exemplary mathematical description of the of an object in the BFP is displayed. The intensity distribution B in the BFP, can be described as the Fourier transform

of the initial intensity distribution b through the effect of a lens, with θ being the angle light has been collected in and λ the wavelength of the light.

1.5 Fluorescence

In 1852 Sir G. G. Stokes discovered and characterized a shift towards lower energy when ultra-violet (UV) emissions were absorbed by quinine [Lak06]. This absorption and emission of light process is now known as fluorescence, with the so called Stokes shift describing the loss of energy during the electronic transitions. The concept of fluorescence decisively contributed to life-science research through its use as a reliable way of labeling biological structures of interest for imaging purposes with visible light. The Stokes shift thereby is a key feature, allowing to separate fluorescent emissions from the excitation light. Fluorescence imaging thus provided a drastically improved contrast compared to conventional light microscope imaging as it relies on emissions from the sample itself and not on sample interactions with an external light source. These advantages have put fluorescence microscopy forward and established it as a research tool in the majority of life-science laboratories.

1.5.1 Fluorescence principles

While a chromophore is only defined by its light absorption properties, lumophores also have the ability to emit the absorbed energy in form of light. As the lumophores considered in this thesis are emitting fluorescence, the term fluorophore with henceforth be used to describe them. The interaction of photons with matter is quantized with an energy $E = h \cdot \nu$, with h Planck's constant and ν the frequency, meaning that photon emissions represent discrete energy steps during electronic transitions. The energy states for a single atom are also discrete as electronic transitions are characterized by fixed transition energies. For complex fluorescent molecules however, additionally to the electronic states (transition energy in the range of 1-5 eV), energy dependent rotational ($\approx 10^{-3}$ eV) and vibrational (0.1-0.4 eV) states can arise from molecule rotations or atomic vibrations [HW03]. The observed energy transitions are spectrum-like, both for the absorption and the emission of photons, due to the multitude of possible electronic transitions. The Kasha rule describes that similar emission spectra can be generated with different excitation wavelengths [Lak06], highlighting the multitude of possible electronic states and the spectrum-like character of a fluorescence processes. An example of the absorption and emission spectra of the fluorophore Alexa Fluor 647 is shown in the figure 5.10 a.i.

The probability of occupation of excited states is infinitesimal ($E=k_B \cdot T \approx 0.025$ eV at room temperature), according to the Boltzmann statistics ($\approx 10^{-30}$).

$$\frac{N_{S_1}}{N_{S_0}} = e^{-(E_{S_1}-E_{S_0})/k_B \cdot T} = e^{-\Delta E/k_B \cdot T} \quad (1.4)$$

The spontaneous population of electrons in the excited state N_{S_1} in relation to the population in the ground state N_{S_0} is of very low probability, making spontaneous emission of fluorescence basically non-existing. Light absorption and subsequent population of the excited states are subjected to the Franck Codon principle [HW03; Dem16], which simplifies the transition by assuming the atomic nucleus is immobile during electronic transitions, due to its immensely larger mass (compared to electrons), and enabling almost instantaneous transitions (10^{-15} s). The probability of absorption of a photon by an atom or molecule are highest when their dipole moment are aligned. Additionally, charge separation to an excited state through light absorption can be represented by wave functions. The overlap of the ground state wave function and the wave function in the excited state can be used to approximate the probabilities of transition.

An excited fluorophore has different ways of relaxing back into the ground state, which can be radiative (e.g. fluorescence and phosphorescence) but not necessarily. The Jablonski diagram 1.3 depicts different possible energetic states that an electron can populate and transitions that can occur between those states. The thick black lines represent the electronic states, while the lighter black lines represent the vibrational states (rotational states have been omitted for clarity). The simplification through the Franck Codon principle allow to depict the absorption and emission of light as direct vertical lines in the diagram, thus as a pure change in energy.

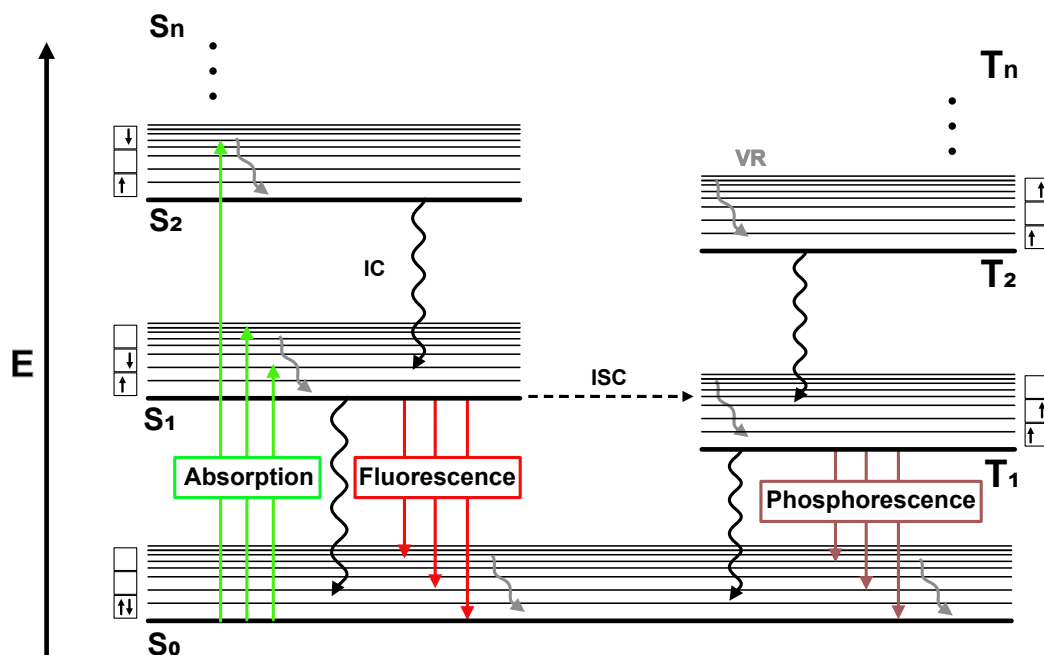


Fig. 1.3.: Different electronic transitions and interactions with photonic absorption/emission visualized in a jablonsky diagram. Energy is increasing vertically. S_0 is the ground state. S and T denote the excited singlett and triplet electronic sates. **ISC** stands for inter system crossing. **IC** is internal conversion. **VR** is the vibrational relaxation. Thick black lines represent the electronic states, while thin black lines, the vibrational states .Rotational states have been omitted for clarity reasons.

Through light absorption, an electron is elevated from the ground state S_0 to an excited state S_n . For most fluorophores, undergoing internal conversion (IC) relaxes the electron to the first excited state S_1 . Vibrational relaxation (VR) brings the electron to the lowest vibrational state of S_1 from which, according to Kasha's rule [Lak06], the relaxation to the ground state S_0 can occur by photon emission with the remaining energy. In the ground state, VR brings the electron back to the lowest vibrational state of S_0 . The energy loss through the IC and VR can commonly be seen as a shift towards higher wavelengths, the Stokes shift. The emitted photons are the fluorescence with a lifetime of around $\approx 10^{-8}$ s, much slower than the IC ($\approx 10^{-12}$ s).

Another possible relaxation mechanism is the conversion through spin flip. Inter-system crossing (ISC) describes the state where the electron spin of the highest occupied molecular orbital (HOMO) is parallel to the spin of the electron in the lowest unoccupied molecular orbital (LUMO), changing the multiplicity from a singlet to a triplet state (T_1). Through IC and VR, the electrons can be brought to the lowest vibrational triplet state, then relax to the ground state through a radiative process called phosphorescence. The spin flipping conversion into the triplet state is forbidden, thus of low probability. Additionally, relaxation of triplet electrons is also accompanied by a spin flip as the Pauli principle forbids two electrons to have the same quantum numbers within an atom [Dem16], thus increasing the lifetime of this state (up to several seconds) [Lak06].

1.5.2 Fluorescent probes and sample preparation

In order to take advantage of the specific fluorescence signals for cell imaging, different types of probes and strategies to introduce the dye into the sample are used. Fluorescence and the underlying materials having fluorescent properties can be found in nature. The elucidation of aequorean bioluminescence (in jellyfish) and the expression of the green fluorescent protein (GFP) within bacteria started the development of fluorescent proteins [Tsi09], enabling live-cell imaging with high specificity. Nowadays a myriad of fluorescent proteins can be transiently or stably expressed within cells in a palette of different colours as every protein can be engineered to optimally work for specific experiments or microscopy techniques. Alternatively, target proteins can be expressed as a fusion protein with HALO-tag [ELC15] or SNAP-tag [Col13]. These tags can then be labelled with organic dyes to label targets in (live-) cells. Organic dyes are generally brighter and different organic dyes can label the same tag.

Organic dyes can be attached to an antigen of choice via immuno-staining. Antibodies or their fragmented parts or nanobodies [Rie+12; BG17] can be labelled with fluorescent dyes to stain the cellular structures of interest [Im+19b]. Alternatively to the organic dyes (e.g. Alexa Fluor 647), quantum dots (semiconductor particles with band-gap matching the excitation light), gold nanoparticles and other fluorescent probes can be used to stain the structures of interest.

For live staining cells, different concepts have been developed [GAT98; Geo+04]. In this project, a reagent for simple live-cell staining was used. The Silicone rhodamine fluorophore can be combined with jasplakinolide and functions as a staining probe. This reagent named SiR-Actin [Luk+14] is fluorogenic, cell-membrane permeable and attaches to the structure of interest in living samples, here F-actin. Other structures such as tubulin can be targeted with rhodamine dyes.

1.5.3 Fluorescence microscopy

Conventional bright-field light microscopy uses a light source to illuminate the complete sample. In the resulting image, contrast is created by the diffraction and absorption of light at the edges of sub-cellular structures, where the amount of transmitted light is reduced. The same is valid for X-ray and electron microscopy, where contrast is generated by the absorptive and diffractive properties of a sample at a given spot, in specific the electron density i.e. corresponding to the atomic number of the elements or atomic layers and shells. The high resolution of these imaging methods with short wavelength particles thus lack in specificity, as proteins differ little from one another in their atomic composition.

What makes fluorescence microscopy exceptional is that the measured signal originates from the sample. Fluorescent labels have been developed and functionalized to specifically label a structure of interest within cells. The resulting measured signal is a representation of the distribution of fluorescent molecules on the sample. This highlights the importance of adequate labeling strategies to prevent the introduction of sample preparation artefacts within the acquired data.

In order to image fluorophores, it is crucial to separate the excitation light from the emitted fluorescence. In this case, the Stokes shift [Lak06], previously mentioned in 1.5.1, allows to separate the photons by wavelength using an optical filter. The cut-off wavelength is chosen according to the used fluorophore thus blocking the excitation light and transmitting a majority of the emitted fluorescence. The additional use of emission filters can further spectrally refine the acquired signal.

A simplified version of a wide-field fluorescence microscope is depicted in 1.4. The field of view (henceforth FOV) within the sample is illuminated homogeneously with the excitation laser. The fluorescence captured by the objective is spectrally separated from eventual reflections of the excitation light by using a dichroic mirror. Fluorescent emissions can further be filtered with an emission filter to improve the image quality and are finally focused on a camera or other type of photon detector.

1.6 Image quality and resolution

Imaging methods based on visible light are necessarily limited in terms of resolution and quality. In this section the image formation process is introduced, to explain what

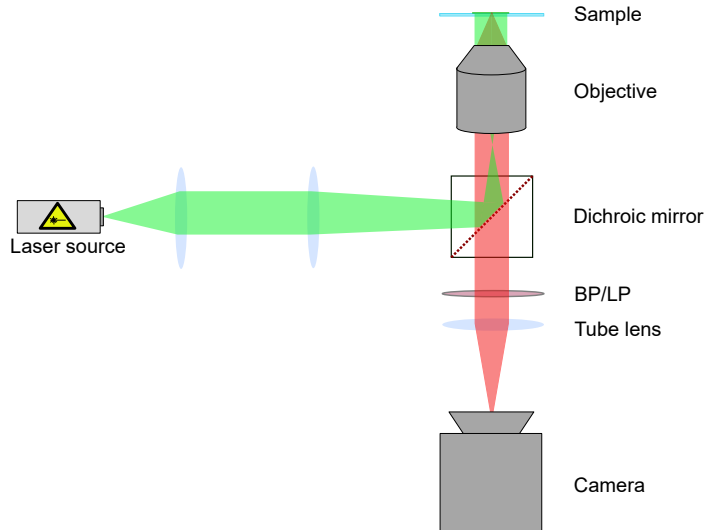


Fig. 1.4.: Simplified wide-field fluorescence microscope principle. Excitation light (green light path) is reflected by the dichroic mirror to homogeneously illuminate the sample. Fluorescence (red light path) is passing the dichroic mirror and focused on the detector for imaging.

limits optical microscopy. The imaging errors impeding image quality are also discussed, as their effect might be of importance when using low-budget optics.

1.6.1 Image formation and optical resolution

According to Huygens wave propagation principle, planar waves hitting an aperture will create a new wavefront as each point of the wavefront is considered a source of spherical wavelets [Dem08]. In the simplified case of an aperture in the size range of the wavelength, a single spherical wave is created and produces a diffraction pattern when projected on a surface in far distance from the aperture. The unavoidable wave character of light creates fluctuations on the measured intensity on a screen at distance D as the waves interact constructively or destructively, depending on the distance to the aperture center. In figure 1.5, this diffraction effect is schematically shown.

Hereby d_A is the size of the aperture, D the distance to the screen, $\delta = d_A \cdot \sin(\alpha)$ the optical path length difference and α the angle in relation to the optical center. From this path difference, the interference can be expressed as a function of the phase angle difference $d_{phase} = \frac{\pi}{\lambda} \cdot d_A \cdot \sin(\alpha)$ where λ is the wavelength of the incoming wave. The resulting intensity equals the squared quadratic value of the total electrical field, as suggested in figure 1.5. The intensity distribution can be approximated from a common light propagation equation as follows (equation 1.5):

$$E_{tot} = \int_{d_A} E_0 \cdot \cos \left(\omega t - kr + \frac{\pi}{\lambda} \cdot y \cdot \sin(\alpha) \right) dy \quad (1.5)$$

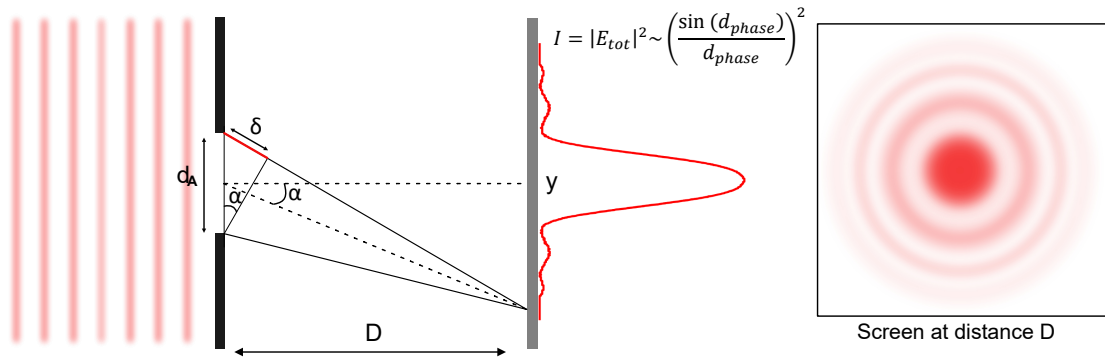


Fig. 1.5.: Light diffraction and interference at an aperture. Image formation: Greek letters α and β convoluted with a simplified point spread function. Image acquisition process induces diffraction limited resolution.

With ω the angular frequency, t the time, k the wave number and t the time (vector directions have been left out for this simplified consideration). The same diffraction principle occurs when light propagates through any kind of aperture and cannot be removed from any imaging devices. The representation of a single light emitting source e.g. a fluorophore on a detector, with optics limited by their apertures, will thus result in a diffracted pattern. This function describing the representation of single point emitter patterns will forth-on be named point spread function (PSF). To approximate the PSF, the intensity distribution I of the Fraunhofer diffraction pattern of a back-illuminated pinhole can be described as a function of the observed angle α , with I_0 the maximal intensity of the PSF and J_1 the first order Bessel-function.

$$I(\alpha) \propto I(0) \left(\frac{J_1(r)}{r} \right)^2 \quad \text{with} \quad r = \frac{2\pi}{\lambda} n a \sin(\alpha) \quad (1.6)$$

Here, a represents the size of the particle. The work of Ernst Abbe concluded that the full width at half maximum (FWHM) of a PSF was fundamentally limited by the wavelength of the used light, thus limiting the FWHM at half of the wavelength. Solving equation 1.6 for r gives $|r| \approx 1.61$. In 1873, by observing a grid with high spatial frequency, he estimated the minimal distance between two objects where both could still be identified as single objects[Abb73]. The minimal observable distance $d_{min} = 2a$ where a is the grid spacing, when the intensity drops to half. An estimation of the minimal resolvable distance is given in equation 1.7:

$$1.61 = \frac{2\pi}{\lambda} n a \sin(\alpha) \iff d_{min} = \frac{2 \cdot 1.61 \lambda}{2\pi n \cdot \sin(\alpha)} \approx \frac{\lambda}{2n \cdot \sin(\alpha)} \quad (1.7)$$

The main factors that are influencing optical resolution are represented in equation 1.8 which gives a theoretical resolution limit for light microscopes, according to E. Abbe. This limit suggests that optical microscopy is fundamentally limited by light diffraction

i.e. objects that are smaller than d_{min} will always be blurred into a PSF of the minimal resolvable size.

$$d_{min} = \frac{\lambda_{em}}{2n \cdot \sin(\alpha)} = \frac{\lambda_{em}}{2NA} \quad (1.8)$$

Abbe also introduced the numerical aperture (NA) which characterises the capacity of an objective lens to gather light. These findings influenced microscopy to not focus on magnification as the achievable resolution can not be increased by higher magnification. When imaging a fluorescent emitter in a sample e.g. a single molecule, the observed pattern on a detector will thus always be a blurred spot. This physical limit in resolution can be seen in all types of standard light microscopy and is schematically depicted in figure 1.6. For this reason, further increasing the magnification is not necessarily beneficial, as the attainable resolution when imaging single molecules is fundamentally limited for visible light.

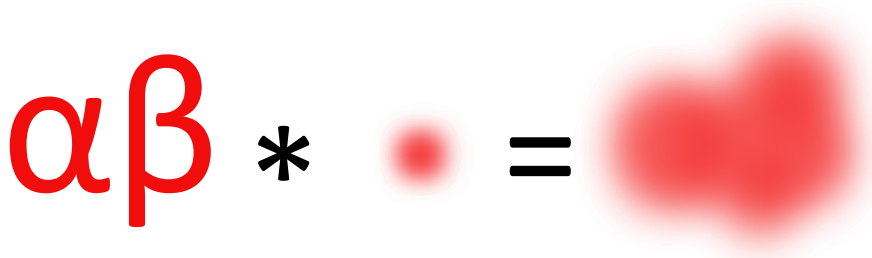


Fig. 1.6.: Microscopy image is the result of a convolution between the object of interest and the PSF. Image formation: Greek letter α and β convoluted with a simplified point spread function. Point spread function represents the smallest resolvable distance (FWHM \approx 200 nm). Image acquisition process induces diffraction limited resolution.

$$I(x, y) = [O * PSF](x, y) := \iint_{-\infty}^{\infty} O(x, y) PSF(x - i, y - j) di dj \quad (1.9)$$

Equation 1.9 describes the image formation process mathematically in a simplified manner. The image (I) can be considered as a convolution of the imaged object (O) and the point spread function (PSF), a setup specific function describing the plane representation of a single point source in the object plane. This fundamental resolution limit will affect all images acquired with a wide-field setup operating in the visible light spectrum (as shown in figure 1.4). Techniques to overcome this resolution limit and detect single molecules with a higher accuracy can be used on wide-field setups and generally in fluorescence based microscopes. Those used in this project are presented in section 1.9.

1.6.2 Imaging errors

The occurrence of imaging errors has different origins, the difficulty of producing optics being the most common one. The manufacturing price scales with the quality control in regard to optical aberrations in the optics production. In chapter 3 the motivation

to reduce the errors originating from the objective is mainly motivated by the reduction of possible error sources, as these errors induced by the used high price objectives are nearly non-existent. The technical difficulty to increase the optics size accentuates this effect. For this reason telescopes have switched from lenses to mirrors, as the errors in lens production scale with its size. Microscopy is restricted to certain lens sizes and correcting aberrations is challenging as it often relies on the use of adaptive optics or high-quality aberration-corrected optics. In both cases, their implementation is challenging to combine with a low-budget concept. Here, a few of the most common imaging errors originating from optics are presented [Dem08], as they will likely be encountered when building or using low budget optics.

Chromatic aberration: Depending on its wavelength, incoming light is diffracted in different angles by the lens. The resulting focal point of the lens is wavelength dependent, resulting in multiple focal points. This complicates the overlay and comparison of fluorescent samples imaged in different channels.

Spherical aberration: Spherical aberration is an imaging error arising from the manufacturing of lenses, which is necessarily connected to lens curvature design. An imperfect surface curvature of the lens can cause differences in the focusing ability of the lens, depending on the position where light interacts with the lens. If the focal point of photons hitting the periphery of the lens is different than the one of photons hitting the center of the lens, the lens is subjected to spherical aberration.

Coma: Commonly a sign of a misaligned microscope, but also a possible lens error, coma changes the aspect of a PSF to resemble a comet tail. Coma is characterized by different off-axis (can be in X or Y) focal points of the lens, for photons interacting with the lens at the periphery compared to the center of the lens. It is often a sign of a tilted lens in the optical path or a tilted sample.

Astigmatism: The PSF appears as elongated along one axis. The elongation changes from the one axis to the other one, depending on the distance to the focal point of the lens, introducing axially dependent asymmetry into the image formation. The error arises from tilting of the lens or from uneven curvatures along one of the axes. This results in different curvatures thus focal points in X and Y. Astigmatism can be a voluntarily introduced artefact, as described in subsection 1.9.6.

1.7 Cameras

The detectors used in fluorescence microscopy have a considerable impact on the final image quality [Cox17]. The development of camera technologies has significantly influenced the life-science imaging field and continues to do so. In this section, the influence of the pixel-size of a detector and how it contributes to the final images resolution are disclosed. Furthermore, a general introduction into the main camera technologies and

noise sources are given. This will enable to identify the essential elements of scientific instruments and to which extent a low-budget alternative could replace it.

1.7.1 Camera technologies

Photon detectors in microscopy have for a long time been dominated by the CCD (Charge coupled device) technology [Cox17], which has climaxed in terms of sensitivity with the electron multiplying devices. The EMCCD (electron multiplying CCD) cameras provided an increased sensitivity towards fluorescent signals and thus established themselves as the standard for all applications with low signal intensity. The linear dependency between the signal strength and the chosen gain through electron multiplication allows to consistently increase a signal to noise ratio (SNR).

The recent development of the CMOS technology (Complementary Metal Oxide Semiconductor (logic)) have increased the sensitivity of modern sCMOS cameras (s = scientific) to a level only previously reached by EMCCD devices. The two technologies have nowadays similar sensitivities, but the increased frame-rate combined with the lower cost, the lower energy consumption and the prospect of larger chips are giving the CMOS cameras the advantage in the long term. Similarly, the advances in CMOS technology have drastically reduced the price of highly sensitive detectors. Even the regular CMOS devices, which do not have manufacturing quality and a refined linear relationship between input photons and output signals, are able to capture low intensity signals [Pho]. The CMOS cameras also have a much lower power consumption, motivating the development of the technology, notably in smartphones, thus enabling cameras built into cell-phone to have sensitivities enabling the detection of single molecules [Die+19b]. Cameras on smartphones have the disadvantage that the underlying signals are directly processed by the manufacturer's specific software and that the chip has a polychromatic coating. This means that a Bayer pattern is filtering the photons reaching a pixel according to their wavelengths. Every pixel is divided into four sub-pixels, one only registering photons in the red wavelength range, one only registering photons in the blue wavelength range and the final two only registering photons in the green wavelength range. This allows a chromatic image acquisition but imaging a emissions in a similar wavelength range (here AF647 $\lambda_{max} = 647$ nm) would reduce the photon registration by 75%. In general, CMOS cameras have low noise values, high frame rates, less degradation over time (compared to EMCCDs), large field of views (FOV) and physically small pixels (high resolution). These factors confirmed the decision to choose an independent monochromatic CMOS camera as detector for this project.

1.7.2 Camera resolution

The choice of camera can have a considerable impact on imaging. Additionally to the optical resolutions, the camera parameters as well as the emission pathway of a microscope can influence the achievable resolution. According to Abbe's resolution limit (eq. 1.8), given the following parameters: $\lambda = 650$ nm and $NA = 1.5$, the minimal resolvable distance

should be approximately $d_{min} = 217 \text{ nm}$. This however can only be achieved if the size of the pixels in the final image have the appropriate size i.e. smaller than the smallest identifiable feature. The pixel-size represents two different values in the context of microscopy. The physical pixel-size is the dimension of each pixel on the chip (down to $1 \mu\text{m}$ for CMOS chips). As the microscope magnifies the sample, the part of the sample that is represented on each pixel is smaller by the factor of magnification. The effective pixel-size can be calculated by dividing the physical pixel-size by the magnification. Small variation in the manufacturing of lenses or the positioning of optics can influence the pixel-size. In this project, we thus calibrate the pixel-size with an object of known dimensions to ensure correct size measurement for quantitative imaging.

In an ideal noise-less world, further magnifying the sample while reducing the sampling size would allow to better represent PSF of a given emitter, enabling to estimate the center of the PSF with higher accuracy. However, this does not apply in real experiments since all camera types are subjected to noise, as further discussed in subsection 1.7.3. Further magnifying the sample (= reducing pixel size) would thus neither increase the resolution as the acquired signal is diffraction limited and additionally reduce the signal to noise ratio (SNR) of every pixel. Since the acquired images are diffraction limited, there is an adequate pixel-size that is small enough to resolve the structures of interest but as large as possible to optimize the SNR. Here, the Nyquist sampling theorem is chosen as a criterion to set the magnification and subsequent detector pixel-size.

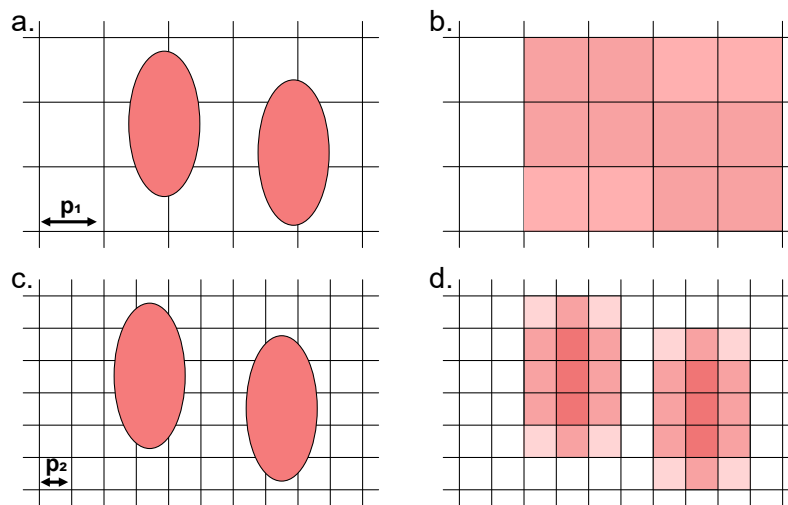


Fig. 1.7.: Nyquist sampling theorem in the case of camera pixels. **a.** Sample on a simulated pixel grid. Sampling rate is similar to the object size. **b.** The objects can not be distinguished from one another when imaged on a camera. **c.** same objects on a pixel grid with double sampling rate ($p_1 = 2 \cdot p_2$). **d.** Two objects can be identified in whatever position of the underlying grid.

The basic principle of the Nyquist theorem is that the sampling rate needs to be twice as high as the smallest signal that can be distinguished [Sha49]. In the case of microscopy, the diffraction limit provides the smallest resolvable distance. The chosen sampling rate,

in this case the pixel-size, should thus not be larger than half of the minimal distance two objects need to have to be distinguished i.e. the resolvable distance according to Abbe's resolution formula. A pixel-size of 90-100 nm is the optimal range for wide-field imaging as the magnification is large enough to match Nyquist, but the SNR is kept in a reasonable range. This choice of the right sampling rate is graphically shown in figure 1.7. A sampling rate of about $2.3\times$ smaller than the minimal resolvable feature has been empirically found to be optimal [Pho] (can vary depending on the application). If the sampling rate is larger than the before calculated rate, the acquisition is subjected to undersampling, thus increasing the FOV with possible loss of resolution. In the contrary case, oversampling means that the pixel-size is chosen too small, reducing the signal to noise ratio in the pixels resulting in a possible loss of resolution. This can be avoided by binning the pixels, thus counting a 2×2 matrix of pixels into a single one (or 3×3 etc...). Oversampling can however be useful for advanced techniques such as deconvolution [Sag+17; Bec+19].

1.7.3 Camera noise

All detectors are subjected to different noise sources that have influence on the quality of the acquired images. Noise is uncertainty in the acquired signal whereas background is actual signal from the sample but which is emitted by fluorophores which are either from defocused axial positions or from fluorophores that are not bound to the initially labelled structure of interest. Noise is subjected to statistical distributions [Pho], depending on its origin. The requirements of a given experiment e.g. a high temporal resolution (= short exposure times) will increase the noise contribution to the measured signal, effectively reducing the SNR. This predicament is especially challenging when using a low budget camera where sensitivity is considerably lower.

The first noise source is the read noise, which gets constantly generated when reading a signal during the conversion of photo-electrons into a voltage at the analog to digital converter unit (ADC). It is often described by a normal distribution, depending on the digitizer unit, and can be reduced through slower readout speeds as well as electronics design. The second noise source is the photon shot noise, which arises from the discrete character of photons detection. Photons are emitted randomly over time which, in the detection process, can induce signal depending fluctuations that follow a Poisson distribution. The $SNR \equiv \sqrt{N}$, with N the number of detected photons, plays a more important role for signals of low intensity. The third important source of noise is the dark current i.e. electrons that have been thermally generated on the detector and falsify the pixel values. The dark current also follows a Poisson distribution as these electron releases occur randomly. Dark current can be reduced by cooling the detector e.g. with a Peltier element or a good cooling geometry of the camera chip. Other secondary noise sources are affecting the acquired signal such as the EM gain decay or the excess noise factor which are fluctuations in the electron multiplying process in EMCCD cameras. Further noise

sources play a role that is negligible compared to the ones presented here, and are not relevant in the experiments conducted in this project.

1.8 Advanced microscopy settings

1.8.1 Angle of illumination

Depending on the type of sample as well as the structure of interest, the contrast and the image quality can be improved by adapting the illumination angle of the excitation light to best illuminate the desired portion of the sample. The back focal plane (BFP) of the objective is a plane where the light distribution of the emitted fluorescence is distributed according to the angle of emission, as mentioned in equation 1.3 (center: small angles ; edge: large angle)(angle increases with increasing distance from the center i.e. the optical axis). In a similar manner, when focusing the excitation light in the BFP, the angle of the excitation beam illuminating the sample can be changed by orthogonally moving the beams focus point within the BFP. The laser beam is still parallel to the optical axis but not entering the objective through the center anymore. The distance to the optical axis is proportional to the angle of illumination.

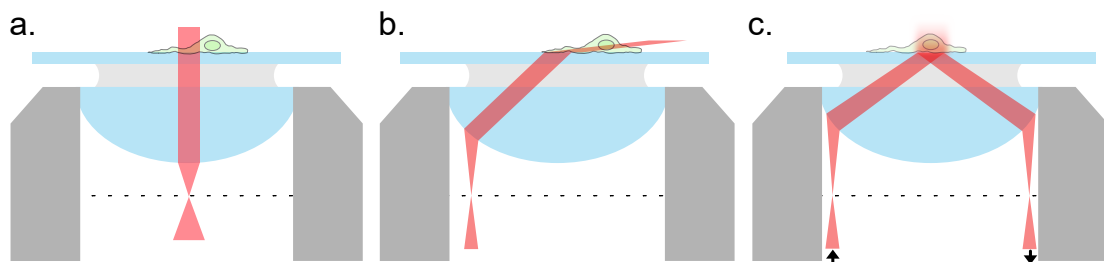


Fig. 1.8.: Schematic of an objective with the different illumination angle possibilities **a.** Epi illumination: excitation light enters center of the objective illuminating the whole sample. **b.** HiLO: The illumination is emitted by the objective with an angle illuminating a sheet of light within the sample **c.** TIRF: excitation light experiences total internal reflection at the interface, exponentially evanescent light intensity illuminates parts of the sample at the vicinity of the interface.

The most common and simple case is the epi illumination [WB12], as depicted in figure 1.8 **a.**. The excitation beam is on the optical axis and the orthogonal to the covers-glass thus the sample. The illumination is homogeneous but a drawback is that all fluorescence from different fluorophores at different axial planes are acquired simultaneously, reducing the signal to background ratio (SBR) of a given image.

The highly inclined and laminated optical sheet (HILO) illumination [Lim+11], as depicted in figure 1.8 **b.** makes use of the light diffraction at the glass-sample interface to partially illuminate the sample. By only illuminating a sheet within the sample, the acquired fluorescence signal is spatially confined within the illuminated region. The captured emissions have an improved SNR, as background emissions are reduced. Beam

position within the BFP, as well as the NA of the objective influence the angle of the beam.

As mentioned in subsection 1.6.1, the NA is paramount for high resolution imaging. The high-NA allows to acquire photons emitted in high angles and reciprocally to illuminate the sample from a high angle. Total internal reflection fluorescence (TIRF) [Fis09] is depicted in figure 1.8 c. and takes advantage of the high-NA of the objective. The excitation light reaches the sample-glass interface with an angle that is superior to the critical angle α_{crit} , the maximal angle where Snells law still applies $n_1 \sin(\alpha) = n_2 \sin(\beta)$. In this case n_1 is the refractive index of the coverglass, n_2 the refractive index of the sample (water), α the incidence angle of the excitation light and β the angle of the diffracted light. Even though the beam gets totally reflected, the near field component of photons illuminating the sample with an angle higher than α_{crit} are generating electric fields that can transgress the interface and induce fluorescence of the fluorophores at its vicinity. The range in which fluorophores can be excited is generally around a few hundred nanometers above the coverglass. The intensity of this evanescent electric field diminishes exponentially with increasing distance from the interface thus eliminating most background emissions [Fis09]. TIRF microscopy is often used to substantially reduce background when imaging a sample.

The mismatch in refractive index between glass ($n_{glass} = 1.5$) and air ($n_{air} = 1$) would already induce total reflection at the interface between the objective and air [Hec15]. Even at lower illumination angles, the multiple light diffraction at the glass-air-glass interface (Objective-air-coverglass), originating from the differences in refractive indices, are reducing image quality. The angle of acceptance of the objective is limited due to total reflection according to Snells law. Modern objectives account for a part of the aberrations with high quality lenses and corrective objectives. However, in order to have a high NA and to acquire the strongest possible signal, it is necessary to account for the mismatch in refractive indices at these interfaces. To use high NA objectives, immersion oils with a refractive index as close as possible to the one of glass ($n_{oil} \approx 1.5$) were engineered. This allows to have minimal differences in refractive index thus minimal aberrations from the objective to the sample. Methods such as TIRF microscopy are only possible because of the use of immersion oil, but even in epi illumination, the photon yield of an oil immersion is high, resulting in improved signal acquisition.

1.8.2 Confocal microscopy

A simple way to increase the images signal background ratio (SBR) is to intentionally eliminate background light emitted from different planes to enhance the quality of a sample plane in particular. The improved imaging quality of laser scanning confocal microscope [CJB11] is based on this principle. A simplified schematic is depicted in figure 1.9. The excitation light (green path) is focused on a single point on the sample. Scanning the sample is done by precisely tilting a mirror with a piezoelectric element or linear

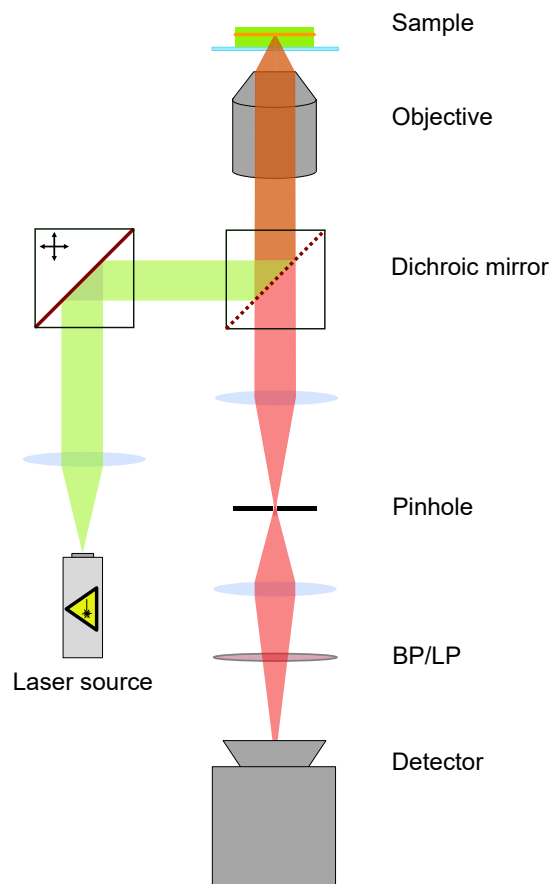


Fig. 1.9.: Schematic of a basic confocal microscope. Pinhole is limiting the detected fluorescence emissions to a specific axial plane in the sample. Emissions from other planes are blocked. Fluorescence of a specific plane of interest are imaged onto the detector with improved SNR.

galvanometer based motors. The emitted fluorescence (red path) from the plane of interest is focused by a lens onto the detector while out-of-focus fluorescence emissions are blocked by a pinhole positioned in the Fourier plane of the lens i.e. emissions from the focused sample plane are focused into the pinhole. Emissions from the planes above and below are out of focus when at the pinhole plane thus having a majority of their emissions blocked by the pinhole. The size of the pinhole should match the numerical aperture imposed by the optical elements onto the light and should thus be chosen according to the emission wavelength to optimize the sectioning quality. The introduced confocality considerably improves the SNR of fluorescence microscopy images compared to wide-field microscopy (1.4) and even increases the image resolution $d_{min} = 0.51\lambda/2NA$ [CJB11]. The easiest design for confocal microscopy is the laser scanning version. Basically, piezo-electric elements, galvanometer based motors or acousto-optical filters can move the focus point of the beam with high precision across the sample and scan it following a given pattern. The confocal microscope used in this thesis has a spinning disc unit. This one is composed of a micro-array of lenses and corresponding pinholes, both positioned in an Archimedes spiral shape. Different spots of the sample are simultaneously illuminated and imaged.

The spinning motion of the spiral shaped micro-arrays allow to scan the complete field of view (FOV). The scanning procedure is slower than the spinning disc thus has a lower temporal sensitivity, but has a better signal to noise ratio (SNR). Both methods have their advantages, depending on the specific experimental requirements.

1.8.3 Deconvolution

Any kind of fluorescence captured by an objective is diffraction limited. Techniques such as deconvolution try to remove the blurring of the PSF by using mathematical knowledge about the PSF shape and the image formation. Deconvolving an image to reduce the impact of the PSF on the final image by modelling the PSF in 3D, and is not a trivial technique. It is however an established tool to improve the contrast in image stacks with different axial positions of 3D structures and is rather used for displaying of 3D data-sets. The necessary know-how, the high 3D scanning precision and the availability of other techniques image scanning techniques (such as light sheet microscopy [Die+19a]) are ruling deconvolution out for the here presented project. Other methods to achieve higher resolution are possible to implement into the planned setup and are introduced in following section 1.9.

1.9 Super-resolution microscopy

The smallest resolvable distance described by the Abbe limit shows that the resolution scales linearly with the wavelength. So using lower wavelengths is a possibility to improve the resolution. Methods such as X-ray microscopy [Say+77], X-ray tomography [Wei+00] and electron microscopy (EM) [Rus87], [Svi17] (also positron microscopy) are often used in to resolve structures with higher resolutions as their short wavelengths allow much higher resolutions than microscopy in the visible light spectrum. However, when it comes to imaging biological samples, the information about the molecular composition of the imaged structures can more challenging to obtain. The contrast in these methods is generated through the sample's absorption of the light/electrons. Since all proteins and cellular structures are organic matter made from the same elements, it is challenging to discern a specific protein from others. The advantages of fluorescence microscopy (section 1.5.3) are still relevant for life science studies. The current development of microscopy is advancing towards methods that are able to combine the high specificity with a high resolution. A way to get both information is e.g. to take advantage of the resolution of an EM acquisition and combine it with the high specificity provided by a fluorescence signal [Gie08] [Gie+05].

The goal of this project being to build a high resolution light based microscope, the methods presented here will thus focus on optical microscopy techniques that allow overcome the light diffraction limit. The Nobel prize in chemistry of 2014 [Com] gave credit to the engineering of chemical labels and the usage of illumination patterns in microscopy experiments in order to breach the light diffraction barrier in fluorescence

microscopy. Surpassing this 200 nm resolution limit has provided new insights on the cellular structures, their organisation and the underlying processes at the nanoscopic level. Here, the most used methods are introduced with emphasis on single molecule localization microscopy (SMLM), a techniques that will have further applications in this project.

1.9.1 SIM and STED

In SIM microscopy, interference patterns are taken advantage of to increase the amount of gathered information [Gus00]. When a pattern interferes with a sinus wave-like structured illumination, the resulting pattern are Moiré fringes, which entail double the spatial information along the axis orthogonal to the wave. By repeating this procedure in different angles, the area of the image in the frequency space doubles, meaning that objects with half the size of the smallest resolvable feature can be seen when returning to normal space. In the case of microscopy, the known mathematical shape of the illumination combined with the known mathematical shape of the smallest distinguishable feature on the sample (diffraction limited PSF) allow to mathematically reconstruct an image with doubled resolution. Further concepts using structured illumination try to further improve the achievable resolution, but will not be discussed here.

Stimulated emission depletion microscopy (STED) is an imaging method developed from the confocal imaging. Upon excitation, a fluorescent probe has different mechanisms to relax from the excited (ON) state to the ground (OFF) state. The spontaneous relaxation, accompanied by fluorescent emissions, can be reduced through the use of stimulated emission, inducing relaxation with light emission of the same wavelength as the stimulated emission. As both mechanisms compete, the relaxation through stimulated emission can be favoured by increasing the stimulated emission laser density. This allows to reversibly deplete fluorophores within the sample. In STED microscopy, the depletion beam is doughnut shaped [Wil+06]. At the center of the doughnut the depletion intensity is null, allowing an additional excitation beam (with shorter wavelength) to induce fluorescent emissions. Fluorescence can be then be separated from the emissions of the depletion laser with optical filters. The non-linearity between the fluorophore depletion percentage and the depletion laser intensity considerably reduces the sample area from which fluorescence is emitted. The emitted fluorescence is still diffraction limited, but can be confined to a smaller region of the sample, effectively increasing the resolution of the reconstructed STED image. The minimal resolvable distance can thus be changed to $d_{min} \approx (\lambda)/(2n \cdot \sin\alpha \sqrt{1 + I/I_{sat}})$, where I and I_{sat} are the depletion laser intensity and the saturation intensity of the depletion. Just like in a laser scanning confocal microscope (section 1.8.2) the depletion beam and the excitation beam are scanning the sample. As repeating the scanning procedure with very short displacements, the process is time intensive and acquiring the signal with an APD (avalanche photo-diode) is more effective and precise. The intensity values measured at every position are then reconstructed into

an image where every single pixel represents one measurement of a small area of the sample.

1.9.2 Other methods

The fluctuations in fluorescence intensity of every fluorophore can be used to estimate their positions with higher confidence. Even though these methods do not allow to directly estimate the position of every single molecule, a lesser improvement in resolution can be achieved. The underlying mechanism is that by acquiring longer videos of a sample, the intensity of the fluorescence will vary due to the stochastic nature of electrons cycling between electronic states. Auto-correlation (see subsection 1.9.8) of the time dependent fluorescence intensity gives a sub-pixel estimation of possible fluorophore position, as was demonstrated by methods such as SOFI (Super-resolution optical fluctuation imaging) and NanoJ SRRF (super-resolution radial fluctuations) [Der+10; Gus+16].

Another approach that has gained recent popularity is expansion microscopy [Gho+23]. The innovating homogeneous expansion of the sample in three dimensions physically increases the size of the sample. With a normal wide-field microscope, an increase in resolution can be observed, as the same pixels represent a smaller part of the sample after the expansion process. Compared to other microscopy methods, the magnification increase is achieved by sample preparation, which facilitates the usage of this technique for biological imaging essays. Modern improvements in the expansion method are aiming to monitor proteins in cells where ultra-structures can be made visible with light microscopy [MB20]. The emitted fluorescence from such a sample is still diffraction limited but breaches the resolution limit through the expansion factor.

1.9.3 Single molecule localization microscopy

Single molecule localization microscopy (SMLM) regroups different techniques which are an interdisciplinary combination of technologies, together enabling to substantially increase the resolution of a biological structure using fluorescence. In this project, the focus will be on (*d*)STORM [RBZ06; Hei+08], as method of choice in the experiments presented in this thesis.

Single molecule localization: When looking at a single molecule in a bright-field fluorescence microscope, the PSF pattern will always be present on the detector. The shape of the PSF however is mathematically known. This allows to model the observed pattern and fit the PSF to localize the estimated position of the single molecule with higher accuracy. The PSF of a system is often challenging to predict, as all active optical elements affect its shape. The closest approximations would be best described with an Airy function but in the past decades, computational resources were limited. Still nowadays, running an SMLM algorithm continues is computationally demanding. To speed up the localization process and reduce the computational demand of a localization algorithm, the fitting

procedure is done with a Gaussian filter. The graph in figure 1.12 **d** shows the difference between Gaussian and airy fitting of a raw data-set. The localization precision is so similar that different other aspects of the experiment are more relevant to the localization accuracy than the function used for fitting [SR10]. A model of such a 2D Gaussian fit that is used to localize the position of a single molecule according the acquired diffraction pattern is shown in equation 1.10.

$$G(x_c, y_c) = \frac{A}{2\pi\sigma_x\sigma_y} \exp \left[-\frac{1}{2} \left(\frac{x - x_c}{\sigma_x} \right)^2 - \frac{1}{2} \left(\frac{y - y_c}{\sigma_y} \right)^2 \right] + B \quad (1.10)$$

Hereby, x_c and y_c are the respective centroid position, A the intensity and B the background. σ_x and σ_y are respectively the uncertainties of the localization. One possible localization procedure using Gaussian filtering is shown in figure 1.10. The raw-data is processed with a Gaussian filter (alternatively also by derivatives of the Gaussian filter [Rie20; Ove+14]). The processed image is then fitted with a 2D-Gaussian to locate the position of the fluorescing single molecule with higher accuracy.

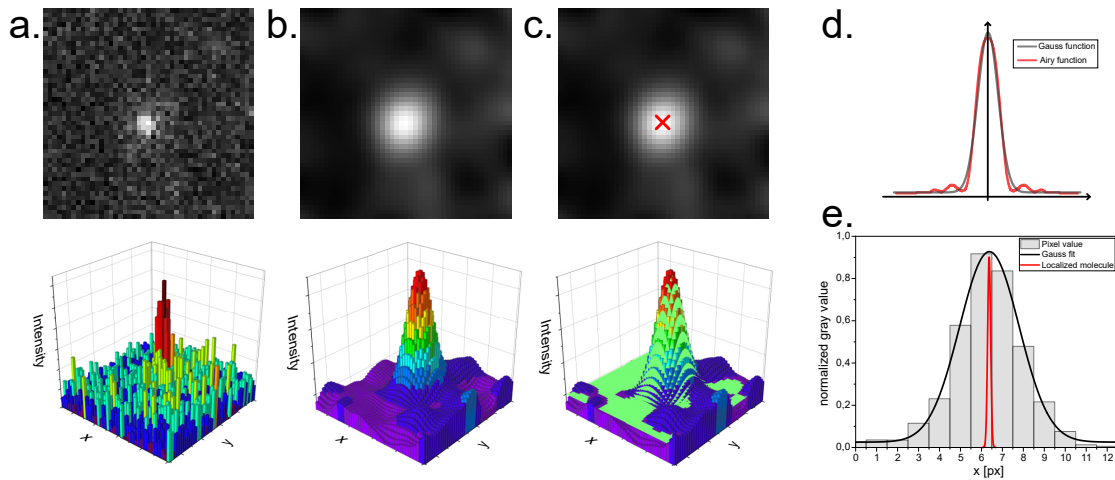


Fig. 1.10.: Single molecule localization process. **a.** Raw image of a single molecule as captured on the Photometrics Delta 512 EMCCD detector, with corresponding plotted 3D representation. **b.** Same molecule as in **a** processed with a Gaussian filter. **c.** Smoothed PSF image is fitted with a normal distribution to determine the centroid of the molecule. **d.** comparison between Airy and Gaussian functions. **e.** One dimensional representation of a localization with higher accuracy positioning of the single molecule position (red curve) compared to the pixel signal (grey bars).

Intuitively, a stronger signal yields a higher image quality. In the case of SMLM, the localization precision scales with number of collected fluorescence photons [ORW04]. Different setup dependant factors have to be taken into account to determine how accurately the position of a single molecule can be estimated. In a wide-field setup, fluorescence originating in other focal planes are also collected, falsifying the acquired signal by a background b . This can be accounted for using methods such as aperture-photometry [FSL17] to subtract local background from the measured intensity, or can be reduced using illumination methods such as TIRF (subsection 1.8.1). The pixel-size a and the noise

factors of the detector generate pixelation noise that has to be taken into account when localizing a single molecule. The prediction of the precision of a localization position Δx has been estimated by [TLW02] and altered by Mortensen [Mor+10] on the basis of new experimental evidence. The localization precision according to the latter is displayed in equation 1.11 and is valid for X and Y.

$$\langle \Delta x^2 \rangle = \frac{\sigma^2 + \frac{a^2}{12}}{N} \left(\frac{16}{9} + \frac{8\pi b^2 \sigma^2 + \frac{8\pi b^2 a^2}{12}}{Na^2} \right) \quad \text{hence} \quad \langle \Delta x \rangle \approx \frac{\sigma}{\sqrt{N}} \quad (1.11)$$

Here, σ is the standard deviation of the PSF. The pixel-size should thus be in an appropriate range, as mentioned in section 1.7. The localization precision of a dye emitting 1000 photons with a pixel-size of around 100 nm is well below 10 nm, which is a considerable resolution improvement compared to diffraction limited (DL) images of single molecules. In order to use the localized positions of single molecules to reconstruct an image of higher resolution, the ability to identify every single molecule is paramount. The Rayleigh criterion defines the minimal distance between two single molecules where both can still be considered as two distinct objects [Ray79; Bor+19]. This criterion becomes relevant when using SMLM localization algorithms, to define a limit where objects are distinguishable. In a similar way, the portion of molecules that are simultaneously in an ON-state should be low enough to make the overlapping of two PSFs as unlikely as possible. The Rayleigh criterion is schematically shown in figure 1.11.

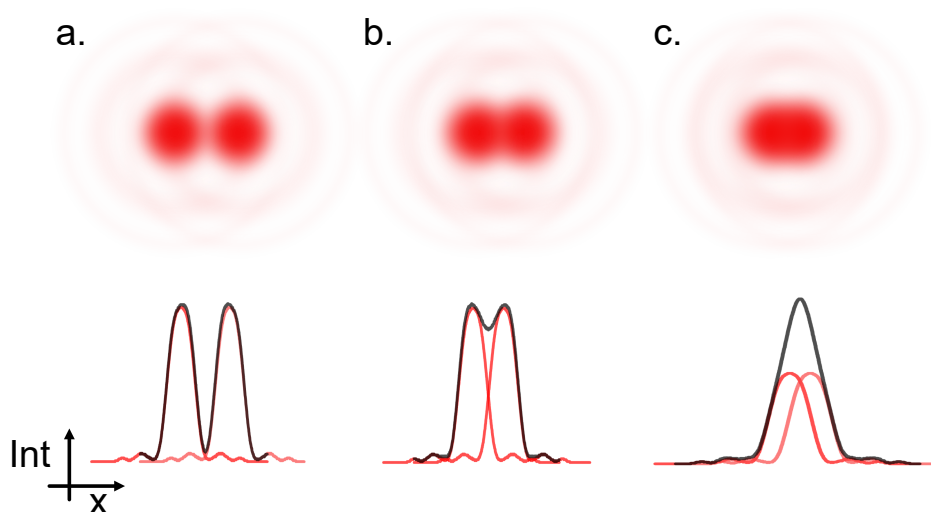


Fig. 1.11.: Rayleigh criterion for single molecule distinction. a. Two single molecules can clearly be distinguished from one another. b. Rayleigh criterion, limit distance to clearly distinguish the two molecules. c. Molecules are too close thus indistinguishable from one another.

As shown in 1.11, the simultaneous detection of two molecules in close vicinity ($< d_{\text{Rayleigh}}$) does not allow to discern the them. To perform SMLM, most molecules should be in a stable non-fluorescent state while a sparse subset is fluorescent. In order to have the highest possible chance to localize every single molecule that switches into the bright state the rate at which molecules switch into the dark state should be chosen

accordingly to have a statistical distance between simultaneously fluorescing molecules that is superior to the Rayleigh distance.

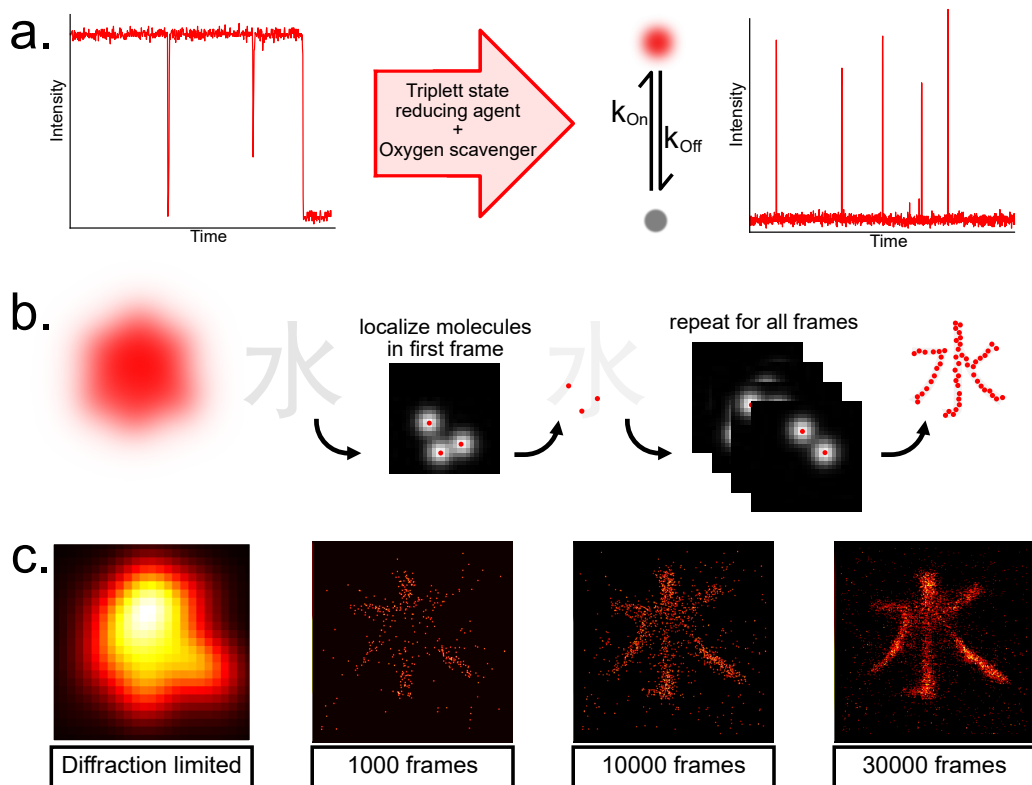


Fig. 1.12.: Working principle of SMLM as shown on the example of (*d*)STORM. **a.** Single molecules are brought from a fluorescent state to a stable non-fluorescent state with sparse blinking events ($k_{OFF} \gg k_{ON}$). **b.** Left: Diffraction limited image of the sample. Right: Single molecules are localized frame by frame. A sufficient number of frames reconstructs the sample. **c.** Simulation with FluoSIM ([Lag+20]) of the sample in **b.** with reconstruction state after different number of frames. Images represent $2.5 \times 2.5 \mu\text{m}$.

Switching fluorophores in *d*STORM: The *d*STORM method makes use of reversibly photo-switchable fluorophores which can be switched from a fluorescent (ON) state into a stable non fluorescent (OFF) state (see figure 1.12 a). The rate at which the fluorophores switch into a dark state (k_{OFF}) needs to be significantly higher than the bright state rate (k_{ON}). A factor of over 1'000 between ON- and OFF-rate [Lel+21; vS14] is necessary to stochastically have enough molecules in a non-fluorescent state to localize the fluorescent subset of single molecules. The factor is also dependant on the labelling density of the sample, as there is no guarantee that the fluorescent are distanced by more than the Rayleigh distance, the high OFF-rate as well as the stochastic process are ensuring the localization of a majority of the single molecules. The Alexa Fluor dyes, Cy5 dyes and ATTO dyes, which belong to the family of cyanine and oxazine dyes are photo-reduced by potent electron donors [Lin+11]. Thiols e.g. β -mercaptoethylamine (MEA) are quenching and stabilizing the triplet state at milli-molar concentrations. The removal of oxygen can trap rhodamine dyes in their radical state for hours or put cyanine as well as oxazine

dyes in a higher electron affinity state. Both these effects are facilitated upon radiation. By combining the buffer with oxygen scavenging systems, a long lasting stable and reversible triplet state is generated, enabling to induce single fluorescence events within the mostly non fluorescent sample, for single molecule localization microscopy [vS14]. The fluorescent state is recovered through the molecular oxygen in aqueous solvents for rhodamine and oxazine based dyes. For cyanine based dyes, it can also be induced by illumination in oxygen depleted solutions.

Reconstruction: The collected information about the positions of every single molecule are then, just like in a pointillistic artwork, assembled into a reconstructed image ([Hei+08]) where every localization is represented by a normalized Gaussian with Δx (from equation 1.11) as σ or other representation methods such as the average shifted histogram [Ove+14]. These reconstructed images have a significantly improved resolution compared to images acquired with a diffraction limited wide-field or a confocal based method [RBZ06].

1.9.4 Alternative SMLM methods to *d*STORM

Apart from *d*STORM, other SMLM methods take advantage of dye technologies to induce fluorescence of a sparse subset of the dyes. DNA-PAINT (DNA points accumulation for imaging in nanoscale topography) [Sch+17] labels the sample with DNA strands (docking). During the measurement, dyes linked to a complementary DNA-strand to the one on the sample (imagers) are added to the sample. Through transient binding of the imagers, a strong enough signal to differentiate a single molecule from the background and thus localize the position of the docking strand molecule can be integrated. The advantages of DNA-PAINT are the low background as the binding is very specific and the possibility to replace the buffer and image different structures with the same emission wavelength. The method however is rather slow, but efforts have been made to speed up the process, and the recently developed fluorogenic DNA-PAINT [Chu+22] allows to acquire data-sets with similar speeds to *d*STORM. Another widely used technique is PALM (Photo-activated localization microscopy) [Bet+06]. Here, the used fluorophores are exogeneously expressed genetic fusion constructs with a photo-activatable fluorescent protein, that switch from a non-fluorescent state to a fluorescent state, once photo-activated with another wavelength (e.g. UV light). The photo-activation is a random process that can be tuned with the intensity of the photo-activation light. This method has a highly specific staining and low linkage error as the fusion protein is genetically embedded in the structure of interest. The lower brightness of fluorescent proteins compared to organic dyes remains a challenging engineering task. The method however is still very robust, and can be performed at similar acquisition speeds as *d*STORM.

1.9.5 Single particle tracking

In contrast to FCS and FRAP (mentioned in subsection 1.3.1), single particle tracking (SPT) follows single molecules on the membrane, providing insights into the diffusion properties of particles, even allowing to identify different populations based on e.g. their diffusion coefficient [She+17]. Performing SPT requires certain sample and setup features, described here specifically for the case of membrane molecule tracking with light microscopy as is schematically demonstrated schematically in figure 1.13. First, a fluorescent label needs to be attached to the membrane molecule of interest. Then, a setup with steady illumination and a fast frame rate are necessary to best temporally map the particle's diffusion. Finally, a tracking algorithm will link different positions of the same molecule at different time points to one trajectory. To substantially increase the spatial resolution of a particle's position, the PSF of the tracked fluorophores are fitted, as described in 1.10. The high spatial and temporal resolution of a trajectory can then undergo data analysis steps to determine different features such as the diffusion coefficient (as mentioned in subsection 1.3.1) and the moment scaling spectrum (MSS) amongst others. The accuracy of the fitting [CWG01; Mor+10] and the tracking algorithms [SK05; Tin+17] have made SPT a widely appreciated tool for molecular dynamics characterization.

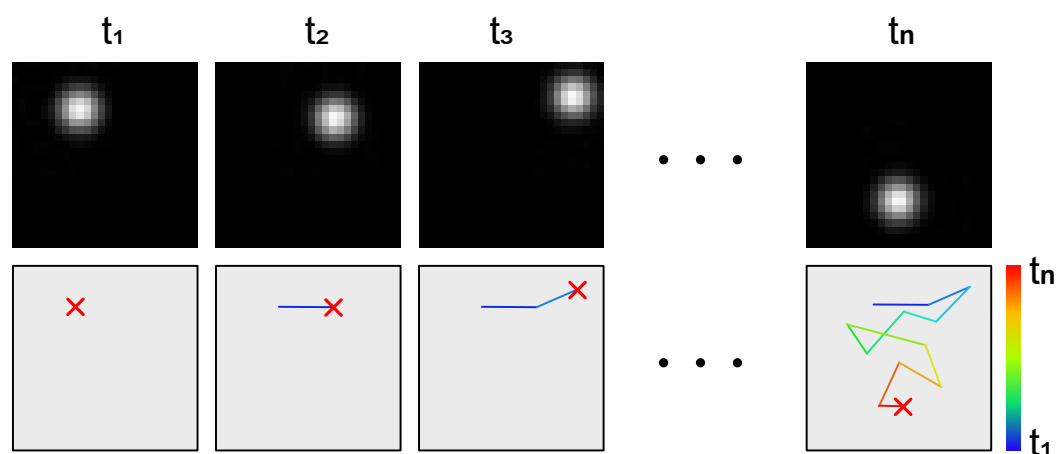


Fig. 1.13.: Principle of single particle tracking. The position of a photo-stable fluorophore e.g. a quantum dot (QD) is localized over a time series of frames (from t_1 to t_n). Localized positions of a molecule are computationally linked to map its trajectory over the elapsed time. Resulting track can then be used for further analysis steps.

SPT can be has proven to be an useful tool to study the properties of the cell membrane and characterize its molecules according to parameters extracted from the SPT analysis, such as the diffusion coefficient and mobility. Applications in the reproduction of 2D cellular structures and mapping cellular features according single particle characteristics are further applications of this method [Alb+16b; She+17; Li+20b]. The additional advantage of SPT is the simple implementation of the technique in any microscope with wide-field illumination. No additional laser is needed and the algorithms to perform the

analysis [SK05; Tin+17] are published and openly available on widespread platforms such as ImageJ [SRE12].

The outputs of a single particle trajectory are a table containing the position of a particle at discrete time-points. To characterize the motion of a molecule, a common movement feature to observe is the diffusion coefficient, which is often calculated using the mean squared displacement (MSD) of a particle [QSE91]. As the motion of a particle can be cancelled out by randomness, the squared displacement i.e. the area explored by a particle during a given time-lapse is a more reliable value to study molecular dynamics. For a particle diffusing through the plasma membrane, the time-dependent position can be written as $f(t) = [x(t), y(t)]$ where x and y are the corresponding coordinates. Normally, a diffusion process would be described with the probability of a particle at every time-point but the ensemble average for calculating the MSD can be approximated as the time average for the trajectory of a single particle [QSE91].

$$MSD(t) = \iint |f(t+t') - f(t')| dt' \quad (1.12)$$

Furthermore, since in an experimental measurement of single particle diffusion, the estimation of the position is done at discrete time-points ($n\Delta T$ with n the number of time-points and ΔT the time difference between two measurements) instead of being a continuum. The MSD (e.g. for x in equation 1.13) can be considered as a sum of the time dependent particle displacements p .

$$\langle MSD_x(t)^2 \rangle = MSD_x(n\Delta T) = \sum_{i=0}^N \frac{(p(x_{i+n}) - p(x_i))^2}{N+1} \quad (1.13)$$

For Brownian motion of a particle in a 2D plane (e.g. within a cell-membrane), the MSD linearly increases with the time-lag $t_{lag} = n\Delta T$ and correlates to the diffusion coefficient D , as derived in equation 1.1.

$$MSD(t_{lag}) = 4D \cdot t_{lag} \quad (1.14)$$

The diffusion of membrane molecule can be anomalous due to e.g. barriers limiting its motion [Met+14]. The additional dependency on the localization frequency of the particle motivates the development of more precise parameters to describe the type of motion a particle undergoes. Different types of motion translate into a loss of the linear dependency of the diffusion coefficient depending on the time lag. with an exponent α , the dependency scales with t_{lag}^α , differentiating particle motility according to the dependency to t_{lag} . The moment scaling spectrum (MSS) slope is a specific case of the MSD, introducing a parameter which enables to qualitatively and quantitatively characterize the type of motion a particle is undergoing [Ewe+05]. An MSS slope of 0 translates to immobility of the particle. For $MSS < 0.5$ the motion can be qualified as Brownian. For $MSS > 0.5$, the motion is super-diffusive.

1.9.6 SMLM in 3D

Cellular structures are three dimensional and often require imaging strategies that display the structure of interest in 3D in order to study their functions [Let+15]. The axial resolution of a microscope still lags behind the lateral ability to localize molecule. Ideal imaging of 3D structures would require an isotropic resolution along all axes. To localize a single molecule in all three dimensions, different methods have been developed to introduce an axial dependant feature to measure the axial position of a single molecule. The imaged PSF of a fluorophore broadens when imaged out of the focus plane. This can be quantified in terms of an increasing FWHM when localizing the centroid with a Gaussian filter. However, it remains problematic that the broadening of the PSF occurs both above and below the focus plane. Different methods rely on identifying and differentiating the layers above and below the focal plane by either introducing an asymmetry between both conditions, or by introducing other features to distinguish between them. One of the most commonly used group of techniques is called PSF engineering. The use of optics enable to introduce optical "errors" such as for example astigmatism. This changes the shape of the PSF above and below the focal plane, providing a PSF shape that is to every Z position [Oli+13; Lel+21]. Another common way to introduce 3D information is called biplane imaging. The emission beam is split into two, a known axial offset being introduced between both paths. Every PSF is thus registered twice, at different Z-positions. From the PSF shape of a molecule in each channel, a pair of PSF shapes which is specific to every Z-position can be extrapolated. More techniques exist [Bou+15; FSL17; Lel+21] to unlock the 3D information, but will not be mentioned here.

1.9.7 SMLM algorithm and further analysis and FIJI

The prolific SMLM field has pushed the development of different software analysis solutions in the past decade. A good comparison between some of the most used solutions is given in the "super-resolution fight club" [Sag+19]. As the experiments presented here are mostly in 3D and are a proof of principle of low budget SMLM, the requirements are met by most of the available SMLM software. I chose to proceed with the Super-resolution Microscopy Analysis Platform *SMAP* [Rie20] software for its easy handling in Matlab, as well as its good performances. The necessary license for MATLAB might be a limiting factor for some users. ImageJ/FIJI [SRE12; Sch+12a] have proven to be free versatile platforms for image analysis that include a variety of plugins to localize and process SMLM data-sets [Lin19]. For this reason I chose the ImageJ-plugin *ThunderSTORM* [Ove+14] as a second option, for its quality and availability. Using a single software package also is advantageous as it facilitates to implement other established ImageJ plugins for data processing and analysing. Producing analysis pipelines or even batch processing modules is also facilitated through the use of similar formats on the same platform.

In terms of accessibility, the easiest solution would be to write a separate localization algorithm and implement it in the software controlling the microscope. This would

represent a significant amount of work within this project but would open the opportunity to have home-built software solution, adapted to the specificities of the instrument and adaptable by the users for their needs. Furthermore, since the coding language Python 3 has seen a significant increase in its number of users, a custom solution within Python 3 would allow more people to adapt a given code for their purposes. The increase of image analysis development in python can also be seen with the recent popularity of Napari [Sof+22], the python equivalent of ImageJ, more specialized in handling large data-sets. Open-source software options for SMLM applications have been considered, and the MiEye [Als+22] algorithm is implemented in the acquisition software used in this project, however the data-sets in this thesis have not been analysed with it.

1.9.8 Cross-correlation

Cross-correlation is a signal processing method to evaluate the degree of similarity between two signals or time series as a function of their mutual displacement towards one another [AHK21]. The underlying mathematical operation is shown in equation 1.15. A variant of this method is the auto-correlation where the signal is evaluated against itself. It can be used to measure the pixel-size of a setup or to quantify the periodicity of a structure e.g. actin along the axon initial segment [Alb+16b]. A simplified version of the cross-correlation concept is displayed in one dimension in figure 1.14. As one of the signals is spatially shifted in relation to the second one, the resulting correlation between both signals (in this case the same signal shape) varies between 0 (no overlap) and 1 (complete overlap).

$$h(x, y) = f * g(x, y) := \iint_{-\infty}^{\infty} f(x, y)g(x - i, y - j)di dj \quad (1.15)$$

In the context of microscopy, the signals in question are images thus 2D signals with 2D correlation maps instead of graphs. This process has interesting applications in image analysis and data processing. Widespread applications are the overlaying of images of the same sample acquired with different techniques or channels, thus accounting for a shift or a different magnification between the channels. Another important application in this project is the correction of drift, that microscopes experience during longer acquisition times, thus inducing imaging artefacts when uncorrected. This is achieved by splitting imaging data-sets in subsets which are then compared to one another to analyse their similarity and extract the time dependent sample motion and remove its influence in the reconstructed image.

1.9.9 How to measure resolution

Estimating the resolution of microscopy images is not trivial, especially for SMLM, where the resulting image is a pointillistic reconstruction of the fluorophore distribution on the sample. The position of single molecules centroids can be estimated with below 10 nm

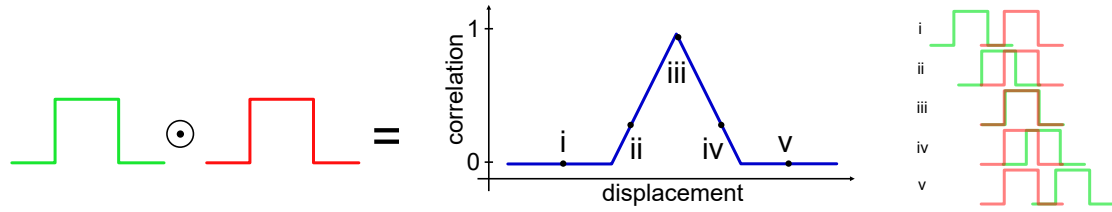


Fig. 1.14.: Simplified cross-correlation concept in one dimension. The correlation of two rectangular signals is measured as a function of the displacement of the green signal compared to the red one. Resulting cross-correlation in blue with five exemplary points highlighted. Inspired from [AHK21].

accuracy. The accuracy of the localization inversely depends on the number of acquired photons (sqrt of it) as displayed in equation 1.11 [ORW04; Mor+10; Lel+21]. This however is not the resolution at which specific structures in the sample can be discerned. To make affirmations about the resolution of an image acquired with a given instrument, one possibility is to look at a structure of interest which size is documented and known from previous studies. This allows to assess if the measurement done with ones experimental setup and analysis settings matches the value extrapolated from measurements in other studies, but does not provide information about the accuracy of structure reconstruction through SMLM.

Another possibility is to use Fourier ring correlation (FRC) correlation to compare reconstructed subsets of the full data-set to and compare them thus estimating the smallest resolvable overall structure. The FRC is a signal processing tool that has emerged in recent years as an established method to measure the resolution of an image in the described correlative way [Nie+13]. In a conventional microscopy image, the diffraction limit (equation 1.8) is the minimal distance at which features can still be resolved. In a DL image is Fourier transformed (according to equation 1.3) and represented in the frequency space, the resulting image would have the large features in the center and smaller features further away from the center. The shortest resolvable distance Δd would correspond to the the the value given by the Abbe formula 1.8 and would thus be a circle in the frequency space with a radius corresponding the inverse of Δd .

In figure 1.15 the raw data-set of an SMLM acquisition has been split into two sub-stacks, which have both been reconstructed into SMLM images. Both these images are then fast Fourier transformed (FFT = computational/numerical Fourier transformation) and correlated to one another. As the FFT images are represented in the inverse space, the size of a given feature decreases with the distance from the center of the image. The size of the circle corresponds to the smallest identifiable feature. Scanning through the FFT image from the center outwards allows to determine the largest radius where features can still be distinguished, corresponding to the reachable resolution of the image. The correlation of both subsets of the same acquisition is plotted as a function of the spatial frequency. By thresholding the correlation, a value for the achievable resolution can be

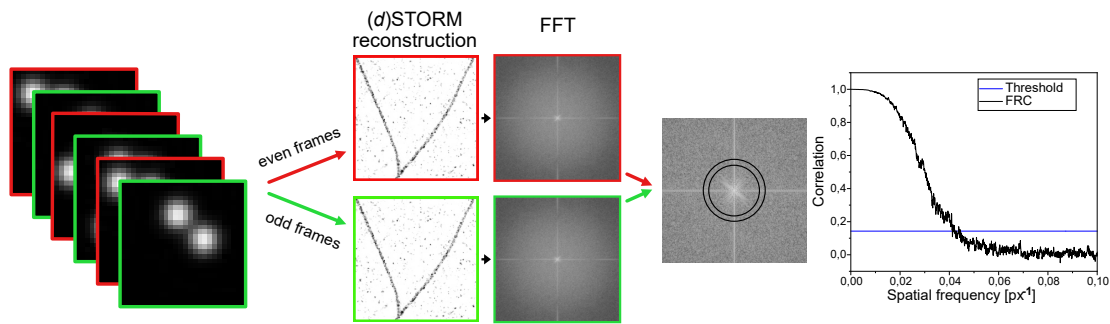


Fig. 1.15.: Fourier ring correlation analysis for resolution estimation. A raw SMLM data-set is split into odd and even frames to generate two separate reconstructions of the same structure. Through FFT, the Fourier space images of both reconstruction are compared to determine the smallest distinguishable features in the real space. According to the chosen thresholding criterion, the FRC-based resolution is estimated.

estimated. ImageJ plugins ([Cul+18; DGR19]) allow to estimate the resolution while choosing the right threshold criteria [vS05]. The use of FRC can be beneficial to estimate the resolution of an image, but also to estimate a correct focal plane or other applications involving image quality assessment.

1.9.10 Clustering of SMLM data

Clustering is a tool that allows to separate a given population or a data-set into groups i.e. clusters based on common feature. The algorithms are artificial intelligence (AI) techniques and count to the unsupervised machine learning category i.e. the clusters are chosen by the machine without having received an input about what kind of groups to expect. For example, the suggestions of movies on streaming platforms can be done by clustering user profiles with similar preferences. Another example was the identification of infection hot-spots during the Covid19 pandemic by tracking the location of infected people. In the context of microscopy, clustering is often performed according to the spatial distribution of a given molecule population. The complexity of three dimensional distributions leaves two dimensional systems as preferred study object e.g. the cell membrane. Techniques such as STED and SIM are easy to use and probably the methods of choice to image structures, as a direct feedback on the quality of the sample is available to the user. SMLM methods are a well suited tool to visualise and understand molecular organization and cellular substructures at the nanoscopic scale. Although they require intensive analysis, having information about every single molecule can be a considerable advantage. The type of data generated (localization tables) also enables the use of different quantification tools, as the information of any reconstructed image already exists as a *.csv* or *.txt* file. In this section the emphasis will be put onto clustering .

1.9.11 Clustering algorithms

The focus of the cluster analysis done in this thesis is on cell-membranes, which can be approximated as a 2D surface. The distribution of molecules can be characterized by different parameters, notably the density of the molecules. As aggregation of specific molecules can act as a molecular switch to start signaling pathways at the cell interface, the distribution of these molecules on the cell surface can give insights into cell signaling and critical densities at which such processes originate.

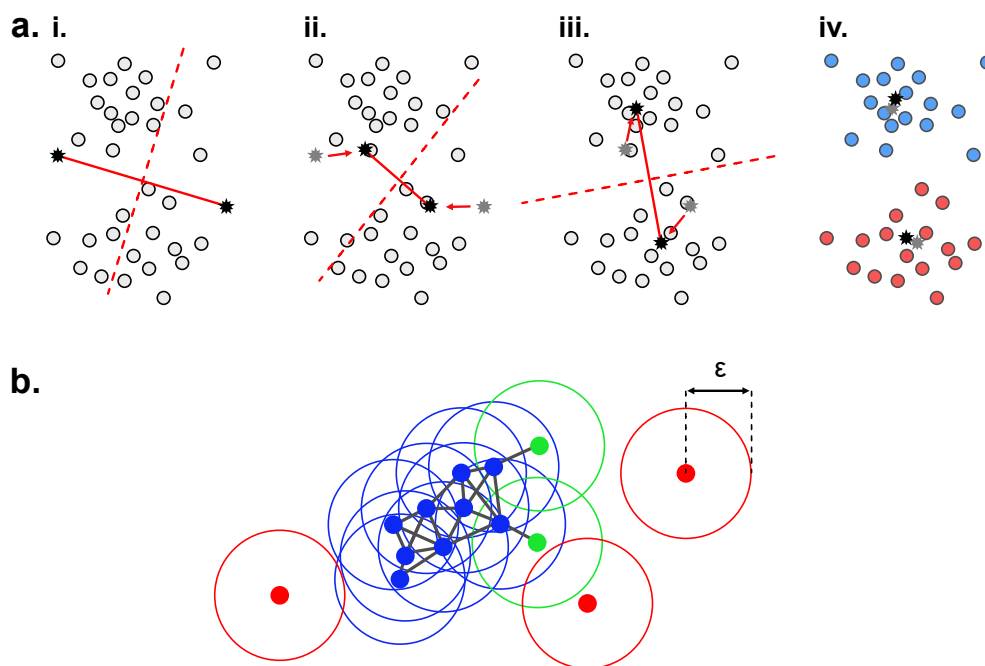


Fig. 1.16.: Simplified K-means and DBSCAN clustering methods. **a.** K-means algorithm. Seeds are positioned randomly (i). The secant to the connecting line delimits the data-set into two groups, the arithmetic center of mass is calculated (ii). Procedure is repeated until changes are minimal (iii). Final clusters in red and blue (iv). **b.** DBSCAN with threshold of at least three points within ϵ to be part of the cluster (blue). Green points are at the edges and do not count to the core, red points are not affiliated in any way.

The SMLM imaging of cell membrane molecules provides the information of the position of individual molecules. Using clustering algorithms, the size, density and number of clusters can be determined. Here, three of the most commonly used clustering algorithms in the context of SMLM data-analysis are presented, to provide an overview of their functioning.

K-means: The number of expected clusters is an input parameter. Seeds are placed onto the data-set and the points are divided according to the orthogonal line halving the connecting straight line between both seeds (figure 1.16). The seeds are then moving to match the arithmetic mean of the points position on their side of the dividing line. The procedure is repeated until the seeds position best match the cluster distribution. This

value can be set by e.g. setting a percentage of data-points changing clusters after a cycle [AR14; KNH20a].

DBSCAN: In density-based spatial clustering of applications with noise, the assignment to a cluster is decided by the local molecular density. In figure 1.16 **b**, the circle of diameter ϵ must entail a set number of molecules N to be part of the cluster (blue). Data-points with too few other points in their vicinity (green) are borderline but are not part of the cluster core. Outlying molecules (red) can easily be distinguished from the clustered points. The combination of ϵ and N gives a density parameter that can be used to threshold the affiliation to a cluster [AR14; KNH20a].

ToMaTo: Topological Mode Analysis Tool (ToMATo) is a persistence based clustering tool [Cha+13] that additionally to the density of the point cloud considers the topology of the molecule distribution. The persistence P is used as a metric to connect or separate neighbouring clusters with similar densities, or register some clusters as noise. Persistence diagrams allow to distinguish prominent clusters from topological noise, and obtain a more precise estimation of cluster features in noisy systems. This algorithm has already been adapted to analyse SMLM data-sets [Gri+15].

1.9.12 Bayesian approach

The choice of adequate clustering parameters is often subjective, in general as well as in the context of SMLM data clustering. Bayesian data analysis can be used as a general method to select the optimal clustering result from priorly suggested parameters, settings and models. This approach simplifies the clustering of SMLM data-sets by reducing the bias introduced by the user.

Baye's theorem is a statistical tool to predict conditional probabilities, based on prior events influencing the outcome [PKA15]. The dependency of such conditional probabilities is shown in equation 1.16.

$$P(A|B) = \frac{P(B|A) \cdot P(A)}{P(B)} \quad (1.16)$$

In a practical example, the Covid19 testing kits can be used as false positives and false negatives do not make it 100% reliable. The probability of being infected given a positive test ($P(A|B)$) is determined as the product of the probability of the test being positive given one is infected ($P(B|A)$) and the probability of being infected ($P(A)$) divided by the probability of having a positive test ($P(B)$). To summarize, the conditional probability of an event depends on the likelihood of an event and the prior knowledge one has about the system. In order to use Bayesian analysis [Gel+13], likelihood functions of prior events and their statistical distribution need to be found or estimated. In the context of SMLM clustering, Bayesian data analysis can be used to test various assumptions of the expected clustering behaviour and make a projection [Rub+15]. The methodology applied in the

experiments presented in this thesis is described in [Kut+21], and further information as well as the source code can be obtained in the GitHub repository [KS].

1.10 Open-source concept

In order to push forward the limits of human knowledge in natural sciences, innovative technologies and their applications to solve current challenges are paramount. The high precision required by scientific instruments that are necessary to perform modern research assays goes hand in hand with increased complexity and price. Because of the considerable research funds invested in the development of such instruments, providing low budget solutions is not the goal of high-tech companies and will probably not be in a foreseeable future [Hoh+22]. Additionally, a important amount of knowledge and experience is necessary to answer a scientific question using innovative technologies. These factors are limiting the access to scientific progress and discoveries to countries that have the means and the infrastructure to run research programs [Wen23]. At the same time, research is increasingly focusing on very precise topics and the findings are phrased in ways that require considerable background knowledge to understand it. The accessibility of science has thus become challenging to the general public [Hay92]. This challenge is further accentuated by the price publishers impose on journal readers that are not affiliated to academic institutions.

These challenges, whether lacking knowledge or hardware, have opened the way to a new research branch that focuses on increasing the accessibility of science. The open-source community tries to overcome these types of challenges. This entails affordable hardware, free online resources, cooperation platforms, distribution networks and more. Initiatives such as the concept of sharing materials [Lav21] (here chemicals) or publishing findings in open source journals [Law01] both tend to indicate that science could benefit open-source approaches, supporting the emergence of new open-source projects. In this thesis, I aim to demonstrate the the feasibility of high-quality microscopy using an open-source concepts and hardware.

1.11 Open-source microscopy

Open source microscopy is the branch of microscopy aiming to provide free methods and solutions for producing microscopy hardware. An open-source concept needs to fulfill certain criteria such as interoperability of the interfaces (i.e. open development), involvement of the communities, the sharing of knowledge and more. An overview over these criteria is described in [Hoh+22]. Open hardware, in particular open microscopy is affected by production constraints. Commercializing hardware is a challenging task for people in academia, which lack time, funds and know-how to start their businesses. On the other hand, investors often opt to patent innovating products with the outlook for the

investment to be profitable. These challenges are still persisting but have motivated the emergence of different concepts for open microscopy.

The production of hardware is facilitated and supported by the development of 3D printing technologies, helping scientists to easily prototype their concepts. Laboratory equipment can be reliably produced at a much lower budget as has been shown by [Mai+17], while maintaining sufficient manufacturing quality. Frequently used equipment e.g. pipettes, can be 3D printed and match quality requirements of the international standardization organisation [BBE18] thus offering a serious alternative for research groups with limited funding. 3D printing can even support the deployment of microscopy systems [Die+19b; Sha+16] with the support of openly available software and customized electronics. The concepts in open microscopy can be divided into two main categories.

The first category originates in microscopy laboratories which aim to produce an alternative to commercially available setups while keeping the imaging quality comparable to their counterparts. A large number of techniques could be reproduced at a considerably lower budget, compared to their commercial counterpart. This includes lower budget SMLM capable microscopes [Als+22] [Aue+18] [Dan+22] [Hol+14] [Kwa+16] [Mar+19], modules for confocal imaging [Hal+22], light sheet systems [Voi+19] [Die+20], FRET (Förster resonance energy transfer) imaging [Amb+20], nano-fluidics [Alm+19] modular platforms [Li+20a], high throughput methods [Li+20a] [Wal+15] amongst many others. The general idea is to facilitate the access to those instruments, materials and techniques. The cost is greatly reduced compared to commercially available systems, however the total cost is still a limiting factor.

The second category represents the output of different investigators which aim to produce cost efficient platforms, instruments and microscopy setups thus providing maximal accessibility even to the general public [Mai+17] [CCP14] [Die+19b] [Die+20] [Sha+16] [Her+16]. The low budget manufacturing as well as the frequent lack of components to induce and detect fluorescence do not allow these instruments to be applications for quantitative scientific imaging. The resolution of these instruments however is sufficient to allow to actively use them in diagnosis e.g. by detecting malaria parasites in remote regions of developing countries. Diagnosis can even be implemented in a high throughput manner as demonstrated by the SQUID platform [Li+20a].

Motivation and thesis aim

2.1 Motivation

Nowadays, cellular and molecular mechanisms are still not completely understood. This creates the demand to drive the microscopy field towards higher spatial and temporal resolutions to tackle these challenges. This has been the focus of a part of researcher working in microscopy development, notably with methods such as Minflux [Bal+17; Sch+21] or correlative cryoEM and SMLM [Tui+19], which are the current state of the art in terms of associating spatial resolution to a fluorescence based signal. Pushing towards this frontier to meet the requirements of innovative scientific research in life science is also done with focus on other features, for example to develop applications for volumetric imaging (following the saying: "tissue is the issue") or for high temporal resolutions. Techniques such as the lattice light sheet [Che+14] are the state of the art to image large cell volumes with high spatial and high temporal resolution. Further development is put into automating microscopy and improving the existing high throughput capabilities of microscopes [PE06]. The variety of possible assays show in the plethora of experiment-specific designs e.g. the monitoring of neural dynamics in freely behaving animals with single cell resolution [Guo+23]. These techniques combine design, physical principles or chemical dye technologies to push microscopy limitations one step further. The high budgetary means necessary to access this type of instrumentation are however limiting the number of users having access to innovative scientific research to a subset of scientists. One can argue that breaching other frontiers than spatial, temporal and volumetric resolutions also constitute a very worthwhile endeavour. The rise of open-source microscopy was motivated by the idea to provide affordable microscopes combined with an open approach facilitating to share methods and data. While low budget microscopes have been developed to provide imaging solutions with high accessibility, the images they produced often lack in quality to enable quantitative data analysis. Other approaches focus on open custom solutions for microscopy techniques, not focusing on the instrument's budget. The resulting data quality is similar to the one produced with commercial systems. However, an open question remains: Is it possible to produce high quality data with a low-budget microscope, and what parts of the microscope cannot be replaced without compromising on image quality?

As a specific application of photonics and cell biology, the aim of this project is to build a microscope based on a low budget framework supplemented by affordable parts and 3D printing, to produce high quality images in common life science imaging assays. Omitted the objective, all the components are low budget to maximize accessibility. Lower price

alternatives for the objective lens are also tested. The work would provide a proof of concept that high quality data can be generated on a microscope based on 3D printed components, with substantial cost reduction. The availability of all the materials to reproduce the instrument and the option for every user to adapt their setup to their needs abide the guidelines of open-source development. Ideally, this concept aims to facilitate the access to scientific research through development of affordable open-source hardware and software.

Thesis structure

In this thesis, a microscope based on an open source concept is built. The microscopy concepts used are described in the introduction. The detailed layout of the setup as well as the methods used to 3D print the components are summarized in chapter 3. The sensitivity and stability of the microscope are first characterized to determine which imaging assays are possible. Then different imaging methods are performed with the microscope, ranging from lower magnification imaging of cell nuclei to super-resolution applications. A final experiment will assess the quality of low-budget objectives. The results will be discussed for each experiment. Finally, the chapter will be closed with possible improvements on the setup. In chapter 4, the analysis methods used to process microscopy data are presented. Experiments on cell segmentation and clustering of SMLM data-sets are presented and discussed. All materials, techniques, software and settings used for the results presented in chapter 3 and 4 are collected within the material and methods part (chapter 5).

Open source microscopy: results and discussion

3.1 Open-source UC2 based setup

In order to combine a high-quality objective with common optics within an open-source based setup, various options are available. Producing relevant scientific output through quantitative studies from high-quality images of biological structures requires mechanical stability, reliable illumination and detector sensitivity amongst others. In order to fulfill these requirements and enable experiment specific setup changes, an adaptable system is necessary. In this project, the low-budget framework provided by the UC2-toolbox [Die+19a; Die+20] was chosen to structure the microscope. The cube-based framework was combined to high-quality optics i.e. an objective lens, which is the core of any microscope and paramount for high resolution imaging. Using a high quality objective facilitates high resolution imaging and reduces the number of possible error sources during the imaging process. In section 3.6, insights into the possible use of lower budget optics are given. Furthermore, platforms such as GitHub are a perfect starting point to share information, computer codes and data. The open source concept aims to freely share information while promoting a spirit of community where users are also developers, thus actively take part in the evolution process. The UC2 GitHub repository [Ope] is used in this project for exactly these purposes.

3.1.1 Open-UC2 framework and 3D printing

Building an optical setup or handling optics requires platform that maximizes mechanical stability. The most direct method is to mount different optics directly upon an optical table, using the appropriate mounts. This however bears the challenge that every optical element needs to be adjusted to the optical axis in its height and different degrees of freedom, such as the angle of the optics. A cage or rail system would each make alignment of optics significantly simpler by decreasing the degrees of freedom a part has in relation to the optical axis. Using these systems also has the positive side effect that the mounting process is quicker and easier thus encouraging different users to bring their changes to the system. Building optical setups with a much lower budget necessarily makes it more difficult to have a similar level of stability and precision. However, the general design should also have a way to reduce the degrees of freedom of the parts.

The basic building block of the the UC2-toolbox is the cube (first presented in [Die+19a]). The cubes used in this project are the new mold injected version of the cubes, making

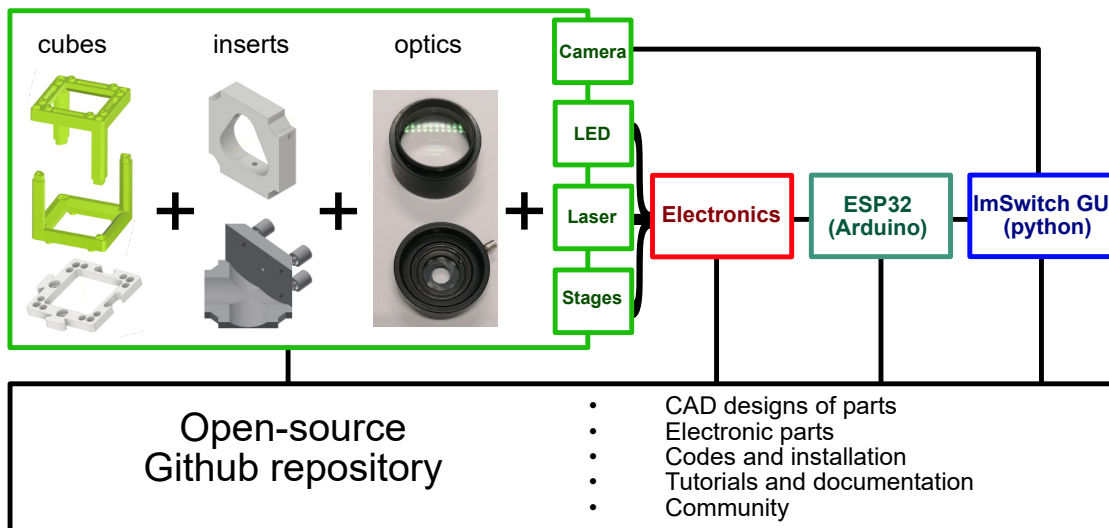


Fig. 3.1.: From single cubes to a complete setup, the open-source concept of UC2. Fundamental building blocks are the cubes which are connected via puzzle pieces. 3D-printed mounts and optics are complemented with electronically controlled devices. Steering is provided by a combination of the ESP32 and a python based GUI. All materials and methods to the setup building are openly available on the GitHub repository.

their manufacturing significantly more reliable in terms of quality, mechanical and thermal stability, thus improving the setup as well as the images it will generate. In figure 5.5, the qualitative difference between a 3D printed part and a mold injected part is displayed with simple microscopy of the pieces surface. This is especially noticeable when looking at the gap size between two parts and the associated effects of the degree on freedom of the cube. The high precision of the mold injected parts make the whole building procedure more reproducible by giving the actual 3D printed parts less movement tolerance. This mechanical stability matches the one provided by the rail or cage system. The estimated increase in precision compared to printed cubes is a factor of $4 \times$ [Wan+22], but depending on the needs of a given experiment, the self printed one might already be sufficient. With the cubes and the available 3D parts, different setups can be built using optical elements from different manufacturers, which initially have not been made to be compatible with one another. This feature allows users to adapt optics they have at hand for their setup. For automation and microscope steering, the cubes, mounts and optics are supported by electronics and a corresponding graphical user interface (GUI) to increase user-friendliness. These two parts are described in subsection 3.1.2. A representation of the complete framework, including the open-source platform is displayed in figure 3.1.

The open-source guidelines are indispensable in order to create an open standard for cost efficient microscopy, one of the main goals being to maximize the accessibility. On the general GitHub repository [Ope] CAD designs of the cube as well as all other parts in use can be found and be downloaded for direct 3D printing. All relevant repositories for any setup building, from CAD files, through electronics to software and tutorials, are listed in 5.6. Such a platform also bears the advantage of having a community of users,

which can share information, collaborate and benefit from already completed work. This idea of sharing a platform and spreading knowledge allows to involve users of different backgrounds in scientific methods and contribute to science communication as well as inspire younger generations.

3.1.2 Electronics and Software

The electronics are essential for the setup automation. The current accessibility of low-budget electronics is a driving factor facilitating the development of open-hardware and low-budget automation solution e.g. for light microscopes [Wen23]. The AlviuM 1800 U-158m CMOS camera was chosen for its monochromatic chip, the comparatively low price, the comparatively high quantum efficiency and for the simple connection via USB 3.0.

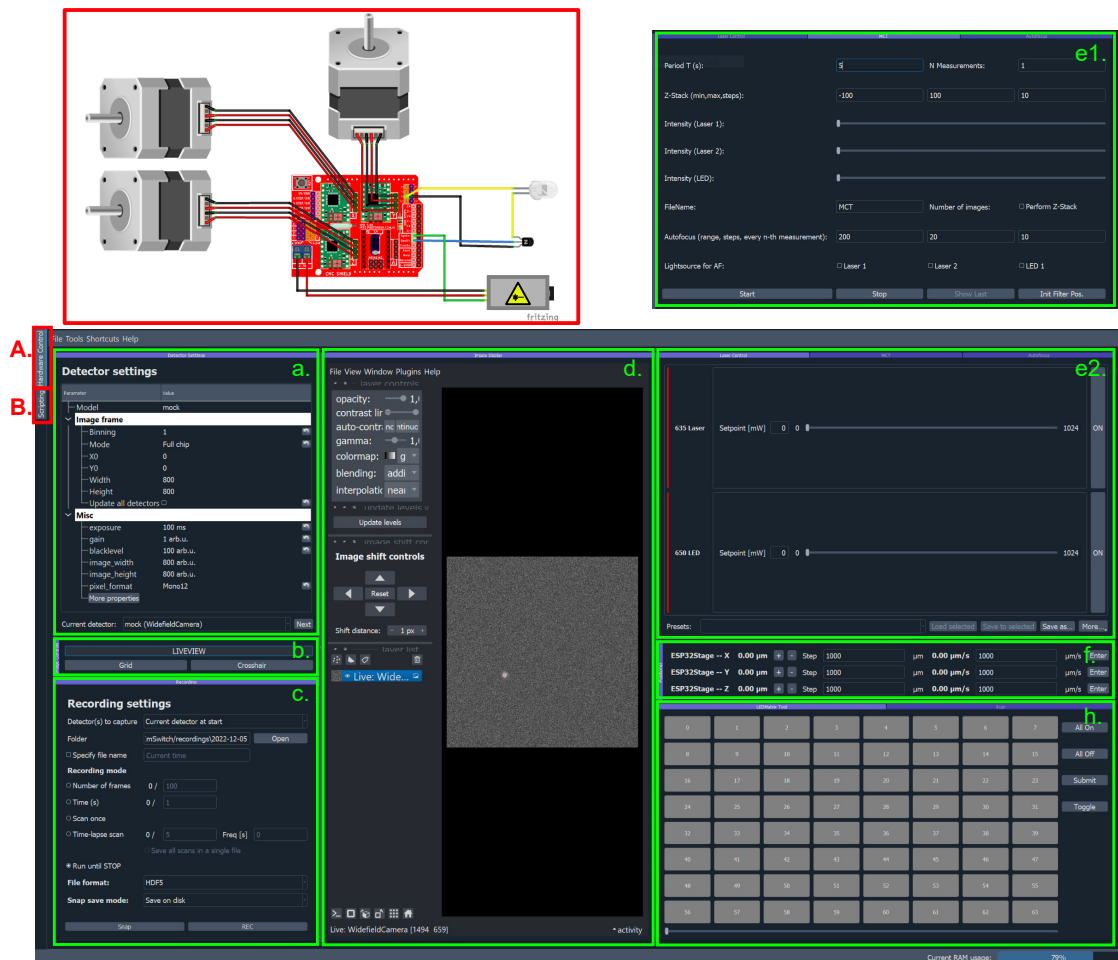


Fig. 3.2.: Electronics and adapted ImSwitch GUI. [Mor+21] **Top left:** electronic circuit for stage, LED and laser control (made with Fritzing software). **A.** Hardware control window. **B.** ImScript scripting window. **a.** Detector settings window. **b.** Live-view activation of the camera. **c.** Recording settings. **d.** Live image and displaying options. **e1.** and **e2.** Different widgets for laser control and MCT sequential acquisition of time-lapses and stacks. **f.** XYZ-stage control. **h.** Optional control panel for an array of LEDs.

By establishing a connection between the hardware and the software, the stages can be motorized to steer and automate the microscope. In terms of open-source hardware control different options are available. Earlier versions e.g. used the framework provided by the Open-Flexure microscopy platform [Sha+16]. The current version operates using the Python based ImSwitch open-source platform for microscopy control [Mor+21], providing an user-friendly graphical user interface (GUI) and a customizable as well as adaptable framework. My collaboration partner, Dr. Benedict Diederich developed "UC2-ESP32", a novel firmware integrated into the ImSwitch structure. By making use of an unified REST API-like interface, the control of different electronic components (motors, LEDs, lasers etc...) can simply be established via USB or WiFi.

To facilitate the installation and the distribution of the tools, Dr. Benedict Diederich also developed an online-based flash tool which updates the newest firmware onto the Wemos ESP32 D1 R32. By complementing the ESP32 with a CNC-shield, a fully functional electronic control unit is established. In the chapter 5 table 5.6, a link to the repository with the documentation to the online flashing tool is provided.

Finally, the "UC2-REST" Python library adapts and integrates the USB serial into ImSwitch. This allows to directly get full access to the controls of motor, laser and LED functionalities through the GUI, which additionally controls the Alvium 1800 U-158m CMOS camera (Allied Vision) through adapted drivers. Consequently, the whole image acquisition process and full control over the different electronics is feasible using the GUI. A supplementary SMLM raw-data analysis module based on the MicroEye framework [Als+22] was also implemented into the latest version of ImSwitch, to provide a full SMLM analysis pipeline, from raw-data acquisition to super-resolved image reconstruction.

3.1.3 Wide-field microscopy setup hardware

As introduced in figure 3.1, the setup is based on UC2 cubes, complemented with 3D-printed mounts, low budget optics and affordable electronics with custom made automation. I here present a wide-field microscope with different optical paths distributed within three layers. The vertical dimension of the Z-stage including the objective influenced the layout of the setup to be more cubic with three stacked layers of cubes. This compact build is not only advantageous for stability as cubes are connected to many other cubes, but also shaping the microscope into a shape that would fit in most incubators. A stable connection between cubes is established by the puzzle pieces. Doubling the connection by using puzzle pieces on the top and on the bottom of a cube is an empirically successful method to maximize the structure's stability. A detailed list of the used parts and their prices is listed in subsection 5.4.4 in table 5.7, with the corresponding CAD designs and assembly files in the setup specific repository 5.6.

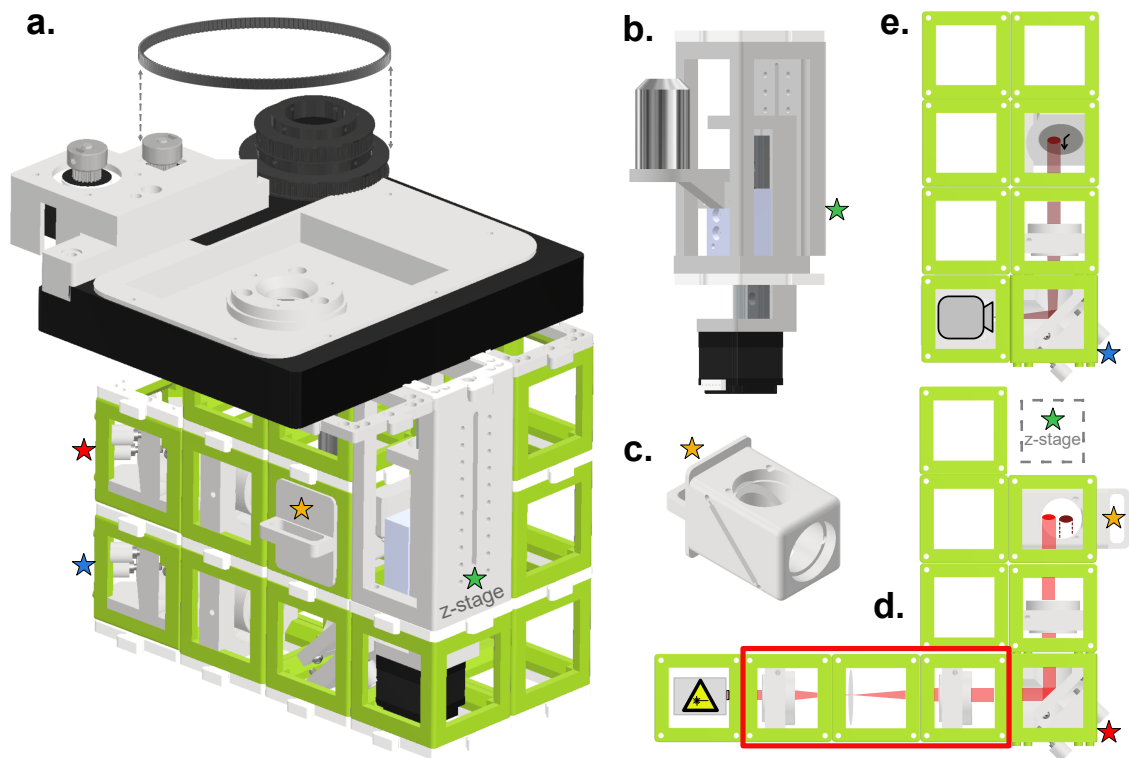


Fig. 3.3.: CAD design of the UC2 based wide-field microscope. **a.** The complete setup is based on the UC2 cubes (green) which are connected via puzzle pieces (white) and divided into three main layers. Top layer is the XY-stage; motor rotation is translated into linear motion via timing belts (as shown on top for one axis). The different coloured stars are visualisation aids to recognize the same parts with different spatial representation. **b.** The Z-stage of the setup (marked with a green star) including objective. **c.** Filter cube (marked with yellow star). Corresponding filter characteristics are shown in figure 5.10. **d.** Excitation pathway layer (marked with a red star). Laser emissions (light-red light path) is bundled by a lens and deflected towards the objective by the filter cube. Telescope and diffuser (red rectangle) are optional optics to broaden and homogenize the laser. **e.** Detection layer (marked with blue star). Fluorescence emissions (dark-red light path) are focused on the detector (Alvium 1800 U-158m CMOS camera from Allied Vision).

The top layer of cubes is supporting the XY-stage and does only contain the objective as optical elements. The one displayed in figure 3.3 is a low-budget commercially purchased objective. Its weight, stability and precision are a good trade-off for most fluorescence imaging assays. To motorize the stage, the rotor torque is transposed onto the manual translation knobs through timing belts and gears (figure 3.3 a). This enables to generate linear motion of the stage along two axes.

The middle layer constitutes the excitation pathway. The laser is focused onto the BFP of the objective with a $f = 100$ mm lens. Depending on the used laser, the beam can be magnified and homogenized to obtain an even illumination of the whole FOV. A block composed of three cubes (or four, depending on the magnification) can be placed between the laser and the before mentioned lens. A telescopic build enlarges the laser shape while a diffuser homogenises the beam. A more detailed description on the illumination can

be found under section 5.3.4. The position of the laser spot can be adjusted along the horizontal and vertical axis with mirror mounts that can be tilted along two axes. The reflective surface of mirrors need to have direct contact to air as an additional glass layer can induce multiple reflections and create interference patterns. An aperture was used to determine the optical axis and center the remaining components accordingly. The excitation layer additionally comprises the filter cube, which is a 3D printed mount for the dichroic mirror as well as excitation and emission filters. The specifics about the used filters and their spectra are visualized in figure 5.10.

The bottom layer arbors the microscopes detection path. The fluorescence emission originating from the sample is gathered by the objective, transmitted through the dichroic and the emission filter, then focused by a $f = 100$ mm lens onto the camera. A mirror in the detection path facilitates positioning of the camera and the optical path. It is precise, heavy and stable while being competitive in terms of price and user friendliness. Holder can be printed according to the sample: figure with different sample and holder designs.

3.1.4 Stages

Commercial microscopes and their self built counterparts use piezo-actuators to reliably convert an voltage into a precise physical displacement (several nanometers). The movement of e.g. a stage or an objective are very precise and reaches the nanometer range in a reproducible way. Piezo-electric based stage actuators as well as high end stepper motors always come with a considerable price and their implementation within a low-budget stage comes along with considerable challenges. Nevertheless, moving the sample in relation to the objective, both along the lateral and vertical axes, is indispensable to conduct experiments on real biological samples. In the here presented setup, two commercially acquired stage options are presented for the XY and Z stages. While the Z-stage already has an in-built motor, the XY-stage is motorized by nematic motors connected to the manual knobs of the stage via timing-belts and gears. The size of the used gears influence the step-size of the stage. Here, a step-size of several μm is sufficient.

The GitHub repository to the general UC2 building parts (table 5.6) provides two options to build a custom XY or a Z stage, based on 3D printed parts. The XY-stages uses translational micrometer strews, which are motorized the same way as the commercial stages. The Z-stage consists of a long screw with a very fine threading, to which the objective holder is attached. A bolt holds the screw at the right position, while the motor allows to adjust axial position through rotation of the screw. Both these options are not as stable as the commercial options, which provide much more mechanical stability through the metal casing. Additionally, the stage is less prone to temperature effects from the electronics heating up e.g. under incubator conditions. Finally, the price of the used commercial stages is so competitive, that the use of self built stages gives no substantial advantage.

The XY-stage shows reliable lateral movement, allowing to place a cell precisely in the center of the FOV. Features such as scanning the sample in X and Y are possible. More details about the method and the reliability of the stage are provided in subsection 3.2.3. The Z-stage also works reliably, but focusing on the samples is challenging, as the 3D printed objective holder does not guarantee a completely horizontal position. Additional friction between sample and objective through the oil makes focusing more challenging with high magnification objectives. The quality of the stage as well as an estimation of the step-size of the low-budget stage is conducted using fluorescent beads in subsection 3.2.1.

3.1.5 Imaging modalities

A wide range of imaging techniques can be covered with the UC2 based microscope. Wide-field fluorescence imaging could be done for dyes with emissions in the far-red spectrum. Additionally, structural information could be gained from bright-field images (materials and methods figure 5.6). The choice of using a CMOS camera with a high sampling rate allowed to use the microscope for applications requiring high temporal resolution. The USB 3.0 connection to the computer is not the fastest possible, but was a good compromise as the connectivity to a maximum of computers is provided.

The illumination can be simply changed by adding or removing the magnifying and diffusing module. Alternatives such as the fiber laser can be used for simplicity. A fiber laser option was also characterized and used on the setup (Appendix subsection A.1.1), by adapting a fiber holder into a cube and collimating the light with a lens. The use of a TIRF-capable objective motivated the implementation of TIRF illumination, effectively increasing the SNR. First attempts have proven problematic as the excitation and emission paths are not aligned to the optical axis anymore. Motorizing a mirror for shifting the laser-spot from the center to the edge of the objective BFP would be a reliable and automated way to do TIRF microscopy, using the right objective. However, the linear translation of mirrors is a feature that still has to be developed.

On the software side, the ImSwitch-GUI allows to set all relevant imaging parameters, such as the laser or LED power, the stage position and the camera acquisition settings. The MCT widget enables to acquire Z-stacks, time-lapses and multi-channel imaging, with possible combinations of these acquisition modalities. The advantage is the fast laser triggering, especially if factors such as the photo-damage received by the sample need to be minimized. Further parameters such as the format of the acquired data can be set in ImSwitch e.g. *.tiff* format for simple snapshots and *.hdf5* for fast image acquisition and saving. The ImScript module additionally allows the user to write customize illumination, stage motion and illumination paradigms according to the studied sample. A few examples are displayed in the appendix in the section A.3. With simple commands, the laser can be turned ON/OFF, all three stages can be moved, an image can be acquired and a waiting

time until repetition of the procedure can be set set. The whole scripting is Python-based, a widespread and comparatively simple programming language.

The combination of the appropriate illumination, the according optics (filters, objective, tube lens), the camera integration time and possible stage or camera features during the planned imaging experiment open up a variety of different imaging modalities which enable the user to adapt the UC2 device to their specific experiment.

3.2 Wide-field image quality

After setting up the illumination and getting the electronics as well as the software to work, all the necessary components were ready to perform microscopy experiments on the setup. With the red laser and the appropriate filter set, different samples stained with dyes emitting fluorescence in the far red spectrum, such as AF647, could be imaged. Laser intensities were kept at around $50\text{-}100\text{ W/cm}^2$, with exposure times ranging from 50 to 100 ms.

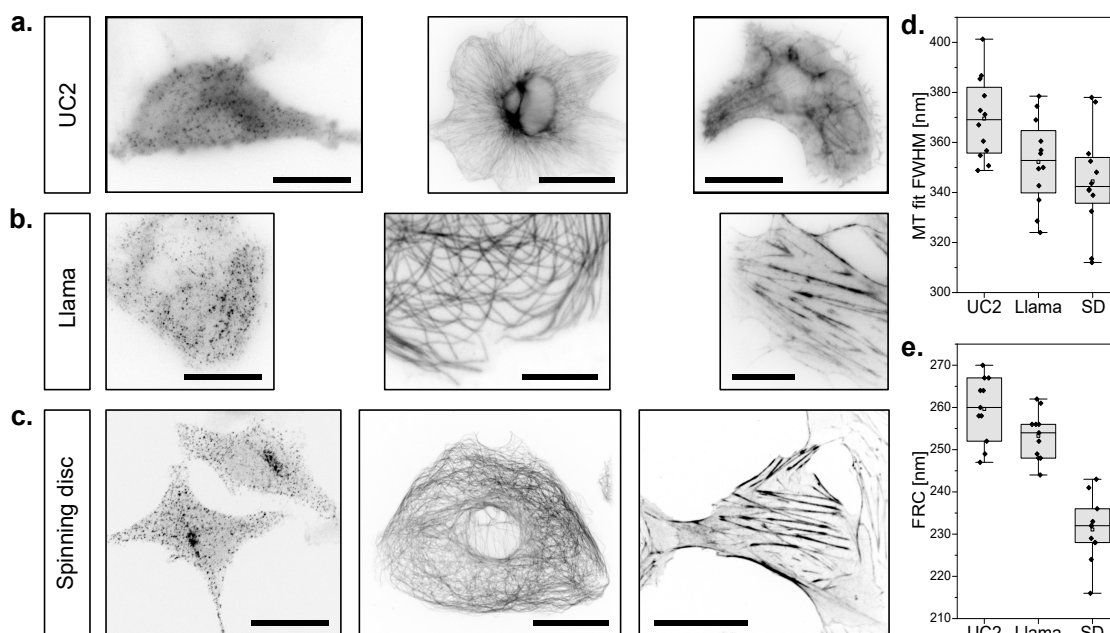


Fig. 3.4.: Comparison of different samples imaged with the UC2, the Llama and the confocal setup (SD = Spinning Disc). HeLa CLC-GFP cells fixed and stained with AF647 conjugated nanobodies, immuno-stained CV-1 cell against microtubules (also AF647) and CV-1 cells incubated with SiR-actin are imaged using the UC2 setup (a), the Llama setup (b) and the confocal spinning disc (c). The scale bars represent $25\ \mu\text{m}$. (a) d. FWHM of the same microtubules sample measured in the three setups (a to c). e. FRC of different samples measured for the three setups. Regions outside the cells were ignored. Methodology is summarized in the material and methods part figure 5.12.

In order to verify the quality of the acquired data, images obtained from the same sample were compared to images acquired on a commercial microscope and the Llama microscope (a home-built high quality wide-field TIRF capable setup[Alb+16a], described

in section 5.1.2). Biological features in the sample as well as the attainable resolution (measured with FRC method) were extrapolated. The UC2 setup allows to qualitatively discern all relevant features in the samples. When quantifying these features, the images with the highest resolution and also the thinner extrapolated microtubule diameter are generated by the confocal setup. The reduced background signal makes the image clearer in general, enabling to make the most reliable claims based on imaging only, from the three setups shown in figure 3.4. As expected, the wide-field images lack behind in resolution. The difference however between both wide-field setups is modest. This suggests that the objective is the key element of the imaging process, as other elements can be replaced with price friendlier alternatives with low loss in quality. The imaging in wide-field can be performed with different objectives. The retaining of image quality respective to objectives with different magnifications an NA can be observed qualitatively. The appendix figure A.3 shows immuno-stained microtubules at different magnifications ($20\times$, $40\times$ and $60\times$ magnification). The imaging quality can be reproduced at different magnification steps.

To make the FRC measurement reproducible, the cell images have been segmented in ImageJ, only considering the region inside of cells for the analysis. Through a mask, the cells are separated from the background. The mask can be generated through thresholding in ImageJ, or through machine learning solutions e.g. the ones presented in chapter 4. The average of the FRC block inside the mask is then used as resolution value. A more detailed overview of the used methodology is provided in figure 5.12.

3.2.1 Single molecule imaging and focusing

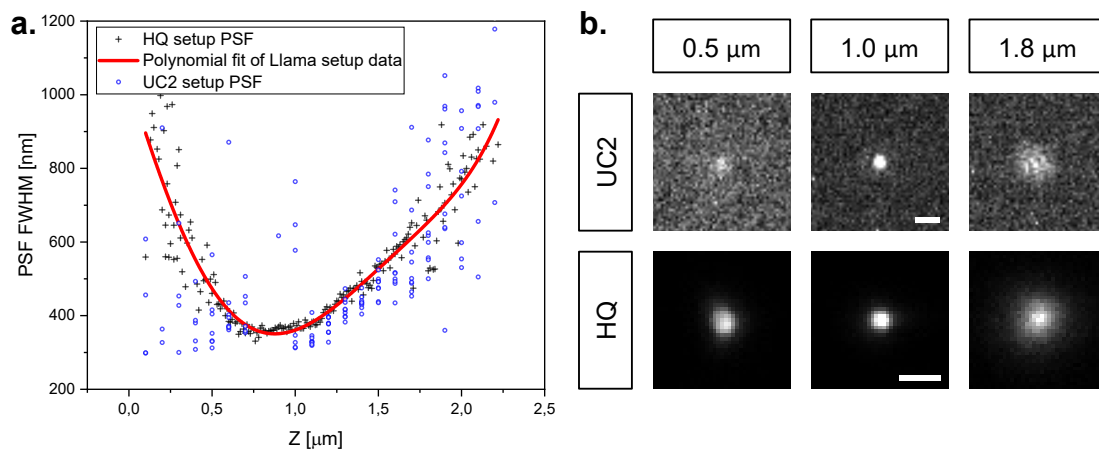


Fig. 3.5.: Z-stack of single molecules and stage calibration **a.** Z-position dependant PSF-FWHM of TS beads for Llama and UC2 setup. Step-size for Llama setup was 10 nm and estimated at 125-150 nm for the UC2-stage. Several beads in the same frame have been overlaid for the UC2-data. B-spline fit was done on the Llama data. **b.** Examples of PSFs at different focal positions. The scale bars displayed for the 1.0 μm position represent 1 μm respectively.

When imaging a single fluorescent emitter, the blurred spot observed on the camera is a convolution of the actual object with the PSF (subsection 1.6.1), and is specific to the setup.

Acquiring images of Tetra Speck (TS) beads result in higher detection intensities but will still show the same diffraction pattern as a single molecule, as long as the bead is smaller than the diffraction limit. The beads are thus a suitable model system to examine the single molecule sensitivity of our setup and quantify stage drift during a measurement with sub-pixel accuracy. Under this assumption, the TS beads can be used as a model imaging system to characterize the PSF of single molecules, and to measure the drift to quantify the stability of the setup. Also, the possibility to discern single beads is a promising step towards using the microscope for single molecule applications. The used TS beads for the stability experiment as well as the sample preparation are described in the section 5.7.4.

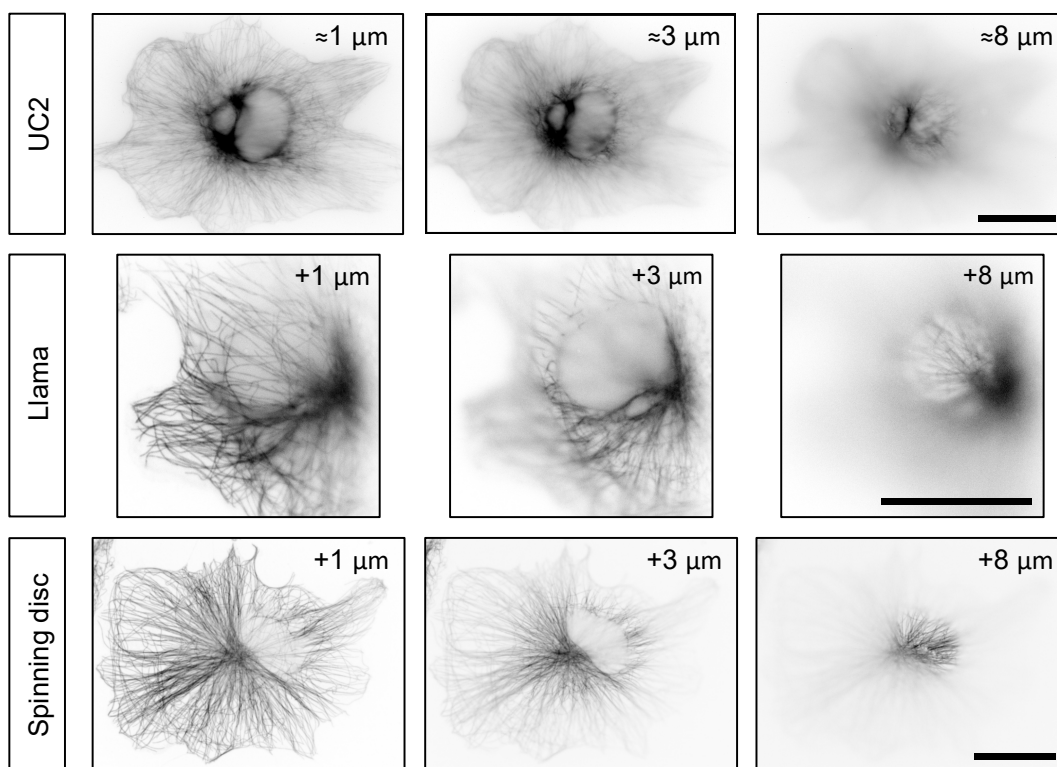


Fig. 3.6.: Z-stack of MT-stained cells **c**. CV-1 cells immuno-stained against microtubules with AF647 at different axial stage positions. UC2 Z-position is estimated. Z-position in Llama and spinning disc microscopes measured according to the piezo position readout. Scale bar represents 30 μm .

In the experiment displayed in figure 3.5, the single TS beads are imaged at different focal planes to calibrate the positioning of the Z-stage. In **a**, using the same objective, TS beads were imaged on the Llama setup and the UC2 setup. On the Llama setup, the accurate piezo-actuator allows to fit the PSF-FWHM Z-stack with a B-spline. The data acquired with the UC2 setup at the smallest adjustable step-size was overlaid on the same graph. The step-sizes are not as regular as on a piezo-driven stage, and the fluctuations are much stronger due to the reduced detector quality (will be further discussed in subsection 3.5.1). The overlaying of both data-sets allow to estimate the step-sizes on the motor with higher precision than the mechanical data provided with the stage (minimal step-size =

axis thread size divided by the number of steps per thread of the axis). In **b**, this principle is shown on raw-data of TS-beads.

In figure 3.6, the focusing ability is tested on CV-1 cells immuno-stained against microtubules with AF647. Different focal planes can clearly be recognized. The axial position was estimated with the UC2-setup. However, purely from a visual perspective, the set Z-position seems to match the calibrated position set with the Llama and spinning disc microscopes, which both have high axial precision due to the reliability of a piezo-actuator component positioning.

3.2.2 Drift characterization and stability

In subsection 3.2.1, it is established that single beads can be detected and the camera has enough sensitivity to allow fitting of the PSFs. To image over prolonged periods of time, mechanical stability of the setup is paramount. The cubes used in this project are already the upgraded mold injected version (mentioned in [Wan+22]). The smooth surfaces and manufacturing precision of the mold injected pieces (figure 5.5) greatly improves the setups stability compared to 3D printed versions of the cube. The general geometry and layout of a setup can influence its stability. The chosen compact build of the UC2 based setup is imposed by the Z-stage (requiring three vertical cube layers) and is advantageous for measurements inside the incubator. Furthermore, a compact build has increased stability as the cubes are connected to more neighbours, thus limiting the degree of possible movement. Attaching cubes with two rows of interconnecting puzzles parts, the first one below and the second one above the cubes, has proven to make a considerable improvement in stability. Further movement restrictions can be implemented by taping or gluing certain components. The relatively heavy XY-stage is also adding stability to the setup. The environment surrounding the setup can also be chosen or adapted to minimize drift of the setup. Airflow at the vicinity of the microscope should be minimized. Vibrations of the diffuser or of instruments on the same table need to be removed or damped. The different improvements made on the setup made it possible to stably image single fluorescent beads over a prolonged time period, thus opening up opportunities to perform experiments with single molecule sensitivity.

Removing drift completely from a microscope seems to be an impossible challenge. Fortunately, drift can be post corrected to a certain extent. In figure 3.7, the drift is characterized for the setup on an optical table and on a laboratory bench. In both cases, the microscope was placed upon a layer of foam material. The centroid of fluorescent beads were then measured once per minute to monitor the particles displacement with sub-pixel accuracy.

The measured drift in figure 3.7 **a** and **b** was reproducible and was consistently lower than $2\ \mu\text{m}$ over a duration of two hours, both on an optical table and on a laboratory bench. The measurements on the laboratory bench showed bigger jumps in the particle's

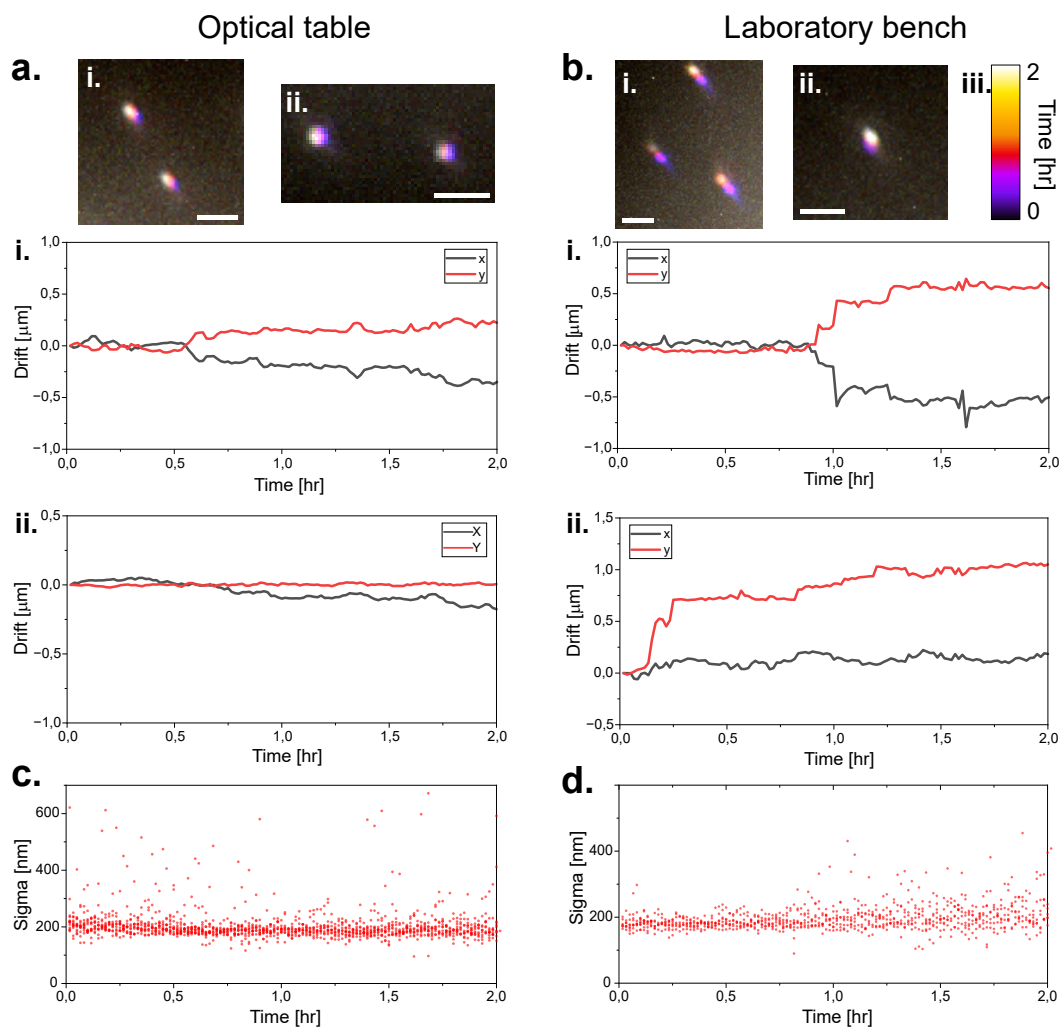


Fig. 3.7.: Drift characterization on the UC2 setup **a.** Drift of TS beads sample on a cover glass over two hours on a vibration damped optical table. Temporal colour coded bead position in **i.** and **ii.** are quantified in the corresponding graphs below. Colour code is displayed in **b.iii.** **b.** Drift of TS beads sample on a cover-glass over two hours on a regular table. Temporal colour coded bead position in **i.** and **ii.** are quantified in the corresponding graphs below. Colour code is displayed in **iii.**. Scale bars represent $2\ \mu\text{m}$. **c.** Time dependent sigma of the PSFs of several localized beads of the sample displayed in **a.i** over a period of two hours. **d.** Time dependent sigma of the PSFs of several localized beads of the sample displayed in **b.i** over a period of two hours. Bead positions in x and y as well as sigma were determined with ThunderSTORM [Ove+14].

position, compared to the optical table. These jumps were probably the result of vibrations such as steps or closing doors in the laboratory, which have a clearer impact when not damped. The average sigma of TS beads over time, **c** and **d** are a measure to qualitatively describe the changes in focus of the beads. The measurement indicated that the variation of the axial position over time was not important and will likely not impact wide-field imaging assays.

The acquisition of single particle tracking data typically takes minutes, the drift should thus not have a noticeable effect on the trajectories of particles that are only observed

for several seconds. The *d*STORM measurements can be achieved in 15-20 minutes. In that time frame, drift of several hundred nanometers is in a range small enough that it can be corrected using fiducial markers or cross-correlation, ideally both. For live cell measurements of several hours, the drift is low enough that the FOV remains almost unchanged over the experiment. This effect is even less relevant when using an objective with lower magnification. These experiments lead to believe that the low-budget microscope's drift is in a low enough range to enable the application of various relevant imaging assays, even showcasing the possibility (from the stability perspective) to perform single molecule microscopy experiments. The drift, over the duration a SMLM measurement is achieved in, is comparable to the drift present in commercial setups.

3.2.3 Large field of view imaging

The imaging modalities mentioned in subsection 3.1.5 suggest the feasibility of imaging structures which by size exceed the FOV, through sequential positioning of the XY-stage and image acquisition. The XY-stage is a low-budget commercially acquired component. An alternative was used in the first iteration, consisting of micrometer translation mount combined to a 3D printed framework. The translation mounts, even though much preciser in their motion, are more expensive and come with a multitude of engineering challenges, making it the less practicable solution. The CAD designs to build an XY-stage from translational mounts can be found under the UC2 components library (GitHub repository listed in table 5.6).

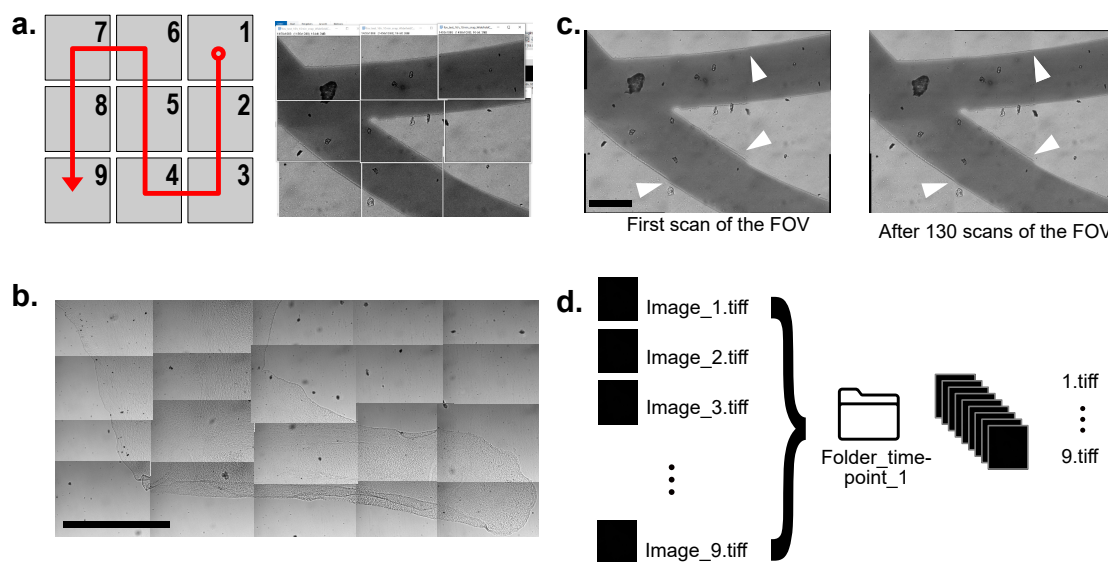


Fig. 3.8.: Large field of view imaging. **a.** Image stitching procedure with ImageJ stitching plugin [PST09](listed in table 5.4). Sample was marker writing on a cover-glass and was imaged with a 20 \times objective. **b.** Manual stitching of a mouse embryo leg (provided by Angelos Rigopoulos). Scale bar represents 400 μm . **c.** The stitching according to **a** can reliably be repeated over 100 \times . White arrows indicate differences in focus. Scale bar represents 250 μm . **d.** Batch processing concept. Images are renamed then divided into folders which can be batch processed with an ImageJ macro.

In order to image larger samples or tissues, the magnification can be reduced, often at the cost of resolution. An alternative is to tile a big sample into smaller field of views then stitch these images together into a complete image. Plugins in ImageJ enable a simple execution of this operation[PST09]. In figure 3.8, the procedure is demonstrated by imaging marker lines on a cover-glass. The direction of the stitching and its matrix size were chosen within the plugin. In **c**, the stitched result is displayed. The white arrows indicate unfitting focal planes at the transition between images. The self-built XY stage is capable of reproducing the same movement with high accuracy over hundred times, while keeping the observed FOV unchanged (with the 20× magnification). This opens up the possibility to substantially increase the observed cell population within a single experiment, thus enhancing the statistical power of studies. The automation of a microscope enables the deployment of big FOV acquisition over longer time periods. The corresponding ImScript code for the sequential acquisition of a 3 × 3 matrix is shown in the appendix listing A.3. Through the automated sorting of the data (figure 3.8 **b**), the batch analysis of a larger FOV can be performed with minimal additional manual analysis.

Another main application of the tiling method are histological studies e.g. the organisation of cells in tissue or structures that are substantially larger than the FOV provided by a setup. In figure 3.8, a mouse embryo leg slice provided by Angelos Rigopoulos (Stricker Lab) is reconstructed. Due to the backlash of the commercial stage, the steps in X and Y are not homogeneous enough to run the tiling through an algorithm.

A persistent problem when imaging single cells is that there is no continuous structure throughout the images, increasing the difficulty to reconstruct the larger FOV properly. This problem is even more accentuated when imaging in the fluorescent channel. A possible solution is to use cover-glasses including a grid-like pattern, where the grid can be used as superstructure, assisting stitching with information acquired in the bright-field channel. The fluorescence images then just use the reconstruction matrix from the bright-field channel.

Future improvements: The commercial stage is not steady enough to guarantee reproducible linear translation. Using different hardware or mechanically correcting the backlash of the stage would help resolve this challenge. The development of an auto-focus would also be necessary to keep all images in the same plane and reduce the reconstruction artefacts. Finally, improvements in the illumination would simplify the procedure, as an uneven illumination hinders the extraction of quantitative information. Having a completely uniform laser or LED illumination across the FOV would be possible approaches.

3.3 Live-cell imaging

Live-cell imaging is a major research tool to provide information about metabolic functions and help develop application-oriented treatments. In the case of microscopy,

different imaging assays allow the real time study of cellular interactions, cell signaling, cell migration and much more [Col14]. In order to showcase the range of applications of the UC2-based instrument i.e. monitor biological processes at different time and resolution scales, I here present live-cell measurements at room temperature with high-resolution over several hours. Then, I showcase the possibility of image acquisition within the incubator over a time-span of several days. The challenges of long-term imaging i.e. the stability issue as well as the photo-bleaching and photo-toxicity induced by fluorescence microscopy will also be discussed, while presenting simple solutions.

3.3.1 Photo-damage and photo-toxicity

The transposition of different microscopy techniques onto live-cell imaging has already been tried. All fluorescence based live-cell imaging necessarily comes with laser induced photo-damage which can physiologically impair the sample or even cause cell death, amongst different other challenges [SHS16]. In the case of live-cell imaging, the absorption of visible light by different molecules within the sample induces photo-damage [Col14], which can lead to false results and conclusions in the conducted experiment. In addition, the introduced fluorophores can be degraded through oxidation in the excited state. This can generate reactive oxygen species (ROS), which can oxidize DNA, proteins and unsaturated fatty acids [Ich+17], resulting in possible mutations or loss of molecule functionality. Additionally, molecules that are naturally present in cells (e.g. flavins and porphyrins [Ich+17]) can also degrade through reaction with oxygen and produce ROSs. The photo-toxicity and the tolerable light dose for model cell systems have been quantified to be around 25-300 J/cm² [Sch+12b], and different methods have been developed to measure and recognize photo-toxicity [Tin+12]. Amongst all the challenges of live-cell imaging [SHS16], different microscopy techniques can be applied to reduce the induced photo-damage and allow longer more reliable imaging. The pitfalls experienced in live-cell experiments are well documented e.g. the cell division in cell culture conditions [KR06] or effects of photo-damage on mitosis [DC03]. The compromise between sample health and temporal or spatial resolution limits the effectiveness of live-cell imaging and still presents different challenges that are currently being tackled. Obviously, specific illumination modes present in techniques such as light sheet microscopy [Ich+17] have proven to be most adapted to live-cell imaging due to the inherent low irradiation dose and thereby limited induced photo-toxicity.

In the microscope built in this project, the applicable imaging techniques are limited to those feasible with wide-field illumination. The obvious first measure is to reduce the sample irradiation to the necessary minimum. Then, when performing e.g. live-cell super-resolution imaging or general wide-field imaging, the chosen wavelength can be adapted to reduce the photo-induced damage. The near ultra violet (UV) light is most toxic for cells whereas near infra-red (IR) is the least toxic [Wäl+15]. By switching to fluorophores with longer wavelengths, the photo-toxicity during a live-cell imaging assay

can be reduced with relatively small loss of resolution, thereby increasing the duration of the experiment substantially. The mode of irradiation is also influences overall sample health. Lower doses of irradiation over a longer period of time induces less photo-damage than the same total dose delivered over a shorter time period [MK13]. This indicates that low toxicity over prolonged time is easier for the sample to survive. Stretching a live-cell experiment to distribute the irradiation dose over time, if possible, would thus be desirable.

3.3.2 Room temperature

The mechanical stability of the microscope allows imaging of cells for several hours with an oil objective and minimal lateral drift of the sample. The here presented live-cell experiment demonstrates, that the axial stability is also high enough to keep cells in focus over several hours without adjusting the objective's position. To showcase the feasibility of high-quality live-cell imaging, I imaged CV-1 cells at room temperature over several hours. In figure 3.9, the actin filaments of the cells were labelled with the live-staining Silicone Rhodamine dye SiR-actin. The information from the fluorescence channel is complemented with a second channel, showing the edges of the cell-membrane and larger organelles through bright-field imaging of the sample. Both signals can be merged to correlate basic spatial information with the specificity of a given fluorescence staining. The illumination of the bright-field images was not even and has been corrected using the methodology described in the material and methods part, subsection 5.3.3.

The measurement in figure 3.9 could be done over a period of five hours without significant drift in XY and Z. The measurement of the drift in subsection 3.2.2 predicted such a stable behaviour and could be reproduced within a living sample at room temperature. The acquisition used a script to sequentially turn on the laser, acquire an image and turn off the laser, then repeat the procedure for the LED. A waiting time of one minute is set, repeating the measurement of both channels once per minute for five hours. The stability showcases the possibility to monitor cellular processes over hours with diffraction limited accuracy and resolutions comparable to commercial setups. If the temporal resolution of one frame per minute is not required, the bleaching of the fluorophores and photo-damage induced to the sample can be significantly reduced. This enables to push against the main limitation of such live-cell assays. In this case the cells have been illuminated for around 5 s every minute for over 3 hours. The imaging method using an ImScript code requires short sleep times between the different commands, thus increasing the illumination duration. The accumulated light energy is around 28 J over the 5 hours, with an approximated laser power of 28-30 mW distributed over the FOV. This value is significant as the actin-filaments are more difficult to discern later during the measurement, even though the bleaching of the sample was kept in an acceptable range. The illumination time of the sample could be optimized and lowered considerably. The acquisition process only takes around 50-100 ms. With appropriate laser triggering, the illumination time can

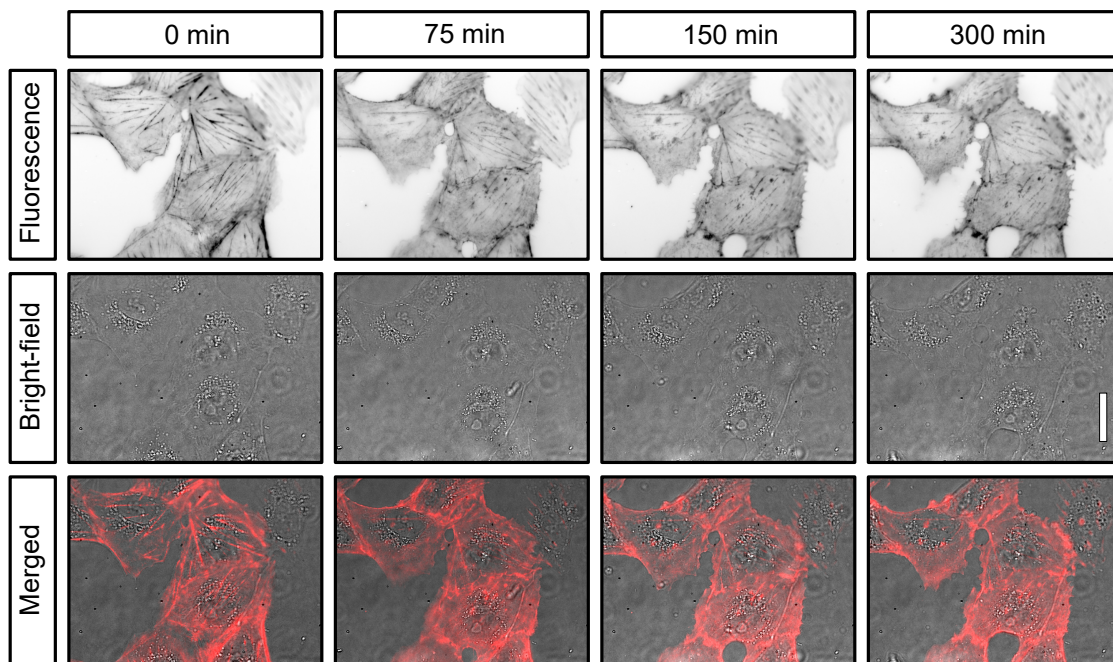


Fig. 3.9.: Live-cell imaging of CV-1 cells over five hours at room temperature. Fluorescence is emitted by SiR dyes staining the actin of the CV-1 cells. Bright-field images have been corrected to remove the illumination gradient of the raw images. Merged images show the SiR-Actin fluorescence (red) over the bright-field image (gray). Scale bar represents 30 μm .

be limited to the duration of the image integration time itself. The MCT option within ImSwitch was then developed and later used for the purpose of reducing laser irradiation of the sample. Another measurement of live HEK cells stained with the SYTO nucleic dye is shown in subsection A.2.1, and displays the effects of too high illumination densities on the sample.

3.3.3 Challenges in live-cell imaging

After undergoing the proposed modifications and leaving the microscope in the incubator for two days before the experiment start, the setup adapted enough to provided sufficient mechanical stability to perform live-cell imaging in two channels for a prolonged period of time. Additionally to the drift, different errors can occur during the measurement, especially because of the duration and climatic conditions. On the technical side, different hardware failures can stop the measurement or induce a loss of communication between the computer and the microscope. These include updates from the computer, non-responsive ESP32 or other ways of losing connection such as a loose cable connection. Additionally to these rare events, external vibrations from opening the incubator, slamming the door while closing it or people walking by the incubator can cause sudden motion of the sample, stage or of other parts within the setup. Voltage peaks can also interrupt the computer connection or move the stage but are practically non-existent in the power grid. Finally, a challenge that is promptly going to be solved is the loss of synchronisation

between illumination and image acquisition, which can result in different illumination intensity thus different contrast in the acquired images over time. This challenge can be alleviated by manually writing an acquisition script (e.g. the script shown in appendix listing A.3). The script turns the LED or the laser on and off through ImScript commands, which are slower than using the MCT. This results in longer illumination times within the sample and consequently inducing more photo-damage. This feature has been visually displayed in materials and methods subsection 5.3.5, where the illumination duration are compared between the ImScript acquisition and the MCT.

On the other side, the sample preparation can also influence the outcome of the experiment. Samples can dry out over time, an effective mean to prevent this is to refill the incubator reservoir before the experiment, use the 8-well (or 4-well) sample chambers with a lid so that CO₂ can still penetrate the chamber but water evaporation from the medium is greatly reduced. Other challenging sample features are the effects of prolonged light illumination on the sample. This represents an important issue, as described in subsection 3.3.1, but can be limited by setting the illumination scheme appropriately.

3.3.4 Incubator Measurements

Moving the microscope into the incubator bears stability challenges induced by the combined action of incubator vibrations, increased temperature and humidity effects on the components. These effects are amplified on the 3D printed parts. First test measurements inside the incubator have shown drift so significant, that the use of the 60× oil immersion objective was excluded. A few micrometers axial drift already made the acquired data unusable with an oil immersion objective. The live-cell experiments were therefore performed using a 20× magnification air objective. However, even the air objective exhibited too much drift to allow for long term imaging. The focus could not be kept because the commonly used PLA material for the 3D printed parts lacks thermal stability [Lay+19], and the effects of the softening plastics were already noticeable at incubator temperatures. Efforts have been made in reducing the strain on the plastic parts e.g. by replacing 41 g metal sample holder with a 2.8 g 8-well cover glasses (from Ibidi). A design for a self printed sample holder is also available, but was not used here. Longer screws were introduced into the 3D printed objective holder, to stabilize the structure, like a skeleton. Finally, the infill of the 3D printed parts has been increased, making the parts more dense thereby enhancing their stability.

Nonetheless, these improvements were insufficient to hold the focus at 37° C over the time-span of several days. A decisive step towards solving this challenge was to replace the printing material for the components most subjected to physical stress inside the incubator. Compared to PLA, the higher printing temperature needed for ABS [Prua; Lay+19] make the printing process more challenging by increasing the risk for errors, but the resulting parts are much better adapted to the incubator conditions [Wen+16]. As far as humidity is concerned, preheating the setup under dry conditions prevents the formation of water

droplets on cold surfaces when introducing the setup into an incubator with saturated humidity, effectively reducing the risk of further image aberrations or electronic damage. Finally, many incubators have a ventilation system to ensure even distribution of heat and CO₂. The microscope should be placed in the incubator in a way to prevent direct airflow from the ventilation. The microscope is furthermore positioned upon a thick plate of foam material, a simple but reliable way to reduce the effects of incubator vibrations. The USB cable of the camera as well as the USB cable of the electronic board are connecting the microscope (within the incubator) to a laptop placed on top of the incubator (see figure 3.10 b). As soon as the sample is positioned on the sample holder, the incubator can be closed as the automation of the microscope allows to do all steering remotely. A user-friendly feature is the possible control of the microscope stages and illumination via a *PlayStation 4* remote joystick. The Bluetooth connection between the microscope and the controller can however be lost for certain types of incubator, depending on their wall thickness and permeability for micro-wave frequencies such as Bluetooth.

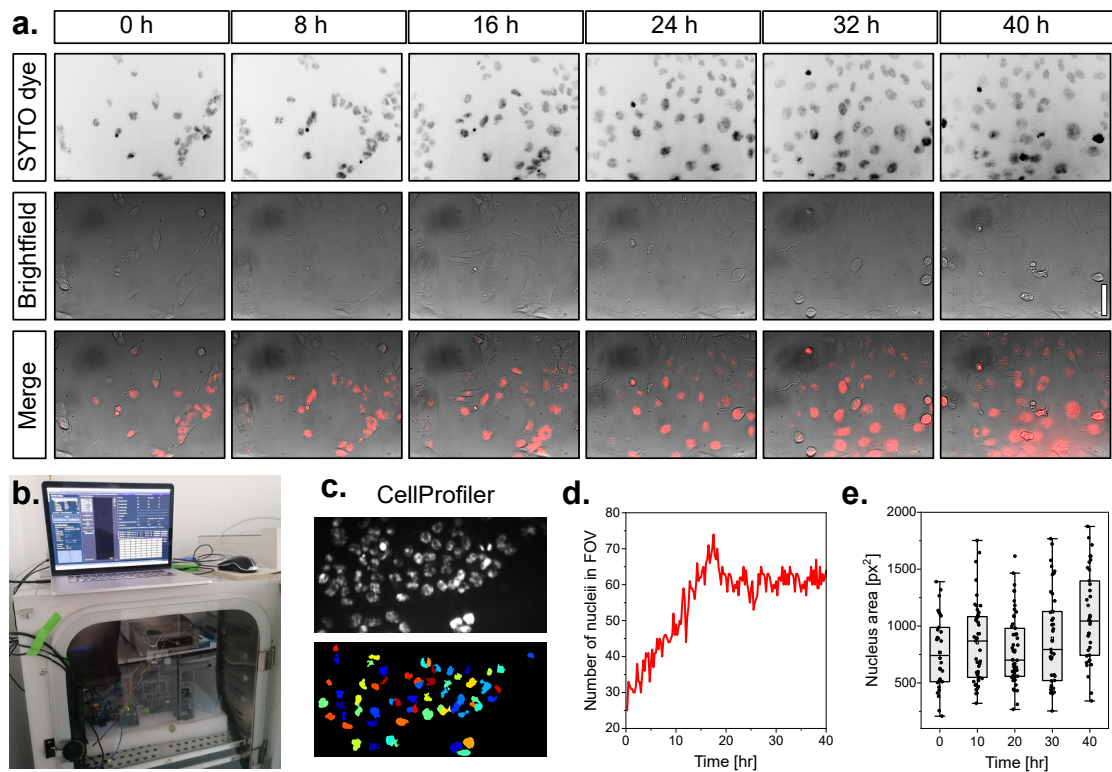


Fig. 3.10.: Live-cell imaging of T98G cells over two days inside the incubator. **a.** Continuous imaging of wild-type T98G cells in both available channels, over a duration of 40 hours under incubator conditions (i.e. 37° C, high humidity, 5% CO₂). Fluorescence channel shows nuclei stained with SYTO far-red nucleic dye. Bright-field images have been Background corrected. Scale bar represents 30 μ m. **b.** Photograph of the experimental setup, including the acquisition computer outside the incubator with cable connection to the setup placed inside the incubator. **c.** CellProfiler for segmentation and quantitative processing of fluorescence data. **Top:** Fluorescence image. **Bottom:** Masks generated by CellProfiler. **d.** Number of cell nuclei counted over time. **e.** Area of the registered nuclei over time. For clarity, only values every 10 hours are shown.

In figure 3.10, T98G cells are imaged over a period of several days. The nuclei are made visible in the fluorescence channel by using the SYTO far-red nucleic dye. The illumination over the two days was not completely stable but still allowed to image the whole sample with time intervals of 15 minutes over two days. Here, the acquisition of stacks every 15 minutes allowed to choose images with optimal focus in the post processing steps. With ten-fold acquisition with 25-30 *mW* laser power and a total of 160 acquisitions, the irradiated energy is within or below the range of 1 J. The low irradiation and the far-red wavelength allowed long term imaging without significant changes in cell morphology. The stopping cell division suggests an accumulation of photo-damage after a period of rather normal growth. The ten-fold illumination for each time point combined with a wide-field based setup seems limit the time window where image acquisition are possible. As mentioned in section 3.3.1, the longer illumination with lower photon dose benefits the sample's health. By doubling the time-steps, or reducing the number of acquisitions per time point, sample health can be maintained for longer time. Furthermore, an auto-focus in the bright-field channel would reduce the illumination dose per time point considerably. The stability of the microscope inside an incubator is still one of the limiting factors, even though the drift can be contained in a range where live-cell imaging assays are possible. Further optimizing of the experimental conditions is needed to improve the live-cell capabilities.

The amount of data produced is cumbersome to analyse manually and was thus assisted by scripting and other computer-based methods to reduce the analysis time. This holds especially true if the here presented live-cell experiment was combined with a high throughput method e.g. the parallel imaging of cells at different locations in the same sample by moving in XY. This opens up new possibilities in using this microscope for screening assays (e.g. on 96-well plates) or to image larger samples.

The use of high-throughput methods can be a decisive advantage in averaging out anomalies from data-sets of samples displaying variable phenotypes such as cells. The possibility to count cells or simply characterising basic features of a sample are simple and repetitive tasks that should be automated with already available solutions including machine learning. The rising use of artificial intelligence will provide more solutions, especially for more complex assays, but for ease of use and for users who desire a lower technical complexity, CellProfiler is a suitable option. CellProfiler [Car+06] is an unsupervised machine learning module which was used for automatic registration and segmentation of cell nuclei. The modules used in the analysis pipeline as well as their functions are listed in the subsection 5.5.2. In figure 3.10 **d** and **e** cell growth was measured by counting the number of detected nuclei within the FOV. Additional features such as the nucleus area can also be extracted automatically. More advanced image processing steps and high data-throughput are available when using an updated more potent version of CellProfiler [McQ+18].

To summarize, the automatic computer assisted analysis of microscopy images is possible and can be applied by everyone, even without any programming experience. The quality of the staining can still be improved as the clumped nuclei are difficult to discern, even by eye. The quality of the generated data is however sufficient to conduct long-term experiment and easily extrapolate sample parameters through machine assisted analysis.

3.3.5 Autofocus

A general challenge in long term imaging is the sample drift. While the lateral motion of the sample can be accounted for in the analysis and is decisively smaller than the FOV, the axial drift defocuses the sample and reduce the image quality considerably. This challenge of axial displacement is present in most microscopes and is, in our case, accentuated by the framework made of plastic, as well as the high temperature and humidity in the incubator. The obvious solution is to change the Z-position of the sample accordingly through time so that all images are acquired with the same focus. The challenging part is to automate and implement a focus feature in the image acquisition pipeline.

An simple solution is to take Z-stacks over time and manually choose the Z-position with the best focus for any given time point. Additionally to the immense work load this represents if done manually in a measurement with hundreds of time points, the prolonged illumination can cause photo-damage and ultimately kill the cells in the sample. This holds especially true for the laser illumination. The stacks with the far-red LED are not damaging the cells that much as the light is not concentrated on a small field of view, and can thus be used as auto-focus channel. In the appendix subsection A.3, an example of contrast measurement developed with my collaborator Dr. Amin Zehtabian is provided. Combined with the batch analysis function in FIJI, these tools can be used to swiftly choose the images with highest contrast (i.e. best focus) within a big data-sets. Additionally, for keeping the focus over time, a widget in ImSwitch allows to choose a channel to conduct an auto-focus operation during long term experiments. The current implementation however is not able to retain the focus as well as the combined use of stack acquisition and FIJI script. This will however be an improvement that will be implemented in a short future.

The use of an LED array can be problematic for bright-field imaging, as multiple light sources induce interference patterns in the sample of interest. The Fourier transform of the images could be used to determine features defining the axial distance to the optimal focus plane. An example of the LED array and the FFT of in-focus and out-of-focus images is given in the Appendix, subsection A.1.2.

3.4 Single molecule applications

The drift characterization using sub-diffraction emitters such as Tetra Speck (TS) beads have confirmed the possibility of detecting and localizing single molecules on a given sample for a prolonged period of time, with limited drift. This leads to think that the setup

can be used for characterization of membrane molecule dynamics with methods such as single particle tracking (SPT), or to substantially increase the resolution of an image through single molecule localization microscopy (SMLM) methods. I here demonstrate the feasibility of these two methods and investigate the limitations of using a low-budget approach for imaging assays.

3.4.1 Single particle tracking

The drift characterization has confirmed the possibility of detecting and localizing single molecules while the sample is kept immobile for a prolonged period of time. One big advantage of CMOS cameras in general is their acquisition speed (section 1.7), compared e.g. to EMCCD devices. I here demonstrate the feasibility of single molecules dynamics characterization by tracking single particles on the membrane of living cells. This provides the possibility of performing live-cell assays with high temporal resolution on the UC2 setup.

Tracking sensitivity in SPT is a trade-off between temporal and spatial resolution, which are both linked to the photon budget of a given fluorophore. The underlying challenge in the case of moving molecules is the short exposure time as well as the motion blur induced by motion during the integration time, which are both reducing the accuracy with which the position of a particle can be determined. In order to localize a molecule with high accuracy and precision, a high number of acquired photons is necessary (equation 1.11). At the same time, short exposure times increase the temporal resolution but reduce the amount of photons available for localization. To maximize both parameters, estimating the movement speed of the studied protein is a reliable way to not temporally over-sample the acquisition. The use of very bright and photo-stable fluorophores also helps to increase the photon budget and enables to determine values like the diffusion coefficient over a longer time-span. In this experiment, quantum dots are used because of their high stability and brightness. The semi-conductor probes have a band-gap corresponding to a fluorescent emission maximum at $\lambda_{max} = 655$ nm, a value compatible with the laser and filter-sets present in the setup. To maximize the emitted fluorescence from the QDs thus increase the SNR, the laser illumination is set at high intensity. The streptavidin labelled quantum dots were attached to the (glycosylphosphatidylinositol) GPI membrane molecule via a GFP-biotin construct. Live cell medium was used after adding the functionalized QDs and removing the residual unbound particles. A more detailed protocol of the experiment can be found under protocol 5.7.11. The schematic of the tracking experiment is shown in figure 3.11 **a**. Exemplary tracks with two magnified tracks are displayed in **b** and **c**.

It is possible to extract quantitative information from the tracks originating from the SPT experiment. The localization of the QDs is precise enough to follow single particles over longer time-lapses. Every single track registered within the raw data by the Mosaic algorithm ([SK05]) from the SPT experiment displayed in figure 3.11 is analyzed, providing various information on every single trajectory, such as the diffusion coefficient, the MSD or

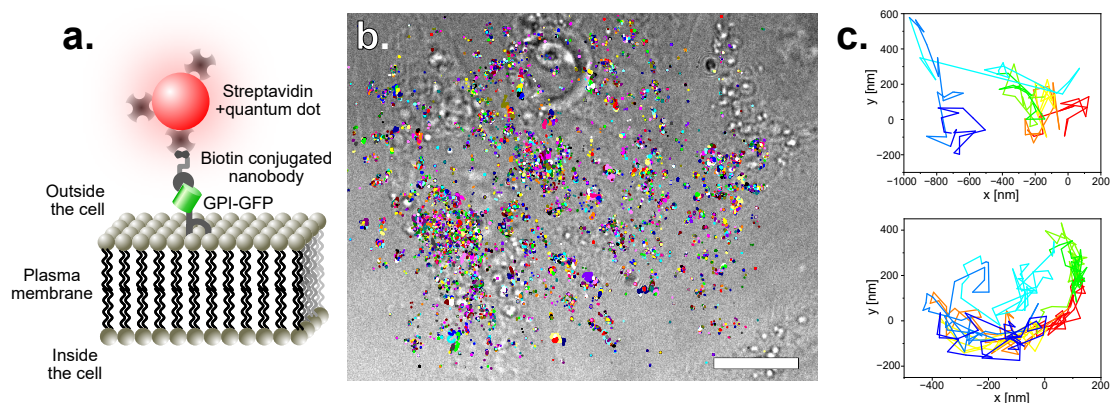


Fig. 3.11.: Single particle tracking of GPI-GFP labelled with quantum dots **a.** Schematic of the SPT experiment. **b.** Wide-field image superimposed with tracks of the corresponding data-set. Scale-bar represents $10\ \mu\text{m}$. **c.** Exemplary tracks of two particles among the ones displayed in **b.** Tracks were generated and analysed using *Mosaic* [SK05].

the MSs. A statistical distribution of the diffusion coefficients as well as the moment scaling spectrum of the tracked population are used to characterize the behaviour of the molecule population. To reduce possible effects of too short tracks, track lengths shorter than 20 time points have been discarded. After performing SPT on 9 cells, around 5'000 tracks longer than 20 time points are registered then analysed to make a statistically relevant representation of the GPI diffusion behaviour.

In figure 3.12, plotting the diffusion coefficient (**a**) and the MSS slope (**b**) clearly show two populations. The first population has a mean diffusion coefficient around $0.001\ \mu\text{m}^2/\text{s}$, which corresponds to an MSS slope of around 0 and represents an immobile population which is possibly trapped or bound unspecifically to a non diffusing component. The diffusion coefficient varies because different molecule position, within the range of the localization precision (eq.1.11), can occur for an immobile molecule due to fluctuations in background, in noise and in the emission of fluorescence photons. The second population has a diffusion coefficient of around $0.1\ \mu\text{m}^2/\text{s}$ and a corresponding MSS slope between 0.25 and 0.5. These values are in accordance with previous studies [Li+20b] for the diffusion of GPI within the plasma membrane.

The shorter the time lag between two measurements of a particle's position, the higher the accuracy of the trajectory mapping. An additional experiment aimed to determine the shortest exposure time that can be used to still get correct quantitative output from the SPT measurement. This would provide insight in the accuracy of the microscope and the maximal temporal resolution it can achieve. The needed temporal resolution is variable, depending on the speed of the single particles. The CMOS camera, despite its speed, is limited to around 60 frames per second. This value was determined by averaging the acquisition time of 1000 frames with exposure times of 5 ms. The time stamp of every acquired image can be read out from the Python interface/prompt (here Anaconda prompt) on which the ImSwitch-based GUI is started on. One limiting factor for the acquisition

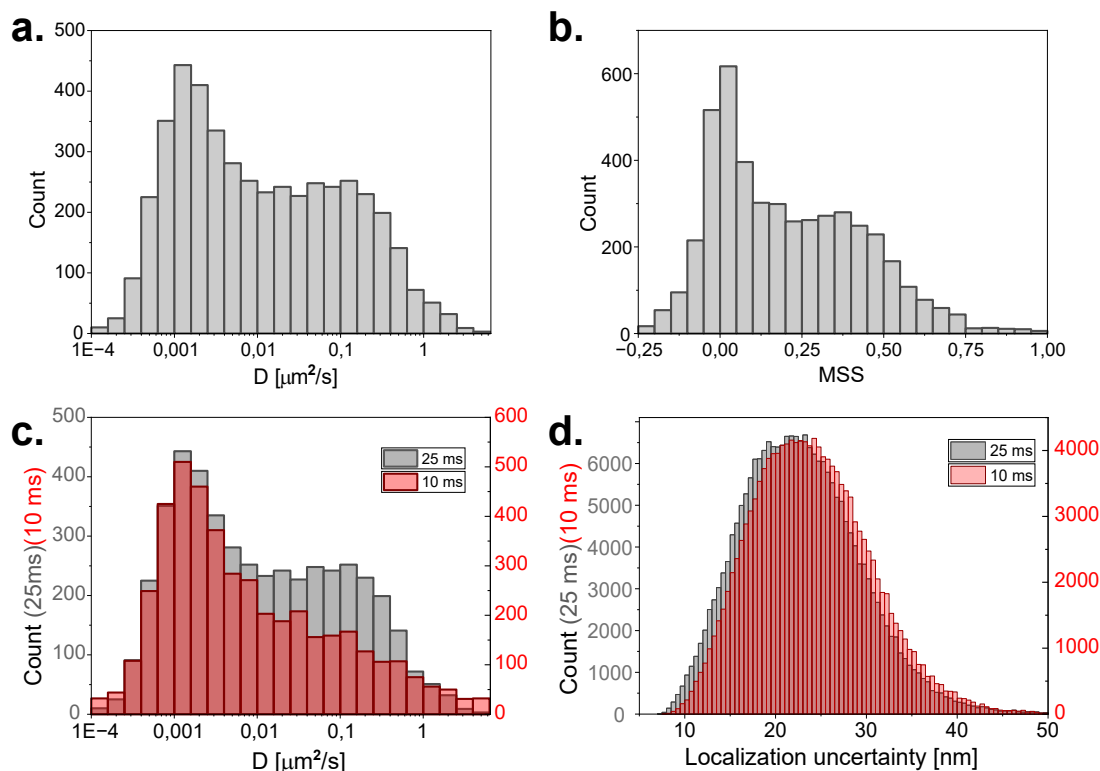


Fig. 3.12.: Diffusion coefficient and MSS as determined through SPT data. **a.** Diffusion coefficient of approximately 5'000 molecules (with tracks longer than twenty time-points) is displayed in a logarithmic histogram. **b.** Moment scaling spectrum of the same population displayed in **a**. Exposure time in **a** and **b** is 25 ms. **c.** Comparison of the diffusion coefficient of the same population with 25 ms and 10 ms exposure time (corrected and double laser intensity). **d.** Histogram of the localization uncertainty of the two data-sets displayed in **c**, laser intensity was doubled for the acquisition with 10 ms exposure time. Diffusion coefficients and MSS were determined with *Mosaic* [SK05] and localization precision with *ThunderSTORM* [Ove+14].

speed is the size of the FOV. The current software options do not allow to acquire smaller cropped ROI. Any stack acquisition thus captures the whole camera chip. This however is a challenge that can and will be tackled in the near future. In figure 3.12 **c**, the same populations of GPI-GFP labelled with quantum dots are plotted, once with 10 ms and once with 25 ms. For the population with 10 ms, the laser power has been doubled and the time interval between two time points has been set to around 17 ms in *Mosaic* [SK05] during the analysis, because even though an image is acquired with 10 ms exposure time, the acquisition rate per second is still limited to 60. The integration time is thus longer than the exposure time and was accounted for in the analysis. Drift has been ignored during the SPT analysis. The localization precision, as displayed in figure 3.12 **d**, shows that with the doubled laser power, the difference between the two exposure times is negligible. In figure 3.12 **c**, the two populations are visible with both acquisition times. The mobile population however is not as well represented with the lower acquisition time. As the measurements were done in an alternating scheme, the probability that the number of bound QDs was reduced is highly improbable. Possibly the higher laser power might

influence the acquisition of longer tracks. The detection of moving particles seems to be challenging with the shorter acquisition times.

Based on these observations, reducing the exposure time below the maximal frame rate, corresponding to the highest possible integration rate of the camera, does not make sense. An empirical value of 20-25 ms could be set as optimal for SPT, and also as lower boundary for temporal resolution. It enables to conduct experiments with a good balance between spatial resolution and sampling rate.

3.4.2 SMLM: optimal number of frames

From the drift experiment (subsection 3.2.2), the sampling rate (subsection 3.4.1) and the ability of the setup to gather enough photons to localize the centroid of a single molecule, all the elements to perform SMLM seem to be provided. However, SMLM is subjected to different sources of artefacts that decrease the quality of the final reconstruction [Bur+15; WB15]. One of the factors resulting in artefacts is the number of frames necessary for a high quality reconstruction. A too low number of frames might not contain enough blinking events to adequately represent the structure. On the other side, too many frames introduce artefacts due to multiple localization of the same molecules. This is specially true in densely labelled samples or high density regions within a sample. In this project, the acquired images always are the full camera chip (1456×1088 pixels) in a *.hdf5* format thus bringing data handling challenges with increasing data size. I here estimate the optimal frame-number necessary for a good *d*STORM reconstruction.

The optimal number of frames for SMLM experiments depends on the blinking speed, the blinking buffer and laser illumination density [Le1+21]. Efforts are being made to fasten up SMLM imaging [Lin+15] with accordingly fast algorithms [Hua+13] and for different SMLM techniques e.g. fluorogenic DNA paint [Chu+22]. In our case, the frame acquisition speed as well as the reduced laser density are limiting factors. On the example of *d*STORM of actin rings in neuronal axons the number of frames until which the resolvable image features as well as the imaging errors are decreasing was estimated at 30'000 frames [Cul+18]. Here, with a different sample and experimental settings, the experiment was reproduced with similar methodology. In figure 3.13, the FRC resolution of a *d*STORM measurement of cellular microtubules (on CV-1 cells) is measured for different frame numbers on the Llama microscope (section 5.1.2) with similar illumination density as are present in the UC2 setup. A frame number of around 25'000 to 30'000 has been extrapolated to be optimal for the SMLM acquisition with the UC2 system, as shown in figure 3.13.

The average value of 73 nm shown in figure 3.13 **b** is an average over the whole cell. This value can be higher when looking at specific regions of the image. Especially regions of the FRC map where no signal is expected have a very low resolution, as random blinking from unspecifically bound molecules can not properly be correlated. Furthermore, the

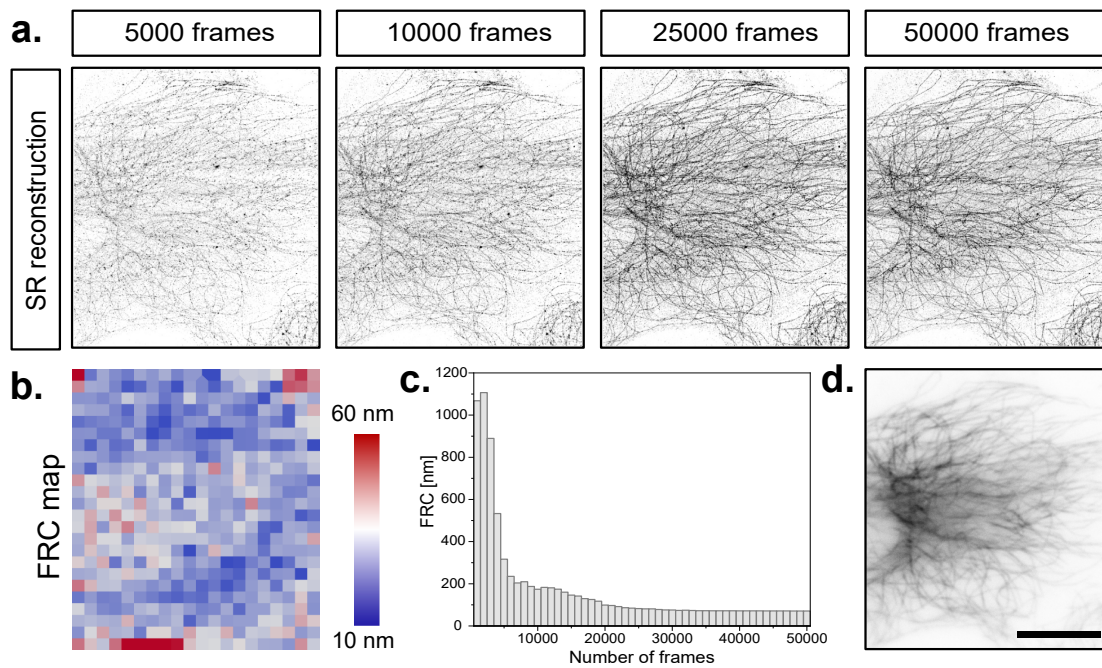


Fig. 3.13.: Determining the optimal number of frames for an SMLM experiment using FRC. **a.** *d*STORM reconstruction of NRK52E cells immuno-stained against tubulin at different frame numbers. **b.** Corresponding FRC map of the 50'000 frames image in **a.**, generated with the NanoJ-SQUIRREL ImageJ plugin [Cul+18]. Averaged over-all resolution is 73 nm. **c.** Plotted average FRC for different frame numbers. Final resolution stagnates around 71 nm. **d.** Wide-field image as reference. Scale bar represents 10 μ m, also applicable to the images displayed in **a.**

epi-illumination is adding additional fluorescence from out of focus planes to the acquired signal. This can clearly be seen, as the resolution diminishes with increasing sample thickness, as shown in figure 3.13 **b** around the nucleus. This leads to the conclusion that flat samples (e.g. CV-1 cells) and an analysis at set distance from the nucleus are the logical first step to maximize the chances of success when transposing the experiment to a low budget system. Additionally, the number of acquired frames will be set to 30'000, as increasing the data-set size will not affect resolution, even if the experiment seems to indicate that the resolution is also not decreasing with more frames. Limiting the number of acquired frames also bears advantages in data handling and simplifies the drift correction.

3.4.3 *d*STORM of cellular microtubules

After determining the optimal number of frames, I here demonstrate the reconstruction of cellular microtubules with substantially increased resolution using the popular SMLM method *d*STORM. The raw data was acquired with the open-source based UC2 setup. Cellular microtubules are a well studied structure [Alb+13] which has been characterized in different microscopy techniques. Based on the available knowledge on the microtubule structures, they were chosen as a model system to demonstrate the possibility of perform-

ing SMLM with a low budget setup. Furthermore, to facilitate comparison, because of the amount of already present applications and the constraint to use far-red dyes, the fluorophore of choice for the SMLM experiments is the red cyanine dye Alexa Fluor 647 (AF647) [Geb+21].

In figure 3.14, the *d*STORM of immuno-stained microtubules in CV-1 cells is displayed. The staining protocol is elaborated in the subsection 5.7.6. The analysis of the data-set was done with ThunderSTORM [Ove+14] following the methodology described in subsection 5.5.1. The SMLM techniques has clearly improved the resolution of the image as shown in **a**. The zoomed in ROIs in **b** and **c** clearly show that features can be distinguished below the diffraction limit. The profiles measured along the microtubules are fitted with two Gaussian functions with an approximate distance of 40 nm between them. A more detailed display of measured microtubule diameter will be given when assessing the resolution of the microscope, in subsection 3.5.2. The drift in X and in Y was in the range of a few hundred nanometers during the 15 minutes acquisition time, and was corrected using cross-correlation (figure 3.14 **d**). Fiducial markers have also been added to the sample as supplementary method to remove drift from the SMLM reconstruction, but were not used in the measurement displayed in figure 3.14. The surprisingly good performance of this low budget system can be seen based on two known imaging artefacts when imaging microtubules. First, the railroad track shaped structure (figure 3.14 **e**) is an imaging artefact created when transposing a 3D tubular structure onto a 2D image plane. When summing up the signal emitted by a cylindrical structure at all focal planes, the density of fluorophores is higher at the edges than in the middle. The two peaks can be fitted with two Gaussian functions [Dem+11], resulting in a projection of the microtubule diameter. The second imaging artefact can be seen when measuring the distance between the two peaks as it is influenced by a linkage error introduced by the primary and secondary antibody. Microtubules have a diameter of around 25 nm [Pol+17] but distance of 35-38 nm between the two measured peaks are a projection extrapolated from SMLM images of immuno-stained samples [Wu+20].

The acquisition is, at the current state, only possible for the whole FOV simultaneously and selecting a smaller ROI has to be done post acquisition, using image analysis tools such as FIJI or Napari [Sof+22; Sch+12a]. The total acquisition time of the whole data-set was around 15 minutes and thus comparable to common commercial SMLM solutions. The fast acquisition is also currently only possible using the *.hdf5* file format for data saving on the hard-drive of the operating computer. The challenge arising from such data-sets is that special plugins are needed to handle the files as a result of their increased size (95.6 Gb for 30'000 frames). Regular *.hdf5* files can be loaded into the random access memory (RAM) of the computer if it is sufficiently large (table 5.5) using the ImageJ import function to open an *.hdf5* file with the corresponding plugin [Rue+]. Accordingly, the RAM ImageJ is allowed to use has to be increased to be larger than the file itself. For most computers, with lower RAM, the image stack must be loaded into FIJI as a virtual stack, thus not be loaded into the RAM. This has been achieved using the N5-plugin [Saa+22], which

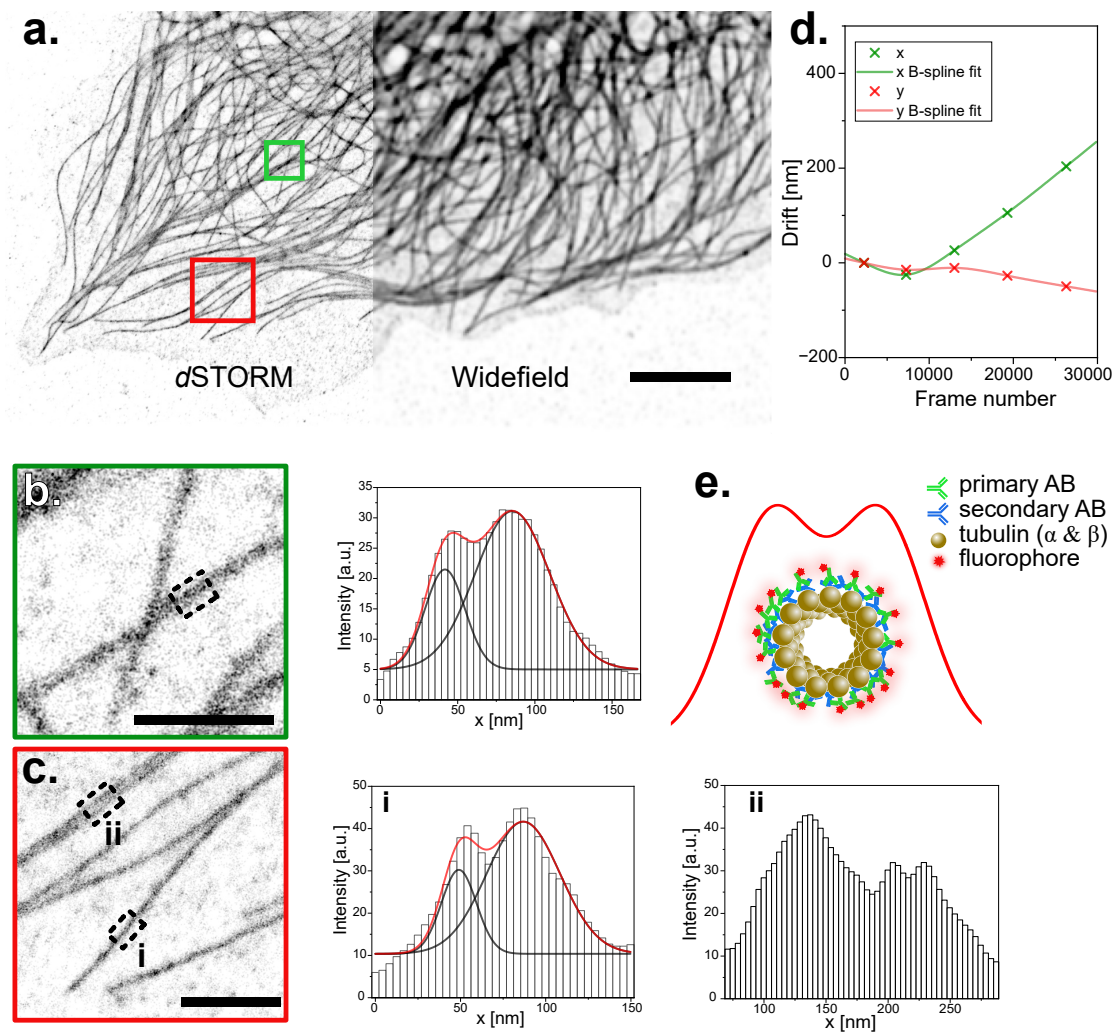


Fig. 3.14.: dSTORM imaging of microtubules on the UC2 microscope in epi-illumination. a. Immuno-stained microtubules in CV-1 cells are shown in wide-field and with *d*STORM. Scale bar represents $5\ \mu\text{m}$. **b.** and **c.** show two regions of interest marked from **a** that are magnified and the averaged profiles along 200 nm of microtubules are shown as proof of principle. Profiles are fitted with a double Gaussian. Peak to peak distances of $(38\pm 2)\ \text{nm}$ for **b** and $(43\pm 2)\ \text{nm}$ for **c.i** are extrapolated. Scale bar represents $1\ \mu\text{m}$ in the magnified ROIs. **d.** Drift during the raw-data acquisition period of the reconstructed image displayed in **a**. **e.** Simplified schematic of the front view of a microtubule sample after immuno-staining and the resulting railroad tracks. **f.** Comparison of the extrapolated microtubule diameter for the UC2 and the Llama setup.

allows simple handling of large *.hdf5* files. General sources of most ImageJ plugins used for the SMLM imaging are displayed in table 5.4. The acquisition of raw-data as *.tiff* files is slower as each image is saved individually, but might be competitive in speed if the data can be acquired with a smaller FOV. Furthermore, the maximal frame rate achievable by the camera might even be faster than the one determined in subsection 3.5.2, if the size of the FOV is reduced.

As a comparison to the UC2 setup, the same immuno-stained microtubule sample as presented in figure 3.14 is imaged with the Llama setup, an established SMLM-capable setup

[Alb+16a]. The resulting images are displayed in figure 3.15. The difference between the UC2 and Llama setup is difficult to see as the image is a reconstruction of localization points displayed with higher resolution (average shifted histogram visualization). The identification of the two peaks, both in the image as well as in the profile plots seem to indicate a better quality with the Llama setup. The extrapolated microtubule diameters of around 36 nm are also in better accordance with the values found in literature. Ideas that could account for this difference will be provided in the subsection 3.5.2. The overall finding from this experiment is that SMLM imaging experiments are definitely possible with the UC2 setup, sub diffraction-limit structures can be identified and the gained quantitative information is almost in agreement with the values provided in literature.

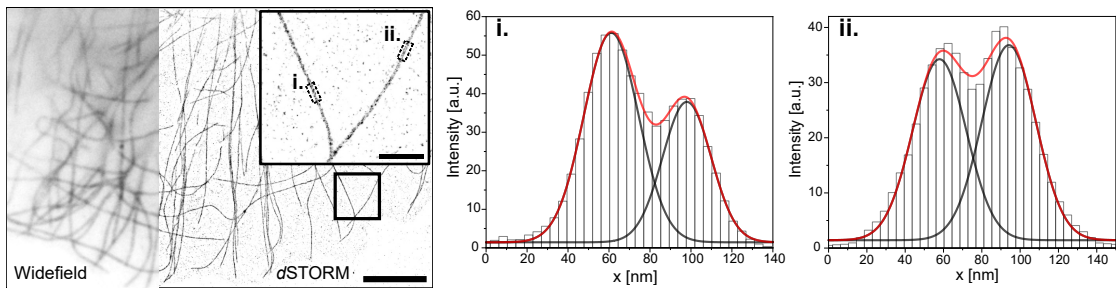


Fig. 3.15.: *d*STORM imaging of microtubules on the Llama microscope in epi-illumination. Same sample as in figure 3.14 imaged in widefield and reconstructed with *d*STORM. Scale bar represents 5 μm . Region of interest is magnified (scale bar represents 1 μm) to look at two single microtubules, which profiles are plotted in **i.** and **ii.** by averaging the signal over 200 nm along them. Profile is fitted with a double gaussian. Peak to peak distances of (36.2 ± 1.2) nm for **i.** and (36.9 ± 1.2) nm for **ii.** are extrapolated.

In the appendix A.5, the same sample as in figure 3.15 is imaged with a TIRF illumination, thus improving the SNR and reducing fluorescence from background regions. The extrapolated microtubule diameters are similar to the ones measured with epi-illumination. Advantage of TIRF is the elimination of most background emissions. As the used objective is also TIRF-capable, measurements in TIRF-illumination have been tried on the UC2 setup but were unsuccessful. The shift of the illumination beam within the back focal plane is difficult to achieve using only one tiltable mirror, as the excitation path does not follow the optical axis anymore. Furthermore adjusting the rest of the setup to this illumination would not allow to produce high-quality data [Mon+21]. The design of a translatable mirror for shifting the excitation laser within the BFP but still parallel to the optical axis might be a solution to image in TIRF with the UC2-setup, but is not yet implemented in the current design. Imaging with TIRF-illumination is thus possible with a translation mirror. By changing the emission path to allow the positioning of a Bertrand lens to verify that the illumination is in the right angle [Fis09], the usage of TIRF illumination can be made consistent for the UC2 setup.

3.5 Image quality and resolution estimation

3.5.1 Camera quality

Measured on single TS beads, the difference in SNR between the Llama setup (SNR = 5.5 ± 0.3) and the UC2 setup (SNR = 2.5 ± 0.5) is clear. As the same objective was used and similar laser densities ($\approx 200 \text{ W/cm}^2$) were illuminating the sample in both measurements, the difference in signal contrast must mainly be attributed to the detector quality. Comparison of Photometrics delta 512 with the Alvium 1800 U-158m CMOS camera from Allied Vision reveal differences in their quantum efficiencies, the linearity between photons and grey values, the amount of noise and more. As expected, the camera errors mentioned in subsection 1.7.1, are predominant in the low-budget solution.

This quality difference influences the localization precision of single molecules, as a shift can clearly be seen in the distribution (figure 3.16 a). The difference is however still in an acceptable range. With higher exposure times, high-quality images can still be acquired using the low-budget detector. Using techniques that intrinsically have reduced background, such as TIRF microscopy, light sheet illumination or PALM in the case of SMLM could reduce the gap in image quality. Obviously, the use of brighter dyes and better illumination techniques would further improve the image quality.

Not all imaging assays require high SNR, but image resolution and signal quality are strongly dependent on camera sensitivity. For this reason, the acquisition fluorescent signals with very limited photon budget such as Ca^{2+} imaging will always be challenging with the UC2 setup as the camera will not provide a good enough SNR to reliably image the fluorescence. The signal is however strong enough to enable single molecule localization and corresponding reconstruction of labelled structure. The achievable resolution in the final image does depend on various factors, especially when reconstructed, and will be further discussed in subsection 3.5.2. The use of aperture photometry, a common concept in astronomy, might also be an useful post-acquisition tool to correct the measured intensity of single molecules by accounting for the local background they are in. Aperture photometry measures the intensity within an annulus around the PSF of a fluorophore to account for local background at the vicinity of the single molecule's position. The use of this technique is possible with FIJI [FSL17], and can help to measure more reliable fluorescence intensities, even with a low-budget camera.

3.5.2 Resolution

The estimation of image resolution is non-trivial, especially for SMLM reconstructions (see subsection 1.9.9). Here, three different criteria have been considered to give an estimation of the image quality generated by the setup. The same experiment executed on the Llama microscope is taken as comparison. The difference in camera quality (subsection 3.5.1) can clearly be seen when looking at parameters such as the localization precision in figure 3.16a. The histogram representing the localization precision of the UC2 system is clearly shifted compared to the Llama setups one, both data-sets being acquired with the

same sample and similar conditions (same objective, both epi-illumination, similar laser powers). The higher noise and the resulting diminished SNR are suggested to be the source of the reduced precision. However, it is to notice that the general precision of the built setup is good and definitely sufficient to reconstruct images with substantial resolution improvement. The resulting images being a reconstruction of the single molecules positions, the resolution has also to be considered on different scales.

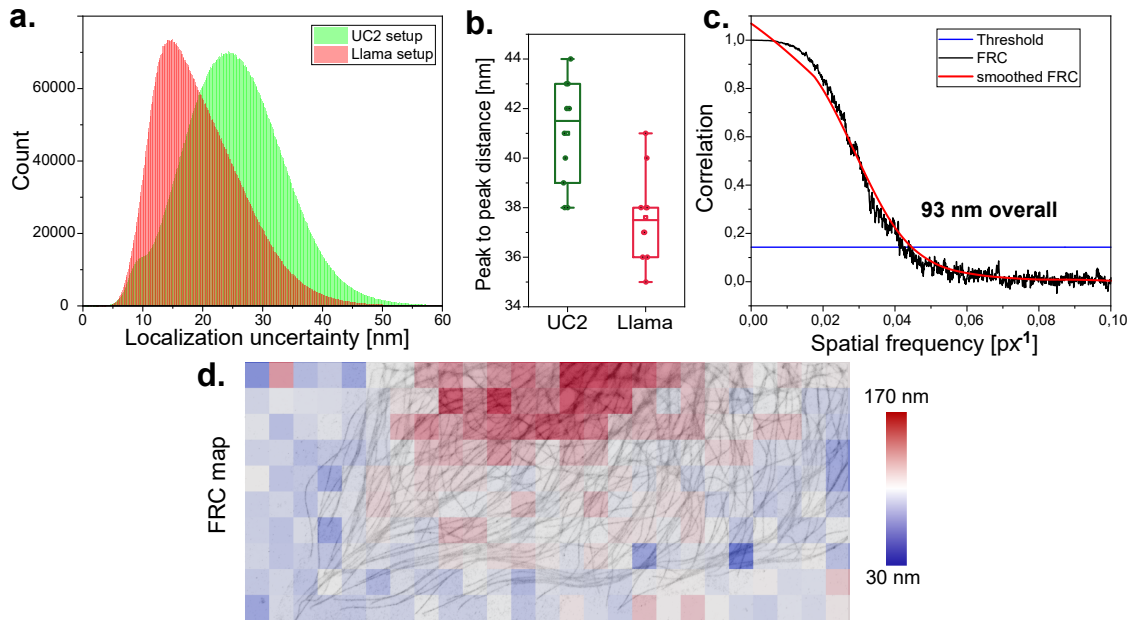


Fig. 3.16.: Resolution estimation of SMLM images acquired with the UC2 setup. **a.** Localization precision of around $8 \cdot 10^6$ single molecules (accumulated from several measurements) for the Llama and the UC2 setup, with the same 1.49 NA 60x Olympus objective. **b.** Measured peak to peak distance on the railroad-track shaped profile of *d*STORM reconstructions of microtubule for both setups. **c.** FRC average of the complete reconstruction presented in figure 3.14. Threshold criteria fixed to $1/7$ [vS05]. **d.** FRC-map of the *d*STORM data-set generated with NanoJ-Squirrel [Cul+18].

Another possibility to estimate the correct spatial reproduction of given structures is to measure a known sample feature and to compare it with a high-quality setup measurement of the same sample and compare the extrapolated value to those mentioned in previously published literature. In figure 3.16b, the measured distance between the two fitted peaks along the railroad track shaped artefact of reconstructed microtubules are compared, again between the UC2 setup and the Llama setup. The extrapolated diameter is larger than the actual microtubules as the antibody staining generates a linkage error between the fluorophore and the target structure. The diameter measurement shows that the reconstructions with the Llama setup are in agreement with the values measured in previous studies in the context of SMLM reconstruction [Dem+11; Wu+20], within the variance of the analysed profiles. The diameter measured with the UC2 setup is larger but still overlapping the Llama values with regard to the error-bars. This discrepancy originates from the reduced localization precision and the lower mechanical stability of the setup. Possible axial drift could also influence the final reconstruction. The difference

in image quality can be made clear when comparing the magnified ROIs of figure 3.14 and 3.15, where the supposed railroad tracks are not as clearly seen in the reconstructions of the UC2 data.

Finally, as was already used in subsection 3.4.2, the FRC is an established way to estimate image resolution in the SMLM field [Nie+13]. In figure 3.13 the overall resolution seems to be settling around 70 nm on microtubule measurements on the Llama setup. This value could be reproduced within SMLM measurements of the same immuno-stained CV-1 cells used in figure 3.14. The measured overall resolution is an average of the the measured value in the different squares displayed in the FRC map (figure 3.13 and 3.16). In both cases, we can discern that the estimated resolution is diminishing with increasing proximity to the nucleus, as the ability to localize single molecules is hampered by out of focus signal originating from the 3D structure. TIRF measurements can help to minimize these effects but are, at the current state, challenging to realise with the UC2 system. The presented setup provides an average resolution around 93 nm. The difference to the Llama setup measurement is a cumulative influence of the lower camera quantum efficiency, the reduced SNR, the subsequent lower localization precision and overall the possible imaging errors of the remaining low-budget components of the system.

The possible localization of single molecules as well as the identification of cellular structures, which are still matching the values displayed in literature within their variance, are a proof of concept of the possibility to generate high-quality with a low budget system. The images are lacking in accuracy and resolution compared to refined high-quality systems, but performing SMLM and using the microscopy images for quantitative studies are possible.

3.6 Low-budget objectives

The objective quality is paramount for achieving high-quality images in any given imaging method. In the setup described here, the high-quality objective is limiting the accessibility of the method, due to its inherent high production and acquisition cost. In order to tackle this challenge, the suitability of two lower budget objectives for high-quality imaging is assessed. This allows to determine for which experiments the provided image quality is sufficient. Consequently, this experiment can help to gain insight into how the device can effectively be used to promote and enable scientific research. The relevant research purposes and the limits in terms of budget for the acquisition can be determined with these experiments. The two objectives including their corresponding specifications and pixel sizes are listed in table 5.1.4.

The difference in image quality is clear between the high-quality and the low-budget $20\times$ magnification objectives. With 0.8 to 0.45, the high quality objective has an NA almost double the low budget objective's one. This means that the collection of emitted light is significantly reduced for the low budget objective, thereby reducing the SNR. The

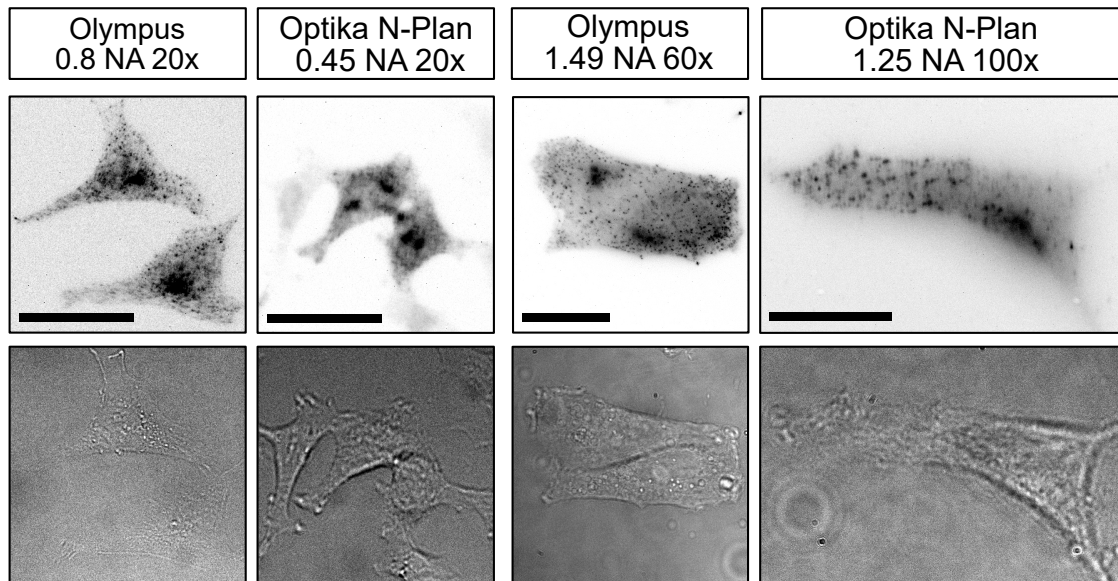


Fig. 3.17.: Comparison of high- and low-budget objectives on the example of clathrin coated pits on HeLa cells. Stable HeLa cell-line with Clathrin light chain-GFP stained with AF647 conjugated anti-GFP nanobodies. Same sample was imaged with different objectives on the same UC2 based microscope. The scale bars in the 20 ×, 60 × and 100 × magnified images respectively represent 30 μm.

contrast of fluorescence collected from the clathrin coated pits compared to the background as well as the bright-field images show a clear difference in quality, which can be seen by eye. Recognizing larger features such as nuclei is possible with the low-budget objective, however its usage for quantification of fluorescence signals is challenging as the reduced signal quality falsifies object sizes. The low-budget objective is thus an alternative that can find use in certain applications but as expected compromises in image quality compared to high budget objectives.

From a first visual assessment, the quality of the 100 × magnification objective allows to distinguish features with similar accuracy to the high-quality objective. The shape of the clathrin coated pits, as displayed in figure 3.17, show slight elongations in X and in Y which is a sign for astigmatism. This imaging error generates different PSF shapes depending on the focus positions, originating from e.g. a an uneven lens curvature along the X and Y axis. Although it might be an useful feature to localize molecules in 3D, the PSF asymmetry is undesired for high quality imaging. The SNR is also lower than observed in the images acquired with the high quality objective. The high magnification objective has a 1.25 NA, which is sufficient to gather enough fluorescence to localize the position of single molecules but has no significant improvement in the resolution of the cell. Furthermore, the pixel-size of the setup does not match the criterion previously established with the Shannon Nyquist theorem, as the magnification was increased, effectively distributing the same fluorescence signal upon more pixels. This results in a decreasing SNR, which can also be seen when looking at the localization accuracy of the microscope, being reduced by the low budget objective. When using the 100 × objective for single molecule applications,

I first imaged Tetra Speck beads. The 3D Z-stack displayed in figure 3.18 **a** discloses slight astigmatism as suspected from the wide-field images. The lower NA and higher magnification clearly shift the localization precision as displayed in **b**. The number of molecules in the statistics compared to the high-NA objective is relatively low, but the trend is very clear. With an average localization precision around 30 nm, the SMLM imaging is lacking in quality. This is visible in **c**, where the depiction of CCP (Clathrin coated pits) is not as clear as in figure A.6, where the same sample has been imaged on the Llama setup. The acquisition parameters have been kept similar between both measurements and also compared to the other *d*STORM images acquired on the UC2 setup (25'000 frames with a laser power of 900 mW/cm²).

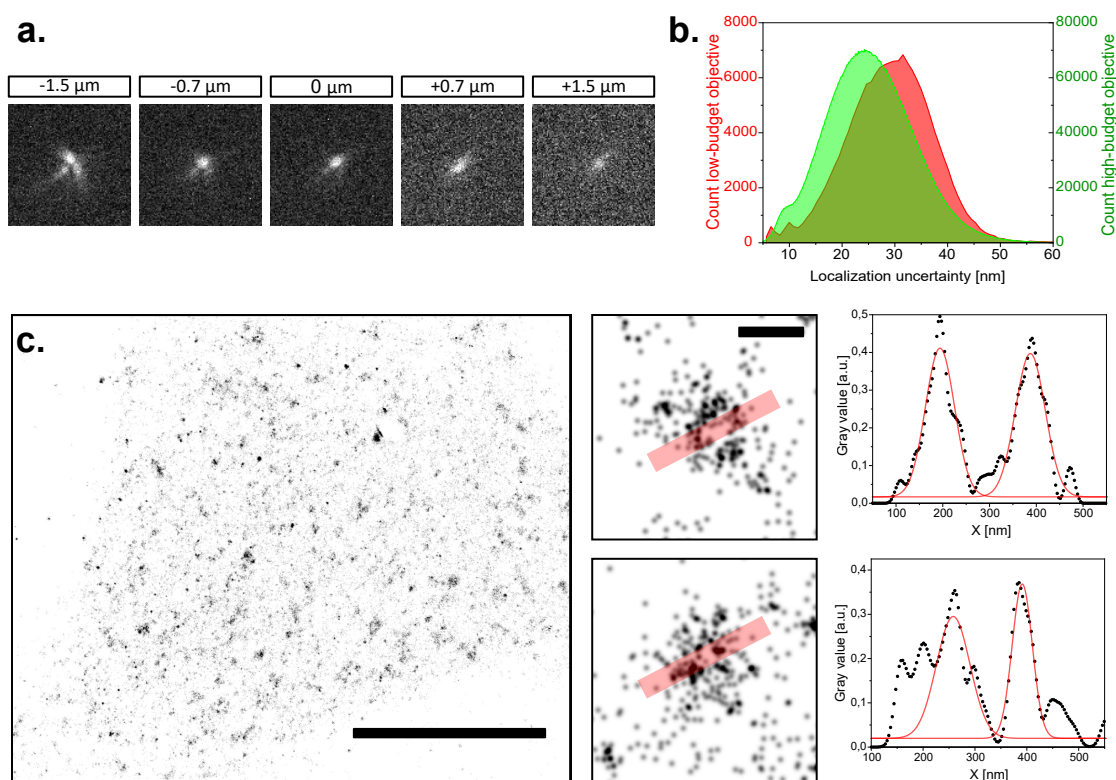


Fig. 3.18.: Single molecule applications on UC2 setup with low-budget objective. **a.** Z-stack of single fluorescent beads with the low-budget objective. **b.** Comparison of the localization precision of the UC2 setup with the high- and low-budget objectives. **c.** *d*STORM reconstruction CLC-GFP in HeLa cells immuno-stained with AF647 conjugated nanobodies. Scale bar for **c** represents 10 μ m. Two CCPs have been magnified with the profiles along the red transparent line displayed on the right. Scale bar for the magnified regions of interest represents 200 nm.

CCPs have different shapes, depending on the stage of endocytosis they are in. When the pits are formed, the observed CCPs change into a spheric shape which is displayed as a circle-like structure in SMLM measurements. The look at single selected CCPs can confirm the higher reproducibility and quality of imaging with the high-quality microscope.

For the Llama setup, peak-to-peak distances of (163 ± 6) nm and (189 ± 6) nm have been extrapolated. The UC2 setup shows peak-to-peak distances of (203 ± 7) nm and

(213 ± 7) nm, which both are still in an expected range for CCPs (appendix figure A.6). The higher localization accuracy and the general lower quality of the raw-data are impeding the ability to represent biological structures with the low-budget objective.

Nevertheless, the localization of single molecules is possible and SMLM techniques can be performed, even though the resulting image and reconstruction qualities clearly lack behind on high quality solutions. The use of this objective for wide-field imaging with limited quantification is possible. By adapting the tube lens, the pixel-size can be increased, subsequently improving the SNR. SMLM imaging is challenging, and not as reliable as with the high-quality objective, but feasible. For teaching purposes, the quality provided by the low-budget objective is sufficient. The experiments with the low-budget objectives have demonstrated the importance of high-quality optics i.e. objectives for high-quality imaging. It is however remarkable how many experiments could still be achieved with the low-budget solutions and shows that high-resolution is not always necessary. Cellular features can easily be identified with the low-budget objectives, but quantification of fluorescence microscopy will still lack behind data acquired with high-quality objectives. Low-cost objectives are the last big step towards an entirely low-budget system. The acquired data suggests a clear difference in data quality as expected. The image quality is however sufficient to conduct a wide array of imaging assays including SMLM techniques. Especially the objective with the $20 \times$ magnifications can be used for general screening, low resolution applications and teaching. Features such as cell morphology and larger cell structures can be identified using the fluorescence channel. Similar low budget solutions exist for e.g. the diagnostics of Malaria [Li+19].

The low-budget objective reduces the price of the complete setup to a range of 2000-3000 €, effectively meaning a 100 to 200-fold price reduction, compared to commercial systems. This competitive price would give the presented instrument an advantage accessibility and deployment. Institutions e.g. in countries with limited budget might gain access to imaging instruments and have the chance to build a life science curriculum in optics and life science, or participate in life science research with the microscope. This price advantage significantly increases the accessibility of the setup, giving access to educational content and practical experience in optics as well as in life-science to more users. Performing high-quality imaging is not possible in a reliable way. The reduced NA and manufacturing quality enable a fundamentally lower photon detection accompanied by a less reliable reproduction of biological structures. Newer staining methods combined with brighter dyes might assist in bridging the quality difference, the presence of imaging errors will however not be impeded. Methods such as expansion microscopy and current developments (such as pan-expansion [MB20]) magnify a sample enough to allow imaging with lower magnification. Potentially opting for a high-quality objective with less magnification might also be worth considering, given that knowledge transfer enables the application of these techniques to expand. Furthermore, the optics such as the tube lens have also not been adapted to the $100 \times$ objective yet. Compared to the $60 \times$, the 1.5-fold magnification reduces the pixel-size to over-sample the acquisition, the

pixel-size being $3.1 \times$ smaller than the diffraction limit (optimal around $2.3 \times$). Further adjustments on the setup towards the specifications of the lower NA objectives could improve the image quality to a slight extend.

To summarize, the quality of the optics i.e. the objective lens in particular, is paramount for high-quality imaging. Unfortunately, this also means that imaging biological samples with high enough accuracy to allow for quantitative analysis is seemingly bound to a higher budget. Improved manufacturing techniques may in future alleviate this challenge. The usage of these objectives however still find application in lower resolution experiments, in long-term live-cell monitoring and in a variety of possible teaching assays.

3.7 Possible Setup improvements

In order to match the experimental needs of most users, different improvements can be made on the microscope. This will allow to tune the capabilities of the microscope towards the biological functions that are planned to be studied with the system as well as to adapt the needed biological imaging techniques to the setup [Cox17]. An immediate idea is the implementation of an illumination providing different wavelengths. The result would allow to study several cellular structures simultaneously, enabling the system to image substantially more fluorophores. Studies on cellular co-localization of certain proteins and simultaneously monitoring the cooperation of different organelles in cellular pathways are examples of possible extensions of the microscope's applications.

The top-light illumination can be improved to gain more structural information from biological samples. Possible improvements are the embedding of the LED into a Köhler illumination setting [Neu20] or the implementation of a differential interference contrast module [Ros77]. Both these illumination modes can be implemented in the current version of the setup and would make wide-field imaging more reliable without increasing the costs significantly. The use of standardized methods, e.g. for illumination, will make the use of the UC2 based microscope both reliable in the fluorescence channels [Mon+21] but also reproducible and systematic. Reproducibility has always been a challenge regarding the interpretation of imaging data [Fan18]. This is especially true for open-source concepts which often use different hardware, low-budget pieces and different acquisition schemes additionally to the variability of sample and staining. The introduction of a normalized method to illuminate the sample, both in fluorescence and in top-light illumination, would contribute to more reliable imaging using the UC2 device. In order to reduce the amount of external illumination, 3D printed panels can be used to seal the open cube sides, thereby eliminating undesired light pollution and reducing image background.

The microscope in its current build can still be improved in ways independent of the biological applications. First, the user-friendliness can be further increased to facilitate the construction and the deployment. An obvious example would be to make the electronics fully pluggable, thus removing all necessary soldering from the building process. The

usage of high-power LEDs (several Watt) would not only improve the sensitivity for SMLM applications, but also reduce the safety requirements to operate the microscope, especially when it is used for teaching purposes. The wide-field imaging modalities and the necessary illumination intensity should still be sufficient for most imaging assays. The online flashing tool (discussed in subsection 3.1.2) is already a big step towards simplifying installation, but installing ImSwitch might still be a challenging task, due to the different Python packages that have to be installed. The development of a stand-alone software package could be a helpful asset in this endeavour. In the GUI itself, a few features can and will be improved with modifications in the code. The possibility to image a cropped FOV instead of the whole chip could increase acquisition speed, and be useful in experiments relying on high temporal resolution e.g. the study of single molecule dynamics in the plasma membrane. Binning of the camera pixels is still a feature that is not working properly, and would be useful to have (e.g. for the 100× low-budget objective). Furthermore, the acquisition time is set for all channels simultaneously, resulting in different contrast values if one were to image two channels with different brightness levels. A possibility to set different exposure times for each channel is an improvement idea that will be realised in the near-future. For long measurements, new ideas (hardware or software) are necessary to improve the capability of keeping a sample in focus over a prolonged time period and will be implemented in the auto-focus widget of ImSwitch to improve the live-cell imaging options. A first test was done by using an array of LEDs instead of a single top-light illumination LED, as a method to get a clear pattern differentiating the focal plane from the rest. The Fourier transform of the observed top-light image shows very distinct features which provide a clear parameter, from which the axial position or the distance in relation to optimal focus can be estimated. This principle is demonstrated in figure A.2 the Appendix subsection A.1.2. The resulting bright-field images are not suitable for imaging as the multiple light sources do not allow a clear representation of the different cell features. However, by only using one of the LEDs in the array, images with similar quality than with the high power LED can be generated.

Finally, updating the materials and tutorials concerning the construction of a microscope including software control is a further step towards more user-friendliness. All these improvements are most effective when shared and pushed forward by a community of microscopists. The development of the repositories, the expansion of the UC2 community and the active sharing of designs, codes, methods and results will in the long-term strengthen the advantages of such an open-source concept. A challenging aspect of producing open-source hardware and software is that, compared to publishing research findings where minimal amounts of data are made public for publication, a much deeper documentation is necessary to really make the developed instrument useful and sustain its impact in resolving modern challenges. Furthermore, open-source platforms and projects often rely on few individuals. The establishment of a community might help to keep the platforms up to date if the original authors retire or stop providing maintenance for the tool. A possible asset could be the assistance of artificial intelligence in developing

open-source platforms and improving the hardware's compatibility and modularity. This can for example include helping users to write treibers, or assist the management the platform and helping adapt software solutions for different operating systems.

To sum up, many options are available to upgrade the setup, adapt it to specific experiments and thereby cover a wider range of biological imaging assays. The setup can be used for quantitative imaging but further development is required to make the microscope more user friendly and imaging more reliable, thereby unlocking its full potential. Different improvements can be made enable more biological applications and questions to be studied with the UC2 based microscope. To provide teaching material and effective knowledge transfer, the framework surrounding the hardware is equally important. Efforts are made to provide a detailed documentation and allow users to reproduce the setup.

Data-analysis and clustering: results and discussion

The rapid development of artificial intelligence (AI) and its constant implementation into new applications make it a very powerful tool. A multitude of recent applications assisting the analysis of life-science data can be found. In the case of microscopy, many machine learning (ML) based approaches are allowing to increase the throughput and to reduce the repetitive manual analysis of data-sets. In the context of life-science imaging, acquisition for sample preparation and imaging instruments are not widely available, especially in developing countries. The data-analysis steps can however be conducted anywhere, as long as a computer is provided. The availability of online processing tools (e.g. Google Colab) even enables the use of computational resources for analysis steps that are too high for common laptops. The use of such tools can facilitate the inclusion of researchers into collaborations and concentrate research efforts on meaningful experimental steps instead of repetitive analysis of results.

In this chapter, a few options are presented that can be applied to analyse the type of data generated with the UC2 setup. The focus was put on methods with ease of access in data-handling, the required computational resources and the user-friendliness. The aim is to show with a few examples that certain data-analysis steps can be processed more efficiently by complementing the analysis with machine learning. These analysis steps become even more relevant as the data-sets produced by different imaging assays consistently get larger. The applications shown here range from cell recognition, to the characterization of cellular features and clustering in SMLM data sets. Established solutions for SMLM image analysis [Spe+21; HK22] can be extended further to analysis methods such as e.g. clustering [KNH20b], thereby enabling the extraction of quantitative information from the acquired data-sets.

4.1 Cell segmentation

As mentioned in subsection 3.3.4, CellProfiler [Car+06] is an unsupervised machine learning solution to recognize and segment cellular features from microscopy images. This means that the machine has not been trained to recognize these features, but rather relies on parameters that can be chosen by the user (brightness, size and more) to recognize features. Segmentation of cells or given organelles can be done with ImageJ by manually drawing the borders. By thresholding intensities, the amount of analysis can be reduced, but is still not really reliable, depending on the fluorescence intensity distribution in the images. Solutions such as CellProfiler enable creating application specific pipelines.

The measurement of fluorophore brightness, cell area or organelle distribution can be automated, greatly facilitating the analysis of large data-sets (e.g. long-term imaging experiments). CellProfiler can also be combined with other machine learning solutions like CellPose [Str+21], which is specialized in the segmentation of cells, thereby optimizing the pipeline.

For the segmentation of cells, different recent tools have been put forward. One of them is CellPose, a machine-learning based solution which was trained to recognize cells [Str+21]. This means that the machine used data-sets annotated by humans as a reference to identify cells on its own. The distinct sample features that the algorithm uses for recognition are unknown, but are extracted from the training-data provided to the machine. The machine has not been trained to recognize a specific cell-line that has been loaded into it. However, the training data-set provides samples with similar phenotypes to distinguish cells in general. This enables the algorithm to give a reliable estimate of the cells position, shape and borders. The access to using this data-processing method is further simplified as a GitHub version as well as Google Colab notebook are available, thus providing higher computational power and graphic processing power to users lacking computational means.

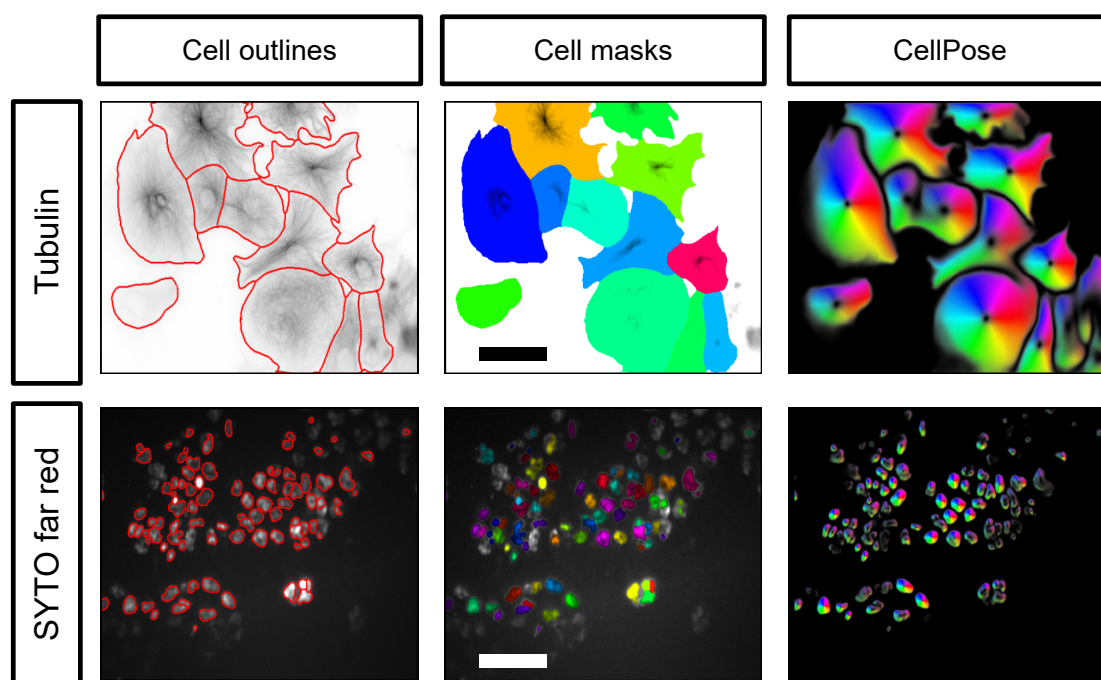


Fig. 4.1.: CellPose for automated training-free segmentation. **Top:** Fixed CV-1 cells immuno-stained against tubulin imaged with $40\times$ magnification. Scale bar represents $50\ \mu\text{m}$. **Bottom:** Live T98G cells stained with SYTO far red nucleic dye with $20\times$ magnification. Scale bar represents $100\ \mu\text{m}$. Analysis was performed with CellPose [Str+21].

In figure 4.1, the CellPose algorithm was used to segment two different samples imaged at different magnifications. The first sample is fixed CV-1 cells immuno-stained against tubulin, imaged with the $40\times$ Olympus objective on the UC2 setup (see table 5.1.4). The cell outlines were predicted accurately, allowing to extract the masks and to segment

every single cell in the presented data-set. The same could be observed in the second sample, where live T98G cells stained with the far red SYTO nucleic dye and imaged with the $20\times$ Olympus objective. The majority of cell nuclei could be recognized, without giving any other information to the network than the estimated object size in pixels. This segmentation tool is a powerful alternative or extension to tools such as CellProfiler and can be an asset in providing simple data-analysis assistance. The recognition of top-light illuminated cells is however still challenging, as the contrast of the borders does not differ much from the contrast generated by organelles within the cells. Especially aggregated cells are challenging to detect and segment. Another recently published article (still in the review process) "segment anything" [Kir+23] was tested. Cells could easily be distinguished from the background, but adjacent cells were often not separated as different objects. The algorithm is not supervised and did not get any training on microscopy images. The method thus still has a huge potential and future data analysis can be more accurate by adjusting the machine learning method to a specific image type.

4.2 Machine learning for SMLM data analysis

Machine learning solutions exist to quantify structures of a specific shape or intensity within the sample. The use of deep learning methods combined with SMLM can be used to identify the underlying sub-units of macro-molecular assemblies [Zeh+22] e.g. by identifying ring like structures and quantifying them. These models however have been specifically trained to identify the specific features from the training data only, and special care needs to be taken to prevent a biased analysis. Using the acquired super-resolved reconstructions of clathrin coated pits (CCP) on HeLa cells, a quantitative distribution of their areas can be implemented with minimal effort. Tools such as CellPose can also be used to batch process features smaller than cells, without extensive training of the network. The details of the machine learning options set for this analysis are described in subsection 5.5.3.

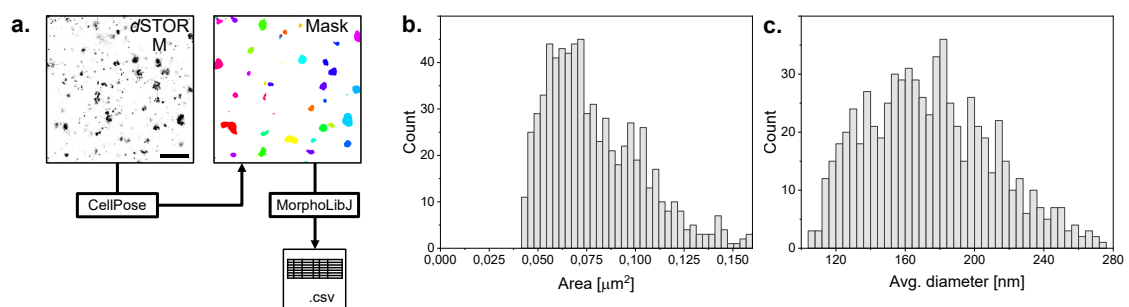


Fig. 4.2.: CellPose for automated training-free quantifying clathrin coated pits sizes. **a.** Analysis pipeline: *d*STORM images of immuno-stained CCP on HeLa cells are divided in $5\times 5\ \mu\text{m}$ ROIs, segmented with CellPose, then the segmented regions are quantified with MorphoLibJ [LAA16]. **b.** Histogram of the area occupied by a CCP. **c.** Average diameter of CCPs.

The resulting masks when analysing the CCP data loses information about the objects topology, the different shapes of the CCPs could not be extrapolated from the analysis. The result however is sufficient to measure simple features such as the object area, the average diameter or even circularity of every detected object, using plugins such as MorphoLibJ [LAA16]. The plots displayed in figure 4.2 show an area of around 0.06 to 0.12 μm^2 , corresponding to the expected 100-200 nm diameter (c). These results are in accordance with the expected size for CCP. The model used here is not very accurate, as it has not been trained to recognize clathrin coated pits. The Colab notebook however also provides a simple infrastructure, to train the network on data to generate a pipeline specific to the structure of interest. Adapting a network to a specific cellular sub-structure is thus possible with little background knowledge and low resources.

This machine learning based analysis was then applied to the CCP *d*STORM reconstruction acquired with the UC2 setup in combination with the low-budget objective. The data quality was not sufficient to extrapolate a reasonable estimation of the expected size and area of the pits. This shows that the acquisition of high quality data is still paramount, as the analysis steps rely on the quality of the raw data.

4.3 Clustering of SMLM data

The communication between cells and their surroundings rely on trans-membrane signaling pathways. These communication processes can be triggered by the binding of membrane receptors with ligands. The aggregation of a specific ligand can thus lead to local enrichment of a given membrane protein, which can then generate an intra-cellular signal or trigger the execution of a signaling event. The number of molecules locally aggregating at the plasma membrane has to reach a certain threshold in order to enable the triggering of a signaling process [PPL02]. The ability to observe and quantify local enrichment of the density of specific membrane molecules can be used as read out to quantitatively describe the emergence of cellular signaling events.

In this specific application, the clustering information is gathered by acquiring super-resolution images (*d*STORM) of fixed cells. The SMLM data-sets are first reconstructed, drift-corrected, filtered and grouped. Then, the data is used in the form of a *.csv* or *.txt* file-format, for further processing. The BaClAva software [Kut+21] was developed as a simple user-friendly tool to provide access to clustering of SMLM data, with minimal parameter input from the user. The here presented data has mostly been processed with the ToMATo [Pik+19] clustering algorithm, due to its high accuracy, when predicting clustering behaviour of SMLM data-sets.

4.3.1 Bayesian Cluster Analysis and visualization application

Clustering of the localization data generated by SMLM reconstructions has evolved into a readout method for membrane protein function, with various algorithms and tools

published for this purpose [KNH20a; Owe+10]. To make use of the available tools, high expertise in SMLM data generation and clustering are required. In order to approach this challenge, S. Kutz developed in cooperation with me, an efficient GUI-based tool for Bayesian cluster analysis of SMLM data-sets (BaClAva). Through parallelisation of the computational tasks on the different computer cores, the processing time is efficiently decreased. The Bayesian engine in combination with the clustering algorithms additionally enables to conduct the clustering steps with minimal input parameters from the user. Prediction or evaluation of clustering is simplified by the possibility to simulate SMLM raw-data of clustered cell membranes, offering access to all functionalities within the GUI. I contributed to the project by benchmarking the performances of the algorithm. This was achieved by simulating SMLM raw data-sets to assess the accuracy of BaClAva and determine the detection threshold of cell membrane clusters imaged with SMLM. Parameters such as the density ratio between the clusters and the randomly distributed background molecules on the rest of the membrane, the size of the clusters that can be detected and the necessary data processing steps to enable cluster detection are taken into account. Finally, I SMLM reconstructed images of membrane receptors to conduct clustering quantifications on real biological samples.

4.3.2 Benchmarking through raw-data simulation

In order to benchmark the performance of BaClAva, a reliable way to generate clusters of known size is necessary. First tests used SpyAvidin hubs to promote cluster nano-assembly of controllable size [Fai+14]. However, a conclusive control over cluster sizes as well as density proportion between cluster and background could not be generated using SpyAvidin hubs. One intuitive alternative to producing SMLM data-sets with controlled cluster sizes and densities is to simulate them. The FluoSIM [Lag+20] software offers various possibilities to reproduce, predict or in general simulate different fluorescence microscopy experiments, and was used here to produce *d*STORM raw data-sets. The simulated data was designed according to the methodology described in subsection 5.6.1. The *.tiff* files generated with FluoSIM are then analyzed with SMAP (see subsection 5.5.1), with the same parameters as would be used for real data-sets acquired with the Llama microscope, to keep the analysis pipeline as close as possible to real experiments. The aim of the simulations is to determine the limits and the accuracy of the Bayesian engine. In this first attempt the capability of the algorithm to detect and correctly quantify a set number of clusters was examined. Thereby, the density factor between the clusters and the background was an essential parameter to investigate. The analysis was conducted with the ToMATo algorithm [Pik+19] as it seems to perform similarly well to DBSCAN [Nie+23] and accounts for sample topology.

Ideally, every localization should represent a single molecule that was stained. However, a single fluorophore (e.g. AF647) can produce several blinking events during an SMLM acquisition. Additionally, cycling of electrons between the ground state and the excited

state lets the emissions of a same single molecule be captured in several subsequent frames. The multiple detection of blinking events originating from the same organic molecule can introduce artefacts and falsify the quantitative study of cluster densities and sizes. For this reason, filtering and grouping parameters have an essential role in clustering of SMLM data-sets. The grouping procedure analyses subsequent frames and verifies if a molecule that is detected in one frame is also present in the following frames within a predefined spatial range. Single molecules can also stop emitting fluorescence for one or several frame as the whole process is stochastic, and then still come back into an emitting state. Grouping thus considers a radius dx around a molecule in which detection in subsequent frames are expected, as well as the number of frames dT that a single molecule is "allowed" to be in the OFF-state to still be assigned to the molecule detected in previous frames. This way, fluorescent emissions from the same molecule detected in different frames are grouped together into a single localization, effectively approaching the number of localizations to the actual number of stained molecules in the sample.

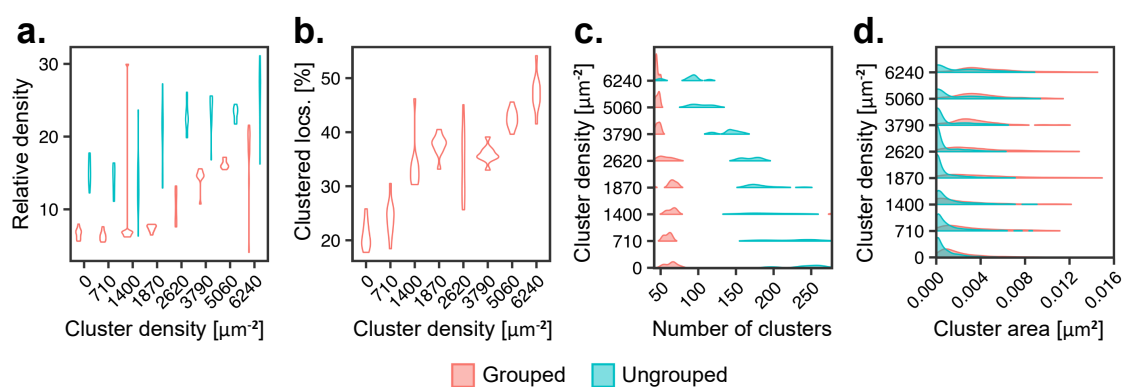


Fig. 4.3.: Benchmarking BaClAva with simulated SMLM raw-data of molecules clustering on the cell membrane. **a.** Relative cluster density compared to the background for different cluster density conditions. **b.** Percentage of clustered localizations for different cluster density conditions. **c.** Number of clusters detected at different cluster density conditions, ground-truth was 50 clusters. **d.** Cluster area for different cluster density conditions. Grouping was done using the methodology described in subsection 5.5.1. Modified from [Kut+21].

In figure 4.3, 4000 molecules have been distributed in the FOV for each condition, with varying percentage of clustered molecules compared to the background (table 5.8). The raw data was reconstructed and the localization tables analyzed with BaClAva. In **a**, the measured relative density between cluster and background is strongly influenced by the grouping procedure. This behaviour is confirmed by **c**, where the number of clusters can be approximated to 40 for different cluster densities (ground truth: 40), a value that can not be extrapolated from ungrouped data-sets. The lowest density ratio between cluster and background was around a factor 1.2 (table 5.8), meaning that for grouped data, minimal increased densities within the clusters can be detected. With a cluster to background ratio of 1.2 to 5.1, the number of detected real and false clusters seems similar, indicating that

reliable representations of the ground truth can be made with density ratios superior to 5.

The four graphs in figure 4.3 show **1.** that the determining the right number of clusters is easier with high densities compared to the background, **2.** that the grouping procedure is essential and ungrouped data can not be processed correctly, **3.** that more experiments and a more density ratios between cluster and background are needed to determine the threshold where the Bayesian cluster analysis can still discern clusters from background with high accuracy. The measurements here presented were all reconstructions from stacks with 50'000 frames. As the analysis is based on localization tables and not images, a basic script can discard frames from the data-set. By varying the frame number, the experimental acquisition of data can be optimized for clustering analysis. Furthermore, different fluorophores and different blinking rates could be tested. The distribution of molecules within clusters could also affect the detection. These factors as well as the laborious manual data production in FluoSIM led to the development of an own simulation software as an alternative to FluoSIM. I also conceptualized an alternative possibility to simulate raw SMLM data with my student Roman Svetlickii. The methodology of the self-written simulation module is described in subsection 5.6.4. The code is openly available on the GitHub repository [KS] in the simulation module/widget. Additional simulations might thus provide more insight into the accuracy of BaClAva. A framework evaluating the performances of clustering algorithms [Nie+23] also relies on simulated data to characterize their performances.

The prevention of a bias produced by automated data processing still remains a challenge, requiring additional controls and vigilance when using automated analysis. The results of analysis methods involving machine learning have to be considered with care, as training a deep learning network still requires expertise and errors might falsify of possible findings. For this reason, benchmarking experiments combined with different controls are important steps to verify the validity of a machine learning based analysis. In the case of the Bayesian cluster analysis tool that was developed, the simulation of clustered cell membranes were used to determine the accuracy of the clustering algorithm. Through a GUI, a parallelized data-processing and the Bayesian engine, a freely available and user-friendly tool was generated. This lowers the hurdle to the usage of cluster analysis as a method to extract more information from SMLM data, as other clustering solutions are not necessarily focused on user-friendliness. The simulation module in the software also allows to make predictions on an experiment based on prior knowledge. The analysis is limited to SMLM data-sets from its nature. Extension of the analysis to data-types that are not lists of the single molecules positions will not be possible with BaClAva. The extension to 3D data-sets and 3D simulations might however be an interesting feature, as the 2D analysis limits the studied cell parts to flat surfaces such as the membrane. As BaClAva accounts for the localization precision, the reduced accuracy in localizing the axial position of molecules will reduce the accuracy of the analysis but still be possible. These possible extensions will have to be combined to new benchmarking experiments.

The data analysis led to the realization that pre-processing SMLM data-sets, as well as proper data-acquisition are crucial to the clustering endeavour. Many artefacts in SMLM reconstruction are affecting the cluster analysis, and especially clusters with low density compared to the background are challenging to discern. Newer methods such as DNA-PAINT or even the Fluorogenic version could help reduce the amount of unspecifically bound molecules. Methods such as PALM might also be advantageous due to the high specificity and the more predictable fluorescent emission events of the fluorophore. The cluster analysis can not perform miracles as the underlying sample preparation is paramount. By improving dyes, staining methods and buffer compositions, the sample preparation can be improved to substantially reduce undesired artefacts in the sample production step.

The increasing computational speeds and evolving clustering algorithms, especially through the support by machine learning [Wil+20], will further make a difference in this field of study.

4.3.3 Clustering biological proteins

In order to showcase the algorithm's validity on real data, three cellular receptors with different expected levels of molecule aggregation at the plasma membrane are imaged then cluster analysed. An omnipresent trans-membranes receptor that can be found in cancer cells is CD95. The ligand activation of this receptor results either in apoptosis or survival, making it a potentially promising study target for cancer therapy [MLW13]. Here, the receptor is studied in the T98G glioblastoma cell-line. As a member of the tumor necrosis factor receptors, CD95 is expected to aggregate on the membrane, also due to its signaling function [LJL20]. A certain clustering pattern should thus be observed for the CD95 receptor, that is compared to a positive and negative control.

Clathrin is involved in endocytic pathways regulating the abundance of certain proteins at the plasma membrane. Steps of clathrin mediated endocytosis can be visualized in fixed cells through the formation of clathrin coated pits (CCP). By staining for clathrin light chain (CLC), formation of CCPs and the local aggregation of clathrin can be reconstructed with dSTORM, providing a positive control for clustering behaviour of membrane molecules.

GPI-anchored (glycosylphosphatidylinositol) proteins are linked to the extracellular leaflet of the plasma membrane through a lipid anchor [PB08]. Because of its free diffusion and subsequent random distribution on the plasma membrane, aggregations of GPI should only be generated by physical hindrances or by coincidence. The clustering behaviour of GPI should thus be a good negative control, with local molecule aggregations corresponding to random distribution. Depending on the accuracy of the clustering algorithm and the density of a given protein on the plasma membrane, even randomly distributed proteins can form clusters to some extent.

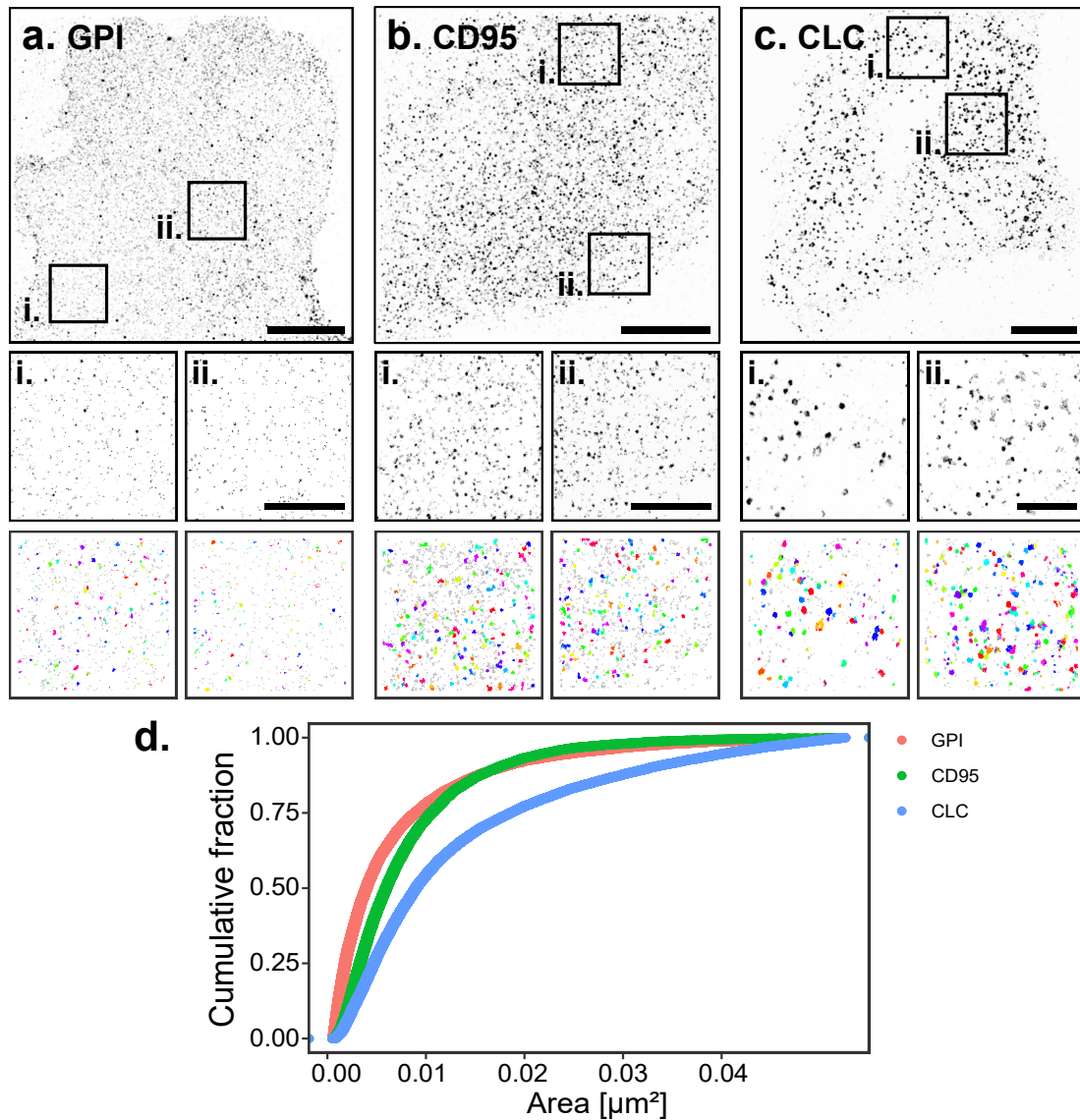


Fig. 4.4.: Clustering with BaClAva on biological samples. Three different membrane molecules, GPI **a** in CV-1 cells, CD95 **b** in T98G cells and CLC **c** in HeLa cells are stained with AF647 conjugated nanobodies and reconstructed. The reconstructions are divided into smaller ROIs (e.g. **i** and **ii**) which are analysed with BaClAva (images with coloured spots i.e. clusters). **d.** Cumulative fraction of the registered single molecules as a function of the cluster area. Scale bars in the large images represent $10\ \mu\text{m}$ and $3\ \mu\text{m}$ in the magnified ROIs. Modified from [Kut+21].

In figure 4.4, the clustering behaviour of different membrane receptors is compared. The SMLM images have been acquired using TIRF illumination. As the cell membranes lies flat on the cover-glass and the structures of interest do not have significant axial dimension, the use of TIRF reduces the sample background and ensures that the localizations originate from the plane of interest, improving the image quality. The *d*STORM reconstructions are first divided into smaller ROIs, which are then processed in BaClAva. The detected clusters in a few exemplary ROIs are displayed in the third row, the clusters having been assigned random colours. The cumulative area occupied by single molecules is plotted as

a function of the cluster area. The initial increase in the cumulative fraction represents the single molecules in the background, that have the localization precision of the SMLM localization as area. With increasing cluster area, the area occupied by clusters with the right size are added to the fraction. The shape of the cumulative fraction of cluster areas gives an estimate of the cluster sizes within the sample. The visual representation of the SMLM images in figure 4.4 already show differences in terms of clustering behaviour. To make these differences measurable, for each sample, 8 to 10 cells have been imaged with 5 to 8 ROIs extracted from each cell reconstruction.

The diverse biological pathways attributed to the CD95 receptor might be linked to different ligands. If the receptor is activated by the same ligand, the aggregation and conformation of CD95 at the membrane could be responsible for the different cell signaling pathways [LJL20]. The determining factors for the signaling pathways for CD95 have not been unveiled at a molecular level. Efficient activation of the receptor with its cognate ligand seems to induce apoptosis in cancer cells [Gül+19]. Studying the distribution of CD95 in sub-domains of the plasma membrane and investigating the changes induced by ligand activation could provide insights into the underlying mechanism inducing apoptosis. Preliminary experiments on the changes in clustering upon addition of the ligand did not yield a statistical difference in receptor clustering.

The algorithm has enough sensitivity to monitor density fluctuations on the plasma membrane. Methods such as PALM might improve the quality of the analysis, as the blinking behaviour is more predictable and the background reduced. A possible error source can also arise from artifacts [Bur+15] to which membrane molecules are especially prone to. In particular, the fixation method becomes relevant as it might introduce these errors [HS17]. Ideally the study of such clustering events is done in living cells to best demonstrate the aggregation process. However, live cell SMLM still remains challenging [Lel+21; Spe+21]. A possible extension of the analysis method and the experimental setting to cluster single particle tracking data would also be an useful alternative.

Materials and methods

5.1 Microscopy setups

In this chapter, the specifications of the microscopes used in this thesis are listed. A part of the microscopy data presented in this thesis has been acquired using a modified version of the home-built setup mentioned in [Alb+16a]. These changes are summarized in this section. As the low budget microscope is integral part of the results, the main methods involving the construction or alignment of the setup are presented here, while the general architecture, main modules and imaging results have been summarized in chapter 3. The data analysis steps, the used chemicals and protocols used for sample preparation are also presented in this chapter.

5.1.1 Low budget digital USB microscope

As a simple way to image various surfaces and cells, the Caimda microscope was used. The USB microscope can be used with any computer and even smartphones. Its compact size and low energy consumption allows to acquire image of objects or samples that would be difficult to do with regular microscopes. This kind of microscope matches the category of low budget instruments (about 20 €) that are perfect to inspire the general public to engage in microscopy and get involved in the research process. However, the quality of the detector as well as the challenging adaptability to certain key imaging modalities, such as fluorescence microscopy, are limiting its usage in life science imaging experiments. The use of a polychromatic camera is reducing the detection efficiency of the detector for a specific wavelength. Combined to the lack of spectral separation of fluorescence from excitation, quantitative image analysis is not feasible at useful scale ranges. Furthermore, controlling such an instrument is always linked to the treiber software that is delivered along with it. Circumventing the controlling software is possible but challenging. To summarize, this microscope is very practical, easily accessible and a good instrument to spark the enthusiasm of anybody interested in microscopy. On the other side, it also shows the limitations of low budget solutions and which challenges the setup developed in this thesis should be able to tackle.

5.1.2 Llama Setup: a home-built wide-field microscope

In this section, a home-built TIRF capable microscope with single molecule sensitivity is introduced, henceforth referred to as the Llama setup. The setup, as used in the experiments described in this thesis has been modified compared to its original design

[Alb+16a]. The defective AOTF (Acousto Optical Tunable Filter) was replaced with the same model with the corresponding MDS frequency generator of AA optics (AA Optics AOTFnc-400-650-TN S/N: 1001/350409). The frequencies for the different laser wavelengths have been calibrated. The set frequencies and powers are listed in table 5.1.

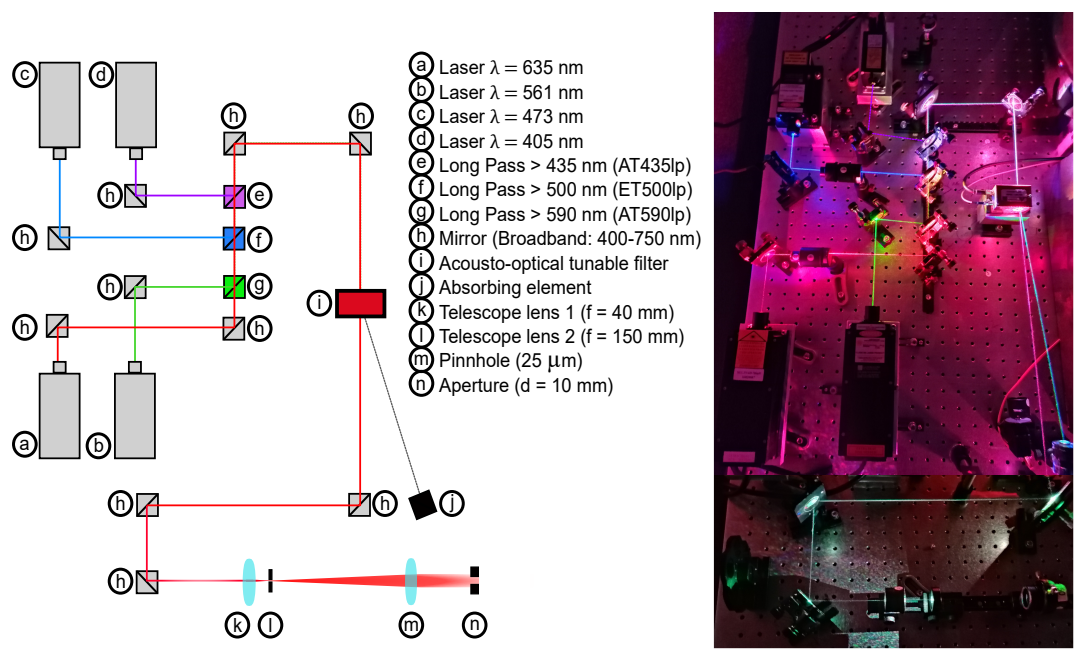


Fig. 5.1.: Schematic and corresponding photograph of the updated homebuilt wide-field microscopy setup. (Llama microscope) **Left:** Schematic of the illumination path, including a description of the optics used. **Right:** Photographic montage of the setup. Laser beams were made visible with a liquid air spray and long exposure times. The UV laser path has been drawn for visibility. The bottom part has all lasers superposed simultaneously for visibility purposes. Remaining parts of the setup were unchanged from the state in [Alb+16a] are a regular wide-field fluorescence setup, as schematically depicted in figure 1.4.

	Laser wavelength	AOTF frequency	AOTF power
	[nm]	[MHz]	[dB]
AAAOTF Channel 1	405	151.8	22.5
AAAOTF Channel 2	473	118.0	22.5
AAAOTF Channel 3	556	93.7	22.5
AAAOTF Channel 4	639	79.3	22.5

Tab. 5.1.: List of empirically set AOTF frequencies as set up in the micromanager file.

For simplified control of the driver, the AOTF channels were set up into a custom Micro-Manager (win. 64bit 1.4.23) file. This hardware control interface specialized in microscopy components was already being used for camera live display and image acquisition before the here mentioned changes. As the internally preset deflection frequencies do not all perfectly the laser wavelengths used in the setup, the optimal frequencies with the highest output in the laser path were empirically determined and set to the maximal output power. These values are set in the external mode of the AOTF with the AOTF tester, provided

with the instrument. These preset values are then set in MicroManager and can be used to adjust the laser intensity by a slide bar, inducing changes in the laser intensity exiting the AOTF for illumination.

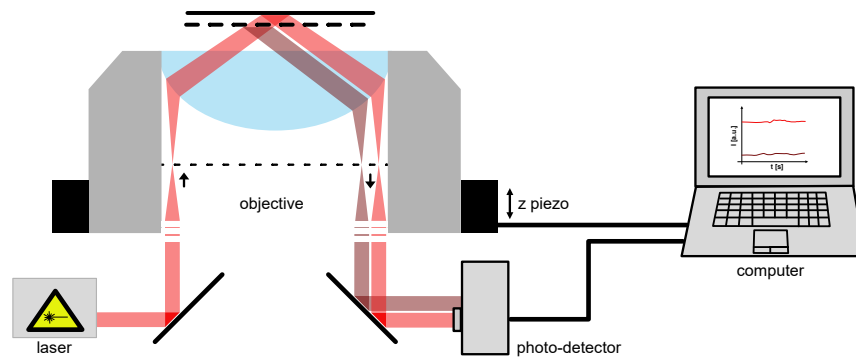


Fig. 5.2.: Schematic of the focus lock on the Llama wide-field microscopy setup. Laser light experiences total internal reflection at the cover-slip-sample interface. Reflected light intensity is measured at photo-detector. Changes in z induce changes of measured intensity by moving the beam position. The feedback loop aims to keep the z -position constant during experiments.

Additionally, the paths of the lasers have been altered to allow control over all laser wavelengths using the same platform. In the updated version of the setup, all laser intensities are controlled by the AOTF. The new setup is visualised in 5.1. As the lasers have a limited lifetime, three (red green and UV) of the ones shown in figure 5.1 are the replaced versions. Further changes have been brought to the spatial filter in order to have a more homogeneous illumination in the FOV. In the current setup the focal distances of the telescope lenses have been unchanged $f_1 = 40 \text{ mm}$ $f_2 = 150 \text{ mm}$ and the $d_{\text{pinhole}} = 25 \mu\text{m}$ was adapted for an optimal illumination intensity profile. The emission path of the setup is a conventional wide-field setup, similar to the one depicted in figure 1.4. The filters and other electronics are connected to a NI unit, a hardware interface that can be controlled with Labview. The whole system is stable and isolated from vibrations through an optical table (Newport), however drift is still present. An useful feature of the setup is the focus lock, which is also controlled with LabView and allows to keeps the distance between the objective and coverglass even for prolonged time periods. A low intensity far-red laser is introduced into the excitation path of the microscope. The angle of incidence of this beam in the objective is set to undergo total internal reflection at the cover-glass sample interface. The reflected beam is deflected from the emission path with a mirror. The reflections of the focus lock laser are adjusted to hit a simple photo-detector with a small surface when the objective is at a distance where the focal plane of interest is in focus. When the distance between objective and sample changes, or when drift modifies the focus, the focus lock laser beam is deflected, reducing the intensity measured on the detector. The Labview block diagram connects the Z-piezo of the objective with the intensity of the photo-detector. Through a feedback loop, the piezo positions the objective in order to maintain a constant value at the photo-detector.

Finally, for optimal camera settings, the gain of the EMCCD camera (delta 512 Photo-metrics) is calibrated on a weekly basis. The calibration process consists of closing the aperture in front of the camera chip and illuminating the camera chip with an intensity calibrated LED. The values measured by the camera at a specific gain value can thus be compared to the reference to correct the effect of the gain and keep a linear relationship between detected photons and digitally measured signal. Subsequent measurements have the intensity value corrected accordingly to the gain to minimize the signs of degradation of the camera chip and make imaging more reproducible.

5.1.3 Spinning disc

The used confocal microscope has a spinning disc unit (Yokogawa CSU-X1) combined to an Olympus IX71 body and 1.49 NA 60 × objective with different lasers and alternatively an Hg-Arclamp. An additional 1.2× magnification factor is set with the internal lens design microscope body. The image acquisition is done using an Orca flash 4.0 sCMOS detector with a 6.5 μm physical size and 90 nm measured output image pixel-size. The whole microscope is operated using the Metamorph software. The spinning disc, similarly to other confocal imaging devices, axially sections the sample to only collect photons emitted from a specific plane in the sample, thereby minimizing background. The spinning disc, instead of scanning the sample, has a micro-lens array disc designed in the shape of an Archimedes spiral, allowing to image several spots on the sample simultaneously. Through additional spinning of the disc, and the positioning of the micro-lenses, the whole FOV is scanned within the exposure time of the detector. A second disc containing the pinholes removes fluorescence from undesired axial emissions. The spinning disc thus has a speed advantage but produces similar image qualities to other confocal solutions.

5.1.4 Pixel sizes

Setup-objective combination	Pixel-size [nm]
Llama setup + Olympus (UPLAPO60XOHR) 1.49 NA 60x	96.2
UC2 setup + Olympus (UPLAPO60XOHR) 1.49 NA 60x	104.1
UC2 setup + Olympus (UAPON40XO340-2) 1.3 NA 40x	162.6
UC2 setup + Olympus (UPLXAPO20X) 0.8 NA 20x	319.4
UC2 setup + Olympus (LMPLFLN10XBD) PLN 0.25 NA 10x	661
SD setup + Olympus (UPLAPO60XOHR) 1.49 NA 60x (with 1.2x magn.)	90.3
SD setup + Olympus (UPLXAPO20X) 0.8 NA 20x (with 1.2x magn.)	273.1
UC2 setup + Optika N-Plan (M-169) 1.25 NA 100x	67.2
UC2 setup + Optika IOS N-Plan (M-166) 0.45 NA 20x	316.1

Tab. 5.2.: Pixel-size of the different objectives on different microscopes

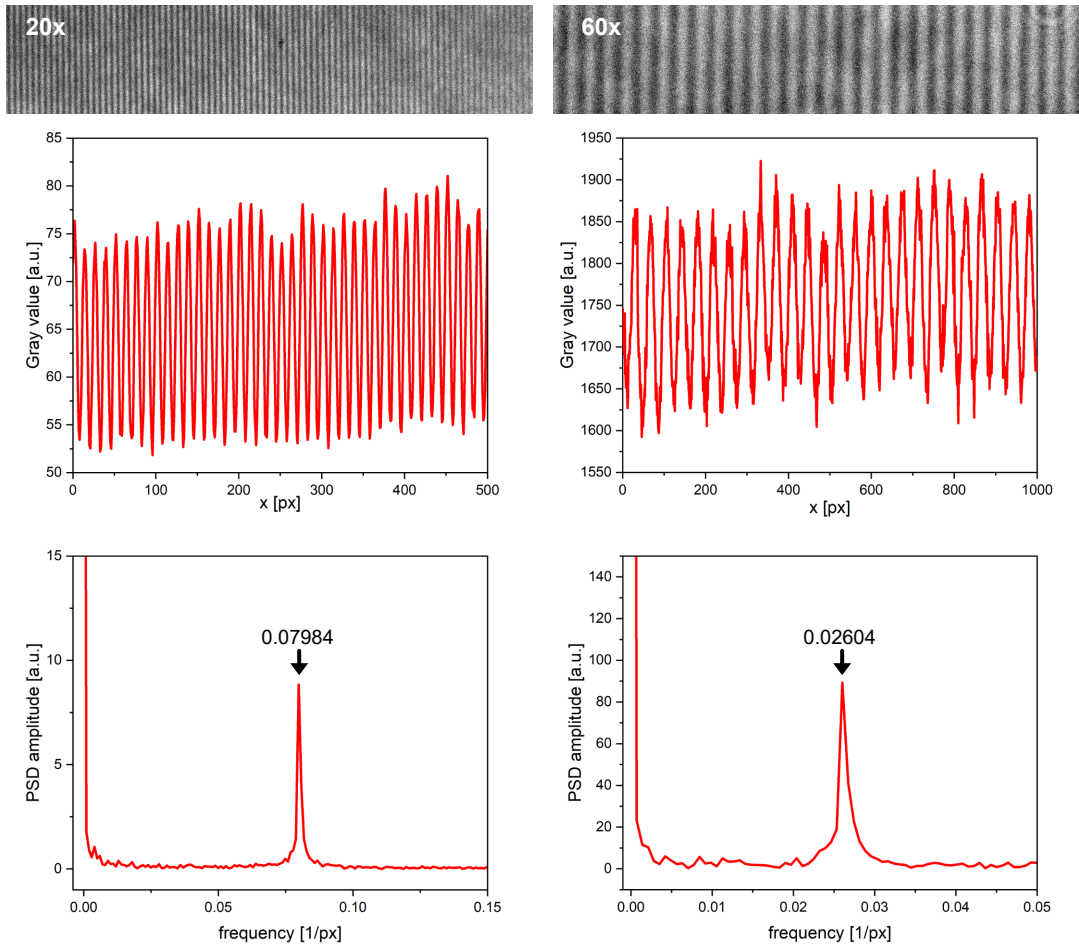


Fig. 5.3.: Measuring the pixel-size at the UC2 setup for the 20x and 60x objectives. **Top:** bright-field image of a calibration grid with $4\ \mu\text{m}$ lattice spacing for the 20x objective (left) and the 60x (right). **Middle:** Intensity profile across the grids. **Bottom:** Power spectral densities along the profiles. Peak values from which the pixel size is extrapolated are shown with arrows.

In order to use a microscope to perform quantitative studies, it is imperative to calibrate the instrumentation accordingly. The physical pixel-size of cameras is several μm large ($16\ \mu\text{m} \times 16\ \mu\text{m}$ for the Photometrics Evolve delta 512 EMCCD and $2.4\ \mu\text{m} \times 2.4\ \mu\text{m}$ for the Alvium 1800 U-158m CMOS), but with the magnification by the objective and other lenses, every camera pixel on the final image represents a smaller part in the field of view. The pixel size in the sample plane can be estimated by dividing the physical pixel-size by the magnification. To have a more precise estimation, a calibration grid with known lattice spacing ($4\ \mu\text{m}$) is placed along the X- or Y-axis of the microscope and imaged. The physical pixel-size is identical along both axes, the sample plane pixel-size should thus be identical along X and Y, if the optical path is not subjected to errors (e.g. astigmatism). From the acquired image the grid profile is extracted as a table of position-dependant grey values. The repetitive pattern is suitable for a Fast Fourier transformation (FFT) which allows to measure the repetition frequency of this pattern. The power spectral density of this FFT

will peak at the exact frequency of the lattice spacing. Using the known lattice spacing value of $4\ \mu\text{m}$, the pixel-size in $\mu\text{m}/px$ can be extrapolated.

This procedure has been followed for every microscope and objective used. The procedure is shown in figure 5.3 for the $20\times$ and $60\times$ objectives used on the UC2 setup. For all other combinations of objectives and microscopes, the same methodology was used to calibrated the pixel-size. An overview of all effective pixel-sizes (calculated according to 1.7.2) is shown in table 5.1.4.

5.2 3D design and printing

The modularity and adaptability of the UC2 toolbox is partly a result of the 3D printed parts it is using. On the UC2 GitHub repository, the CAD files for different mounts to adapt optics to the UC2 setup are provided, allowing to adapt most optical components to the system. Other components can be mounted by designing a custom adapter. The first step in the designing process is to measure out the size of the actual object [HC20]. Precise values can often be found in the technical drawings or in the specification sheets of an element. Then, the measured dimensions are used to design the 3D models. Computer Aided Design (CAD) software such as Autodesk tinkerCAD (for simpler shapes) and Autodesk Inventor Professional 2023 (for more complicated shapes and assembling pieces) are used to design an adapter. The finished designs can then be exported in common 3D model formats like *.obj* or *.stl* formats (also *3MF*, *STEP* and *AMF* but were not used in this project).

The 3D models are then loaded into Prusa-Slicer, the corresponding software of the manufacturer of the used 3D printer, in the case of this project: the Prusa i3 MK3S printer. In Prusa Slicer, file formats such as *.obj* or *.stl* amongst others can be imported and visualized as a 3D model on a virtual printing bed with accurate dimensions. The user chooses the printer model in the settings and selects the parameters accordingly. This includes the used printing plastic which have different characteristics, the corresponding temperature (specific for each plastic), the printing speed and quality, the support structures (printer can not print in the air), the percentage of infill of a bulky structure, and other parameters. These are all set according to ones requirements before the slicing procedure.

Finally, the 3D model can be sliced into a *.gcode* file format. This format is an instruction for the 3D printer to guide the nozzle, setting the order and the direction the filament is printed in, for every single layer. The filament can only be printed onto the heating bed or onto already printed filament structures, and the final model is always printed from bottom to the top (at least for a filament based printer). Support structures are added to support the printing of structure that cannot be printed upon an already printed filament. The support structure prevents gravity from altering the filament's shape with before hardening.

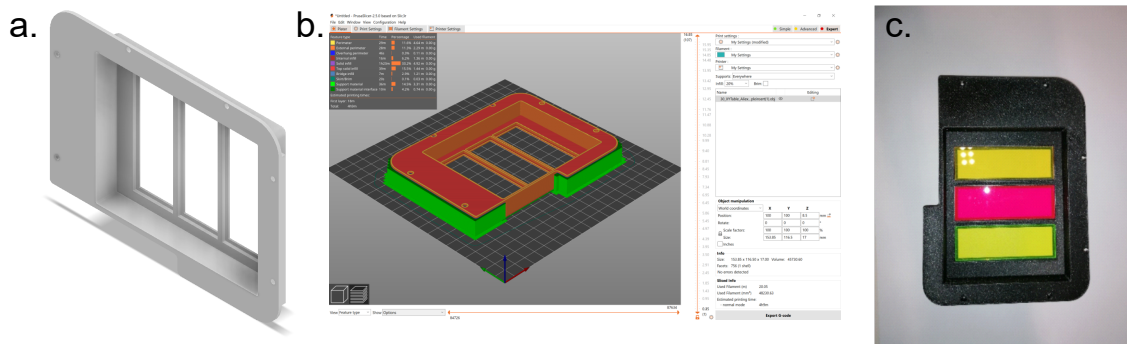


Fig. 5.4.: Steps in the creation of a 3D printed part i.e. a sample holder for rectangular sample chambers. **a.** 3D CAD of the sample holder as generated from a CAD program e.g. in *Autodesk Inventor 2023*. **b.** Design is imported into the *Prusa slicer* software. Parameters are chosen according to the requirements. Orange and red parts represent the object itself. Green parts are support structures. **c.** Final 3D-printed sample holder with fluorescent slides.

At the end of the printing process, supporting structures are removed before using the printed part. These finished parts can then be used in combination with optical elements, and implemented into an assembly structured by mold injected cubes. The main steps of this process are summarized in figure 5.4, starting with the CAD design and ending with the finished 3D component.

Screw threads and their counterparts are challenging to design and to print in high definition. However, the used plastic is soft enough to allow screws and other threads to be twisted into it and maintain a stable connection between the 3D-printed part and the screw/thread. This allows us to circumvent the thread printing and simplify different stability issues. The materials used for 3D printing are relatively soft and can be modified by drilling into them, or be deformed by heat of e.g. a soldering iron.

5.2.1 Printing quality

In this project, two kinds of filamentous plastics have been used to 3D-print materials. The PLA filament was chosen because it is a standard material in filament-based 3D prototyping. The ABS filament has adequate thermal characteristics that will be of use for imaging assays inside an incubator, more details are provided in section 3.3. The price of printed pieces can be estimated by the amount of filament used to print it, which can be calculated manually, or set-up in Prusa-Slicer. Components printed with PLA filament (Prusament) had an infill of 20-40%, a nozzle temperature of $T_{nozzle} = 215^{\circ} \text{C}$ and a bed temperature of $T_{bed} = 60^{\circ} \text{C}$ [Prub]. Components printed with ABS filament had an infill of 20-40%, a nozzle temperature of $T_{nozzle} = 255^{\circ} \text{C}$ and a bed temperature of $T_{bed} = 100^{\circ} \text{C}$ [Prua].

The whole UC2 concept relies on the use of cube structures with 3D printed mounts and parts to position the optics. This transfers stability the accuracy of positioning active optical elements onto the precision of the 3D printing. As the filament printing technology is most

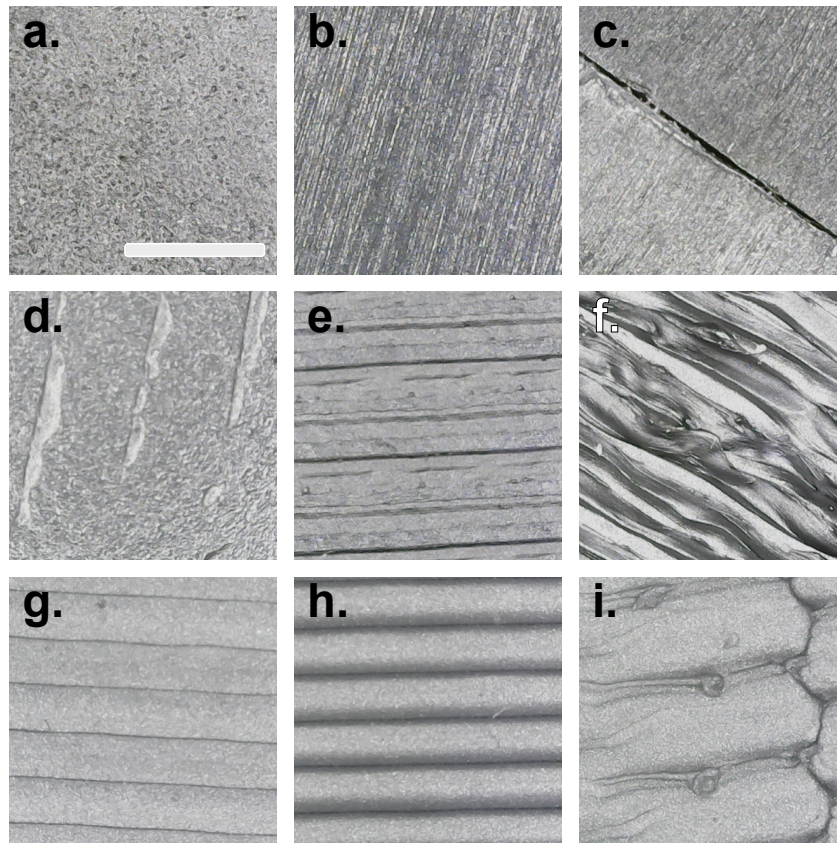


Fig. 5.5.: Quality of 3D printed materials surface. Surface of mold injected puzzle piece **a.** and of a mold injected cube **b.** as well as the junction between two cube parts **c.** Bottom surface **d.** (facing the printing bed) and top surface **e.** (any other surface of the 3D printed part) of a part printed with ABS filament. **f.** Surface of a 3D printed part with the ABS filament and too low temperature or too quick cooling due to inadequate conditions surrounding the printer. Surface facing the printing bed **g.** and final printing layer surface **h.** of a part printed with PLA filament. **i.** Printing error with the PLA filament due to inadequate thermal conditions surrounding the printer. All images have been acquired using the Cainda USB microscope (subsection 5.1.1). Scale bar displayed in **a** represents 1 mm.

widespread and comparatively affordable, the 3D parts described in this project have all been produced with a filament printer. The type of 3D printer is however not relevant, as long as certain quality standards are maintained. An empiric value for the precision of a 3D printed component in size compared to the CAD file is a manufacturing tolerance of 0.25 mm. In figure 5.5, the surfaces and possible printing errors for the filaments used in this project (PLA and ABS) are displayed. Parts displaying the printing errors, as displayed in figure 5.5 **h** and **i** should not be used within a setup. The types of material used depend on the thermal properties required by the experiment.

5.3 UC2 setup alignment

General alignment method: In order to adjust all optics, as far as possible, centering them according to the optical axis, an aperture is used. The laser is positioned to emit a

beam at half height of the cube. An aperture is positioned to match the intensity maximum of the laser. The laser spot is then aligned using the mirror mount to vertically exit the objective by monitoring the spots position on the ceiling. On a fluorescent surface sample, the position of the illumination can be seen, and the mirror in the detection path can be tilted to image the maximum of the laser spot on the center of the camera chip i.e. the FOV. Opening the aperture allows to give an estimate how centered the beam is.

5.3.1 Illumination

To have a centered top-light illumination when imaging samples in bright-field (BF), the illumination must be invariant in relation to the stage motion. As the whole XY-stage is moving in relation to the objective, the illumination has to be fixed at the base of the stage or at the microscope body in order to uncouple the motion of the stage from the illumination. This positioning allows to have the same illumination for all stage positions. The challenge in the current design is the strength of the BF imaging signal as most of the photons are blocked by the dichroic mirror as well as the emission filter. To overcome this filter specific challenge, the top-light illumination is done either with a high power white light emitting diode (LED) or an LED with an emission wavelength around $\lambda_{em} = 650 - 660$ nm. A schematic display of the BF illumination layout is given in 5.6.

The emission pathway of the microscope in its current design is limited to detect the fluorescence spectrum of far-red dyes (as given by the filter sets used, see figure 5.10). Additional channels can be implemented by using motors, or dichroic mirrors with different spectral properties. Far-red wavelengths seem to be best adapted for live cell imaging [Wäl+15; Ich+17; Sch+12b]. Simultaneously, the fluorophore AF647 is one amongst the most well studied, characterized and best performing in the context of SMLM. In the initial version, the choice of using a red laser (635 nm) is made. The filters and the sample preparations are made accordingly.

5.3.2 Bright-field illumination

The top-light illumination is connected to the microscope body to prevent illumination changes originating from stage movement. The 3D printed arm is prone to bending over time when used in the incubator. The distance to the sample can be kept fixed with another 3D printed part, but the design of the top illumination should be improved in the long term to e.g. adapt it to more controllable illumination such as DIC and Köhler illumination [Ros77; Neu20]. The high-power (3W) 650 nm Star LED (Cree) can also be replaced by a white LED, offering the possibility to image in three different colours (red, green and blue) with the same illumination source. The ImSwitch GUI is also equipped to control an array of LED lenses, as displayed in subsection A.1.2.

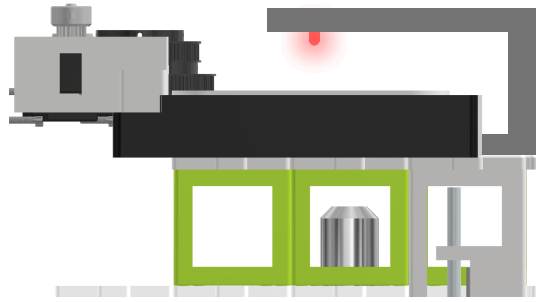


Fig. 5.6.: Top-light illumination of the UC2 setup. 3D-printed arm attached to the main body of the setup holds a high-power (3W) 650 nm Star LED (Cree).

5.3.3 Bright-field images background correction

The acquired bright-field images are not always homogeneously illuminated, as the position of the LED is not systematically centered to the optical axis of the objective, especially when changing the objective. The 3D printed holder for the top-light can not be attached to the XY-stage and is thus rather unstable. Its length is disadvantageous for keeping the light steady, especially when imaging inside a cell culture incubator. For this reason, and predominantly for high magnification imaging, the illumination can be subjected to uneven gradients in light intensity. Solutions could be to redesign the LED holder, possibly with a translation mount or directly improve the top-light into a Köhler illumination [Neu20], for optimal imaging. The here presented bright-field images are not used in quantitative studies, the illumination intensity correction steps are thus not affecting further analysis steps. The images that have been acquired with an uneven illumination can be corrected in different ways. As mentioned in table 5.4, the FIJI plugin "Plane Brightness Adjustment" [MČK11] was designed to tackle this problem. However, image artefacts can be introduced during this procedure, depending on the data-set. This motivated me to try another approach e.g. when background correcting the data-set presented in subsection 3.3.2. If a background image without any sample element on it is available, this one can simply be subtracted from the original image to get an image where only the structures of different contrast are present. A gray value corresponding to the average gray value of the original image is then added to the result to recreate the background of an even bright-field illumination. Both the operations can be achieved with the "Image calculator plus" on FIJI. If the background image is not available, the most out-of-focus image of a given sample can be used (alternatively also an in-focus one) for correction. With a rather linear gradient, filtering the image with a Gaussian blur allows to even out all possible structures from the image and obtain an image with the same illumination gradient, but with removed sample features. In order to remove the structures but not change the illumination gradient, suiting filtering parameters have to be used. Empirical values ranging from $\sigma = 15$ px to $\sigma = 25$ px have proven to work best.

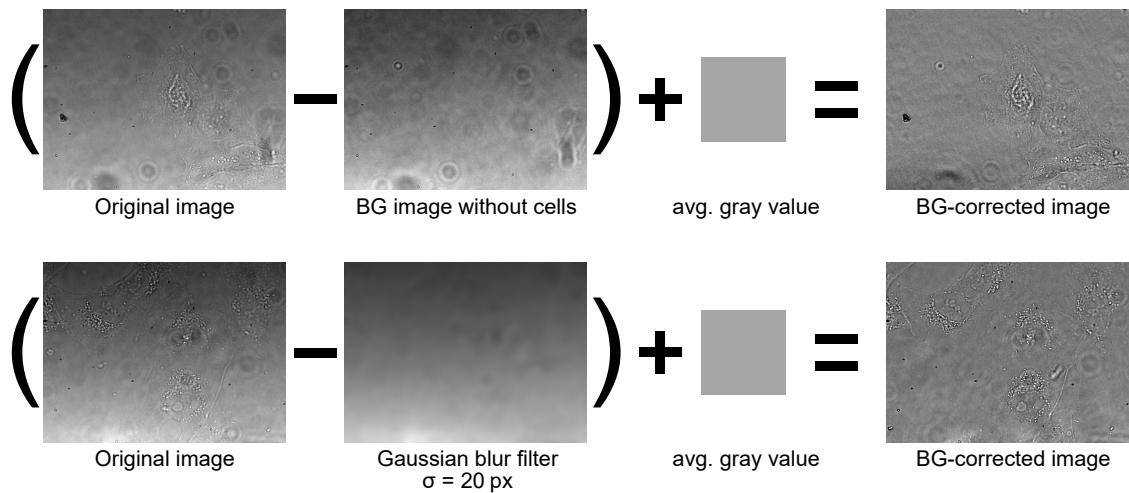


Fig. 5.7.: Background correction for bright-field images. Removal of background gradient through background image subtraction (**top**) and through filtered data-set image subtraction (**bottom**) with average gray value addition to obtain corrected image.

5.3.4 Laser and filters

The use of mirrors with a glass layer can cause the multiple reflection of light and interference effects. The mirrors used in the setup were thus replaced by coated surface mirrors (BB03-E02 Ø 25.4 mm Broadband Dielectric Mirror, 400-750 nm). Two methods have been chosen to characterize the laser illumination. The first one allows to monitor spatial fluctuations of laser intensity over the profile. The second method allows to measure the intensity distribution within a sample.

Characterising the laser profile

A $50\ \mu\text{m}$ wide pinhole (Thorlabs P25HK pinhole) is placed directly in front of the photometer (Thorlabs photometer PM00A with the Thorlabs S121C detector), which is screwed into a translational mount (Thorlabs ST1XY-S/M - XY translator with micrometer drive), allowing the detector to be moved across a given plane with around $5\text{-}10\ \mu\text{m}$ precision. The mount-pinhole-detector construct is placed at a defined distance from the laser and is shifted along the horizontal axis in steps of the same size range as the pinhole size, in this case $50\ \mu\text{m}$. Since the beam is expanded by the distance and the remaining optics that would be present in the setup have been removed, the information we can extract from the graph do not represent laser intensities that would reach the sample but rather a qualitative measure of how the laser intensity is distributed. This experiment can also give insights about the fluctuations of intensity and possible patterns that would illuminate the sample unevenly.

In figure 5.8, the measured laser profile is shown for the pure laser and the homogenized version, where a combination of a telescopic lens build (to magnify the beam), and a rotating cling foil (to diffuse the beam profile) are used [Ma+17]. The cling foil is a low

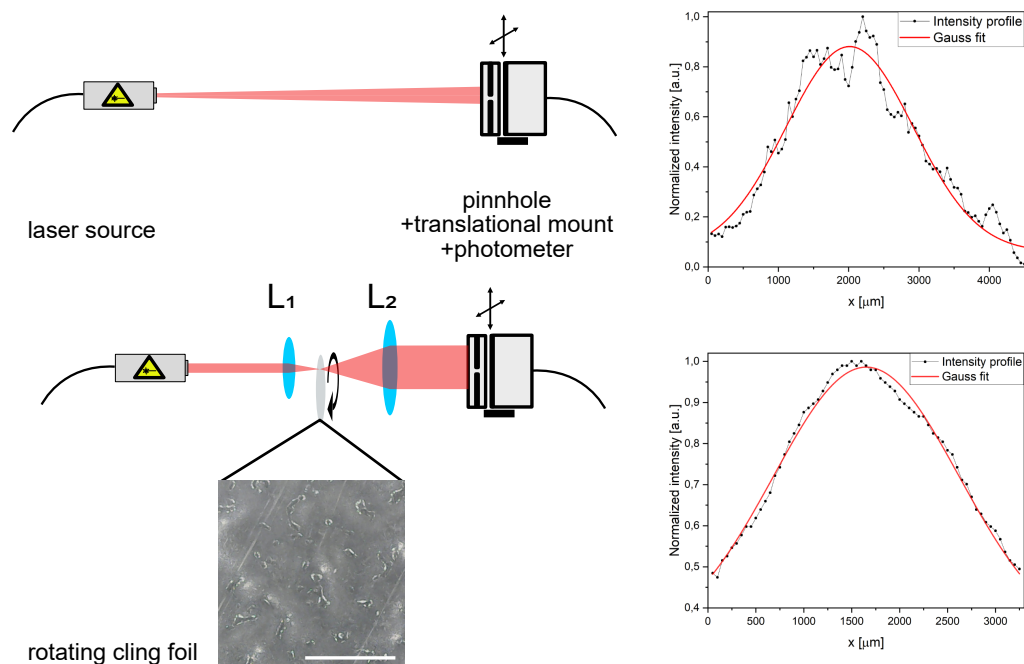


Fig. 5.8.: Laser profile characterisation. Photometer is equipped with a pinhole and a translational mount. The laser profile is measured in steps corresponding to the pinhole size. **Top:** pure laser profile. **Bottom:** Laser is magnified by telescope build and homogenized by rotating cling foil at focal distance of both lenses. Cling foil surface is imaged with Caimda microscope (subsection 5.1.1). Scale bar is 1 mm.

budget and very available alternative to a diffuser. The resulting laser pattern is very close to a Gaussian and can thus be used for assays requiring a homogeneous illumination across the entire FOV.

Using a spatial filter, similar to the one described in sub-section 5.1.2, to optimize the laser beam profile would be a cheap and elegant solution. The precision with which the laser beam can be positioned is at the limit where it would still be possible, but challenging as it would not be feasible with only one mirror. A second mirror could be added to the ray path but would also introduce a supplementary degree of freedom, raising the question if the the system is stable enough to prevent mechanical motions in the μm range over prolonged time periods. Additionally, the final output laser intensity could be reduced as a result of misalignment and drift. For this reason the spatial filter has not been implemented into the setup. Another possible approach would be to use a laser that is coupled to a fiber by the manufacturer. Different optimizations in terms of hardware upgrade will be discussed more in the section 3.7. As a comparison, the laser profile of a single mode laser as well as the profile of a laser cleaned with a spatial filter are shown in figure A.1 in the Appendix. The core fiber of a single mode optical fiber is typically a few microns thick, thus only allowing the propagation of the TEM_{00} mode through the fiber thus giving a pure laser profile (Gaussian). The same laser cleaning procedure can be achieved with a spatial filter, as is used for the Llama microscope in section 5.1.2. The spatial filter combines

a telescopic lens set with a pinhole. The requirement is that the size of the pinhole is adjusted to match the NA of the lens.

Sample illumination pattern

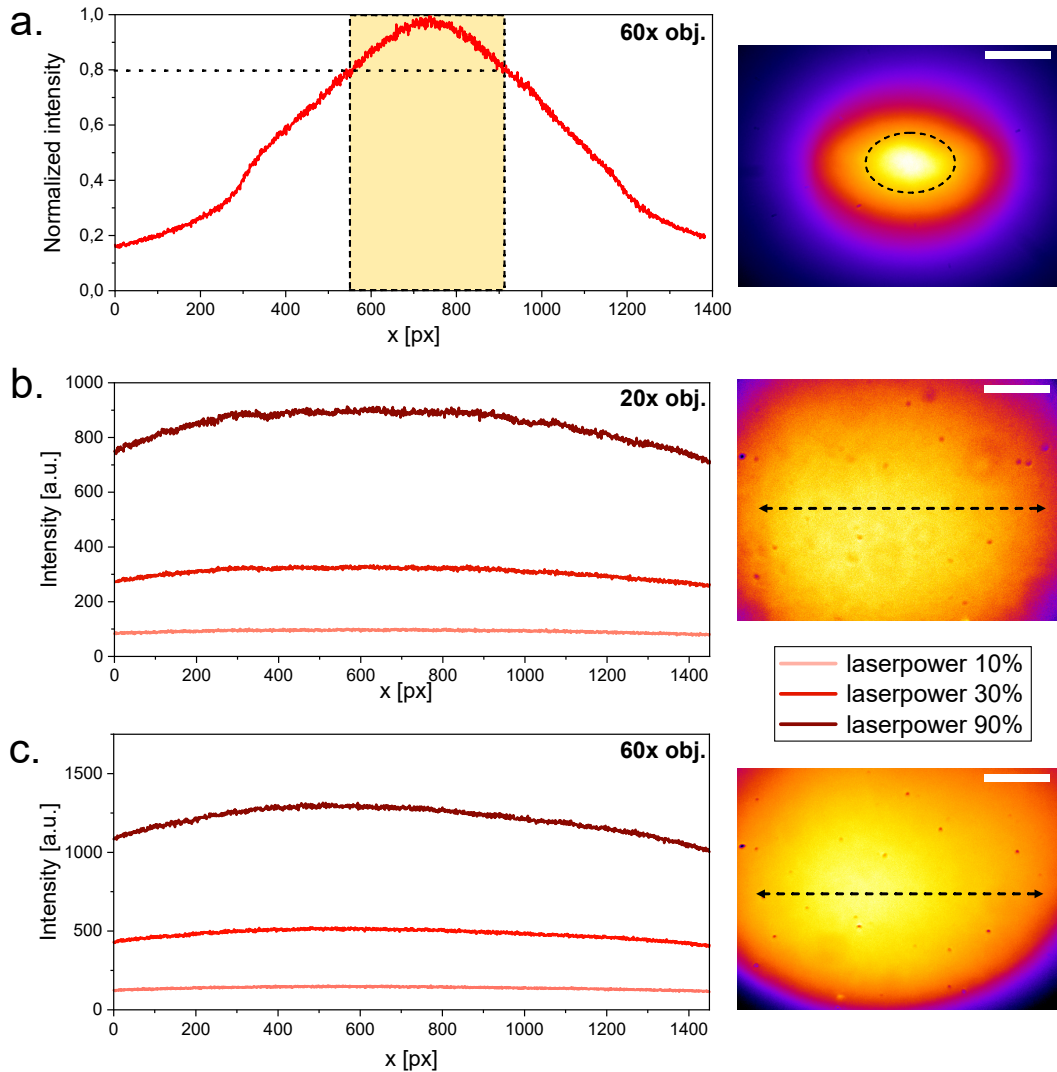


Fig. 5.9.: Different sample illumination modalities measured with a red fluorescent slide. Illumination profile of a Chroma red fluorescent slide, of a laser broadened and homogenised with a telescope lens and a rotating cling foil, with a $20\times$ Olympus objective **a.** and with a $60\times$ Olympus objective **b.**, the corresponding horizontal intensity profile across the camera chip being indicated on the right images. **c.** Laser illumination pattern on Chroma red fluorescent slide with the $60\times$ Olympus objective. Ellipse on the right image represents the ROI where the laser intensity varies by less than 20% of the maximum. Scale bars on the right images respectively represent $30\ \mu\text{m}$ in **a.** and **b.**, and $90\ \mu\text{m}$ in **c.**

The actual laser profile in a sample, when all elements are implemented in the microscope can be analysed by illuminating and imaging an even surface fluorescent slide. Here in figure 5.9, the fluorescence of a red Chroma slide is acquired to monitor the intensity distribution. The focus is set on some dirt particles and scratches at the surface. Drawback

with this method is that the fluorescence is coming from different planes, and filtering fluorescence according to the axial position is challenging, but possible, with methods such as multi-focus microscopy[Abr+13].

We can clearly identify that the the telescope diffuser combination improves the illumination of the FOV with variations in illumination intensities of less than 25% within the FOV. The option without filter however is still interesting as the application of SMLM techniques or others relies on higher illumination densities. The necessary laser density to do *d*STORM is in the range of kW/cm² [Lel+21], and higher densities can increase the speed of the experiment as well as the precision of the localizations.

$$0.8 \times \int_0^\infty \frac{\pi\sigma_x}{2} \exp\left[-\frac{1}{2}\left(\frac{x-x_c}{\sigma_x}\right)^2\right] dx \leq \int_0^a \frac{\pi\sigma_x}{2} \exp\left[-\frac{1}{2}\left(\frac{x-x_c}{\sigma_x}\right)^2\right] dx \quad (5.1)$$

In equation 5.1, an approximation of the usable part of the laser profile is calculated, under the assumption the intensity of the given profile follows a Gaussian distribution. With an empirical requirement that the laser intensity should not vary more than 20% of the maximal intensity, the usable part of the Gaussian represents about 20% of the total integral of the laser intensity. This criterion is challenging to maintain as the resulting FOV is very small. As the laser profile is not symmetric/homogen in its lateral and vertical shape, the region of interest (ROI) for SMLM imaging is approximated with an ellipse matching the region with highest laser intensity, as measured in images of the fluorescence emitted by a fluorescent slide. The usable FOV for SMLM reconstruction is thus limited to about one fifth of the complete chip, as shown in the figure 5.9 a. The illumination density in the whole FOV for the 60 × 1.49 NA objective reaches up to 90 W/cm². When removing the homogenizer and the telescope lens, the maximal laser power reaches 520 W/cm² over the FOV, and can be increased to 970 W/cm² when only looking at the region where the intensity matches the value set in equation 5.1.

Filters

First tests with the low budget laser have shown interference patterns on the images acquired with the camera. After changing to mirrors without glass layer on top to rule out multiple refraction, and making sure the 3D printed materials are not influencing the experiments with fluorescence, the remaining possible source of these patterns was the laser. These light patterns can be diffused and spread over a larger surface with a diffuser, to reduce the pattern intensity. However, the image quality was still not good enough. Additionally, the diffuser reduces the laser density which is needed for applications requiring high laser densities (> 1 kW/cm²) such as SMLM. By looking at the laser spectrum, emissions in similar wavelengths to the fluorescence emitted by far red dyes could be observed. The use of an excitation filter is not desirable in order to remain cost effective but is necessary to achieve the necessary image quality. Additionally, the emission filter could not be changed in such a way that the undesired emissions are

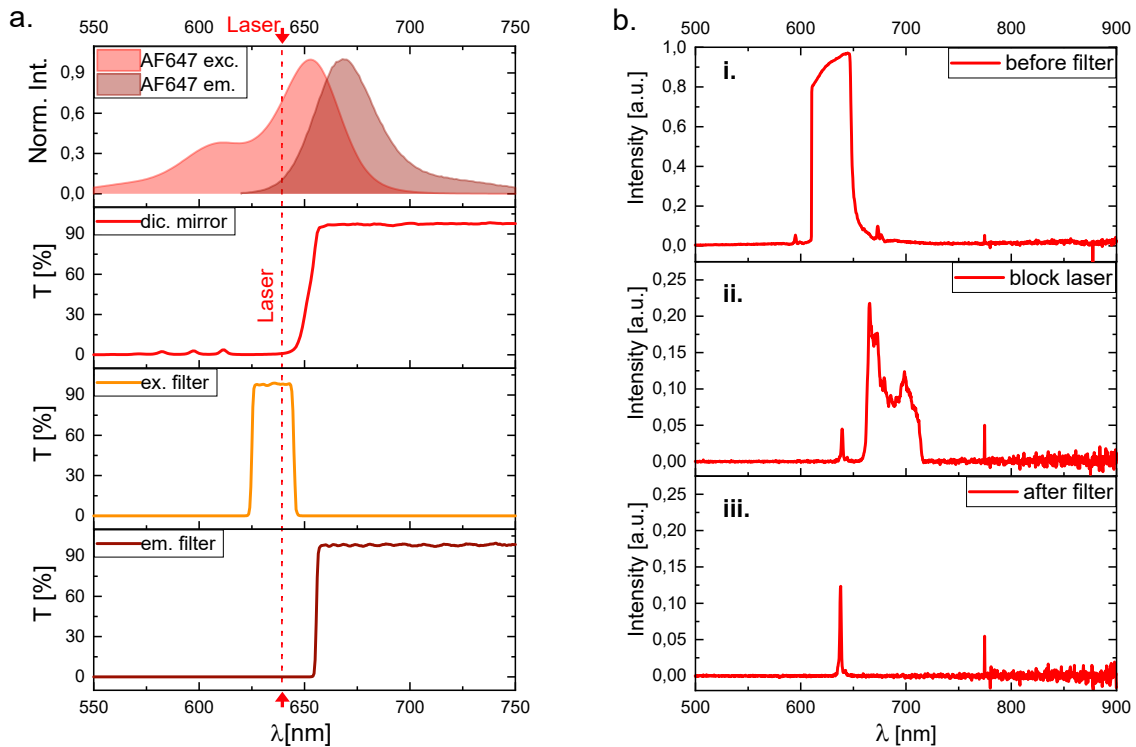


Fig. 5.10.: UC2-setup filter cube and laser spectral characteristics **a.** Spectral characteristics of AF647 and the transmission T of used filters (purchased from Chroma [Chr16]). From top to bottom: 1. the AF647 excitation (*exc.*) and emission (*em.*) spectra; 2. the dichromatic (*dic.*) mirror (Chroma ZT640rdc BS); 3. the excitation (*ex.*) filter (Chroma ZET635/20x EX); 4. the emission (*em.*) filter (Chroma ET655lp EM). The laser wavelength is marked with a dotted line at around 639 nm. **b.** Laser emission spectrum measured with a spectrometer, under different filtering conditions. **i.** Spectrum of the laser as measured at the sample plane (over-saturation at the laser wavelength). **ii.** Spectrum of the laser with main emission wavelength blocked by a filter. Residual emissions in the expected fluorescence wavelength range are observed. **iii.** Laser spectrum at the sample with main laser emission-line blocked by a filter and residual emissions removed by the excitation filter.

blocked, since these are in a similar spectral range to the desired fluorescence. The setup thus has an excitation filter (filter specs) additionally to the emission filter (specs) and the dichroic mirror (specs). As coating technologies get cheaper and constantly improve in efficiency, the additional expenses might be reduced in the future.

A possible alternative simplifying the building as well as the handling of the setup is to use a laser which is already coupled to a single mode fiber. This way, the profile is homogeneous, the optical build is simpler and less prone to errors. Eventual inhomogeneities can be removed by shaking the fiber [Lam+22]. Another interesting feature of using fibers is that different lasers with different wavelengths can be coupled to the same fiber. A low-budget fiber-coupled laser was tested and used in this project. The cube with the laser was replaced with a cube holder the fiber end. a $f = 50$ mm lens is placed at 50 mm from the output to collect parallelize the divergent light from the fiber. In the appendix

figure A.1, the profile of the laser has been characterized using the same methodology as in section 5.3.4.

5.3.5 Illumination schemes

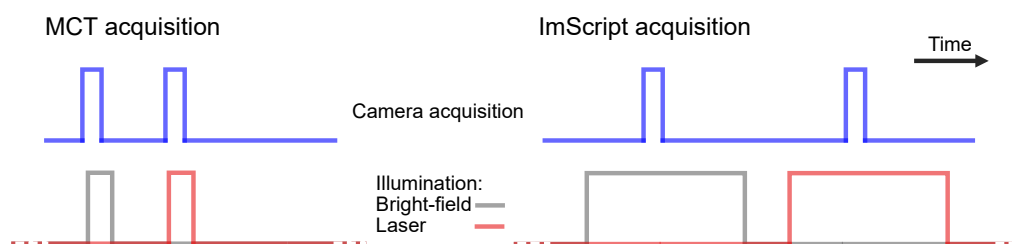


Fig. 5.11.: MCT and ImScript acquisition patterns. ImScript is slower in controlling laser and LED, resulting in longer illumination times.

The slower response of the hardware when using ImScript for acquisition results in waiting times to turn the illumination On/Off. The MCT on the contrary switches much faster, resulting in illumination times barely longer than the acquisition time. The use of the MCT is thus recommended in order to reduce photo-damage during long term live-cell imaging assays. The illumination of the sample can be reduced by a factor of $40 \times$ using the MCT. A challenge is still that short disruptions in the scheme might shift the illumination window, effectively affecting the fluorescence intensity in the acquired image.

5.4 Software and hardware

5.4.1 Software

In this section, the software and plugins used in the thesis are listed. Except for the control of the already established microscopes in the lab, an effort has been made to try to use as many openly or freely available software as possible.

Purpose	Used software
CAD for 3D printed part design	Autodesk tinkerCAD Autodesk inventor 2023
Slicing and g-code generation for 3D printing	Prusa Slicer
Simulations of SMLM data-sets	FluoSIM, Self-written R-script
Hardware control Llama setup	Micro Manager (win 64bit 1.4.23) Labview 2015
Data acquisition and hardware control on SD	Metamorph
Data acquisition and hardware control on UC2	Python based ImSwitch, Vimba Viewer

Electronics design	Fritzing v. 0.9.10
Hardware control UC2 microscope	Arduino IDE 2.0.4
Image processing and data analysis	Fiji, Origin Pro 2023, python 3.8 scripts, Cell Profiler, CellPose
SMLM reconstruction	Matlab 2018a (SMAP 2020) Fiji Win64bit (java 8) (ThunderSTORM)
Different clustering analysis steps	BaClava
Illustrations and figure design	Affinity designer
Thesis writing	L ^A T _E X

Tab. 5.3.: Software used for different tasks in this thesis.

5.4.2 Fiji plugins

Image processing/analysis	ImageJ plugin & corresponding Reference
Single particle tracking	Trackmate [Tin+17] Mosaic [SK05]
Handling .hdf5 files	hdf5 vibez [Rue+]; N5 [Saa+22] Bigdataviewer [Pie+15]
SMLM analysis and reconstruction	ThunderSTORM [Ove+14]
Batch SMLM processing	NeuroCytoLab ChrisTORM batch processing [Let]
Fourier ring correlation	Fourier Ring Correlation ImageJ Plugin [Nie+13] NanoJ Squirrel FRC [Cul+18]
Stitching and tiling	Grid/collection stitching [PST09]
Quantifying segmented objects	MorphoLibJ [LAA16]
Plane brightness adjustment & Stack contrast adjustment	Brightness and contrast adjustment plugin [MČK11]

Tab. 5.4.: Fiji plugins used in this thesis.

ImageJ [SRE12] and FIJI [Sch+12a] are very powerful tools to analyse, process, quantify and visualize microscopy images or data. In this project different plugins have been used to perform the presented analysis. This comprises handling certain data types such as *.hdf5*, batch processing of different plugins, different types of single molecule localization data analysis methods [Lin19], correlation and other image processing plugins. In table 5.4, the different ImageJ/Fiji plugins and scrips used in this thesis are listed. The corresponding sources for the codes or the publications can be found in the bibliography.

5.4.3 Hardware and computers

Computer name	Specifications
Machine learning 1	Operating system: 64-bit windows 10 pro; Processor: Intel(R) Xeon(R) W-2295 CPU @ 3.00GHz; RAM: 64 GB; Graphics card: NVIDIA GeForce RTX 2080 Ti
Personal computer AZ	Operating system: 64-bit windows 10 pro; Processor: Intel(R) Core(TM) i7-4960HQ CPU @ 2.60GHz; RAM: 16 GB; Graphics card: NVIDIA GeForce GT 750M
Ubuntu2020 Analysis	Operating system: 64-bit Ubuntu 20.04.3 LTS GNOME 3.36.8; Processor: 20x Intel® Xeon(R) Silver 4210 CPU @ 2.20 GHZ; RAM:: 125.5 GB; Graphics card: NVIDIA GeForce RTX 2080 Ti

Tab. 5.5.: List of the different computers used in this thesis, including their specifications.

In this section, the used hardware i.e. for the computers, the specifications are mentioned. Indeed, many of the applications and the codes used, partly have a very high demand in computational resources [Kut+21] and corresponding GitHub repository [KS]. The general consensus is to keep the complete analysis simple enough that no special CPU or GPU is needed to repeat the analysis steps presented here. The used hardware is listed in table 5.5 is over average both in GPU and CPU capabilities. Many steps would only take longer on less powerful computers, but the feasibility of every step is possible on a normal computer.

5.4.4 UC2 wide-field microscope materials and parts

In table 5.6, the different repositories needed to access the documentation, the software, the CAD designs, the flashing tool and much more are listed. The whole setup is reproducible using the GitHub repositories, a 3D printer and by buying the last necessary optics and electronics.

Repositories	Link
General openUC2	https://github.com/openUC2/
This setup / UC.STORM	https://github.com/openUC2/UC2-STORM-and-Fluorescence
ImSwitch (UC2 specific)	https://github.com/openUC2/ImSwitch/
UC2-Rest	https://github.com/openUC2/UC2-REST
ESP32	https://github.com/youseetoo/uc2-esp32
Online flashing tool ESP32	https://youseetoo.github.io/

Tab. 5.6.: Repositories and corresponding links of the different aspects of the microscope.

The UC2 microscope presented in chapter 3 is composed of different pieces that have either been designed and printed or bought. In table 5.7, all pieces built into the microscope are listed including their prices. The prices of the 3D printed parts have been estimated according to the used amount of filament and the filament price for PLA/ABS. The price of the different components can vary depending on the produced quantity (for the cubes and puzzles), the purchasing quantity. The prices may also vary over time, the prices listed in table 5.7 are presented as indication. An additional expense that has not been listed here is the price of the objective, which can vary between $> \text{€}10'000$ for the high-quality ones and as low as $\approx \text{€}200$ for a low-budget $20 \times$ one.

Origin	Part name	Quantity	PPU	Price
openUC2	openUC2 IM Cube	42	€5	€210
openUC2	UC2 Puzzle piece	26	€5	€130
UC2 (3D print)	UC2 objective mount linear stage	1	€1	€1
UC2 (3D print)	Linear stage spacer	1	€1	€1
UC2 (3D print)	UC2 insert for kinematic mirror part1	3	€5	€15
UC2 (3D print)	UC2 insert for kinematic mirror part2	3	€1	€3
UC2 (3D print)	Adapter for nut	9	€1	€9
UC2 (3D print)	UC2 insert for 1" Mirror, 45°	3	€5	€15
UC2 (3D print)	UC2 cube insert C-mount v3	1	€5	€5
UC2 (3D print)	UC2 insert for Thorlabs cage	2	€5	€10
UC2 (3D print)	UC2 Insert for Thorlabs 1" lens	2	€5	€10
UC2 (3D print)	UC2 Filter-mount	1	€5	€5
UC2 (3D print)	UC2 insert for Allied Vision camera	1	€7	€7
UC2 (3D print)	Motor-mount for X-Y stage	1	€7	€7
UC2 (3D print)	Sample Inset for X-Y Stage	1	€7	€7
UC2 (3D print)	Timing gear small	1	€2	€2
UC2 (3D print)	Timing gear large	1	€2	€2
UC2 (3D print)	Printed timing belt long	1	€5	€5
UC2 (3D print)	Printed timing belt short	1	€5	€5

Origin	Part name	Quantity	PPU	Price
UC2 (3D print)	Holder for LED array	1	€5	€5
Würth	DIN 912 - M3×0.5×12×10.75	15	€1	€15
Thorlabs	Thorlabs PF 10-03-P01	3	€25	€75
Thorlabs	Thorlabs AC254-050-A-ML	2	€100	€200
Thorlabs	Thorlabs CP33	2	€20	€40
Robotics kit	GT2 Pulley 16 teeth 4 mm perforation for 6 mm timing belts	2	€2	€4
Supermagnete	5 mm Neodym magnets	9	€0.40	€3.6
Euromex	Euromex mechanical 180×155 mm ob- ject table with integrated 75×55 mm X-Y-translation stage, NZ.9505	1	€200	€200
Alibaba	Linear Stage 50 mm, Nema 12, MGN9h	1	€50	€50
Adafruit	Adafruit 64 LED array (8×8)	1	€20	20
Allied Vision	Alvium USB 3.1 camera 1800 U-158m, 1.58 MP, C-Mount, monochrom	1	€445	€445
Laserlands.net	638 nm red laser module 500 mW round dot focusable TTL 3050	1	€40	€40
Chroma	Chroma ET655 filter	1	€250	€250
Chroma	Chroma ZET 636 filter	1	€250	€250
Chroma	Chroma ZT640 filter	1	€250	€250
Total				≈ €2300

Tab. 5.7.: List of pieces and prices for building the UC2 setup. (PPU = price per unit)

5.5 Data processing

5.5.1 SMLM data analysis settings and camera parameters

Analysis with SMAP

Parameters read-out from metadata: The acquisition of *.tiff* files with *Micro-manager* provides a metadata file which lists all parameters of the measurement such as the number of frames, the dimensions of the image, the set laser intensity, the used camera parameters and more. The reconstruction with SMAP extracts parameters such as the electron multiplier gain (set to 300 ×) and the conversion factor (from ADU to photons) (6.7 according to camera manufacturer specification sheet) from the metadata for the analysis. These parameters can also be entered manually if needed.

Analysis settings: During the fitting procedure the minimal distance between two single molecules where both can still individually be fitted was set to 7 pixels. The PSF is fitted

using a differential of Gauss filter with $\sigma = 1.3$ and *dynamicfactor* = 1.7 with the option of free PSF fitting. These parameters have proven to be suitable for our experiment and have been implemented into the *fitfastsimple* workflow.

Filtering parameters: SMAP also has the option to filter the obtained reconstruction according to various parameters. This includes the frame number, the localization intensity, the localization precision and many more. The localization precision has been limited to below 35 nm (matching grouping *dx*). All other parameters have been adapted to the given experiments, aiming to exclude extreme values.

Grouping localizations: After the reconstruction with SMAP, the localization data can further be processed. The grouping procedure accounts for multiple localizations of the same fluorophore in subsequent frames. This prevents large signal disparities in the reconstructed images, originating from longer cycling times in the ON state of certain fluorophores. Two parameters are decisive for this filtering feature. The first one is $dT = 2$, the number of frames a fluorophore can be non-fluorescent but still associated to the same single molecule. The second one is $dx = 35$ nm, the distance a localization centroid can be shifted within two subsequent frames and yet associated to the same single molecule.

Drift correction with cross-correlation: The drift correction has fiducial marker and cross-correlation as options. The first one uses the localization of a bead to subtract sample displacement in a given frame compared to the initial position. The second method uses the method summarized in 1.9.8 to reconstruct temporal subsets of the final image and compares their shape over time to account for sample displacement. Drift correction, grouping and exporting the localization table as well as the reconstructed images have serially been done for every reconstruction.

Batch processing: The localization, reconstruction, grouping, drift-correction and export procedure can also be done in batch, simply by using the batch processing widget in *SMAP* and implementing the desired operations.

Analysis with ThunderSTORM

Analysis settings: ThunderSTORM [Ove+14] analysis is done by loading the camera parameters accordingly. Values for photo-electrons per A/D count as well as base A/D level counts are extracted from the camera specification sheet. Filtering the image is achieved with a Difference-of-Gaussian (DoG) filter with $\sigma_1 = 1.3$ px, $\sigma_2 = 1.8$ px. Different functions have been tried out but did not seem to have a noticeable effect on the final image. To keep the analysis continuous with both plugins the 'DoG' filter was used in both cases. Approximate localization of molecules uses the 'local maximum' method, the 'std(Wave.F1)' as Peak intensity threshold and '8-neighborhood' connectivity. The PSF dimensions are magnified by a factor of 1.66 when using the $100\times$ objective, as signals are both diffraction limited, with both objectives. The σ values are thus adapted ($\sigma_1 = 2.2$ px, $\sigma_2 = 3.3$ px). Sub-pixel localization of molecules uses the 'PSF: Integrated Gaussian' method. Fitting

radius was set to 3 px with Maximum likelihood estimation as fitting method. Initial sigma was set to 1.3 px. Multi-emitter fitting was deactivated, as comparative analysis did not show significant differences under identical experimental conditions when activated.

Grouping and filtering: The ImageJ plugin ThunderSTORM offers options for the post-processing of SMLM reconstruction images or localization files. These allow to filter out certain localizations based on their properties. The first widget is a general filtering of all parameters listed in the localization table. Simple commands allow to filter out localizations with specific features.

```
1 intensity < 1000 & intensity > 100000  
2 sigma > 50
```

Similarly to SMAP, a widget named 'merging' allows to group localizations from the same molecule in subsequent frames into one localization. The maximum distance was set to 35 nm as already used in SMAP, the maximum number of off frames being two. The 'remove duplicates' widget removes molecules that converged to the same position. In the analysed images in this project, it was not used as it is mostly useful to complement the multi-emitter fitting analysis. The 'density filters' widget was not used during the analysis.

Drift correction: The drift correction options in ThunderSTORM are the same as the ones presented in SMAP. In the analyzed images in this project, the standard drift correction method used was cross-correlation. Fiducial markers improve the drift correction, regardless of the chosen correction method.

Batch processing: The batch processing in ThunderSTORM can be done using another plugin relying on it. The ChriSTORM plugin [Let] allows to batch reconstruct raw data or import and visualize localization files.

Reconstruction: The reconstruction is visualized using the average shifted histogram method (Magnification: 25 x & lateral shifts: 3). Alternatively, the normalized Gaussian can be used (Magnification: 25 x & lateral uncertainty: 10 nm).

5.5.2 CellProfiler pipeline

The batch processing of a large data-set of images can be automated using tools such as CellProfiler [Car+06]. The pipeline used in this project is a very basic one using five modules. The first one, "IdentifyPrimaryObjects", identifies and segments the nuclei. The object diameter has been set to be between 25 to 70. Objects above and below this size range are discarded, as well as objects at the borders of the image. Threshold strategy was chosen adaptive with an adaptive window of 100 px. The chosen thresholding method is "Minimum Cross-entropy", with a smoothing scale of 1.5 and a correction factor of 1.4. Lower and upper bounds on threshold were kept to 0 and 1. The Method to distinguish clumped objects as well as the method to draw dividing lines between clumped objects

are both based on intensity. The hole filling in identified objects has been set to "After declump"ping only". The other parameters have been kept to default. The second module "MeasureObjectIntensity" and the third one "MeasureObjectSizeShape" are quantifying size and shape of the objects identified in the first module. The last two modules: "SaveImages" and "SaveToSpreadsheets" are saving the images of the segmented objects and measured features of every object in every image into a table as a .csv file.

5.5.3 CellPose pipeline

The SMLM images of CCP in HeLa cells were divided into smaller ROIs (max. $5 \times 5 \mu\text{m}$), and are fed into the analysis pipeline. This was done by loading the data e.g. onto a Google drive and setting the according links in the Colab notebook. Selected parameters were Data_type: "Single_Images"; model_choice: "Cytoplasm"; Channel_to_segment: "Grayscale"; Nuclear_channel: "None"; Object_diameter: "150"; Flow_threshold: "2.2"; mask_threshold: "-2". The masks of around 60 images from 10 SMLM reconstructions were exported, then batch processed MorphoLibJ [LAA16] for quantification. Tables containing data about every object were then merged with a simple Python script. Further processing of the data was done with OriginPro 2023.

5.5.4 Stitching and tiling

To stitch images together to a larger field of view (FOV), the FIJI plugin Grid/collection stitching [PST09] was used. First the acquisition pattern has to be provided, meaning the type and the order of the image acquisition e.g. in figure 3.8 the option "Grid: snake by columns" with the order "Up & Left" describe the acquisition scheme. Afterwards, the dimension of the image is given by setting the size of the matrix (e.g. 3×3 or 5×5) depending on the data. The tile overlap is a parameter that can be estimated by eye or using cross-correlation tools, and can already be influenced during the data acquisition as the the stage displacement in x and y can be chosen by the user. An empirical overlap of 10-20% is a usable value. The user has to take care that the overlap is similar in x as in y, in the case of the UC2 setup, the steps in x were 1.338 times bigger than in y (chip dimensions $1456 \times 1088 \text{ px}$). The file names were modified accordingly to allow the plugin to recognize the indices in the filenames. As fusion method, "Linear Blending" was chosen. Regression threshold was set to 0.30, Max/avg displacement threshold was set to 2.50, Absolute displacement threshold was set to 3.50. Furthermore the option "Compute Blending" was selected. The remaining parameters have been left to default. The output provided a stitched image and a protocol containing the image positions and blending parameters. As the algorithm relies on recognizable features, the fluorescence images were challenging to reconstruct, as only fluorescent structures were visible and super-ordinated structures were missing. In that case, the provided protocol allowed to accomplish the same stitching operation on a fluorescent set of images as on the bright-field set.

5.5.5 Wide-field image resolution estimation

In order to estimate the resolution of microscopy images, the FRC was used. In figure 5.12, the FRC of a confocal image is calculated. The correlation between two images is much stronger with distinct features, creating a strong gradient between the actual cell and its surroundings. In order to make all measurements consistent, regardless of the local background, the cells were segmented by simple thresholding. The initial image was converted into a binary image, producing a mask of the outlines of the cell. When applying this mask on the FRC map of the image, a resolution limit only considering the cell can be determined. This procedure has been applied on different resolution estimations (e.g. those displayed in figure 3.4).

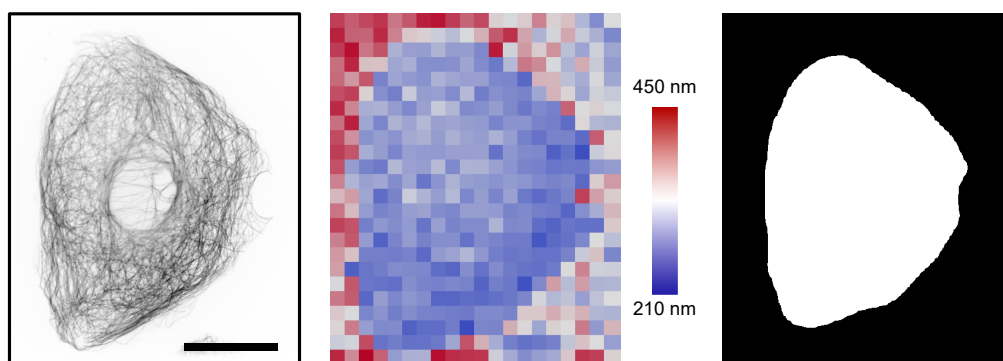


Fig. 5.12.: Segmenting the cell for resolution estimation. **Left.** Confocal image of an immunostained CV-1 cell against microtubules. Scale bar represents $25\ \mu\text{m}$. **Middle.** FRC map of the cell on the left. Due to lack of features, the FRC outside the cell is very variable. **Right.** Mask segmented in FIJI discern cell from background. Only the white part is used to determine the average of the achieved resolution.

5.5.6 Single particle tracking

The tracking of the single particles was done using Mosaic [SK05]. In a 2D data-set, the particle detection is achieved within a 3 px detection radius, with a Cutoff of 0 and an absolute thresholding value of 40-50. The link range and displacement between two frames is set to 3 px, with Brownian dynamics set in the particle linking. The detection is previewed at a subset of randomly chosen frames to verify that the detection parameters are stringent enough. The tracks are then analysed. The time steps between two subsequent frames and the pixel-size of the images are then set, to enable the calculation of various tracking parameters. The resulting tables of measurements on different cells with the same parameters are then joined to have a larger population and statistically meaningful result.

5.6 Simulation of SMLM raw-data

5.6.1 FluoSIM

The FluoSIM [Lag+20] software offers various possibilities to reproduce, predict or in general simulate different experimental conditions in fluorescence microscopy. Although the software seems to be best adapted to analyse experiments involving single particle tracking, SMLM experiments can also be simulated. The goal of the simulations is to determine the limits and the accuracy of the Bayesian engine. In this first attempt we want to examine the capability of the algorithm to detect and correctly quantify a set number of clusters. Thereby the density difference/factor between the clusters and the background is the essential parameter to be modified.

5.6.2 Sample geometry

Background: FluoSIM allows to import geometries from e.g. ImageJ or to draw one by hand. The chosen geometry is simple and result in a small sample. This facilitates the storage and increases the processing speed of the analysis. The basic geometry consists of a rectangle of 25×25 pixels approximately corresponding to a $2.5 \times 2.5 \mu\text{m}^2$ image, with a set pixel-size of $0.096 \mu\text{m}$. The given pixel-size corresponds to the measured value for the commonly used setup for SMLM experiments with the Photometrics delta 512 camera. Inside this rectangle, 40 clusters of 50 nm diameter are distributed randomly. To make this geometry, a script written by J. Rentsch was adapted to meet the above mentioned criteria. The clusters can touch but can not overlap. The goal is to still have distinguishable clusters. All the simulations will then be conducted using the same geometry, making the experiment more reproducible and preventing geometry dependant differences in clustering results.

In figure 5.13 the geometry creation process is depicted. As a reference for the simulation, an actual measurement of an empty sample imaged on the camera chip is used. The pixel values on the image are not processed by FluoSIM, The pixel-grid is merely used to divide the sample into pixels. The size of each of these pixels is defined through this step, and all other sizes are scaled accordingly in the software.

Distributing the molecules: The next step in the simulations was to distribute the molecules of interest according to the created geometry. This was achieved by using the particle diffusion options in FluoSIM. The rectangle was set as Contour (C) and the circles as Trapping (T). For a set period of time, the 4'000 single molecules were left to diffuse freely throughout the sample, which in this case was limited by the contour with the possibility to be trapped inside the trapping regions (the clusters). The diffusing molecules had a set probability of being bound to the trapping regions. Once a molecule was bound, the unbinding probability was set to 0. After the set time, the unbound molecules continue diffusing for the 50 s without binding to any region, to randomize the distribution of

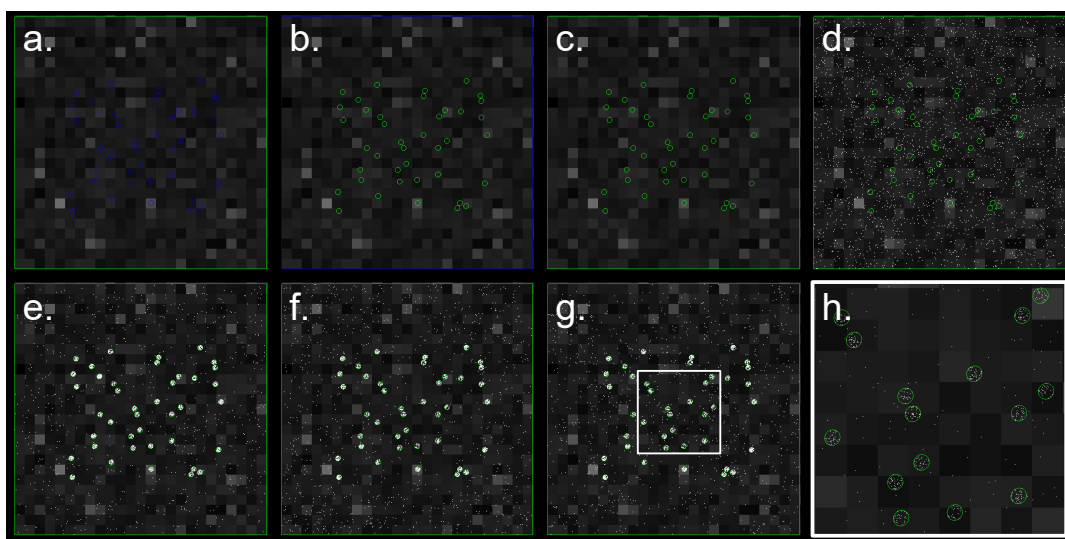


Fig. 5.13.: FluoSIM simulations geometry. **a.** Contour (C) in green. **b.** Trapping (T) in green. **c.** C and T selected. **d.** Molecules randomly distributed in C. **e.** Molecules diffuse for a time period and can be trapped in the Ts. **f.** Molecules within T are moving to randomize their position within the Cs. **g.** Background molecules diffuse around to distribute evenly within C. **h.** Zoom in of the white ROI in **g.**

molecules outside clusters. The same procedure was done for the molecules bound within the clusters. They freely diffused within the cluster without leaving it, randomizing the positions of molecules within clusters. The resulting sample had increased density of molecules in the cluster (T) and the leftover molecules distributed as background. This whole procedure was repeated ten times for different binding times. The binding times and corresponding cluster or cluster/BG densities are listed in table 5.8.

Binding time [s]	50	40	20	15	10	5
Density in cluster [μm^{-2}]	6238	5057	2624	1868	1401	713
St. dev. [μm^{-2}]	630	482	391	390	363	245
Norm. cluster density	19.0	13.0	5.14	3.41	2.45	1.18
St. dev.	3.2	1.7	0.82	0.73	0.64	0.41

Tab. 5.8.: FluoSIM cluster densities for different binding times. Normalized values give a density value in comparison to the background average molecule density.

5.6.3 Creating and analysing SMLM datasets

FluoSIM can generate Gaussians as simplified PSFs from each point where a single molecule has been seeded. The two parameters are the FWHM and the intensity, which have both been extracted from earlier measurements on the AF647 fluorophores [Geb+21]. Then, in order to induce blinking of the molecules, ON- and OFF-rates are set, typically with k_{OFF} greater than k_{ON} by a factor 1000 to 10'000 [vS14], depending on the molecule density. The number of frames has been set to 50'000 as a possible follow-up experiment would be to see the influence of the number of frames on cluster analysis. The raw

data-sets are then analysed with SMAP, as described in subsection 5.5.1. The localization files (.csv or .txt format) are then loaded into BaCLAVA for cluster analysis. Images are generated for simple monitoring.

5.6.4 Selfmade simulations

Distributing the molecules: The boundaries were set by a squared surface. The 500 nm along the border were free of any localization to prevent PSFs being cut-off at the edge in the FOV. Then, cluster seeds were positioned randomly and molecules were distributed within a radius of 50 nm around the seeds. The distribution of molecules within the circle followed a Gaussian distribution, the maximum being in the middle of the cluster. The chosen number of clustered molecules was distributed according to a given average, with a random variation of up to 10%. The remaining background molecules were distributed randomly within the FOV, outside the clusters. Parameters such as cluster size, cluster density and BG density were set in the R-based code.

From molecule to PSF: The output of the distribution is file with all the positions of the single molecules, comparable to a localization table in a SMLM experiment. The next step in the simulation was to create a PSF from a point randomly placed on a grid/matrix (representing the pixels). The procedure was the in verse of the localization in a SMLM experiment. The single point was considered as centroid of a Gaussian function with realistic parameters (intensity and FWHM) extracted from measurements on real single molecule experiments with the same fluorophore (here AF647). To reproduce realistic PSFs from the given Gaussian function, the procedure explained in one dimension in equation 5.2 was computed numerically in 2D within the simulation pipeline. The Gaussian function is integrated over a range (from a to b). This range corresponds to the pixel-size in the final image. The grey value of this pixel was the numerical integral of the Gaussian function over the given range corresponding to a pixel. This was repeated for various sets of a and b but keeping the distance between a and b constant. The whole procedure was done with a 2D Gaussian and accordingly a double integral in X and Y.

$$f(x) = \int_a^b \frac{1}{2} \pi \sigma_x \exp \left[-\frac{1}{2} \left(\frac{x - x_c}{\sigma_x} \right)^2 \right] dx = \frac{1}{2} \left[\operatorname{erf} \left(\frac{b - \mu}{\sqrt{2}\sigma} \right) - \operatorname{erf} \left(\frac{a - \mu}{\sqrt{2}\sigma} \right) \right] \quad (5.2)$$

This way, the PSF intensity values for every pixel were assigned to match the sub-pixel initial position of the single molecule. The localization precision, when analyzing the data, was as high as for real data-sets and was neglected as a clustering artefact in comparison to the noise (introduced in section 1.9.3) and the randomness of the molecule distribution.

Blinking parameters and raw data generation: After choosing the right .tiff format, noise was added to the images to render the images in a more realistic way. The camera noise has been statistically measured by imaging 5'000 frames of the camera chip with a closed shutter, and plotting a histogram of the pixel values. The Γ -like plot was used to introduce random noise into the raw-data-sets. The blinking parameters are chosen

similarly to the FluoSIM experiment ($k_{OFF}/k_{ON} \approx 10^4$). Afterwards, a *.tiff* stack was generated, imitating raw SMLM data-sets.

5.7 Protocols for sample preparation and materials

5.7.1 Chemicals and buffers

In table 5.9 the chemicals used as well as the corresponding manufacturers are listed.

Chemical compound	Manufacturer
α -Biotin- ω -(succinimidyl pro- pionate)-24(ethylene glycol)	Iris Biotech
β -mercaptoethanol	Sigma Aldrich
Bovine serum albumin (BSA)	Carl Roth
Catalase	Sigma Aldrich
DMEM (phenol-red free)	Thermo Fisher scientific
Fetal bovine serum (FBS)	Thermo Fisher scientific
Glucose	Sigma Aldrich
Glucose oxidase	Sigma Aldrich
Glutaraldehyde (GA)	Electron Microscopy Sciences
GlutaMAX	Thermo Fisher Scientific
Hellmanex III	Sigma Aldrich
Horse Serum (HS)	Thermo Fisher scientific
imageIT	Thermo Fisher Scientific
Invitroge TM Live Cell Imaging Solution	Fisher scientific
NaBH ₄ Sodium Borhydride	Sigma Aldrich
NH ₄ Cl Ammonium chloride	Sigma Aldrich
Paraformaldehyde (PFA)	Electron Microscopy Sciences
Penicillin-Streptomycin	Thermo Fisher scientific
Poly-L-lysine	Sigma Aldrich
SiR-Actin	Spyrochrome
Tris-HCl	Sigma Aldrich
Triton TM X-100	Sigma Aldrich
Verapamil	Spyrochrome

Tab. 5.9.: List of chemicals and their manufacturers.

PEM: Buffer was made on water base with 0.1 M PIPES, 2 mM EGTA and 1 mM MgSO₄ (PH 6.95).

PBS: Buffer was made on water base with 137 mM NaCl, 2.7 mM KCl, 10 mM Na₂HPO₄, 1.8 mM KH₂PO₄, (pH 7.4).

dSTORM buffer The dSTORM buffer was composed of 150 mM Tris-HCl, 1.5 % β -mercaptoethanol, 0.5 % (v/w) glucose, 0.25 mg/ml glucose oxidase and 20 μ g/ml catalase (pH 8.8).

5.7.2 Cell culture

The used cell culture medium is phenol red free D-MEM, supplemented with 1 % GlutaMAX and 10 % FCS. To reduce contamination risks, the medium was supplemented with 1 % Penicillin-Streptomycin. The cell medium for the T98G cell-line has additionally 1 % Sodium pyruvate. The cells are split 1:10 every three days with 2 mM EDTA (St.: 0.1 M) and 0.25 % Trypsin (Thermo Fisher scientific).

5.7.3 Cover glass cleaning

The single molecule experiments were very sensitive to background and reducing the number fluorophores bound to the coverslip surface was a simple way to improve the image quality. In the experiments presented in this thesis, mainly two types of cover-glasses were used. The first type were circular 25 mm diameter glass surfaces that can be inserted in corresponding metal holders. The second type were quadratic glass covers that are the bottom part of an 8-well dish (15 μ -slide 8-well Glass bottom, Ibidi). In order to minimize the impurities on the glass surface, the glass surfaces were cleaned before use. This destroyed the glass surface tension, resulting in more homogeneous samples, while increasing the image quality by reducing the background.

The circular cover glasses were placed into the ultrasound bath in a 2 % Hellmanex III for 20 minutes. They were then rinsed twice with Milli-Q H₂O and placed back into the ultrasound bath in a 70-80 % ethanol solution for 20 minutes. After one hour of drying under a ventilated hood, the cover-glasses were placed in the plasma cleaner for 20 minutes.

The 8-well chambers can not be placed into the plasma cleaner as the plexi-glass chambers are not suited for plasma cleaning. The chambers were thus filled with 300 μ l of 1 M KOH each and incubated for 15 minutes. The chambers were then rinsed with distilled H₂O in three steps of 3 minutes each. Finally, the chambers were dried with gaseous N₂.

Experiments involving HEK cells additionally required a Poly-L-lysine coating of the cover-glass for cell adhesion. This was done by covering the glass surface (\approx 200 μ l for the 25 mm cover-glasses) with a 0.1 % poly-L-lysine solution diluted in H₂O for 30 minutes. The glass was then gently rinsed with H₂O.

5.7.4 Tetra speck surface

The 100 nm T-7279 TetraSpeck (life technologies) were diluted 1:1000 in distilled water. Alternatively, the 20 nm F-8783 FluoSpheres were diluted 20'000:1 in distilled water.

Afterwards 50 μl of the solution was diluted in 500 μl of distilled water. The sample was left in a ventilated hood to let the water evaporate. By placing the sample in an oven with airflow at 40-50° C, the water evaporation can be accelerated. When imaging, water was added again into the sample to reproduce realistic refractive index in a biological sample.

5.7.5 Cell seeding

For the SMLM experiments, only the 25 mm circular cover glasses were used. Typically 25'000 CV-1 cells were seeded per cover glass. For the regular fluorescence imaging experiments, 60'000 to 85'000 cells were typically seeded on the circular cover glasses (25 mm). Alternatively, when using the 8-well chambers (Ibidi), approximately 20'000 to 30'000 cells are seeded per well.

5.7.6 CV-1 MT staining

CV-1 cells (Wild-type *Cercopithecus aethiops* kidney fibroblasts) were washed with PEM buffer preheated to 37° C. Afterwards, 500 μl of a 37° C warm PEM solution with 4 % PFA, 0.05 % GA and 0.1 % Triton X-100 was added to the cells for fixation. After 20 minutes fixation, the solution was removed and the sample was quenched for 8 minutes in a 50 mM NH_4Cl solution on PBS base. The sample then underwent three washing steps of 3 minutes each with PEM buffer. The cells were then permeabilized with a 0.3 % Triton X-100 solution on PEM basis for 5 minutes. After one washing step (3 minutes) with PEM buffer, the sample was blocked for 30 minutes in imageIT (Thermo Fisher) followed by one hour of blocking in a 4 % HS, 1 % BSA, 0.1 % Triton X-100 solution on PEM basis. The sample was then incubated, either overnight at 4° C or for 2 hours at room temperature, with two primary mouse anti alpha- and beta- tubulin IgG antibodies (respectively Sigma-Aldrich REF: T5168 and Sigma-Aldrich REF: T5293) diluted by a factor of 1 to 350 in a PEM based solution with a 1 % BSA and 0.1 % Triton X-100. The samples underwent three washing steps of 5 minutes each with a solution on PEM basis containing 1 % BSA and 0.1 % Triton X-100. The cells were then incubated at room temperature for 2 hours with a secondary donkey anti-mouse antibody conjugated to AF647 fluorophores. The antibodies were diluted by a factor of 1 to 250 in a PEM based solution with 1 % BSA and 0.1 % Triton X-100. The three washing steps of 5 minutes each with a PEM-based solution containing 1 % BSA and 0.1 % Triton X-100 were then repeated. The sample was the post-fixated with a 4 % PFA solution diluted in PEM, for 15 minutes. The cells were then quenched with a 50 mM NH_4Cl solution diluted in PBS for 8 minutes. Finally the cells were washed one last time with PBS.

5.7.7 CLC-GFP staining for SMLM measurement

A HeLa cell-line (cervical carcinoma) stably expressing CLC-GFP was used for this staining. Cells were washed with PEM buffer preheated to 37° C. The sample was fixed

with a 500 μl of a 37° C warm PEM solution with 4 % PFA, 0.2 % GA and 0.1 % Triton X-100. After 20 minutes, the sample was quenched for 8 minutes in a 50 mM NH_4Cl solution on PBS basis. The sample then underwent three washing steps of 3 minutes each with PEM buffer. The cells are then permeabilized with a 0.3 % Triton X-100 solution on PEM base for 5 minutes. After one washing step (3 minutes) with PEM buffer, the sample was blocked for 30 minutes in imageIT followed by one hour of blocking in a 4 % HS (horse serum), 1 % BSA (Bovine serum albumin), 0.1 % Triton X-100 solution on PEM basis. The sample was incubated with 50 nM anti-GFP nanobodies (FluoTag-Q) labelled in a 1:1 ratio with Alexa Fluor 647 for 45 minutes diluted in a PEM based solution with a 1 % BSA and 0.1 % Triton X-100. The sample was then washed three times with a PEM solution for 5 minutes each time, to remove unbound nanobodies. The sample was then post-fixed with a PEM based 4 % PFA, 0.2 % GA for 20 minutes. The cells were then quenched with a 50 mM NH_4Cl solution diluted in PBS for 8 minutes. Finally the cells underwent three final washing steps with PEM, and were then ready for imaging.

5.7.8 CD95-GFP staining

The glioblastoma T98G cell-line stably expressing CD95-GFP was used. The cells were washed with PEM buffer preheated to 37° C. The sample was fixed with a 500 μl of a 37° C warm PEM solution with 4 % PFA, 0.2 % GA for 20 minutes. Then, the fixation solution was removed and the cells were quenched with fresh 0.1 % NaBH_4 in PEM for 7 minutes, at room temperature. The sample then underwent three washing steps of 3 minutes each with PEM buffer. Cells were then permeabilized with a 0.2 % saponin solution on PEM basis, for 5 minutes. The sample then underwent three more washing steps of 3 minutes each with PEM buffer. The cells were then blocked for one hour in a PEM based solution with 4 % HS, 1 % BSA. After three further washing steps with PEM, the sample was stained with 50 nM anti-GFP-nanobodies (FluoTag-Q) labelled in a 1 to 1 ratio with Alexa Fluor 647 for 45 minutes. The sample was then post-fixed with a PEM based 4 % PFA, 0.2 % GA for 20 minutes. Afterwards, the sample was quenched with fresh 0.1 % NaBH_4 in PEM for 7 minutes. Finally, the sample was washed three times with PEM and could then be used for imaging.

5.7.9 GPI-GFP staining

A CV-1 cell-line stably expressing GPI-GFP was used for this staining. Cells were washed with PEM buffer preheated to 37° C. The sample was fixed with a 500 μl of a 37° C warm PEM solution with 4 % PFA, 0.2 % GA for 20 minutes. Then, the fixation solution was removed and the cells were quenched with fresh 0.1 % NaBH_4 in PEM for 7 minutes, at room temperature. The sample then underwent three washing steps of 3 minutes each with PEM buffer. The cells were then blocked for 30 minutes with ImageIT. After three washing steps with PEM (3 minutes each), the cells were blocked for one hour in a solution on PEM basis with 4 % HS, 1 % BSA. After three washing steps (3 minutes) with PEM

buffer, the sample was incubated with 50 nM anti-GFP nanobodies (FluoTag-Q) labelled in a 1:1 ratio with Alexa Fluor 647 for 45 minutes diluted in a PEM based solution with a 1 % BSA and 0.1 % Triton X-100. The sample was then washed three times with PEM for 5 minutes each time, to remove unbound nanobodies. The sample was post-fixed with a PEM based 4 % PFA, 0.2 % GA for 20 minutes. Afterwards, the sample was quenched with fresh 0.1 % NaBH₄ in PEM for 7 minutes. Finally the cells were washed three times with PEM, and were then ready for imaging.

5.7.10 Live cell staining

Staining with SiR Actin: The sample i.e. CV-1 cells were washed with medium pre-warmed at 37° C. In 1 ml of warm medium, 1 μl of the 0.5 μMol SiR-actin (Spyrochrome) as well as 1 μl of 1 μMol molar Verapamil (Spyrochrome) were added. The medium of the cells was then replaced by the diluted SiR-actin and Verapamil solution. After one hour of incubation, the sample was removed from the incubator. The medium was replaced with warm live cell medium allowing the sample to be imaged for the following hours at room temperature.

Staining with SYTO far-red nucleic dye: First, the cells were washed in 37° C warm cell phenol-red free culture medium (DMEM + FBS + glutamax). Then, 1 μl of SYTO Red Fluorescent Nucleic Acid Stain (Invitrogen) was diluted into 1 ml of warm cell-culture medium. After removing the medium from the cells, the diluted SYTO dye was added to the sample. Finally, the cells were incubated for 30 minutes with the dye. The sample was then ready for imaging.

5.7.11 QD functionalizing for SPT

A CV-1 cell-line stably expressing GPI-GFP was used for the experiment. To functionalize QDs for targeting GFP on the cell membrane, anti-GFP nanobodies (LaG-16 anti-GFP made in own production according to [Fab+18]) were added to a biotin (α -Biotin- ω -(succinimidyl pro-pionate)-24(ethylene glycol)) solution at double molar excess. The solution was incubated for one hour on a shaker at 300 rpm at room temperature. The nanobody-biotin construct was then purified through three filtration steps using 7 kD MWCO desalting columns. The purified conjugated nanobodies were then added in a 1:1 ratio to the streptavidin coated quantum dots. After 10 minutes of incubation at room temperature, the QDs have attached to the nanobody via the biotin-streptavidin connection. The solution was then diluted in 1 ml of live-cell medium (Thermo Fisher) and was then added to the cells for a 15 minutes incubation step. The supernatant was removed and regular live-cell medium is added to the cells.

Conclusion and outlook

The here presented microscope showcases the feasibility of producing high-quality data with a setup based on low-budget components and 3D printing. Combining the 3D framework from the UC2 toolbox with low-budget electronics and a high-quality objective enabled to image different cellular structures with resolutions similar to those reached by commercial setups. The use of the open-source software ImSwitch as well as the availability of all materials necessary to reproduce the microscope (GitHub repositories) are a great step towards full accessibility of microscopy techniques.

The imaging assays performed with the UC2 microscope require a high degree of stability in order to produce high-quality images. The high precision, adaptability and low-cost of 3D-printers enable fast and reliable prototyping of 3D structures with existing medical applications such as surgical implants and prosthetics [Yeu+20; Zun+15]. Even solutions for replacing laboratory equipment with 3D printing exist [Mai+17]. In this project, the manufacturing as well as the distribution of high-quality instrumentation based on 3D printing was demonstrated. The usage of different plastics (e.g. ABS and PLA [Wen+16; HZM21]) enable to customize applications to the requirements in material flexibility or thermal resistance.

The simple electronic framework and the steering through an user-friendly GUI facilitate the usage of the whole microscope. Additionally, using affordable commercial stages enable the users to position the samples with high accuracy. However, the stage motion is subjected to backlash, impeding the reliable quantitative use of the stage for measuring of axial positions. The minimal axial step-size can be estimated at around 100-150 nm, sufficient for focusing on specific planes. In XY, the sample can be placed centrally within the FOV, and the stage allows reproducible and accurate displacement within the sample. The documentation of open source projects is paramount. The material provided on the GitHub repositories should enable users to reproduce the imaging tool, further tutorials including a video of the assembly are planned. The stability and precision of the system allow to build sophisticated instruments such as interferometers and advanced microscopy applications. This showcases that life science as well as photonics knowledge can be transferred with the same cube based framework.

To lower the budget of the complete setup, an affordable camera was used. The lower camera quality can be accounted for through the acquisition of more fluorescent signal in fixed cells. The image quality is necessarily higher with scientific cameras, however the wide-field fluorescence experiments proved that cellular structures could be identified. Additionally, single molecules could be identified and quantitative analysis could be

performed on the acquired data. A drift in the range of $1\ \mu\text{m}$ was measured within two hours, which is comparable to the drift present in its commercial counterparts.

The stability of the setup enabled the continuous imaging of living cells, at room temperature as well as within the cell culture incubator. The adaptability and the simple replacement of any given part of the microscope allowed to swiftly replace 3D printed parts with a more thermally stable alternative. Cells could be observed without significant damage over a prolonged time period. Furthermore, the effects of photo-toxicity were reduced by limiting the illumination time of the sample, ensuring normal cell division and healthy cell morphology. Further steps have been taken to improve the live-cell capabilities of the microscope, but in terms of resolution and sample preservation, the wide-field build is limited. The UC2 toolbox has already been used to produce more suited live-cell imaging solutions, such as a light-sheet microscope [Die+20], and would be the best choice for larger samples. Further development is currently being worked on to enable the acquisition of high-quality live-cell data with and UC2-based light sheet microscope. This experiment showed the feasibility of monitoring slow cellular processes such as cell division or cell migration, the temporal resolution mainly being limited by the photo-damage cells can withstand without morphological changes. The possibility of placing the whole instrument inside an incubator facilitates long term live-cell imaging significantly, and might become the most sought after application of this microscope. As the alternatives for imaging under incubator conditions are often costly, different research institutions might benefit from a modular long-term imaging solution within the incubator. Additionally regular microscope bodies are difficult to fit into an incubator, and often need further automation steps to be steered from outside. The combined automation and modularity promote the live-cell capabilities of the UC2 system.

The findings presented here suggest the possibility to use the microscope in high safety environments e.g. for experiments with hazardous organisms or viruses. The low production cost of such a microscope make it advantageous for applications where it might need to be discarded after use. The modularity and the compact build make it ideal for customized solutions in high safety level laboratories. Furthermore, if the setup has limited usage due to contamination risks, the high throughput capabilities could help to increase the significance of every performed experiment.

The accuracy in localizing single beads combined with setups stability and the speed of a CMOS camera encouraged the imaging of single molecules on the plasma membrane. By functionalizing anti-GFP nanobodies with biotin, a stable connection is established between streptavidin labelled quantum dots and the GPI-GFP membrane molecules of a stable cell-line. The diffusion coefficient of GPI was determined through analysis of single particle tracking data-sets. The measured value was comparable to the diffusion coefficient of GPI measured in previous studies. This experiment showcases the ability to monitor the dynamics of membrane molecules with high temporal resolution and single molecule precision. The SPT accuracy is limited by factors such as the integration time of

the camera, but computational solutions can improve the situation e.g. by reducing the size of the acquired FOV. A maximal frame-rate of around 20-25 ms has been determined as being optimal for such experiments and is also the lowest threshold, in terms of temporal resolution, that can be achieved with the setup in its current disposition.

Another application of a setup with single molecule sensitivity is the reconstruction of cellular structures with magnified resolution through SMLM, in this project using the method *d*STORM. When imaging microtubules, the projected profile of the hollow tubular structure exhibits railroad-track patterns. These are a known artefact when imaging immuno-stained tubules, and the peak-to-peak distance between the two peaks is used as an approximation of the microtubules diameter. The result extrapolated from the UC2 measurement matches those generated by a high-quality microscope and those measured in other studies, within the extent of the standard deviation. Discrepancies arise from the camera sensitivity i.e. the SNR, the illumination inducing considerable background and the limited laser power. The experiment however shows the feasibility of SMLM, producing data with sufficient quality to conduct quantitative research. This showcases that this microscopy concept provides access to the studying of biological questions requiring higher resolution to tackle. Performing *d*STORM still remains easier on a commercial setup, but the UC2 setup might be a viable alternative for research groups with a lower budget. Furthermore, as for all applications of the microscope, teaching purposes are one of the main scopes of application.

In order to keep the price of the complete instrument in an affordable range (around 3000 €), the usage of low-budget objectives is a potential solution. Two low-budget objectives were tested in an attempt to evaluate for which experiments or biological structures, the image quality produced by the low-budget option is usable. The 20 × objective could barely reproduce clathrin coated pits, a structure that is around 100-200 nm large. The 100 × objective could reproduce nanoscopic structures, below the diffraction limit. The aggregated inaccuracy from the lower manufacturing quality of the optics, the reduced NA and not adapted pixel-size were impeding their usage for quantitative fluorescence experiments. However, the image quality was sufficient for quantifying wide-field image intensities and teaching purposes for SMLM techniques. Cellular features that do not require high resolution (20 × objective) can be imaged with this objective e.g. providing an affordable mean to monitor live-cells over long time periods. All together, quantitative biological research relies on quality of data that is currently not provided by low budget optics. Various assays can be performed with the lowest-budget version of this UC2 microscope. The research applications are limited by the lower image quality, but assays needing less resolution e.g. in diagnostics could benefit from better accessibility. A lower price and the existing automation options also facilitate screening assays with multiple microscopes.

The ever growing data-set sizes and the necessity to describe processes with statistical relevance produce a need for data analysis solutions. For this reason, machine learning

solutions can be an asset in assisting manual evaluation of microscopy images. Here, software packages such as CellProfiler and CellPose were used to register and segment objects of different sizes within the images. CellProfiler enables users to write pipelines to register sample features and quantify parameters such as size or area intensity. The network has not been trained for recognition of these features, removing the training step from the analysis. CellPose has been trained on cell images and identifies various features on cell-lines that did not belong to the training set. The option to train on own data on the Colab notebook provides great accessibility, also to users with lower computational resources. The combination of open-source microscopy and the use of simple machine learning based solutions enables the implementation of high throughput analysis.

An user-friendly cluster analysis tool requiring low know-how from the user has been developed to popularize clustering of SMLM data-sets. The performance of BaClAva has been benchmarked to determine its accuracy through simulations. These have shown that minimal increases in molecular density allow to recognize a majority of real clusters in a noisy background. Over a threshold of five times denser clusters than the background, the quantified number of clusters approaches the ground truth. Parameters such as the number of frames and the molecular blinking properties need to be investigated. To simplify the generation of simulated SMLM raw data-sets, a simulation module has been implemented into BaClAva. Experiments on biological samples allowed to characterize the clustering behaviour of the CD95 receptor on glioblastoma cells, comparing them to appropriate positive and negative controls. This receptor, once activated, can induce a signaling pathway to trigger apoptosis or survival. Further SMLM experiments combined with cluster analysis may give insights into the mechanism triggered by activation of the receptors.

UC2 microscope implications

The usage of affordable optical instrumentation is certainly a step into the right direction for providing as many people as possible the opportunity to part-take in the scientific process. However, laboratories are necessary to grow cells in a sterile environment, to prepare samples and to actively part-take in the research process. The materials, the instruments and the know-how are still not easily accessible. Reducing the cost of a complete laboratory and its equipment will be a challenging task without compromises in quality. Efforts are made towards reducing the cost of chemicals [Lav21] and providing simple solutions for prototyping scientific instrument (e.g. through 3D printing) as has been demonstrated by different projects aiming to reduce material cost by replacing laboratory equipment with its cheaper 3D printed counterpart [Wen23; Mai+17; BBE18]. The production costs of chemical component is low but the high acquisition prices are a result of generated revenues going into financing the past and future research on those chemicals. As patents do run out eventually [Hoh+22], prices of chemicals could drop to a price range where they could be available to institutions with smaller budgets. As

running a laboratory generates long term maintenance costs, trained staff, materials and others, this barrier will remain challenging to overcome.

Another aspect of the open source microscopy implications is the effects such projects can have on a societal level. Additionally to promoting the availability of teaching materials, both in photonics and life-science, open-source microscopes can have a social and humanitarian function. Involving children in science to feed their curiosity and foster hypothesis driven thinking might have effects beyond their education. Involving the public in science improves the public's understanding of the scientific process while giving researchers support, thereby supporting their science based opinion formation in political decisions. The community spirit is also important, as technology alone can not be the solution and individual efforts can barely compete with nowadays fast paced scientific research. Examples of scientific projects designed for communities of amateurs can be found in e.g. "Operation moon watch", where low-budget telescopes were distributed to citizens to develop a network of tracking stations for stellar objects [Lau09]. Similar projects can be found for microscopy with e.g. the Planktoscope [Pol+22], providing a low budget instrument to monitor plankton populations in different oceans. The study of biodiversity, especially with imminent changes in temperature or living conditions of various species, requires adaptable solutions for imaging outside the laboratory. Pathogens and parasites can be detected using with low-budget microscopes, the simple deployment and usability being assets in providing medical diagnostics in developing countries. The possibility to equip the UC2 setup with a 12V battery and a laptop would provide a modular imaging tool outside the laboratory with hours of autonomy, providing an approach to tackle aforementioned problems with a custom application of an open-source microscope.

The practical usage of the open-source framework is already active, with outreach programs such as e.g. Itartra [Ita], which are promoting the education in developing countries (here Madagascar) using low budget solutions such as the FoldScope [CCP14] and modular solutions such as the UC2 tool-box. Open-source solutions to promote scientific work in regions of the world with limited budget are also undergoing rapid development with e.g. platforms such as TRenD in Africa [Ban+] which are promoting solutions for teaching and research in natural science on various levels, going from affordable hardware to knowledge access. Furthermore, the 2020 pandemic encouraged and accelerated the accessibility of free high-quality educational content online, thereby promoting knowledge transfer while abiding the general guidelines of open-source concepts. Efforts of local students and professors additionally can help to remove the language barrier if relevant ([Edu] for Madagascar). I believe, the combined availability of affordable hardware, software, analysis methods, teaching materials and an open-source community will make a difference in providing education and life science research opportunities to people who currently lack the access to those things. The microscope presented in this thesis is optimized for research purposes, limiting its potential usage to life-science teaching in higher institutions. The development of the open-source field however shows the feasibility for affordable solutions on various hardware sophistication levels.

A.1 Alternative illumination possibilities

A.1.1 Fiber based laser as possible replacement for wide-field illumination

The profile and emission pattern of the new single-mode fiber coupled laser was characterized with the same methodology as the laser used in the experiments presented in the thesis. The advantage of a single mode fiber (figure A.1 a) is that the provided laser profile has a Gaussian shape as only the TEM_{00} mode of the electro-magnetic wave is able to pass through the fiber. This laser does not need any further cleaning. The same phenomenon is observed when cleaning a laser through a spatial filter (a telescope build with a pinhole in the common focal point of both lenses). The measured profile of such a spatially filtered laser is displayed in figure A.1 d.

The fiber laser is coupled to the cubes via a fiber mount adapter (Thorlabs SM1FCA2) which is mounted into a cube with an adapted 3D printed lens mount. The excitation light is gathered by a $f = 50$ mm lens at 50 mm distance from the fiber end. The size of the illuminated spot in the sample can be increased by increasing the focal length of the used lens. The resulting illumination will then be more spread but have reduced laser density. The use of fibers facilitates to feed different lasers into the same optical path without much adaptations of the system, especially without tilt sensible filters.

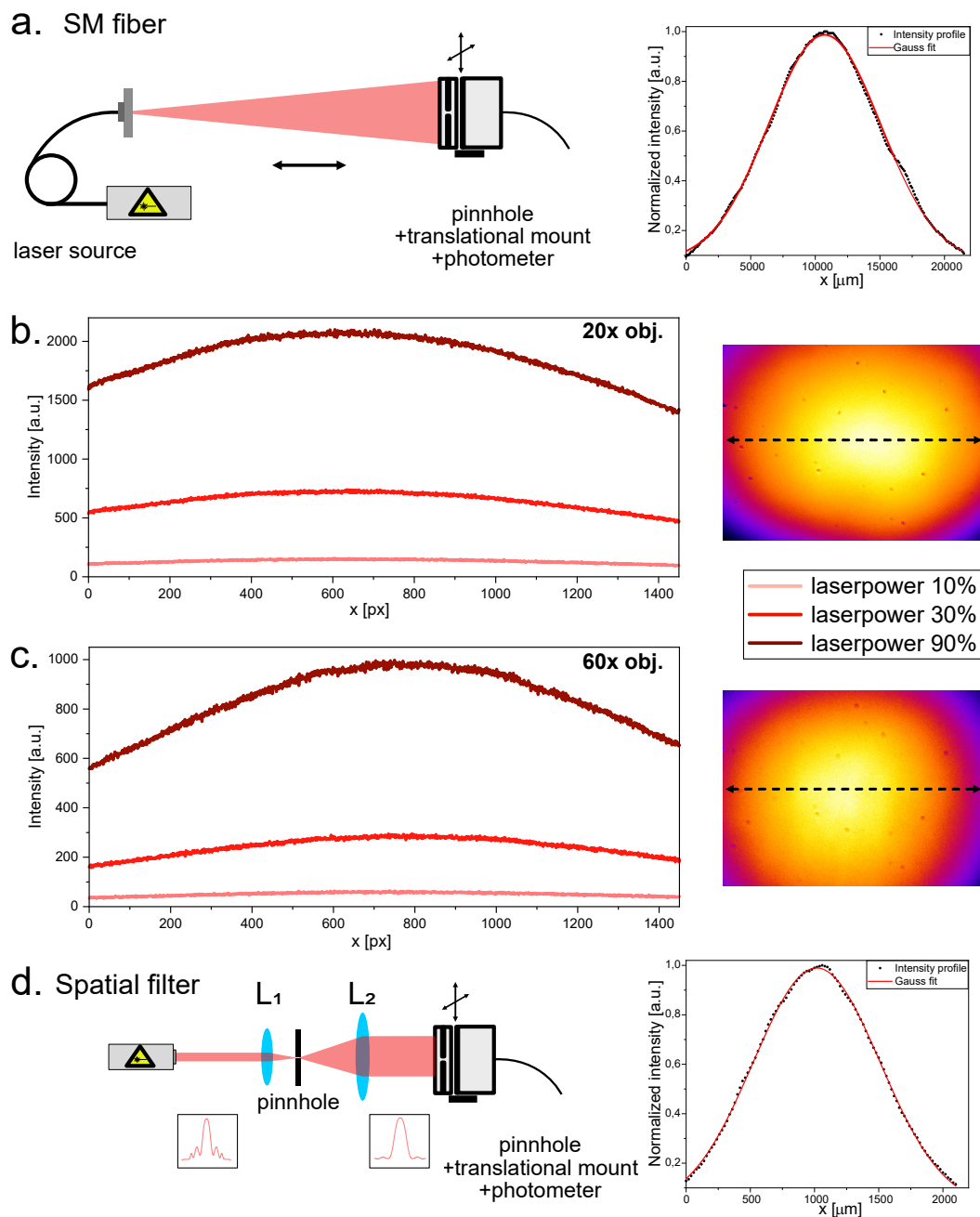


Fig. A.1.: Intensity profile of a single mode laser and of a laser cleaned with a spatial filter **a.** Single mode laser profile is scanned through with a pinhole and a detector. Resulting profile is plotted on the right. **b.** Laser profile on Chroma red fluorescent slide with 20x Olympus objective. **c.** Laser profile on Chroma red fluorescent slide with 60x Olympus objective. **d.** 639 nm laser of the Llama microscope is cleaned with a spatial filter. Profile is scanned through with a pinhole and detector. Resulting profile is plotted on the right.

A.1.2 Possible auto-focus improvement

The use of a LED matrix instead of a single LED leads to interference patterns when defocusing the sample. The resulting images can barely be used for any applications as can be seen in figure A.2 **b.**. The surprising advantage however is that the FFT of the

images are very distinct. This leads to believe that the matrix can be effectively used to filter distinguish the focus plane from the rest. A possible use of this feature would be to use a LED matrix to keep the sample in focus over the experiment. The top illumination should however be kept to a single LED.

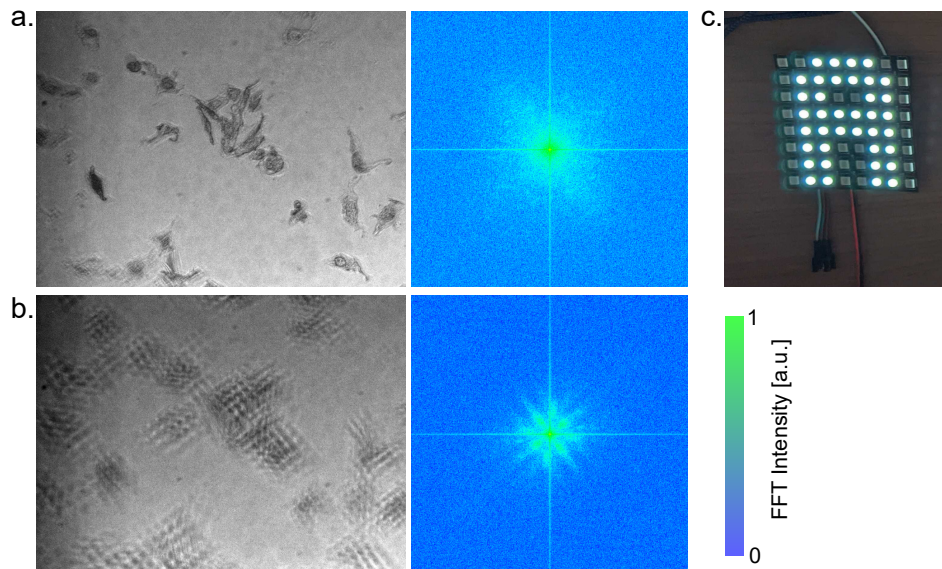


Fig. A.2.: LED matrix for auto-focus improvement **a.** Cells in focus when using a LED matrix as top illumination with corresponding FFT on the right. **b.** Same process for out of focus sample. Intensity of the FFT in arbitrary units. **c.** Example of an LED matrix. Every single LED can be controlled separately.

A.1.3 Wide-field imaging with different objectives

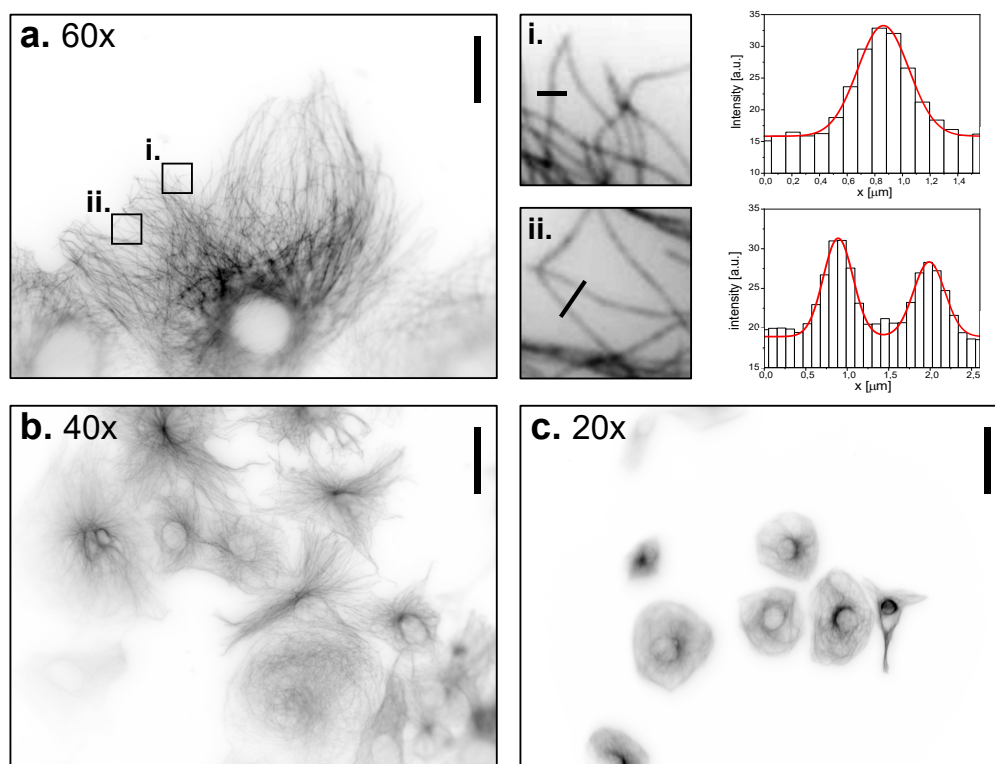


Fig. A.3.: Wide-field fluorescence imaging of immuno-stained microtubules. **a.** $60\times$ magnification objective image of immuno-stained microtubules in CV-1 cells. Two ROIs shown in the image are cropped and magnified as **i** and **ii**. The corresponding profiles to selected single microtubules in the image are displayed next to the magnified ROIs. Scale bar represents $30\ \mu\text{m}$. **b.** $40\times$ magnification objective image of immuno-stained microtubules in NRK49E cells. Scale bar represents $45\ \mu\text{m}$. **c.** $20\times$ magnification objective image of immuno-stained microtubules in CV-1 cells. Scale bar represents $90\ \mu\text{m}$.

A.2 Imaging experiments

A.2.1 live-cell imaging

The HEK cells have been cultivated on coverglasses coated with Poly-L-lysine. The frequent and prolonged illumination of the sample, combined with the lower temperature, compared to the incubator, led to cell death. The stronger adhesion to the cells to one another compared to the adhesion to the coverglass induced this clumping of dying cells over time. The state of the cells can also be monitored according to the brightness of the nucleus, which suddenly increases once the cell has gone into an apoptotic state. In this case the cells have been illuminated for around 3 s every minute for over 5 hours. The accumulated light energy is around 28 J over the 5 hours, with an approximated laser power of 28-30 mW distributed over the FOV. The

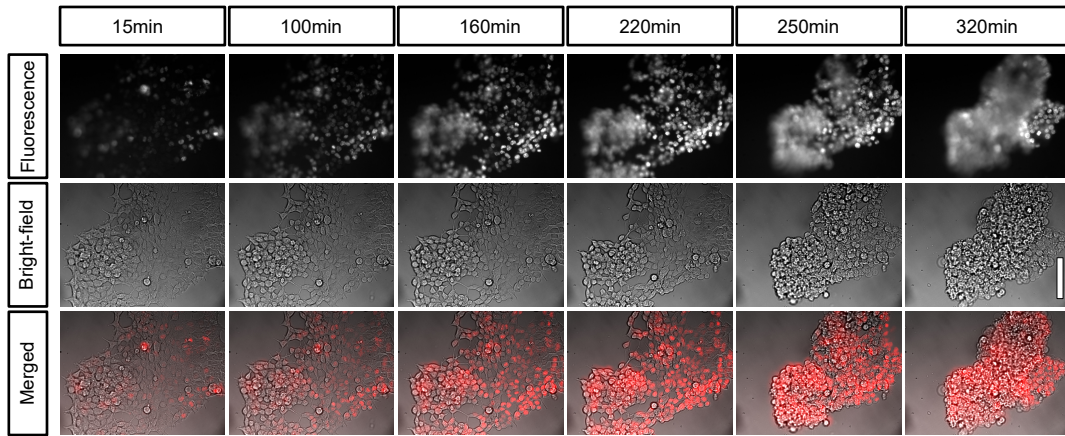


Fig. A.4.: Live-cell imaging of HEK cells over five hours at room temperature with $20\times$ magnification. SYTO far red nuclear staining provides signal in fluorescence channel. Scale bar represents $90\ \mu\text{m}$.

A.2.2 Llama setup *d*STORM of microtubules in TIRF-illumination

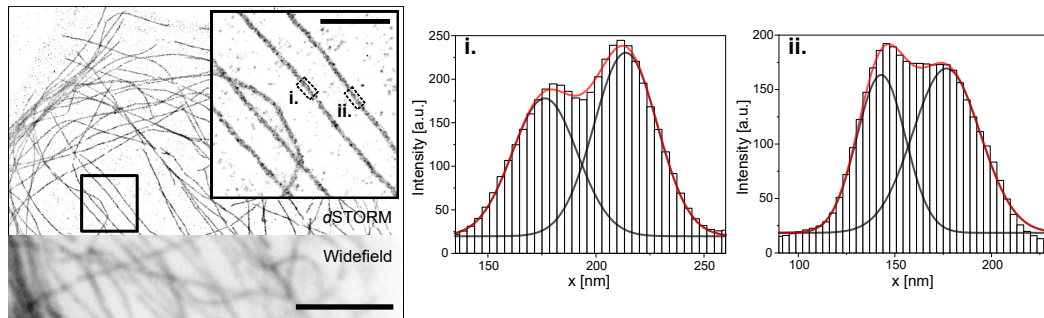


Fig. A.5.: *d*STORM imaging of microtubules on the Llama microscope in TIRF-illumination. Same sample as in figure 3.14 imaged in widefield and reconstructed with *d*STORM. Scale bar represents $5\ \mu\text{m}$. Region of interest is magnified (scale bar represents $1\ \mu\text{m}$) to look at two single microtubules, which profiles are plotted in **i.** and **ii.** by averaging the signal over $200\ \text{nm}$ along them. Profile is fitted with a double Gaussian. Peak to peak distances of $(36.2\pm 1.2)\ \text{nm}$ for **i.** and $(34.8\pm 1.2)\ \text{nm}$ for **ii.** are extrapolated.

A.2.3 *d*STORM imaging of CCP on Llama setup

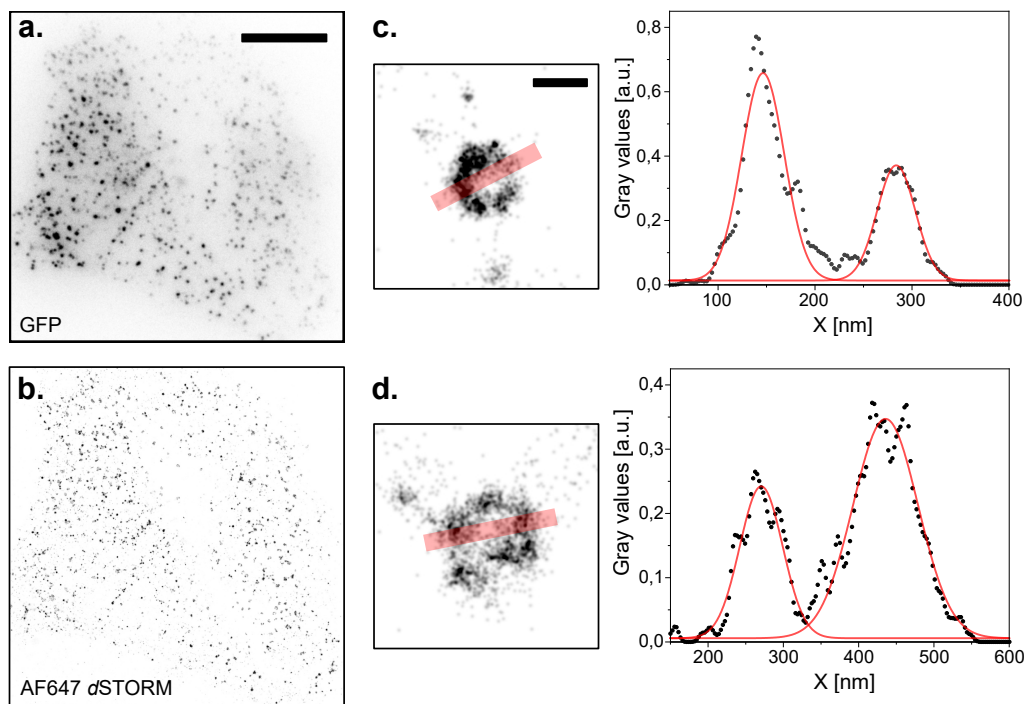


Fig. A.6.: Clathrin coated pits *d*STORM reconstruction on Llama setup. **a.** GFP signal of the stable CLC-GFP HeLa cell-line. **b.** Reconstruction of blinking AF647 dyes on the same cells with *d*STORM. Scale bar for **a** and **b** represents 10 μm . Two CCPs have been magnified in **c** and **d** with the profiles along the red transparent line displayed on the right. Scale bar for **c** and **d** represents 200 nm.

A.3 Scripts and analysis codes

ImScript to acquire a time lapse in two channels

Modified script from the ImScript application examples provided in ImSwitch. Here, an exemplary acquisition of 500 time points in both fluorescence and bright-field channels is shown. Through the sleep-time, the duration between two measurements can be set, influencing the length of the complete acquisition. The 1 s sleep time between different commends is necessary to account for the slow processing.

```
1 import numpy as np
2 import time
3
4 laserName1 = api.imcontrol.getLaserNames()[0] #laser
5 laserName2 = api.imcontrol.getLaserNames()[1] #LED
6 iiter = 1 #variable to count the loops
7 nrofloops = 500 #total number of time-steps
8
9 while iiter < nrofloops:
10     laser = api.imcontrol.setLaserActive(laserName1, True) #laser ON
11     time.sleep(1)
12     api.imcontrol.snapImage() #snap fluorescence image
13     laser = api.imcontrol.setLaserActive(laserName1, False) #laser OFF
14     time.sleep(1)
15     laser = api.imcontrol.setLaserActive(laserName2, True) #LED ON
16     time.sleep(1)
17     api.imcontrol.snapImage() #snap bright-field image
18     laser = api.imcontrol.setLaserActive(laserName2, False) # LED OFF
19     time.sleep(56) #duration between two time-steps
20     iiter +=1
```

ImScript to acquire a 3×3 image matrix via stage translation

Modified script from the ImScript application examples provided in ImSwitch. The procedure is demonstrated here for a 3×3 matrix. The same method could be used for any matrix size. As the stages are all controlled by motors, the difference between a commercial stage and a self-built one will mostly be seen in the step-sizes the user has to set.

```
1 import numpy as np
2 import time
3
4 #mainWindow.setCurrentModule('imcontrol')
5 laserName1 = api.imcontrol.getLaserNames()[0] # control of the laser
6 laserName2 = api.imcontrol.getLaserNames()[1] # control of the LED
7 positioner = api.imcontrol.getPositionerNames() # control of the stages
8
9 iiter = 1 #variable definition for number of loops
```

```

10 nrofloops = 100 #total number of measurements to reach
11 sleeptime = 10 #waiting time between two loops [s]
12 axis1 = "Y" #definition Y-axis
13 axis2 = "X" #definition X-axis
14 axis3 = "Z" #definition Z-axis
15 xstep = 200 #definition x-stepsize
16 ystep = 150 #definition y-stepsize
17
18 while iiter < nrofloops:
19     #pos1_image (0,0)
20     time.sleep(2)
21     api.imcontrol.setLEDAllOn()
22     time.sleep(1)
23     api.imcontrol.snapImage()
24     time.sleep(1)
25     api.imcontrol.setLEDAllOff()
26     time.sleep(2)
27     #pos2_image (0,-1)
28     api.imcontrol.movePositioner(positioner[0], axis2, -ystep)
29     time.sleep(2)
30     api.imcontrol.setLEDAllOn()
31     time.sleep(1)
32     api.imcontrol.snapImage()
33     time.sleep(1)
34     api.imcontrol.setLEDAllOff()
35     time.sleep(2)
36     #pos3_image (0,-2)
37     api.imcontrol.movePositioner(positioner[0], axis2, -ystep)
38     time.sleep(2)
39     api.imcontrol.setLEDAllOn()
40     time.sleep(1)
41     api.imcontrol.snapImage()
42     time.sleep(1)
43     api.imcontrol.setLEDAllOff()
44     time.sleep(2)
45     #pos4_image (1,-2)
46     api.imcontrol.movePositioner(positioner[0], axis3, +xstep)
47     time.sleep(2)
48     api.imcontrol.setLEDAllOn()
49     time.sleep(1)
50     api.imcontrol.snapImage()
51     time.sleep(1)
52     api.imcontrol.setLEDAllOff()
53     time.sleep(2)
54     #pos5_image (1,-1)
55     api.imcontrol.movePositioner(positioner[0], axis2, +ystep)
56     time.sleep(2)
57     api.imcontrol.setLEDAllOn()
58     time.sleep(1)
59     api.imcontrol.snapImage()
60     time.sleep(1)

```

```

61     api.imcontrol.setLEDAllOff()
62     time.sleep(2)
63     #pos6_image (1,0)
64     api.imcontrol.movePositioner(positioner[0], axis2 , +ystep)
65     time.sleep(2)
66     api.imcontrol.setLEDAllOn()
67     time.sleep(1)
68     api.imcontrol.snapImage()
69     time.sleep(1)
70     api.imcontrol.setLEDAllOff()
71     time.sleep(2)
72     #pos7_image (2,0)
73     api.imcontrol.movePositioner(positioner[0], axis3 , +xstep)
74     time.sleep(2)
75     api.imcontrol.setLEDAllOn()
76     time.sleep(1)
77     api.imcontrol.snapImage()
78     time.sleep(1)
79     api.imcontrol.setLEDAllOff()
80     time.sleep(2)
81     #pos8_image (2,-1)
82     api.imcontrol.movePositioner(positioner[0], axis2 , -ystep)
83     time.sleep(2)
84     api.imcontrol.setLEDAllOn()
85     time.sleep(1)
86     api.imcontrol.snapImage()
87     time.sleep(1)
88     api.imcontrol.setLEDAllOff()
89     time.sleep(2)
90     #pos9_image (2,-2)
91     api.imcontrol.movePositioner(positioner[0], axis2 , -ystep)
92     time.sleep(2)
93     api.imcontrol.setLEDAllOn()
94     time.sleep(1)
95     api.imcontrol.snapImage()
96     time.sleep(1)
97     api.imcontrol.setLEDAllOff()
98     time.sleep(2)
99     #back to initial position
100    api.imcontrol.movePositioner(positioner[0], axis3 , -2*xstep) #(0,-2)
101    time.sleep(2)
102    api.imcontrol.movePositioner(positioner[0], axis2 , +2*ystep) #(0,0)
103    print("loop Nr. ", iiter, " of ", nrofloops-1)
104    iiter +=1
105    time.sleep(sleeptime)

```

ImScript to acquire Z-stacks in two channels

Modified script from the ImScript application examples provided. A Z-stack is acquired at every time-step, by sequentially changing the Z-position and acquiring single images. An alternative is to acquire both channels at every Z-position, instead of taking one Z-stack for each channel. The user can however modify the scripts according to their experimental preferences.

```
1 import numpy as np
2 import time
3
4 N_images = 10 #number of images in a stack
5 dz = 10 #stepsize of the stack
6 axis = "Z"
7 T_wait = 110 #waiting time between two acquisitions
8 nrofloops = 2000 #total number of stacks to acquire
9 laserName = api.imcontrol.getLaserNames()
10 positioner = api.imcontrol.getPositionerNames()
11 laserName1 = "635 Laser"
12 laserName2 = "650 LED"
13 iiter = 1
14 nrofloops = 500
15
16 while iiter < nrofloops:
17     laser = api.imcontrol.setLaserActive(laserName1, True)
18     time.sleep(2)
19
20     # take zstack first channel
21     api.imcontrol.movePositioner(positioner[0], axis, -N_images*dz/2)
22     time.sleep(2)
23     for i_pos in range(N_images):
24         api.imcontrol.movePositioner(positioner[0], axis, dz)
25         time.sleep(1)
26         api.imcontrol.snapImage()
27     api.imcontrol.movePositioner(positioner[0], axis, -N_images*dz/2)
28     laser = api.imcontrol.setLaserActive(laserName1, False)
29     time.sleep(1)
30     api.imcontrol.setLaserActive(laserName2, True)
31     time.sleep(1)
32     # take zstack second channel
33     api.imcontrol.movePositioner(positioner[0], axis, -N_images*dz/2)
34     time.sleep(1)
35     for i_pos in range(N_images):
36         api.imcontrol.movePositioner(positioner[0], axis, dz)
37         time.sleep(1)
38         api.imcontrol.snapImage()
39     api.imcontrol.movePositioner(positioner[0], axis, -N_images*dz/2)
40     api.imcontrol.setLaserActive(laserName2, False)
41     print(iiter)
42     iiter +=1
43     time.sleep(T_wait)
```

ImageJ macro to calculate FRC map in batch

The ImageJ plugin: NanoJ Squirrel [Cul+18], is used to batch process the FRC measurement. A SMLM .csv localization table is split into files with incrementing number of frames represented in it (increment: 1000). These files are then split into two files, separating the localizations in odd frames from those in even frames. All files are listed alphabetically in a folder, first following the order of the number of frames, then the suffix of *even* or *odd*. The script then calculates the FRC for all subsequent files. The FRC between two files with different number of frames are discarded. The resulting FRC values are appended into a single file and plotted according to the frame number (figure 3.13).

```
1 inputDir = "/C:/Ando/input/"; #input directory
2 outputDir = "/C:/Ando/output/"; #output directory
3
4 list = getFileList(inputDir); #list of images
5 Array.sort(list);
6 for ( i=0; i<list.length -1; i++ ) {
7     open( input_directory + list[i] ); #open even image
8     OpenIm1 = getTitle();
9     print(OpenIm1);
10    open( input_directory + list[i+1] ); #open odd image
11    OpenIm2 = getTitle();
12    print(OpenIm2);
13    run("Images to Stack", "name=Stack title=[] use"); #make a stack
14    StackTitle = getTitle();
15    print("StackTitle = " + StackTitle);
16    #Use functions of the NanoJ-Squirrel plugin
17    run("Calculate FRC-Map", "blocks=10 pixel=50 show");
18    selectWindow("FRC-Resolution");
19    saveAs("Measurements", outputDir+OpenIm1+OpenIm2+"_FRC_Map.csv");
20    ResultName = getTitle();
21    print(" ResultName = " + ResultName);
22    saveAs("tiff", outputDir+OpenIm1+OpenIm2+"_"+ResultName);
23    close();
24    run("Close All");
25    print('end of loop #' + i+1);
26 }
27 run("Close All");
```

FIJI macro to determine the image with the highest contrast

ImageJ macro written with Dr. Amin Zehtabian's assistance, to measure the contrast in a microscopy image. The script uses statistical features of bright-field images to estimate a contrast value, which is highest when the sample is in focus. The script includes a loop to run the measurement on all images of a folder (e.g. a Z-scan), allowing to determine the image with the highest contrast. With further automation steps, the script could be used to select the Z-position with the highest contrast, within a time-lapse of Z-stacks. The

resulting sequence of images would then all have the optimal contrast. An application for real-time auto-focus would also be possible.

```
1
2 path = getDirectory("Choose Directory");
3 list = getFileList(path);
4
5 // Set a variable to determine the type of image analysis
6 imageType = 0; // 0 to analyze the raw image, 1 to analyze the edges
7     if (imageType == 1) {
8         print("The edges are being processed rather than the raw image");}
9     else {
10        print("The raw images are being processed");
11    }
12
13 // Initialize variables to store the maximum contrast and the corresponding
    file name
14 maxContrast = -1;
15 maxContrastFile = "";
16 maxSTD = -1;
17 maxSTDFile = "";
18
19 for (i = 0; i < list.length; i++) {
20     if (endsWith(list[i], ".tiff") || endsWith(list[i], ".tif")) { // Open
        the image files with format tiff or tiff
21         open(path + list[i]);
22         if (imageType == 1) {
23             run("Find Edges");
24         }
25
26         // Calculate contrast of the current image
27         getStatistics(area, mean, min, max, std, histogram);
28         contrast = max - min;
29         print("Contrast (Max - Min) for image " + list[i] + " is = " +
            contrast);
30         print("STD for image ***" + list[i] + " *** is = " + std);
31         // Check if the contrast is higher than the current maximum contrast
32         if (contrast > maxContrast) {
33             // Update the maximum contrast and the corresponding file name
34             maxContrast = contrast;
35             maxContrastFile = list[i];
36         }
37         if (std > maxSTD) {
38             // Update the maximum contrast and the corresponding file name
39             maxSTD = std;
40             maxSTDFile = list[i];
41         }
42         //run("Histogram"); close();
43         // Close the image
44     }
45     close();
46 }
```

```
47 // Display the requested values
48 print("Image with highest contrast: " + maxContrastFile);
49 print("Contrast: " + maxContrast);
50 print("Image with highest std: " + maxSTDFile);
51 print("STD: " + maxSTD);
```


Bibliography

- [Abb73] E. Abbe. “Beiträge zur Theorie des Mikroskops und der mikroskopischen Wahrnehmung”. *Archiv für Mikroskopische Anatomie* 9 (1 1873), pp. 413–468. DOI: 10.1007/BF02956173 (cited on page 17).
- [Abr+13] S. Abrahamsson, J. Chen, B. Hajj, S. Stallinga, A. Y. Katsov, J. Wisniewski, G. Mizuguchi, P. Soule, F. Mueller, C. D. Darzacq, X. Darzacq, C. Wu, C. I. Bargmann, D. A. Agard, M. Dahan, and M. G. L. Gustafsson. “Fast multicolor 3D imaging using aberration-corrected multifocus microscopy”. *Nature Methods* 10.1 (Jan. 2013), pp. 60–63 (cited on page 106).
- [AHK21] S. Akbari Rohn Abadi, N. Hashemi Dijujin, and S. Koohi. “Optical pattern generator for efficient bio-data encoding in a photonic sequence comparison architecture”. *PLOS ONE* 16.1 (Jan. 2021), pp. 1–27. DOI: 10.1371/journal.pone.0245095 (cited on pages 36, 37).
- [Alb+13] B. Alberts, D. Bray, K. Hopkin, A. D. Johnson, J. Lewis, M. Raff, K. Roberts, and P. Walter. *Essential cell biology*. en. 4th ed. ISBN: 978-0-393-68039-3. New York, NY: Garland Publishing, Oct. 2013 (cited on page 70).
- [Alb+16a] D. Albrecht, C. M. Winterflood, M. S. and T. Tschager, F. Noé, and H. Ewers. “Nanosopic Compartmentalization of Membrane Protein Motion at the Axon Initial Segment”. *Journal of Cell Biology* 215.1 (2016), pp. 37–46. DOI: doi:10.1083/jcb.201603108 (cited on pages 52, 73, 93, 94).
- [Alb+16b] D. Albrecht, C. M. Winterflood, M. Sadeghi, T. Tschager, F. Noé, and H. Ewers. “Nanosopic compartmentalization of membrane protein motion at the axon initial segment”. *Journal of Cell Biology* 215.1 (Oct. 2016), pp. 37–46. DOI: 10.1083/jcb.201603108. eprint: https://rupress.org/jcb/article-pdf/215/1/37/1065836/jcb_201603108.pdf (cited on pages 33, 36).
- [Alm+19] P. Almada, P. M. Pereira, S. Culley, G. Caillol, F. Boroni-Rueda, C. L. Dix, G. Charras, B. Baum, R. F. Laine, C. Leterrier, and R. Henriques. “Automating multimodal microscopy with NanoJ-Fluidics”. *Nature Communications* 10.1 (Mar. 2019), p. 1223. DOI: 10.1038/s41467-019-09231-9 (cited on page 42).
- [Als+22] M. N. Alsamsam, A. Kopūstas, M. Jurevičiūtė, and M. Tutkus. “The miEye: Bench-top super-resolution microscope with cost-effective equipment”. *HardwareX* 12 (2022), e00368. DOI: <https://doi.org/10.1016/j.ohx.2022.e00368> (cited on pages 36, 42, 48).
- [Amb+20] B. Ambrose, J. M. Baxter, J. Cully, M. Willmott, E. M. Steele, B. C. Bateman, M. L. Martin-Fernandez, A. Cadby, J. Shewring, M. Aaldering, and T. D. Craggs. “The smfBox is an open-source platform for single-molecule FRET”. *Nature Communications* 11.1 (Nov. 2020), p. 5641. DOI: 10.1038/s41467-020-19468-4 (cited on page 42).
- [AR14] C. C. Aggarwal and C. K. Reddy, eds. *Data Clustering: Algorithms and Applications*. CRC Press, 2014 (cited on page 40).

- [Aue+18] A. Auer, T. Schlichthaerle, J. B. Woehrstein, F. Schueder, M. T. Strauss, H. Grabmayr, and R. Jungmann. “Nanometer-scale Multiplexed Super-Resolution Imaging with an Economic 3D-DNA-PAINT Microscope”. *ChemPhysChem* 19.22 (2018), pp. 3024–3034. DOI: <https://doi.org/10.1002/cphc.201800630>. eprint: <https://chemistry-europe.onlinelibrary.wiley.com/doi/pdf/10.1002/cphc.201800630> (cited on page 42).
- [Bal+17] F. Balzarotti, Y. Eilers, K. C. Gwosch, A. H. Gynnå, V. Westphal, F. D. Stefani, J. Elf, and S. W. Hell. “Nanometer resolution imaging and tracking of fluorescent molecules with minimal photon fluxes”. *Science* 355.6325 (2017), pp. 606–612. DOI: 10.1126/science.aak9913. eprint: <https://www.science.org/doi/pdf/10.1126/science.aak9913> (cited on page 43).
- [BBE18] M. D. Brennan, F. F. Bokhari, and D. T. Eddington. “Open design 3D-printable adjustable micropipette that meets the ISO standard for accuracy”. en. *Micromachines (Basel)* 9.4 (Apr. 2018), p. 191 (cited on pages 42, 128).
- [Bec+19] K. Becker, S. Saghafi, M. Pende, I. Sabdyusheva-Litschauer, C. M. Hahn, M. Foroughipour, N. Jährling, and H.-U. Dodt. “Deconvolution of light sheet microscopy recordings”. *Scientific Reports* 9.1 (Nov. 2019), p. 17625. DOI: 10.1038/s41598-019-53875-y (cited on page 22).
- [Bet+06] E. Betzig, G. H. Patterson, R. Sougrat, O. W. Lindwasser, S. Olenych, J. S. Bonifacino, M. W. Davidson, J. Lippincott-Schwartz, and H. F. Hess. “Imaging Intracellular Fluorescent Proteins at Nanometer Resolution”. *Science* 313.5793 (2006), pp. 1642–1645. DOI: 10.1126/science.1127344. eprint: <https://www.science.org/doi/pdf/10.1126/science.1127344> (cited on page 32).
- [BG17] E. Beghein and J. Gettemans. “Nanobody Technology: A Versatile Toolkit for Microscopic Imaging, Protein–Protein Interaction Analysis, and Protein Function Exploration”. *Frontiers in Immunology* 8 (2017). DOI: 10.3389/fimmu.2017.00771 (cited on pages 7, 14).
- [Big09] C. Bigg. “Brownian Motion”. In: *Compendium of Quantum Physics*. Ed. by D. Greenberger, K. Hentschel, and F. Weinert. Berlin, Heidelberg: Springer Berlin Heidelberg, 2009, pp. 81–84. DOI: 10.1007/978-3-540-70626-7_24 (cited on page 10).
- [Bor+19] M. Born, E. Wolf, A. B. Bhatia, and P. Knight. *Principles of Optics*. ISBN: 978-1-4831-0320-4. Cambridge University Press, 2019 (cited on page 30).
- [Bou+15] N. Bourg, C. Mayet, G. Dupuis, T. Barroca, P. Bon, S. Lécart, E. Fort, and S. Lévêque-Fort. “Direct optical nanoscopy with axially localized detection”. en. *Nat. Photonics* 9.9 (Sept. 2015), pp. 587–593. DOI: doi.org/10.1038/nphoton.2015.132 (cited on pages 11, 35).
- [Bur+15] A. Burgert, S. Letschert, S. Doose, and M. Sauer. “Artifacts in single-molecule localization microscopy”. *Histochemistry and Cell Biology* 144.2 (Aug. 2015), pp. 123–131. DOI: 10.1007/s00418-015-1340-4 (cited on pages 69, 92).
- [Car+06] A. E. Carpenter, T. R. Jones, M. R. Lamprecht, C. Clarke, I. H. Kang, O. Friman, D. A. Guertin, J. H. Chang, R. A. Lindquist, J. Moffat, P. Golland, and D. M. Sabatini. “CellProfiler: image analysis software for identifying and quantifying cell phenotypes”. *Genome Biology* 7.10 (Oct. 2006), R100. DOI: 10.1186/gb-2006-7-10-r100 (cited on pages 64, 83, 114).
- [CCP14] J. S. Cybulski, J. Clements, and M. Prakash. “Foldscope: Origami-Based Paper Microscope”. *PLOS ONE* 9.6 (June 2014), pp. 1–11. DOI: 10.1371/journal.pone.0098781 (cited on pages 42, 129).
- [Cha+13] F. Chazal, L. J. Guibas, S. Y. Oudot, and P. Skraba. “Persistence-Based Clustering in Riemannian Manifolds”. *J. ACM* 60.6 (Nov. 2013). DOI: 10.1145/2535927 (cited on page 40).

- [Che+14] B.-C. Chen, W. R. Legant, K. Wang, L. Shao, D. E. Milkie, M. W. Davidson, C. Janetopoulos, X. S. Wu, J. A. Hammer, Z. Liu, B. P. English, Y. Mimori-Kiyosue, D. P. Romero, A. T. Ritter, J. Lippincott-Schwartz, L. Fritz-Laylin, R. D. Mullins, D. M. Mitchell, J. N. Bembenek, A.-C. Reymann, R. Böhme, S. W. Grill, J. T. Wang, G. Seydoux, U. S. Tulu, D. P. Kiehart, and E. Betzig. “Lattice light-sheet microscopy: Imaging molecules to embryos at high spatiotemporal resolution”. *Science* 346.6208 (2014), p. 1257998. DOI: 10.1126/science.1257998. eprint: <https://www.science.org/doi/pdf/10.1126/science.1257998> (cited on page 43).
- [Chu+22] K. K. H. Chung, Z. Zhang, P. Kidd, Y. Zhang, N. D. Williams, B. Rollins, Y. Yang, C. Lin, D. Baddeley, and J. Bewersdorf. “Fluorogenic DNA-PAINT for faster, low-background super-resolution imaging”. *Nature Methods* 19.5 (May 2022), pp. 554–559. DOI: 10.1038/s41592-022-01464-9 (cited on pages 32, 69).
- [CJB11] R. W. Cole, T. Jinadasa, and C. M. Brown. “Measuring and interpreting point spread functions to determine confocal microscope resolution and ensure quality control”. *Nature Protocols* 6.12 (Dec. 2011), pp. 1929–1941. DOI: 10.1038/nprot.2011.407 (cited on pages 24, 25).
- [Col13] N. B. Cole. “Site-specific protein labeling with SNAP-tags”. en. *Curr. Protoc. Protein Sci.* 73.1 (Sept. 2013), pp. 30.1.1–30.1.16. DOI: 10.1002/0471140864.ps3001s73 (cited on page 14).
- [Col14] R. Cole. “Live-cell imaging”. en. *Cell Adh. Migr.* 8.5 (Oct. 2014), pp. 452–459 (cited on page 59).
- [Com] C. N. P. Committee. *The Nobel Prize in Chemistry 2014*. en. <https://www.nobelprize.org/prizes/chemistry/2014/summary/>. Accessed: 2023-5-5 (cited on page 26).
- [Cox17] G. Cox. *Optical imaging techniques in cell biology, second edition*. 2nd ed. ISBN: 978-1-4398-4825-8. London, England: CRC Press, Oct. 2017 (cited on pages 19, 20, 80).
- [Cul+18] S. Culley, D. Albrecht, C. Jacobs, P. M. Pereira, C. Letierrier, J. Mercer, and R. Henriques. “Quantitative mapping and minimization of super-resolution optical imaging artifacts”. *Nature Methods* 15.4 (Apr. 2018), pp. 263–266. DOI: 10.1038/nmeth.4605 (cited on pages 38, 69, 70, 75, 109, 141).
- [CWG01] M. K. Cheezum, W. F. Walker, and W. H. Guilford. “Quantitative comparison of algorithms for tracking single fluorescent particles”. en. *Biophys. J.* 81.4 (Oct. 2001), pp. 2378–2388 (cited on page 33).
- [Dan+22] J. S. H. Danial, J. Y. L. Lam, Y. Wu, M. Woolley, E. Dimou, M. R. Cheetham, D. Emin, and D. Klenerman. “Constructing a cost-efficient, high-throughput and high-quality single-molecule localization microscope for super-resolution imaging”. en. *Nat. Protoc.* 17.11 (Nov. 2022), pp. 2570–2619 (cited on page 42).
- [DB20] A. Diaspro and P. Bianchini. “Optical nanoscopy”. *La Rivista del Nuovo Cimento* 43.8 (Aug. 2020), pp. 385–455 (cited on page 11).
- [DC03] R. Dixit and R. Cyr. “Cell damage and reactive oxygen species production induced by fluorescence microscopy: effect on mitosis and guidelines for non-invasive fluorescence microscopy”. en. *Plant J.* 36.2 (Oct. 2003), pp. 280–290 (cited on page 59).
- [Dem+11] G. T. Dempsey, J. C. Vaughan, K. H. Chen, M. Bates, and X. Zhuang. “Evaluation of fluorophores for optimal performance in localization-based super-resolution imaging”. *Nature Methods* 8.12 (Dec. 2011), pp. 1027–1036. DOI: 10.1038/nmeth.1768 (cited on pages 71, 75).
- [Dem08] W. Demtröder. *Experimentalphysik 2: Elektrizität und Optik*. Experimentalphysik / Wolfgang Demtröder. Springer Berlin Heidelberg, 2008 (cited on pages 11, 16, 19).
- [Dem16] W. Demtröder. *Experimentalphysik 3: Atome, Moleküle und Festkörper*. ISBN: 978-3-662-49094-5. Springer-Verlag, 2016 (cited on pages 13, 14).

- [Der+10] T. Dertinger, M. Heilemann, R. Vogel, M. Sauer, and S. Weiss. “Superresolution Optical Fluctuation Imaging with Organic Dyes”. *Angewandte Chemie International Edition* 49.49 (2010), pp. 9441–9443. DOI: <https://doi.org/10.1002/anie.201004138>. eprint: <https://onlinelibrary.wiley.com/doi/pdf/10.1002/anie.201004138> (cited on page 28).
- [DGR19] A. Descloux, K. S. Grußmayer, and A. Radenovic. “Parameter-free image resolution estimation based on decorrelation analysis”. *Nature Methods* 16.9 (Sept. 2019), pp. 918–924. DOI: 10.1038/s41592-019-0515-7 (cited on page 38).
- [Die+19a] B. Diederich, R. Richter, S. Carlstedt, X. Uwurukundo, H. Wang, A. Mosig, and R. Heintzmann. “UC2 – A 3D-printed General-Purpose Optical Toolbox for Microscopic Imaging”. In: *Imaging and Applied Optics 2019 (COSI, IS, MATH, pcAOP)*. Optica Publishing Group, 2019, ITh3B.5. DOI: 10.1364/ISA.2019.ITh3B.5 (cited on pages 26, 45).
- [Die+19b] B. Diederich, P. Then, A. Jügler, R. Förster, and R. Heintzmann. “cellSTORM—Cost-effective super-resolution on a cellphone using dSTORM”. *PLOS ONE* 14.1 (Jan. 2019), pp. 1–18. DOI: 10.1371/journal.pone.0209827 (cited on pages 20, 42).
- [Die+20] B. Diederich, R. Lachmann, S. Carlstedt, B. Marsikova, H. Wang, X. Urukundo, A. S. Mosig, and R. Heintzmann. “A versatile and customizable low-cost 3D-printed open standard for microscopic imaging”. *Nat. Communications* 11 (1 2020), p. 5979. DOI: 10.1038/s41467-020-19447-9 (cited on pages 42, 45, 126).
- [ELC15] C. G. England, H. Luo, and W. Cai. “HaloTag technology: a versatile platform for biomedical applications”. en. *Bioconjug. Chem.* 26.6 (June 2015), pp. 975–986 (cited on page 14).
- [Ewe+05] H. Ewers, A. E. Smith, I. F. Sbalzarini, H. Lilie, P. Koumoutsakos, and A. Helenius. “Single-particle tracking of murine polyoma virus-like particles on live cells and artificial membranes”. *Proceedings of the National Academy of Sciences* 102.42 (2005), pp. 15110–15115. DOI: 10.1073/pnas.0504407102. eprint: <https://www.pnas.org/doi/pdf/10.1073/pnas.0504407102> (cited on page 34).
- [Fab+18] V. Fabricius, J. Lefèvre, H. Geertsema, S. F. Marino, and H. Ewers. “Rapid and efficient C-terminal labeling of nanobodies for DNA-PAINT”. *Journal of Physics D: Applied Physics* 51.47 (Oct. 2018), p. 474005. DOI: 10.1088/1361-6463/aae0e2 (cited on page 124).
- [Fai+14] M. Fairhead, G. Veggiani, M. Lever, J. Yan, D. Mesner, C. V. Robinson, O. Dushek, P. A. van der Merwe, and M. Howarth. “SpyAvidin Hubs Enable Precise and Ultrastable Orthogonal Nanoassembly”. *Journal of the American Chemical Society* 136.35 (Sept. 2014), pp. 12355–12363. DOI: 10.1021/ja505584f (cited on page 87).
- [Fan18] D. Fanelli. “Is science really facing a reproducibility crisis, and do we need it to?” *Proceedings of the National Academy of Sciences* 115.11 (2018), pp. 2628–2631. DOI: 10.1073/pnas.1708272114. eprint: <https://www.pnas.org/doi/pdf/10.1073/pnas.1708272114> (cited on page 80).
- [Fis09] K. N. Fish. “Total internal reflection fluorescence (TIRF) microscopy”. en. *Curr. Protoc. Cytom.* 50.1 (Oct. 2009) (cited on pages 24, 73).
- [FSL17] C. Franke, M. Sauer, and S. van de Linde. “Photometry unlocks 3D information from 2D localization microscopy data”. *Nature Methods* 14.1 (Jan. 2017), pp. 41–44. DOI: 10.1038/nmeth.4073 (cited on pages 29, 35, 74).
- [Gam+06] Y. Gambin, R. Lopez-Esparza, M. Reffay, E. Sierrecki, N. S. Gov, M. Genest, R. S. Hodges, and W. Urbach. “Lateral mobility of proteins in liquid membranes revisited”. *Proceedings of the National Academy of Sciences* 103.7 (2006), pp. 2098–2102. DOI: 10.1073/pnas.0511026103. eprint: <https://www.pnas.org/doi/pdf/10.1073/pnas.0511026103> (cited on page 10).
- [GAT98] B. A. Griffin, S. R. Adams, and R. Y. Tsien. “Specific covalent labeling of recombinant protein molecules inside live cells”. en. *Science* 281.5374 (July 1998), pp. 269–272 (cited on page 15).

- [Geb+21] C. Gebhardt, M. Lehmann, M. M. Reif, M. Zacharias, G. Gemmecker, and T. Cordes. “Molecular and spectroscopic characterization of green and red cyanine fluorophores from the Alexa Fluor and AF series”. en. *Chemphyschem* 22.15 (Aug. 2021), pp. 1566–1583 (cited on pages 71, 118).
- [Gel+13] A. Gelman, J. Carlin, H. Stern, D. Dunson, A. Vehtari, and D. Rubin. *Bayesian Data Analysis*. Chapman & Hall/CRC Texts in Statistical Science. CRC Press, 2013 (cited on page 40).
- [Geo+04] N. George, H. Pick, H. Vogel, N. Johnsson, and K. Johnsson. “Specific labeling of cell surface proteins with chemically diverse compounds”. en. *J. Am. Chem. Soc.* 126.29 (July 2004), pp. 8896–8897 (cited on page 15).
- [Gho+23] S. Ghosh, B. S. Sapkota, R. S. Rao, S. Patil, C. Rajkumar, and S. Lakshminarayan. “Expansion microscopy: A revolution in diagnostic pathology”. en. *J. Microsc.* 290.1 (Apr. 2023), pp. 3–9 (cited on page 28).
- [Gie+05] B. N. G. Giepmans, T. J. Deerinck, B. L. Smarr, Y. Z. Jones, and M. H. Ellisman. “Correlated light and electron microscopic imaging of multiple endogenous proteins using Quantum dots”. en. *Nat. Methods* 2.10 (Oct. 2005), pp. 743–749 (cited on page 26).
- [Gie08] B. N. G. Giepmans. “Bridging fluorescence microscopy and electron microscopy”. en. *Histochem. Cell Biol.* 130.2 (Aug. 2008), pp. 211–217 (cited on page 26).
- [Goo17] J. Goodman. *Introduction to Fourier Optics*. en. 4th ed. ISBN: 978-0974707723. New York, NY: W.H. Freeman, May 2017 (cited on page 11).
- [Gri+15] J. Griffié, L. Boelen, G. Burn, A. P. Cope, and D. M. Owen. “Topographic prominence as a method for cluster identification in single-molecule localisation data”. en. *J. Biophotonics* 8.11-12 (Nov. 2015), pp. 925–934 (cited on page 40).
- [Gül+19] G. S. Gülcüler Balta, C. Monzel, S. Kleber, J. Beaudouin, E. Balta, T. Kaindl, S. Chen, L. Gao, M. Thiemann, C. R. Wirtz, Y. Samstag, M. Tanaka, and A. Martin-Villalba. “3D Cellular Architecture Modulates Tyrosine Kinase Activity, Thereby Switching CD95-Mediated Apoptosis to Survival”. *Cell Reports* 29.8 (2019), 2295–2306.e6. DOI: <https://doi.org/10.1016/j.celrep.2019.10.054> (cited on page 92).
- [Guo+23] C. Guo, G. J. Blair, M. Sehgal, F. N. S. Jimka, A. Bellafard, A. J. Silva, P. Golshani, M. A. Basso, H. T. Blair, and D. Aharoni. “Miniscope-LFOV: A large-field-of-view, single-cell-resolution, miniature microscope for wired and wire-free imaging of neural dynamics in freely behaving animals”. *Science Advances* 9.16 (2023), eadg3918. DOI: 10.1126/sciadv.adg3918. eprint: <https://www.science.org/doi/pdf/10.1126/sciadv.adg3918> (cited on page 43).
- [Gus+16] N. Gustafsson, S. Culley, G. Ashdown, D. M. Owen, P. M. Pereira, and R. Henriques. “Fast live-cell conventional fluorophore nanoscopy with ImageJ through super-resolution radial fluctuations”. *Nature Communications* 7.1 (Aug. 2016), p. 12471 (cited on page 28).
- [Gus00] M. G. L. Gustafsson. “Surpassing the lateral resolution limit by a factor of two using structured illumination microscopy”. *Journal of Microscopy* 198.2 (2000), pp. 82–87. DOI: <https://doi.org/10.1046/j.1365-2818.2000.00710.x>. eprint: <https://onlinelibrary.wiley.com/doi/pdf/10.1046/j.1365-2818.2000.00710.x> (cited on page 27).
- [Hal+22] A. R. Halpern, M. Y. Lee, M. D. Howard, M. A. Woodworth, P. R. Nicovich, and J. C. Vaughan. “Versatile, do-it-yourself, low-cost spinning disk confocal microscope”. en. *Biomed. Opt. Express* 13.2 (Feb. 2022), p. 1102 (cited on page 42).
- [Hay92] D. P. Hayes. “The growing inaccessibility of science”. *Nature* 356.6372 (Apr. 1992), pp. 739–740. DOI: 10.1038/356739a0 (cited on page 41).
- [HC20] J. Horvath and R. Cameron. *Mastering 3D printing*. 2nd ed. ISBN: 978-1-4842-0025-4. Berlin, Germany: APress, May 2020. DOI: <https://doi.org/10.1007/978-1-4842-0025-4> (cited on page 98).
- [Hec15] E. Hecht. *Optics, 5th Edition*. ISBN: 978-8-1317-1807-0. Pearson, 2015 (cited on page 24).

- [Hei+08] M. Heilemann, S. van de Linde, M. Schüttpelz, R. Kasper, B. Seefeldt, A. Mukherjee, P. Tinnefeld, and M. Sauer. “Subdiffraction-Resolution Fluorescence Imaging with Conventional Fluorescent Probes”. *Angewandte Chemie International Edition* 47.33 (2008), pp. 6172–6176. DOI: <https://doi.org/10.1002/anie.200802376> (cited on pages 28, 32).
- [Her+16] R. Hernández Vera, E. Schwan, N. Fatsis-Kavalopoulos, and J. Kreuger. “A Modular and Affordable Time-Lapse Imaging and Incubation System Based on 3D-Printed Parts, a Smartphone, and Off-The-Shelf Electronics”. *PLOS ONE* 11.12 (Dec. 2016), pp. 1–15. DOI: [10.1371/journal.pone.0167583](https://doi.org/10.1371/journal.pone.0167583) (cited on page 42).
- [HK22] Y. Hyun and D. Kim. “Development of deep-learning-based single-molecule localization image analysis”. en. *Int. J. Mol. Sci.* 23.13 (June 2022), p. 6896 (cited on page 83).
- [Hoh+22] J. Hohlbein, B. Diederich, B. Marsikova, E. G. Reynaud, S. Holden, W. Jahr, R. Haase, and K. Prakash. “Open microscopy in the life sciences: quo vadis?” *Nature Methods* 19.9 (Sept. 2022), pp. 1020–1025. DOI: [10.1038/s41592-022-01602-3](https://doi.org/10.1038/s41592-022-01602-3) (cited on pages 41, 128).
- [Hol+14] T. Holm, T. Klein, A. Löschberger, T. Klamp, G. Wiebusch, S. van de Linde, and M. Sauer. “A Blueprint for Cost-Efficient Localization Microscopy”. *ChemPhysChem* 15.4 (2014), pp. 651–654. DOI: <https://doi.org/10.1002/cphc.201300739>. eprint: <https://chemistry-europe.onlinelibrary.wiley.com/doi/pdf/10.1002/cphc.201300739> (cited on page 42).
- [HS17] A. J. Hobro and N. I. Smith. “An evaluation of fixation methods: Spatial and compositional cellular changes observed by Raman imaging”. *Vibrational Spectroscopy* 91 (2017). Prominent Young Vibrational Spectroscopists, pp. 31–45. DOI: <https://doi.org/10.1016/j.vibspec.2016.10.012> (cited on page 92).
- [Hua+13] F. Huang, T. M. P. Hartwich, F. E. Rivera-Molina, Y. Lin, W. C. Duim, J. J. Long, P. D. Uchil, J. R. Myers, M. A. Baird, W. Mothes, M. W. Davidson, D. Toomre, and J. Bewersdorf. “Videorate nanoscopy using sCMOS camera-specific single-molecule localization algorithms”. *Nature Methods* 10.7 (July 2013), pp. 653–658. DOI: [10.1038/nmeth.2488](https://doi.org/10.1038/nmeth.2488) (cited on page 69).
- [HW03] H. Haken and H. Wolf. *Atom- und Quantenphysik*. Physics and astronomy online library. ISBN: 978-3-540-02621-1. Springer-Verlag, 2003 (cited on pages 12, 13).
- [HZM21] M. M. Hanon, L. Zsidai, and Q. Ma. “Accuracy investigation of 3D printed PLA with various process parameters and different colors”. *Materials Today: Proceedings* 42 (Jan. 2021), pp. 3089–3096 (cited on page 125).
- [Ich+17] J. Icha, M. Weber, J. C. Waters, and C. Norden. “Phototoxicity in live fluorescence microscopy, and how to avoid it”. en. *Bioessays* 39.8 (Aug. 2017), p. 1700003 (cited on pages 59, 101).
- [Im+19a] K. Im, S. Mareninov, M. F. P. Diaz, and W. H. Yong. “An introduction to performing immunofluorescence staining”. en. *Methods Mol. Biol.* 1897 (2019), pp. 299–311 (cited on page 7).
- [Im+19b] K. Im, S. Mareninov, M. F. P. Diaz, and W. H. Yong. “An introduction to performing immunofluorescence staining”. en. *Methods Mol. Biol.* 1897 (2019), pp. 299–311 (cited on page 14).
- [Kir+23] A. Kirillov, E. Mintun, N. Ravi, H. Mao, C. Rolland, L. Gustafson, T. Xiao, S. Whitehead, A. C. Berg, W.-Y. Lo, P. Dollár, and R. Girshick. *Segment Anything*. 2023. arXiv: 2304.02643 [cs.CV] (cited on page 85).
- [KNH20a] I. M. Khater, I. R. Nabi, and G. Hamarneh. “A review of super-resolution single-molecule localization microscopy cluster analysis and quantification methods”. en. *Patterns (N. Y.)* 1.3 (June 2020), p. 100038 (cited on pages 40, 87).
- [KNH20b] I. M. Khater, I. R. Nabi, and G. Hamarneh. “A Review of Super-Resolution Single-Molecule Localization Microscopy Cluster Analysis and Quantification Methods”. *Patterns* 1.3 (2020), p. 100038. DOI: <https://doi.org/10.1016/j.patter.2020.100038> (cited on page 83).
- [KR06] A. Khodjakov and C. L. Rieder. “Imaging the division process in living tissue culture cells”. en. *Methods* 38.1 (Jan. 2006), pp. 2–16 (cited on page 59).

- [Kut+21] S. Kutz, A. C. Zehrer, R. Svetlitskii, G. S. Gülcüler Balta, L. Galli, S. Kleber, J. Rentsch, A. Martin-Villalba, and H. Ewers. “An Efficient GUI-Based Clustering Software for Simulation and Bayesian Cluster Analysis of Single-Molecule Localization Microscopy Data”. *Frontiers in Bioinformatics* 1 (2021). DOI: 10.3389/fbinf.2021.723915 (cited on pages 41, 86, 88, 91, 110).
- [Kwa+16] K. Kwakwa, A. Savell, T. Davies, I. Munro, S. Parrinello, M. A. Purbhoo, C. Dunsby, M. A. Neil, and P. M. French. “easySTORM: a robust, lower-cost approach to localisation and TIRF microscopy”. *Journal of Biophotonics* 9.9 (2016), pp. 948–957. DOI: <https://doi.org/10.1002/jbio.201500324>. eprint: <https://onlinelibrary.wiley.com/doi/pdf/10.1002/jbio.201500324> (cited on page 42).
- [LAA16] D. Legland, I. Arganda-Carreras, and P. Andrey. “MorphoLibJ: integrated library and plugins for mathematical morphology with ImageJ”. *Bioinformatics* 32.22 (July 2016), pp. 3532–3534. DOI: 10.1093/bioinformatics/btw413. eprint: https://academic.oup.com/bioinformatics/article-pdf/32/22/3532/49027076/bioinformatics_32_22_3532.pdf (cited on pages 85, 86, 109, 115).
- [Lag+20] M. Lagardère, I. Chamma, E. Bouilhol, M. Nikolski, and O. Thoumine. “FluoSim: simulator of single molecule dynamics for fluorescence live-cell and super-resolution imaging of membrane proteins”. *Scientific Reports* 10.1 (Nov. 2020), p. 19954. DOI: 10.1038/s41598-020-75814-y (cited on pages 31, 87, 117).
- [Lak06] J. R. Lakowicz. *Principles of Fluorescence. 3. Edition*. ISBN: 978-0-387-46312-4. Springer-Verlag, 2006 (cited on pages 12, 14, 15).
- [Lam+22] J. Y. Lam, Y. Wu, E. Dimou, Z. Zhang, M. R. Cheetham, M. Körbel, Z. Xia, D. Klenerman, and J. S. Daniai. “An economic, square-shaped flat-field illumination module for TIRF-based super-resolution microscopy”. *Biophysical Reports* 2.1 (2022), p. 100044. DOI: doi.org/10.1016/j.bpr.2022.100044 (cited on page 107).
- [Lau09] R. D. Launius. “Keep Watching the Skies! The Story of Operation Moonwatch and the Dawn of the Space Age. By W. Patrick McCray.” *Journal of American History* 95.4 (Mar. 2009), pp. 1233–1234. DOI: 10.2307/27694695. eprint: <https://academic.oup.com/jah/article-pdf/95/4/1233/2105415/95-4-1233.pdf> (cited on page 129).
- [Lav21] L. D. Lavis. “Open Chemistry: What if we just give everything away?” *eLife* 10 (Nov. 2021), e74981. DOI: 10.7554/eLife.74981 (cited on pages 41, 128).
- [Law01] S. Lawrence. “Free online availability substantially increases a paper’s impact”. *Nature* 411.6837 (May 2001), pp. 521–521. DOI: 10.1038/35079151 (cited on page 41).
- [Lay+19] M. Lay, N. L. N. Thajudin, Z. A. A. Hamid, A. Rusli, M. K. Abdullah, and R. K. Shuib. “Comparison of physical and mechanical properties of PLA, ABS and nylon 6 fabricated using fused deposition modeling and injection molding”. *Composites Part B: Engineering* 176 (2019), p. 107341. DOI: <https://doi.org/10.1016/j.compositesb.2019.107341> (cited on page 62).
- [Lel+21] M. Lelek, M. T. Gyparaki, G. Beliu, F. Schueder, J. Griffié, S. Manley, R. Jungmann, M. Sauer, M. Lakadamyali, and C. Zimmer. “Single-molecule localization microscopy”. *Nature Reviews Methods Primers* 1.1 (June 2021), p. 39. DOI: 10.1038/s43586-021-00038-x (cited on pages 31, 35, 37, 69, 92, 106).
- [Let] C. Leterrier. *Cleterrier/Christorm: Imagej scripts and macros for processing thunderstorm images* (cited on pages 109, 114).
- [Let+15] C. Leterrier, J. Potier, G. Caillol, C. Debarnot, F. R. Boroni, and B. Dargent. “Nanoscale Architecture of the Axon Initial Segment Reveals an Organized and Robust Scaffold”. *Cell Reports* 13.12 (2015), pp. 2781–2793. DOI: <https://doi.org/10.1016/j.celrep.2015.11.051> (cited on page 35).

- [Li+19] H. Li, H. Soto-Montoya, M. Voisin, L. F. Valenzuela, and M. Prakash. “Octopi: Open configurable high-throughput imaging platform for infectious disease diagnosis in the field”. 2019. DOI: 10.1101/684423. eprint: <https://www.biorxiv.org/content/early/2019/06/27/684423.full.pdf> (cited on page 79).
- [Li+20a] H. Li, D. Krishnamurthy, E. Li, P. Vyas, N. Akireddy, C. Chai, and M. Prakash. “Squid: Simplifying Quantitative Imaging Platform Development and Deployment”. 2020. DOI: 10.1101/2020.12.28.424613. eprint: <https://www.biorxiv.org/content/early/2020/12/29/2020.12.28.424613.full.pdf> (cited on page 42).
- [Li+20b] J. H. Li, P. Santos-Otte, B. Au, J. Rentsch, S. Block, and H. Ewers. “Directed manipulation of membrane proteins by fluorescent magnetic nanoparticles”. en. *Nat. Commun.* 11.1 (Aug. 2020), p. 4259. DOI: 10.1038/s41467-020-18087-3 (cited on pages 33, 67).
- [Lim+11] D. Lim, T. N. Ford, K. K. Chu, and J. Mertz. “Optically sectioned in vivo imaging with speckle illumination HiLo microscopy”. en. *J. Biomed. Opt.* 16.1 (Jan. 2011), p. 016014 (cited on page 23).
- [Lin+11] S. van de Linde, A. Löschberger, T. Klein, M. Heidbreder, S. Wolter, M. Heilemann, and M. Sauer. “Direct stochastic optical reconstruction microscopy with standard fluorescent probes”. *Nature Protocols* 6.7 (July 2011), pp. 991–1009. DOI: 10.1038/nprot.2011.336 (cited on page 31).
- [Lin+15] Y. Lin, J. J. Long, F. Huang, W. C. Duim, S. Kirschbaum, Y. Zhang, L. K. Schroeder, A. A. Rebane, M. G. M. Velasco, A. Virrueta, D. W. Moonan, J. Jiao, S. Y. Hernandez, Y. Zhang, and J. Bewersdorf. “Quantifying and Optimizing Single-Molecule Switching Nanoscopy at High Speeds”. *PLOS ONE* 10.5 (May 2015), pp. 1–20. DOI: 10.1371/journal.pone.0128135 (cited on page 69).
- [Lin19] S. van de Linde. “Single-molecule localization microscopy analysis with ImageJ”. *Journal of Physics D: Applied Physics* 52.20 (2019), p. 203002. DOI: 10.1088/1361-6463/ab092f (cited on pages 35, 109).
- [LJL20] N. Levoine, M. Jean, and P. Legembre. “CD95 Structure, Aggregation and Cell Signaling”. *Frontiers in Cell and Developmental Biology* 8 (2020). DOI: 10.3389/fcell.2020.00314 (cited on pages 90, 92).
- [Luk+14] G. Lukinavičius, L. Reymond, E. D’Este, A. Masharina, F. Göttfert, H. Ta, A. Güther, M. Fournier, S. Rizzo, H. Waldmann, C. Blaukopf, C. Sommer, D. W. Gerlich, H.-D. Arndt, S. W. Hell, and K. Johnsson. “Fluorogenic probes for live-cell imaging of the cytoskeleton”. *Nature Methods* 11.7 (July 2014), pp. 731–733. DOI: 10.1038/nmeth.2972 (cited on page 15).
- [Ma+17] H. Ma, R. Fu, J. Xu, and Y. Liu. “A simple and cost-effective setup for super-resolution localization microscopy”. *Scientific Reports* 7.1 (May 2017), p. 1542. DOI: 10.1038/s41598-017-01606-6 (cited on page 103).
- [Mai+17] A. Maia Chagas, L. L. Prieto-Godino, A. B. Arrenberg, and T. Baden. “The €100 lab: A 3D-printable open-source platform for fluorescence microscopy, optogenetics, and accurate temperature control during behaviour of zebrafish, *Drosophila*, and *Caenorhabditis elegans*”. *PLOS Biology* 15.7 (July 2017), pp. 1–21. DOI: 10.1371/journal.pbio.2002702 (cited on pages 42, 125, 128).
- [Mar+19] K. J. A. Martens, S. P. B. van Beljouw, S. van der Els, J. N. A. Vink, S. Baas, G. A. Vogelaar, S. J. J. Brouns, P. van Baarlen, M. Kleerebezem, and J. Hohlbein. “Visualisation of dCas9 target search in vivo using an open-microscopy framework”. *Nature Communications* 10.1 (Aug. 2019), p. 3552. DOI: 10.1038/s41467-019-11514-0 (cited on page 42).
- [MB20] O. M’Saad and J. Bewersdorf. “Light microscopy of proteins in their ultrastructural context”. *Nature Communications* 11.1 (July 2020), p. 3850. DOI: 10.1038/s41467-020-17523-8 (cited on pages 28, 79).

- [MČK11] J. Michálek, M. Čapek, and L. Kubínová. “Compensation of inhomogeneous fluorescence signal distribution in 2D images acquired by confocal microscopy”. *Microscopy Research and Technique* 74.9 (2011), pp. 831–838. DOI: <https://doi.org/10.1002/jemt.20965>. eprint: <https://analyticalsciencejournals.onlinelibrary.wiley.com/doi/pdf/10.1002/jemt.20965> (cited on pages 102, 109).
- [McQ+18] C. McQuin, A. Goodman, V. Chernyshev, L. Kametsky, B. A. Cimini, K. W. Karhohs, M. Doan, L. Ding, S. M. Rafelski, D. Thirstrup, W. Wiegraebe, S. Singh, T. Becker, J. C. Caicedo, and A. E. Carpenter. “CellProfiler 3.0: Next-generation image processing for biology”. *PLOS Biology* 16.7 (July 2018), pp. 1–17. DOI: 10.1371/journal.pbio.2005970 (cited on page 64).
- [Met+14] R. Metzler, J.-H. Jeon, A. G. Cherstvy, and E. Barkai. “Anomalous diffusion models and their properties: non-stationarity, non-ergodicity, and ageing at the centenary of single particle tracking”. *Phys. Chem. Chem. Phys.* 16 (44 2014), pp. 24128–24164. DOI: 10.1039/C4CP03465A (cited on page 34).
- [Mey+99] T. K. L. Meyvis, S. C. De Smedt, P. Van Oostveldt, and J. Demeester. “Fluorescence Recovery After Photobleaching: A Versatile Tool for Mobility and Interaction Measurements in Pharmaceutical Research”. *Pharmaceutical Research* 16.8 (Aug. 1999), pp. 1153–1162. DOI: 10.1023/A:1011924909138 (cited on page 10).
- [MK13] V. Magidson and A. Khodjakov. “Circumventing photodamage in live-cell microscopy”. en. *Methods Cell Biol.* 114 (2013), pp. 545–560 (cited on page 60).
- [MLW13] A. Martin-Villalba, E. Llorens-Bobadilla, and D. Wollny. “CD95 in cancer: tool or target?” en. *Trends Mol. Med.* 19.6 (June 2013), pp. 329–335 (cited on page 90).
- [Mon+21] P. Montero Llopis, R. A. Senft, T. J. Ross-Elliott, R. Stephansky, D. P. Keeley, P. Koshar, G. Marqués, Y.-S. Gao, B. R. Carlson, T. Pengo, M. A. Sanders, L. A. Cameron, and M. S. Itano. “Best practices and tools for reporting reproducible fluorescence microscopy methods”. *Nature Methods* 18.12 (Dec. 2021), pp. 1463–1476. DOI: 10.1038/s41592-021-01156-w (cited on pages 73, 80).
- [Mor+10] K. I. Mortensen, L. S. Churchman, J. A. Spudich, and H. Flyvbjerg. “Optimized localization analysis for single-molecule tracking and super-resolution microscopy”. *Nature Methods* 7.5 (May 2010), pp. 377–381. DOI: 10.1038/nmeth.1447 (cited on pages 30, 33, 37).
- [Mor+21] X. C. Moreno, S. Al-Kadhimi, J. Alvelid, A. Bodén, and I. Testa. “ImSwitch: Generalizing microscope control in Python”. *Journal of Open Source Software* 6.64 (2021), p. 3394. DOI: 10.21105/joss.03394 (cited on pages 47, 48).
- [Neu20] J. Neuendorf. “Setting-Up Köhler Illumination”. In: *Urine Sediment*. ISBN: 978-3-030-15911-5. Cham: Springer International Publishing, 2020, pp. 7–9. DOI: 10.1007/978-3-030-15911-5_2 (cited on pages 80, 101, 102).
- [Nic13] G. L. Nicolson. “Update of the 1972 Singer-Nicolson Fluid-Mosaic Model of membrane structure”. en. *Discoveries (Craiova)* 1.1 (Dec. 2013), e3 (cited on page 9).
- [Nie+13] R. P. J. Nieuwenhuizen, K. A. Lidke, M. Bates, D. L. Puig, D. Grünwald, S. Stallinga, and B. Rieger. “Measuring image resolution in optical nanoscopy”. *Nature Methods* 10.6 (June 2013), pp. 557–562. DOI: 10.1038/nmeth.2448 (cited on pages 37, 76, 109).
- [Nie+23] D. J. Nieves, J. A. Pike, F. Levet, D. J. Williamson, M. Baragilly, S. Oloketuyi, A. de Marco, J. Griffié, D. Sage, E. A. K. Cohen, J.-B. Sibarita, M. Heilemann, and D. M. Owen. “A framework for evaluating the performance of SMLM cluster analysis algorithms”. *Nature Methods* 20.2 (Feb. 2023), pp. 259–267. DOI: 10.1038/s41592-022-01750-6 (cited on pages 87, 89).
- [Oli+13] N. Olivier, D. Keller, P. Gönczy, and S. Manley. “Resolution Doubling in 3D-STORM Imaging through Improved Buffers”. *PLOS ONE* 8.7 (July 2013), pp. 1–9. DOI: 10.1371/journal.pone.0069004 (cited on page 35).

- [ORW04] R. J. Ober, S. Ram, and E. S. Ward. “Localization Accuracy in Single-Molecule Microscopy”. *Biophysical Journal* 86.2 (2004), pp. 1185–1200. DOI: [https://doi.org/10.1016/S0006-3495\(04\)74193-4](https://doi.org/10.1016/S0006-3495(04)74193-4) (cited on pages 29, 37).
- [Ove+14] M. Ovesný, P. Křížek, J. Borkovec, Z. Švindrych, and G. M. Hagen. “ThunderSTORM: a comprehensive ImageJ plug-in for PALM and STORM data analysis and super-resolution imaging”. *Bioinformatics* 30.16 (2014), pp. 2389–2390. DOI: [10.1093/bioinformatics/btu202](https://doi.org/10.1093/bioinformatics/btu202) (cited on pages 29, 32, 35, 56, 68, 71, 109, 113).
- [Owe+10] D. M. Owen, C. Rentero, J. Rossy, A. Magenau, D. Williamson, M. Rodriguez, and K. Gaus. “PALM imaging and cluster analysis of protein heterogeneity at the cell surface”. *Journal of Biophotonics* 3.7 (2010), pp. 446–454. DOI: <https://doi.org/10.1002/jbio.200900089>. eprint: <https://onlinelibrary.wiley.com/doi/pdf/10.1002/jbio.200900089> (cited on page 87).
- [PB08] M. G. Paulick and C. R. Bertozzi. “The Glycosylphosphatidylinositol Anchor: A Complex Membrane-Anchoring Structure for Proteins”. *Biochemistry* 47.27 (July 2008), pp. 6991–7000. DOI: [10.1021/bi8006324](https://doi.org/10.1021/bi8006324) (cited on page 90).
- [PE06] R. Pepperkok and J. Ellenberg. “High-throughput fluorescence microscopy for systems biology”. *Nature Reviews Molecular Cell Biology* 7.9 (Sept. 2006), pp. 690–696. DOI: [10.1038/nrm1979](https://doi.org/10.1038/nrm1979) (cited on page 43).
- [Pie+15] T. Pietzsch, S. Saalfeld, S. Preibisch, and P. Tomancak. “BigDataViewer: visualization and processing for large image data sets”. *Nature Methods* 12.6 (June 2015), pp. 481–483. DOI: [10.1038/nmeth.3392](https://doi.org/10.1038/nmeth.3392) (cited on page 109).
- [Pik+19] J. A. Pike, A. O. Khan, C. Pallini, S. G. Thomas, M. Mund, J. Ries, N. S. Poulter, and I. B. Styles. “Topological data analysis quantifies biological nano-structure from single molecule localization microscopy”. *Bioinformatics* 36.5 (Oct. 2019), pp. 1614–1621. DOI: [10.1093/bioinformatics/btz788](https://doi.org/10.1093/bioinformatics/btz788). eprint: https://academic.oup.com/bioinformatics/article-pdf/36/5/1614/50553139/bioinformatics_36_5_1614.pdf (cited on pages 86, 87).
- [PKA15] J. L. Puga, M. Krzywinski, and N. Altman. “Bayes’ theorem”. *Nature Methods* 12.4 (Apr. 2015), pp. 277–278. DOI: [10.1038/nmeth.3335](https://doi.org/10.1038/nmeth.3335) (cited on page 40).
- [Pol+17] T. D. Pollard, W. C. Earnshaw, J. Lippincott-Schwartz, and G. T. Johnson, eds. *Cell Biology*. Third Edition. Elsevier, 2017. DOI: <https://doi.org/10.1016/B978-0-323-34126-4.00008-6> (cited on pages 8, 71).
- [Pol+22] T. Pollina, A. G. Larson, F. Lombard, H. Li, D. Le Guen, S. Colin, C. de Vargas, and M. Prakash. “PlanktoScope: Affordable Modular Quantitative Imaging Platform for Citizen Oceanography”. *Frontiers in Marine Science* 9 (2022). DOI: [10.3389/fmars.2022.949428](https://doi.org/10.3389/fmars.2022.949428) (cited on page 129).
- [PPL02] K. L. Pierce, R. T. Premont, and R. J. Lefkowitz. “Seven-transmembrane receptors”. en. *Nat. Rev. Mol. Cell Biol.* 3.9 (Sept. 2002), pp. 639–650 (cited on page 86).
- [PST09] S. Preibisch, S. Saalfeld, and P. Tomancak. “Globally optimal stitching of tiled 3D microscopic image acquisitions”. *Bioinformatics* 25.11 (Apr. 2009), pp. 1463–1465. DOI: [10.1093/bioinformatics/btp184](https://doi.org/10.1093/bioinformatics/btp184). eprint: <https://academic.oup.com/bioinformatics/article-pdf/25/11/1463/950295/btp184.pdf> (cited on pages 57, 58, 109, 115).
- [QSE91] H. Qian, M. P. Sheetz, and E. L. Elson. “Single particle tracking. Analysis of diffusion and flow in two-dimensional systems”. en. *Biophys. J.* 60.4 (Oct. 1991), pp. 910–921 (cited on page 34).
- [Ray79] Rayleigh. *XXXI. Investigations in optics, with special reference to the spectroscope*. Oct. 1879. DOI: [10.1080/14786447908639684](https://doi.org/10.1080/14786447908639684) (cited on page 30).
- [RBZ06] M. J. Rust, M. Bates, and X. Zhuang. “Sub-diffraction-limit imaging by stochastic optical reconstruction microscopy (STORM)”. *Nat. Methods* 3 (10 2006), pp. 793–796. DOI: [10.1038/nmeth929](https://doi.org/10.1038/nmeth929) (cited on pages 28, 32).

- [Rie+12] J. Ries, C. Kaplan, E. Platonova, H. Eghlidi, and H. Ewers. “A simple, versatile method for GFP-based super-resolution microscopy via nanobodies”. *Nature Methods* 9.6 (June 2012), pp. 582–584 (cited on pages 7, 14).
- [Rie20] J. Ries. “SMAP: a modular super-resolution microscopy analysis platform for SMLM data”. *Nat. Methods* 17 (2020), pp. 870–872. DOI: 10.1038/s41592-020-0938-1 (cited on pages 29, 35).
- [Rob15] L. A. Robertson. “van Leeuwenhoek microscopes—where are they now?” *FEMS Microbiology Letters* 362.9 (Apr. 2015). fnv056. DOI: 10.1093/femsle/fnv056. eprint: <https://academic.oup.com/femsle/article-pdf/362/9/fnv056/23926222/fnv056.pdf> (cited on page 11).
- [Ros77] H. E. Rosenberger. “Differential Interference Contrast Microscopy”. In: *Interpretive Techniques for Microstructural Analysis*. Ed. by J. L. McCall and P. M. French. ISBN: 978-1-4684-2370-9. Boston, MA: Springer US, 1977, pp. 79–104. DOI: 10.1007/978-1-4684-2370-9_5 (cited on pages 80, 101).
- [Rub+15] P. Rubin-Delanchy, G. L. Burn, J. Griffié, D. J. Williamson, N. A. Heard, A. P. Cope, and D. M. Owen. “Bayesian cluster identification in single-molecule localization microscopy data”. *Nature Methods* 12.11 (Nov. 2015), pp. 1072–1076. DOI: 10.1038/nmeth.3612 (cited on page 40).
- [Rus87] E. Ruska. “Nobel lecture. The development of the electron microscope and of electron microscopy”. en. *Biosci. Rep.* 7.8 (Aug. 1987), pp. 607–629 (cited on page 26).
- [Saa+22] S. Saalfeld, I. Pisarev, P. Hanslovsky, A. Champion, C. Rueden, J. Bogovic, M. Kittisopikul, and jakirkham. *saalfeldlab/n5: n5-2.5.1*. Version n5-2.5.1. May 2022. DOI: 10.5281/zenodo.6578232 (cited on pages 71, 109).
- [Sag+17] D. Sage, L. Donati, F. Soulez, D. Fortun, G. Schmit, A. Seitz, R. Guiet, C. Vonesch, and M. Unser. “DeconvolutionLab2: An open-source software for deconvolution microscopy”. en. *Methods* 115 (Feb. 2017), pp. 28–41 (cited on page 22).
- [Sag+19] D. Sage, T. A. Pham, H. Babcock, T. Lukes, T. Pengo, J. Chao, R. Vermurugan, A. Herbert, A. Agrawal, S. Colabrese, A. Wheeler, A. Archetti, B. Rieger, R. Henriques, M. Unser, and S. Holden. “Super-resolution fight club: assessment of 2D and 3D single-molecule localization microscopy software”. *Nat. Methods* 16 (5 2019), pp. 387–395. DOI: 10.1038/s41592-019-0364-4 (cited on page 35).
- [Say+77] D. Sayre, J. Kirz, R. Feder, D. M. Kim, and E. Spiller. “Potential Operating Region for Ultrafast X-Ray Microscopy of Biological Materials”. *Science* 196.4296 (1977), pp. 1339–1340. DOI: 10.1126/science.867033. eprint: <https://www.science.org/doi/pdf/10.1126/science.867033> (cited on page 26).
- [Sch+12a] J. Schindelin, I. Arganda-Carreras, E. Frise, V. Kaynig, M. Longair, T. Pietzsch, S. Preibisch, C. Rueden, S. Saalfeld, B. Schmid, J.-Y. Tinevez, D. J. White, V. Hartenstein, K. Eliceiri, P. Tomancak, and A. Cardona. “Fiji: an open-source platform for biological-image analysis”. *Nature Methods* 9.7 (July 2012), pp. 676–682. DOI: 10.1038/nmeth.2019 (cited on pages 35, 71, 109).
- [Sch+12b] H. Schneckenburger, P. Weber, M. Wagner, S. Schickinger, V. Richter, T. Bruns, W. S. L. Strauss, and R. Wittig. “Light exposure and cell viability in fluorescence microscopy”. en. *J. Microsc.* 245.3 (Mar. 2012), pp. 311–318 (cited on pages 59, 101).
- [Sch+17] J. Schnitzbauer, M. T. Strauss, T. Schlichthaerle, F. Schueder, and R. Jungmann. “Super-resolution microscopy with DNA-PAINT”. *Nature Protocols* 12.6 (June 2017), pp. 1198–1228 (cited on page 32).
- [Sch+21] R. Schmidt, T. Weihs, C. A. Wurm, I. Jansen, J. Rehman, S. J. Sahl, and S. W. Hell. “MIN-FLUX nanometer-scale 3D imaging and microsecond-range tracking on a common fluorescence microscope”. en. *Nat. Commun.* 12.1 (Mar. 2021), p. 1478 (cited on page 43).
- [SD75] P. G. Saffman and M. Delbrück. “Brownian motion in biological membranes”. en. *Proc. Natl. Acad. Sci. U. S. A.* 72.8 (Aug. 1975), pp. 3111–3113 (cited on page 10).

- [Sha+16] J. P. Sharkey, D. C. W. Foo, A. Kabla, J. J. Baumberg, and R. W. Bowman. “A one-piece 3D printed flexure translation stage for open-source microscopy”. *Review of Scientific Instruments* 87.2 (2016), p. 025104. DOI: 10.1063/1.4941068. eprint: <https://doi.org/10.1063/1.4941068> (cited on pages 42, 48).
- [Sha+22] A. H. Shaib, A. A. Chouaib, V. Imani, R. Chowdhury, S. V. Georgiev, N. Mougios, M. Monga, S. Reshetniak, D. Mihaylov, H. Chen, P. Fatehbasharadz, D. Crzan, K.-A. Saal, C. Trenkwalder, B. Mollenhauer, T. F. Outeiro, J. Preobraschenski, U. Becherer, T. Moser, E. S. Boyden, A. R. Aricescu, M. Sauer, F. Opazo, and S. O. Rizzoli. “Expansion microscopy at one nanometer resolution”. *bioRxiv* (2022). DOI: 10.1101/2022.08.03.502284. eprint: <https://www.biorxiv.org/content/early/2022/08/05/2022.08.03.502284.full.pdf> (cited on page 7).
- [Sha49] C. Shannon. “Communication in the Presence of Noise”. *Proceedings of the IRE* 37.1 (Jan. 1949), pp. 10–21. DOI: 10.1109/jrproc.1949.232969 (cited on page 21).
- [She+17] H. Shen, L. J. Tazuin, R. Baiyasi, W. Wang, N. Moringo, B. Shuang, and C. F. Landes. “Single Particle Tracking: From Theory to Biophysical Applications”. *Chemical Reviews* 117.11 (June 2017), pp. 7331–7376. DOI: 10.1021/acs.chemrev.6b00815 (cited on page 33).
- [SHS16] S. Skylaki, O. Hilsenbeck, and T. Schroeder. “Challenges in long-term imaging and quantification of single-cell dynamics”. en. *Nat. Biotechnol.* 34.11 (Nov. 2016), pp. 1137–1144 (cited on page 59).
- [SK05] I. Sbalzarini and P. Koumoutsakos. “Feature point tracking and trajectory analysis for video imaging in cell biology”. *Journal of Structural Biology* 151.2 (2005), pp. 182–195. DOI: <https://doi.org/10.1016/j.jsb.2005.06.002> (cited on pages 33, 34, 66–68, 109, 116).
- [Sof+22] N. Sofroniew, T. Lambert, K. Evans, J. Nunez-Iglesias, G. Bokota, P. Winston, G. Peña-Castellanos, K. Yamauchi, M. Bussonnier, D. Doncila Pop, A. Can Solak, Z. Liu, P. Wadhwa, A. Burt, G. Buckley, A. Sweet, L. Migas, V. Hilsenstein, L. Gaifas, J. Bragantini, J. Rodríguez-Guerra, H. Muñoz, J. Freeman, P. Boone, A. Lowe, C. Gohlke, L. Royer, A. PIERRÉ, H. Har-Gil, and A. McGovern. *napari: a multi-dimensional image viewer for Python*. Version v0.4.17rc8. If you use this software, please cite it using these metadata. Nov. 2022. DOI: 10.5281/zenodo.7276432 (cited on pages 36, 71).
- [Spe+21] A. Speiser, L.-R. Müller, P. Hoess, U. Matti, C. J. Obara, W. R. Legant, A. Kreshuk, J. H. Macke, J. Ries, and S. C. Turaga. “Deep learning enables fast and dense single-molecule localization with high accuracy”. *Nature Methods* 18.9 (Sept. 2021), pp. 1082–1090. DOI: 10.1038/s41592-021-01236-x (cited on pages 83, 92).
- [SR10] S. Stallinga and B. Rieger. “Accuracy of the gaussian point spread function model in 2D localization microscopy”. en. *Opt. Express* 18.24 (Nov. 2010), pp. 24461–24476 (cited on page 29).
- [SRE12] C. A. Schneider, W. S. Rasband, and K. W. Eliceiri. “NIH Image to ImageJ: 25 years of image analysis”. *Nature Methods* 9.7 (July 2012), pp. 671–675. DOI: 10.1038/nmeth.2089 (cited on pages 34, 35, 109).
- [Str+21] C. Stringer, T. Wang, M. Michaelos, and M. Pachitariu. “Cellpose: a generalist algorithm for cellular segmentation”. *Nature Methods* 18.1 (Jan. 2021), pp. 100–106. DOI: 10.1038/s41592-020-01018-x (cited on page 84).
- [Svi17] T. M. Svitkina. “Platinum replica electron microscopy: Imaging the cytoskeleton globally and locally”. en. *Int. J. Biochem. Cell Biol.* 86 (May 2017), pp. 37–41 (cited on page 26).
- [Tin+12] J.-Y. Tinevez, J. Dragavon, L. Baba-Aissa, P. Roux, E. Perret, A. Canivet, V. Galy, and S. Shorte. “A quantitative method for measuring phototoxicity of a live cell imaging microscope”. en. *Methods Enzymol.* 506 (2012), pp. 291–309 (cited on page 59).

- [Tin+17] J.-Y. Tinevez, N. Perry, J. Schindelin, G. M. Hoopes, G. D. Reynolds, E. Laplantine, S. Y. Bednarek, S. L. Shorte, and K. W. Eliceiri. “TrackMate: An open and extensible platform for single-particle tracking”. *Methods* 115 (2017). Image Processing for Biologists, pp. 80–90. DOI: <https://doi.org/10.1016/j.ymeth.2016.09.016> (cited on pages 33, 34, 109).
- [TLW02] R. E. Thompson, D. R. Larson, and W. W. Webb. “Precise nanometer localization analysis for individual fluorescent probes”. en. *Biophys. J.* 82.5 (May 2002), pp. 2775–2783 (cited on page 30).
- [Tsi09] R. Y. Tsien. “Constructing and exploiting the fluorescent protein paintbox (Nobel Lecture)”. en. *Angew. Chem. Int. Ed Engl.* 48.31 (2009), pp. 5612–5626 (cited on page 14).
- [Tui+19] M. W. Tuijtel, A. J. Koster, S. Jakobs, F. G. A. Faas, and T. H. Sharp. “Correlative cryo super-resolution light and electron microscopy on mammalian cells using fluorescent proteins”. *Scientific Reports* 9.1 (Feb. 2019), p. 1369. DOI: [10.1038/s41598-018-37728-8](https://doi.org/10.1038/s41598-018-37728-8) (cited on page 43).
- [Voi+19] F. F. Voigt, D. Kirschenbaum, E. Platonova, S. Pagès, R. A. A. Campbell, R. Kastli, M. Schaettin, L. Egolf, A. van der Bourg, P. Bethge, K. Haenraets, N. Frézel, T. Topilko, P. Perin, D. Hillier, S. Hildebrand, A. Schueth, A. Roebroek, B. Roska, E. T. Stoeckli, R. Pizzala, N. Renier, H. U. Zeilhofer, T. Karayannis, U. Ziegler, L. Batti, A. Holtmaat, C. Lüscher, A. Aguzzi, and F. Helmchen. “The mesoSPIM initiative: open-source light-sheet microscopes for imaging cleared tissue”. *Nature Methods* 16.11 (Nov. 2019), pp. 1105–1108. DOI: [10.1038/s41592-019-0554-0](https://doi.org/10.1038/s41592-019-0554-0) (cited on page 42).
- [vS05] M. van Heel and M. Schatz. “Fourier shell correlation threshold criteria”. *Journal of Structural Biology* 151.3 (2005), pp. 250–262. DOI: <https://doi.org/10.1016/j.jsb.2005.05.009> (cited on pages 38, 75).
- [vS14] S. van de Linde and M. Sauer. “How to switch a fluorophore: from undesired blinking to controlled photoswitching”. *Chem. Soc. Rev.* 43 (4 2014), pp. 1076–1087. DOI: [10.1039/C3CS60195A](https://doi.org/10.1039/C3CS60195A) (cited on pages 31, 32, 118).
- [Wal+15] M. P. Walzik, V. Vollmar, T. Lachnit, H. Dietz, S. Haug, H. Bachmann, M. Fath, D. Aschenbrenner, S. Abolpour Mofrad, O. Friedrich, and D. F. Gilbert. “A portable low-cost long-term live-cell imaging platform for biomedical research and education”. *Biosensors and Bioelectronics* 64 (2015), pp. 639–649. DOI: <https://doi.org/10.1016/j.bios.2014.09.061> (cited on page 42).
- [Wäl+15] S. Wäldchen, J. Lehmann, T. Klein, S. van de Linde, and M. Sauer. “Light-induced cell damage in live-cell super-resolution microscopy”. en. *Sci. Rep.* 5.1 (Oct. 2015), p. 15348 (cited on pages 59, 101).
- [Wan+22] H. Wang, R. Lachmann, B. Marsikova, R. Heintzmann, and B. Diederich. “UCsim2: two-dimensionally structured illumination microscopy using UC2”. *Philosophical transactions of the royal society A* 380 (2220 2022). DOI: [10.1038/s41467-020-19447-9](https://doi.org/10.1038/s41467-020-19447-9) (cited on pages 46, 55).
- [WB12] D. J. Webb and C. M. Brown. “Epi-Fluorescence Microscopy”. In: *Methods in Molecular Biology*. Methods in molecular biology (Clifton, N.J.) Totowa, NJ: Humana Press, 2012, pp. 29–59 (cited on page 23).
- [WB15] D. R. Whelan and T. D. M. Bell. “Image artifacts in Single Molecule Localization Microscopy: why optimization of sample preparation protocols matters”. *Scientific Reports* 5 (2015), p. 7924. DOI: [10.1038/srep07924](https://doi.org/10.1038/srep07924) (cited on page 69).
- [Wei+00] D. Weiß, G. Schneider, B. Niemann, P. Guttmann, D. Rudolph, and G. Schmahl. “Computed tomography of cryogenic biological specimens based on X-ray microscopic images”. *Ultramicroscopy* 84.3 (2000), pp. 185–197. DOI: [https://doi.org/10.1016/S0304-3991\(00\)00034-6](https://doi.org/10.1016/S0304-3991(00)00034-6) (cited on page 26).

- [Wen+16] Z. Weng, J. Wang, T. Senthil, and L. Wu. “Mechanical and thermal properties of ABS/montmorillonite nanocomposites for fused deposition modeling 3D printing”. *Materials & Design* 102 (2016), pp. 276–283. DOI: <https://doi.org/10.1016/j.matdes.2016.04.045> (cited on pages 62, 125).
- [Wen23] T. Wenzel. “Open hardware: From DIY trend to global transformation in access to laboratory equipment”. *PLOS Biology* 21.1 (Jan. 2023), pp. 1–16. DOI: [10.1371/journal.pbio.3001931](https://doi.org/10.1371/journal.pbio.3001931) (cited on pages 41, 47, 128).
- [Wil+06] K. I. Willig, S. O. Rizzoli, V. Westphal, R. Jahn, and S. W. Hell. “STED microscopy reveals that synaptotagmin remains clustered after synaptic vesicle exocytosis”. *Nature* 440 (7086 2006), pp. 935–939. DOI: [10.1038/nature04592](https://doi.org/10.1038/nature04592) (cited on page 27).
- [Wil+20] D. J. Williamson, G. L. Burn, S. Simoncelli, J. Griffié, R. Peters, D. M. Davis, and D. M. Owen. “Machine learning for cluster analysis of localization microscopy data”. *Nature Communications* 11.1 (Mar. 2020), p. 1493. DOI: [10.1038/s41467-020-15293-x](https://doi.org/10.1038/s41467-020-15293-x) (cited on page 90).
- [Wu+20] Y.-L. Wu, A. Tschanz, L. Krupnik, and J. Ries. “Quantitative Data Analysis in Single-Molecule Localization Microscopy”. *Trends in Cell Biology* 30.11 (2020), pp. 837–851. DOI: <https://doi.org/10.1016/j.tcb.2020.07.005> (cited on pages 71, 75).
- [Yeu+20] M. Yeung, A. Abdulmajeed, C. K. Carrico, G. R. Deeb, and S. Bencharit. “Accuracy and precision of 3D-printed implant surgical guides with different implant systems: An in vitro study”. *The Journal of Prosthetic Dentistry* 123.6 (2020), pp. 821–828. DOI: <https://doi.org/10.1016/j.prosdent.2019.05.027> (cited on page 125).
- [Yu+21] L. Yu, Y. Lei, Y. Ma, M. Liu, J. Zheng, D. Dan, and P. Gao. “A Comprehensive Review of Fluorescence Correlation Spectroscopy”. *Frontiers in Physics* 9 (2021). DOI: [10.3389/fphy.2021.644450](https://doi.org/10.3389/fphy.2021.644450) (cited on page 10).
- [Zeh+22] A. Zehtabian, P. M. Müller, M. Goisser, L. Obendorf, L. Jänisch, N. Hümpfer, J. Rentsch, and H. Ewers. “Precise measurement of nanoscopic septin ring structures with deep learning-assisted quantitative superresolution microscopy”. en. *Mol. Biol. Cell* 33.8 (July 2022), ar76 (cited on page 85).
- [Zun+15] J. Zuniga, D. Katsavelis, J. Peck, J. Stollberg, M. Petrykowski, A. Carson, and C. Fernandez. “Cyborg beast: a low-cost 3d-printed prosthetic hand for children with upper-limb differences”. en. *BMC Res. Notes* 8.1 (Jan. 2015), p. 10 (cited on page 125).

Websites

- [Ban+] E. Bandason, I. Akinrinade, E. Ngala, P. Akyaw, TReND, and Tom. *TReND in Africa*. URL: <https://trendinafrica.org/> (visited on Feb. 10, 2023) (cited on page 129).
- [Chr16] Chroma Technology Corp. *Knowledge & Resources*. Feb. 2016. URL: <https://www.chroma.com/knowledge-resources> (visited on Jan. 19, 2023) (cited on page 107).
- [Edu] Educmad. *Ressources éducatives*. URL: <http://mediatheque.accesmad.org/educmad/course/index.php?categoryid=169> (visited on Feb. 15, 2023) (cited on page 129).
- [Ita] Itatra. *A non-profit organisation for: "A better and equal education for all."* URL: <https://www.itatra.org/> (visited on Feb. 15, 2023) (cited on page 129).
- [KS] S. Kutz and R. Svetlickii. *Saskiakutz/baclava: GUI for bayesian cluster analysis of SMLM Data*. URL: <https://github.com/saskiakutz/BaClAva> (visited on Feb. 10, 2023) (cited on pages 41, 89, 110).
- [Ope] OpenUC2. *UC2 - Open and Modular Optical Toolbox*. OpenUC2. URL: <https://github.com/openUC2/UC2-GIT> (visited on Jan. 30, 2023) (cited on pages 45, 46).

- [Pho] T. Photometrics. *Camera basics. Educational resources*. URL: <https://www.photometrics.com/learn/camera-basics> (visited on Jan. 30, 2023) (cited on pages 20, 22).
- [Prua] Prusa Research. *Material guide: ABS*. Prusa. URL: https://help.prusa3d.com/article/abs_2058 (visited on Jan. 19, 2023) (cited on pages 62, 99).
- [Prub] Prusa Research. *Material guide: PLA*. Prusa. URL: https://help.prusa3d.com/article/pla_2062 (visited on Jan. 19, 2023) (cited on page 99).
- [Rue+] C. Rueden, R. Ejsmont, G. M. Fleischmann, and K. M. Douglass. *HDF5 VIBEZ: HDF5 plugin for Imagej and Fiji*. URL: https://github.com/fiji/HDF5_Vibez/ (visited on Mar. 14, 2023) (cited on pages 71, 109).

This thesis was typeset with \LaTeX 2 ϵ . It uses the *Clean Thesis* style developed by Ricardo Langner. The design of the *Clean Thesis* style is inspired by user guide documents from Apple Inc.

Download the *Clean Thesis* style at <http://cleanthesis.der-ric.de/>.

List of publications

Publications related to this thesis:

- Ando C. Zehrer, Ana Martin-Villalba, Benedict Diederich, and Helge Ewers. (2023). "An open-source, high resolution, automated fluorescence microscope." bioRxiv, 2023.05.31.542706. doi:10.1101/2023.05.31.54270 (eLife, in revision)
- Saskia Kutz, Ando C. Zehrer, Roman Svetlitskii, Gülce S. Gülcüler Balta, Lucrezia Galli, Susanne Kleber, Jakob Rentsch, Ana Martin-Villalba and Helge Ewers (2021). "An Efficient GUI-Based Clustering Software for Simulation and Bayesian Cluster Analysis of Single-Molecule Localization Microscopy Data." *Frontiers in Bioinformatics*, 1. doi:10.3389/fbinf.2021.723915

Conference contributions

2018:

- **Poster** - „Correlative X-ray and fluorescence microscopy“; Winter school, April 2018, Les Houches, France.
- **Poster** - „Combining density-based artifact-free and Bayesian cluster analysis tools for studying the characteristics of membrane-protein organization“; Single molecule localization symposium August 2018, Berlin, Germany.

2021:

- **Poster** - „An efficient GUI-based clustering software for simulation and Bayesian cluster analysis of single-molecule localization microscopy data“; Single molecule localization symposium September 2021, Lausanne, Switzerland.

2022:

- **Workshop faculty assistant** - „UC2, an open-source microscopy platform.“; Analytical and Quantitative Light Microscopy, September 2022, Woods Hole, United States.
- **Poster** - „Cubistic pointillism - the art of making super resolution cost effective.“; Methods and application of fluorescence, September 2022, Gothenborg, Sweden.
- **Poster** - „Cost effective resolution: from live cells to single molecules.“; SFB TRR186 Annual meeting, Octobre 2022, Berlin, Germany.